CORA Cork Open Research Archive
Cartlann Taighde Oscailte Chorcaí

Title	Ultrasoft magnetic materials processing and characterisation
Authors	Dixon, Ehren
Publication date	2020-08-31
Original Citation	Dixon, E. 2020. Ultrasoft magnetic materials processing and characterisation. MRes Thesis, University College Cork.
Type of publication	Masters thesis (Research)
Rights	© 2020, Ehren Dixon. - https://creativecommons.org/licenses/by-nc-nd/4.0/
Download date	2026-11-08 08:39:18
Item downloaded from	https://hdl.handle.net/10468/10930



UCC
University College Cork, Ireland
Coláiste na hOllscoile Corcaigh

Ollscoil na hÉireann, Corcaigh

National University of Ireland, Cork



Ultrasoft magnetic materials processing and characterisation.

Dissertation presented by

Ehren Dixon, B.Sc.Ed, AMRSC

orcid.org/0000-0002-2503-3699

for the degree of

Masters of Science

University College Cork

School of Chemistry / Tyndall National Institute

Head of School: Dr Humphrey Moynihan
Supervisor: Dr James F. Rohan
Advisor: Dr Dave Otway

2020

Copyright © Ehren Dixon 2020



UCC

University College Cork, Ireland
Coláiste na hOllscoile Corcaigh



Tyndall
National Institute
Institiúid Náisiúnta



Fondúireacht Eolaíochta Éireann
Dá bhfuil romhainn

Science Foundation Ireland
For what's next

To my friends & family

Thank you

+1 INT

Declaration of Orginality:

This is to certify that the work I am submitting is my own and has not been submitted for another degree, either at University College Cork or elsewhere. All external references and sources are clearly acknowledged and identified within the contents. I have read and understood the regulations of University College Cork concerning plagiarism.

Acknowledgements

I want to thank Science Foundation Ireland, whose financial support in terms of their Technology Innovation Development Award allowed this project to be completed. While I cannot thank him enough, I am especially indebted to Dr James Rohan for offering me this fantastic postgraduate opportunity, supervising & supporting me during this project. Here is to the next project!

Special thanks to Dr Declan Casey for the outstanding help and support during the laboratory processes in this project, Pranay Podder for material and device analysis & Joe O'Brien and the whole Tyndall Fabrication team for the production of devices. Additionally, a huge thanks to Daniel Smallwood for working alongside me in the offices, in the lab and in general, putting up with me for the last year.

Many thanks to all the rest of the members of my group including Dr Lorraine Nagle, Louise McGrath, Ian Seymour, Fiona Barry & Aaron O'Donoghue for the help and support I received and hopefully gave in some way.

I would also like to thank Tyndall National Institute for offering me a position here and allowing me the use of their state-of-the-art facilities to complete this project. Many thanks to the rest of staff and students in Tyndall, for their regular fun events and projects which offered some much-needed stress-relief throughout the year.

Thank you to the School of Chemistry & its staff for dealing with me for another year and for giving numerous academic teaching opportunities during this project. A big thanks to University College Cork in general for my entire university / academic life. They have been some of the best years of my life.

Thank you to all my friends & family, in particular, my parents, Lorraine & Marcus, my sister, Niamh, & friends Jake & Stuart. Despite them not really understanding anything about this project or what I do at Tyndall and who will probably never read this dissertation in full, they have given me unyielding support throughout my entire life and this last year has been no exception.

Table of Contents

Declaration of Orginality: ..... **ii**
Acknowledgements ..... **iii**
Table of Contents ..... **iv**
Table of Figures ..... **vii**
Table of Tables ..... **x**
Abstract **1**
Chapter 1 – Background & Literature Review **2**
1.1 – Inductors & Magnetic Properties 2
1.1.1 - Introduction 2
1.1.2 – Inductance 4
1.1.3 – Magnetic Core Properties 7
1.2 – Power Supplies 10
1.2.1 – Introduction 10
1.2.2 – Power Supplies 10
1.2.3 - PwrSoC / PwrSiP 14
1.2.4 – Integrated Magnetics 16
1.3 - Microfabrication 18
1.3.1 – Introduction 18
1.3.2 – Photolithography 18
1.3.3 – Photoresists 23
1.3.4 – Photomasks & Mask Aligners 27
1.3.5 – Adhesion 30
1.4 – Core Deposition 32
1.4.1 – Introduction 32
1.4.2 – Sputter Deposition 33
1.4.3 – Electrolysis Theory 36
1.4.4 – Electroplating 42
1.5 - Soft Magnetic Metals 48
1.5.1 - Introduction 48
1.5.2 – NiFe 49
1.5.3 – CoNiFe 50
1.5.4 – Magnetic Oxides 51
1.6 – Cyclic Voltammetry 54
1.6.1 – Introduction 54

1.6.2 – Metal Oxide Growth 56
Chapter 2 – Experimental 61
2.1 – Fabrication Chemicals & Equipment 61
2.1.1 – Process Chemicals 61
2.1.2 - Process Equipment 63
2.2 - Characterisation Tests 65
2.2.1 – Composition Characterisation 65
2.2.2 – Magnetic & Electrical Characterisation 68
Chapter 3 – Results & Discussion 70
3.1 –Device Fabrication Process 70
3.1.1 - Introduction 70
3.1.2 – Fabrication Procedure: Legend/Key 73
3.1.3 – Fabrication Procedure: Device Construction 73
3.2 – Metal Deposition 80
3.2.1 – Introduction 80
3.2.2 – Copper Deposition 80
3.2.3 – NiFe Core Deposition 82
3.2.4 – CoNiFe Core Deposition 85
3.3 – Oxidation of Metal Cores 89
3.3.1 – Introduction 89
3.3.2 – Oxidation Method 89
3.3.3 - NiFe Oxidation 90
3.3.4 – CoNiFe Oxidation 93
3.4 - NiFe Cores Properties 96
3.4.1 – NiFe Cores Composition Properties 96
3.4.2 – NiFe Cores Magnetic Properties 109
3.4.3 – NiFe Device Imaging 114
3.4.4 – NiFe Devices Properties 119
3.6 – CoNiFe Cores Properties 127
3.6.1 –CoNiFe Cores Composition Properties 127
3.6.2 – CoNiFe Cores Magnetic Properties 140
3.6.3 – CoNiFe Devices Properties 145
3.7 – Summary of Results 155
Chapter 4 - Conclusion 156
Bibliography 159

Appendix A – Device Photomask Set 166

Table of Figures

Figure 1 - (a) Inductor circuit element symbol (4) (b) Tordial ferrite inductor (5) (c) Solenoid air inductor (6) 2
Figure 2 - (a) Solenoid's magnetic field lines (b) Tordorial's magnetic field lines 3
Figure 3 - Hysteresis Loop of a typical ferromagnetic material 8
Figure 4 - Hysteresis loop of the easy axis (left) and hard axis (right) of anisotropic $Ni_{45}Fe_{55}$ 8
Figure 5 - Skin effect of single thickness core (left) and laminated core (right) 9
Figure 6 - Circuit diagram for a simple buck converter 11
Figure 7 - ON (a) & OFF (b) State of a buck converter 12
Figure 8 - Graph of inductor's voltage (a) and current (b) 13
Figure 9 - Example of PwrSoC circuit setup 14
Figure 10 15
Figure 11 - Patterned and developed photoresist layer containing via holes 19
Figure 12 – Lift-off & Etch Photoresist techniques 19
Figure 13 - Left: Sidewall of 90° Centre: Sidewall of >90° Right: Sidewall of <90° 21
Figure 14 - Alignment marks. The block is patterned first, allowing for following alignment marks to line up to the block. 22
Figure 15 – Photolithography of positive and negative photoresists and their resulting pattern 23
Figure 16 - Example of a novalac derivative polymer chain 24
Figure 17 - Diazonaphthoquinone's reaction mechanism to form an indene carboxylic acid. 24
Figure 18 - DVS BCB molecule 25
Figure 19 - DVS BCB polymerisation 26
Figure 20 – The top metal winding photomask design used in this project 27
Figure 21 - Modes of contact for photolithography 28
Figure 22 - Forms of diffraction seen in photolithography 29
Figure 23 - Tape Test classification sheet 30
Figure 24 - Delamination of NiFe from the silicon substrate 31
Figure 25 - Diagram of a Magnetron Sputter Deposition System 33
Figure 26 - Sputter deposition for lift-off technique 35
Figure 27 - Metal - Ion interphase 36
Figure 28 - Polarisation plot showing the rates of both the anodic dissolution and cathodic metal deposition as a function of potential 39
Figure 29 - Movement of ions through the bulk electrolyte, diffusion layer and double layer 40
Figure 30 - Diagram of a basic electroplating setup 42
Figure 31 - Pulse DC waveform 46
Figure 32 - Pulse reverse waveform 47
Figure 33 – Anisotropy energy relative to the magnetization angle 47
Figure 34: A - Permeability B - Saturation magnetic induction C - Electrical resistance of Ni alloys 49
Figure 35 - Electrochemical cell set-up 54
Figure 36 - Voltammogram of Ferrocene ($X^+ + e^- \rightleftharpoons X$) 55
Figure 37 - Voltammogram of cobalt in 0.2M KOH between -1.2V and +0.6V 56
Figure 38 - Voltammogram of iron in 1M KOH between -1.275V and >0V 58
Figure 39 - Voltammogram of nickel in 1M KOH between -1.15V and +0.6V 60

Figure 40 - Varnish Marks on the wafer after electroplating.....65
Figure 41 - Quanta FEG 650 SEM with Oxford X-Max EDX System (Red Box) 67
Figure 42 – Tyndall' MESA HF200P BH Looper system.....68
Figure 43 - Probe Station for testing of devices on a device wafer. Orange Box indicates the Network Analyser and the Blue Box indicates the RF Probes and device wafer holder.....69
Figure 44 - Testing of a device at the wafer level. The device was contacted by the Formfactor ACP 100 Rf Probes in order to create a circuit.....69
Figure 45 - MS1 Inductor Design.....71
Figure 46 - MS2 Inductor Design.....71
Figure 47 - MC1 Inductor Design.....72
Figure 48 - MC2 Inductor Design.....72
Figure 49 – Coercivity measured at different stages of post-processing (slow cycles) for different film thickness.....90
Figure 50 - Metal oxidations set-up: Pt/Ti mesh with Teflon holders securing a wafer. Hg/HgO electrode held between the wafer and mesh.....90
Figure 51 - Voltammogram of the $Ni_{45}Fe_{55}$ electrode.....91
Figure 52 - AD NiFe (Left) & Oxi-NiFe (Right).....92
Figure 53 – Voltammogram of CoNiFe Electrode.....93
Figure 54 - AD-CoNiFe (Left) & Oxi-CoNiFe (Right).....94
Figure 55 – Oxi-NiFe Surface – 1750x Mag (Top) & 5000x Mag (Bottom).....97
Figure 56 - EDX Spectrum of AD NiFe.....98
Figure 57 - EDX Spectrum of Oxi-NiFe.....99
Figure 58 – Top Section of AD NiFe layer, with Sputtered Pt Layer for TEM Analysis 101
Figure 59 – Large portion of nanocrystalline AD NiFe grains.....102
Figure 60 – Individual AD NiFe grain.....102
Figure 61 – SAED of AD NiFe with selected area aperture.....103
Figure 62 - Face centred cubic lattice, with (200) & (111) crystal planes.....104
Figure 63 – 100nm scaling showing a 1um thick layer of Oxi-NiFe on top of AD NiFe 105
Figure 64 – 100nm scaling, showing the surface of Oxi-NiFe & the needle-like grains 105
Figure 65 – 20nm scaling, showing the interphase between the two NiFe materials.....106
Figure 66 – SAED 1 of Oxi-NiFe.....106
Figure 67 – SAED 2 of Oxi-NiFe with a selected area aperture.....107
Figure 68 - Hysteresis Loop of 1.5cm x 1.5cm AD NiFe.....110
Figure 69 - Hysteresis Loop of 1.5cm x 1.5cm sample of Oxi-NiFe.....110
Figure 70 - Light microscope image of the vias and cores of the oxidised devices (left) and as-deposited devices (right).....114
Figure 71 – MC1 coupled inductor with measurements.....115
Figure 72 – MS1 single inductor with measurements.....115
Figure 73 - 3D X-Ray Images of MC1 Inductor.....116
Figure 74 - NiFe wafer after oxidation, showing the iridescent colouring of Oxi-NiFe. Note the bottom of the wafer is AD NiFe - This area was not submerged in the bath and was used as the electrical connection point.....116
Figure 75 - Device Wafers with bottom windings and vias built.....117
Figure 76 - Oxi-NiFe Wafer after Core Etching. Cores show the iridescent colouration. 117
Figure 77 – Fully Constructed Oxi-CoNiFe Device Wafer.....118
Figure 78 - Fully Constructed AD NiFe Device Wafer.....118

Figure 79 - Inductance of NiFe MS1 Inductor Devices....119
Figure 80 - AC Resistance of NiFe MS1 Inductor Devices....120
Figure 81 - Q-Factor of NiFe MS1 Inductor Devices....120
Figure 82 - Inductance of NiFe MS2 Inductor Devices....121
Figure 83 - AC Resistance of NiFe MS2 Inductor Devices....121
Figure 84 - Q-Factor of NiFe MS2 Inductor Devices....122
Figure 85 - Inductance of MC1 Inductor Devices....122
Figure 86 - AC Resistance of NiFe MC1 Inductor Devices....123
Figure 87 - Q-Factor of NiFe MC1 Inductor Device....123
Figure 88 - Inductance of NiFe MC2 Inductor Devices....124
Figure 89 – AC Resistance of NiFe MC2 Inductor Devices....124
Figure 90 - Q-Factor of NiFe MC2 Inductor Devices....125
Figure 91 - AD CoNiFe Surface (Top-Down View)....128
Figure 92 - AD CoNiFe Surface (58° Angle)....128
Figure 93 - Oxi-CoNiFe Surface (Top-Down Viewing)....129
Figure 94 - Oxi-CoNiFe Surface (52° Angle)....129
Figure 95 - EDX Spectrum of Oxi-CoNiFe....131
Figure 96 - Top surface of the AD CoNiFe & Pt / Carbon Layer....133
Figure 97 - 20nm scaling of the top surface of AD CoNiFe....134
Figure 98 - Individual Grain of AD CoNiFe....134
Figure 99 - SAED of AD CoNiFe....135
Figure 100 - SAED of AD CoNiFe with Selected area aperture....135
Figure 101 - 0.5µm Oxi-CoNiFe & its interphases between AD CoNiFe & TEM Pt / C Layers....136
Figure 102 - Interphase between AD & Oxi-CoNiFe.....137
Figure 103 - Oxi-CoNiFe Grains....137
Figure 104 - SAED of Oxi-CoNiFe....138
Figure 105 - SAED of CoNiFe with selected area aperture....138
Figure 106 - Hysteresis Loop of 1.5cm x 1.5cm sample of AD CoNiFe....142
Figure 107 - Hysteresis Loop of 1.5cm x 1.5cm sample of Oxi-CoNiFe....142
Figure 108 - Inductance of CoNiFe MS1 Inductor Devices....145
Figure 109 - AC Resistance of CoNiFe MS1 Inductor Devices....146
Figure 110 - Q-Factor of CoNiFe MS1 Inductor Devices....146
Figure 111 - Inductance of CoNiFe MS2 Inductor Devices....147
Figure 112 - AC Resistance of CoNiFe MS2 Inductor Devices....147
Figure 113 - Q-Factor of CoNiFe MS2 Inductor Devices....148
Figure 114 - Inductance of CoNiFe MC1 Inductor Devices....148
Figure 115 - AC Resistance of CoNiFe MC1 Inductor Devices....149
Figure 116 - Q-Factor of CoNiFe MC1 Inductor Devices....149
Figure 117 - Figure 116 - Inductance of CoNiFe MC2 Inductor Devices....150
Figure 118 - AC Resistance of CoNiFe MC2 Inductor Devices....150
Figure 119 - Q-Factor of CoNiFe MC2 Inductor Devices....151

Table of Tables

Table 1 - E^0 of various metals interphases 37
Table 2 - Magnetic & electrical properties of various soft magnetic metals 48
Table 3 - Magnetic properties of the various forms of $Ni_{45}Fe_{55}$ 51
Table 4 - Each of the four devices and their parameters 70
Table 5 - Chemicals required for a 100 L Bright Copper ACG 8 bath. 80
Table 6 - NiFe PRP Parameters 82
Table 7 - Constituents of the $Ni_{45}Fe_{55}$ Bath 83
Table 8 - CoNiFe Bath Constituents 85
Table 9 - Saccharin adhesion tests 86
Table 10 - CoNiFe Pulse DC Parameters 87
Table 11 - EDX Analysis of AD NiFe 98
Table 12 - EDX Analysis of Oxi-NiFe 99
Table 13 - NiFe BH Looper results - Sample A = 1.5x1.5cm square - Sample B = 4-inch wafer - Sample C = 4-inch wafer 109
Table 14 - % Increase / Decrease in the properties of Oxi-NiFe in comparison to AD NiFe. 111
Table 15 - Relative, Real & Imaginary Permeability & Loss Tangent of AD & Oxi-NiFe. 113
Table 16 - Inductance, AC Resistance & Q-Factor of the MS1, MS2, MC1 & MC2 devices with AD & Oxi-NiFe 125
Table 17 - EDX Analysis of AD CoNiFe 130
Table 18 - EDX Analysis of Oxi-CoNiFe 131
Table 19 - NiFe BH Looper results - Sample A = 1.5x1.5cm square - Sample B = 4-inch wafer - Sample C = 4-inch wafer 141
Table 20 - % Increase / Decrease in the properties of Oxi-CoNiFe in comparison to AD CoNiFe. 141
Table 21 - Relative, Real & Imaginary Permeability & Loss Tangent of AD & Oxi-CoNiFe. 144
Table 22 - Inductance, AC Resistance & Q-Factor of the MS1, MS2, MC1 & MC2 devices with AD CoNiFe & Oxi-CoNiFe 152
Table 23 - Total Composition, Magnetic Core & Device Results for AD & Oxi-NiFe & CoNiFe 155

Abstract

The objective of this research was to develop, characterise and test post-processed magnetic materials used for in-package or on-chip devices such as micro-inductors. The electrochemical post-processing has been shown to improve the magnetic properties of the NiFe alloy. The aim of this research was further to test this process on alloys such as CoNiFe as well as integrating these 'ultrasoft' magnetic materials into on-chip micro-inductors for device functionality testing. A material with a hysteresis of H_c = <10 A/m is referred to as an "ultrasoft" material.

Magnetic devices such as inductors and transformers are essential devices in power supplies. Power supplies have been decreased in size and increased in speed and efficiency over the past few decades with the creation of on-chip power supply circuitries. One key barrier in the miniaturisation of these circuitries in their power storage and transfer devices, inductors, and transformers, which currently occupy ~30% of the circuit's volume.

Decreasing the volume of these devices requires the improvement of their efficiency and functionality, which relates to the magnetic materials used in these devices. Ferrites have been used extensively over the past decades due to their low cost and low loss performance. Unfortunately, ferrite's low magnetic flux density and resistivity make them less suitable for miniature devices or devices which work at high frequencies. Current alternative high flux materials are limited by high cost or high-power loss and work at very low frequencies. Therefore, there is a need for more efficient magnetic material for improved power supplies.

The newly created post-processed magnetic materials and devices were tested for magnetic and electrical properties such as inductance, inductance density, DC resistance, quality factor, and high-frequency response of the devices. They were compared with devices supporting cores made of the as-deposited version of the materials.

Oxi-NiFe, the post-processed version of NiFe, saw a noticeable increase in both its electrical and magnetic properties as a material, as well as showing improved properties as a core in the inductor devices, in comparison to NiFe and the NiFe devices. CoNiFe also showed improvement in both electrical and magnetic properties, as well as device improvements when used as a core, in comparison to the standard NiFe. Oxi-CoNiFe saw diminished properties when compared to CoNiFe.

Chapter 1 – Background & Literature Review

1.1 – Inductors & Magnetic Properties

1.1.1 - Introduction

Inductors are passive energy storage devices that store electrical energy in the form of generated magnetic fields.[1-3] The term passive refers to a component that cannot add to or amplify an electrical signal but can change the signal's voltage and current. Figure 1 (a)[4] shows the inductors electronic symbol, drawn in circuit diagrams. Inductors are typically made by winding a conductor around a core. This core can be air (Fig 1 (c))[5] or a magnetic material (Fig (b))[6] which can amplify the generated magnetic fields.

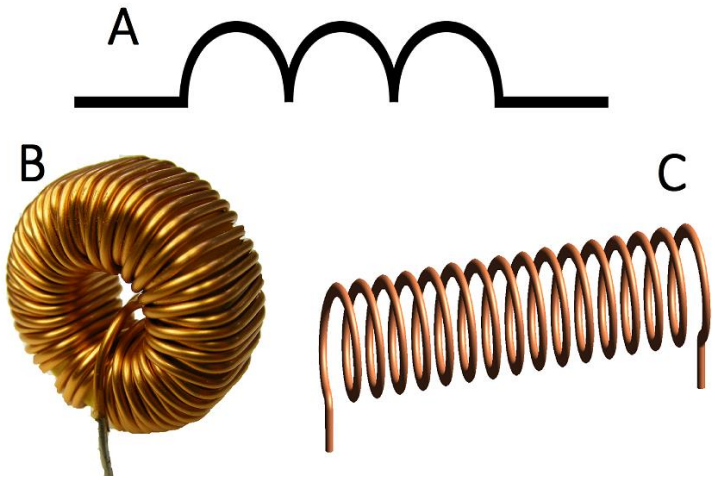


Figure 1 - (a) Inductor circuit element symbol (4) (b) Tordial ferrite inductor (5) (c) Solenoid air inductor (6)

When there is a change in current passing through the inductor, it produces a voltage against the change. The inductor stores the electrical energy by generating magnetic fields. This phenomenon known as "inductance" is explained by Faraday's law of induction and Lenz's law and is an intrinsic property of the device. The inductor is designed to release this stored energy back into the circuit eventually. This storage and release of electrical energy is the primary use of inductors in power supplies. More details on the use of inductors can be found in Section 1.2 – Power Supplies.

The inclusion of a magnetic core allows the inductor to benefit from the materials magnetic properties, improving the inductance. These properties include magnetic saturation, coercivity and permeability. Depending on the values of these properties, the material can be considered either *hard* or *soft*. The material used in inductors must be a *soft* magnetic material, which is material that can be magnetised by an external magnetic field (current passing through the conductor) but will not stay magnetised when the external field is removed. Materials that

retain the magnetism are referred to as *hard* magnetic material. As the inductor is to eventually release all the energy stored in the magnetic fields, having any remaining field means energy is lost from the circuit. However, even material that is referred to as *soft* is not perfect, with the material remaining slightly magnetised. Section 1.2.3 explains the properties of the magnetic materials and how these properties define whether the material is *soft* or *hard*. Section 1.5 describes the *soft* ferromagnetic metal material chosen to be used in this project.

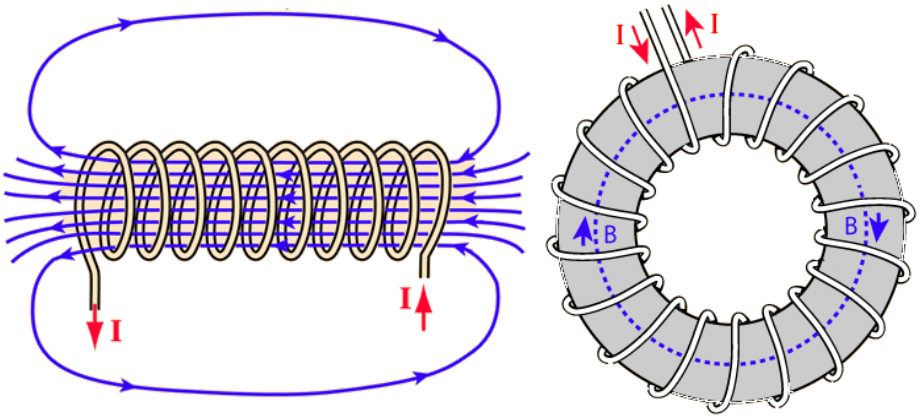


Figure 2 - (a) Solenoid's magnetic field lines (b) Tordorial's magnetic field lines

There are multiple designs of inductors, depending on the way the wire is wound. Solenoids are a type of inductor design used extensively and are shown in Fig 1 (a). This design involves winding the wire in a helix shape, to which a magnetic core can be placed in the centre. Fig 2 (a)[7] shows the magnetic field lines for a solenoid. A magnetic core would amplify the field as it passed through the helix, further improving the inductors properties. Other designs include racetracks and the tordorial, a design where a *torus* or doughnut-shaped magnetic core is wrapped in the conducting wire.[8] As shown in Fig 2 (b), the magnetic field is kept within the torus-shaped magnetic core.

The devices fabricated in this project are solenoid-based inductors. Details on the design and structure of these devices can be found in Section 1.3 - Microfabrication.

1.1.2 – Inductance

Inductance (L), refers to an electrical conductor's ability to oppose a change in the current flowing through it [1-3, 9]. The SI Unit used for inductance is the Henry (H). Inductance is an intrinsic property of the conductor and depends on the shape or geometry as well as surrounding material (magnetic core). Any current through a conductor creates a magnetic field, based on Ampere's Law, and therefore as current changes, so do the magnetic fields. A changing magnetic field, based on Faraday's Law of Induction causes an electromotive force, emf or $\mathcal{E}$. Based on Lenz's Law, this emf or voltage will be in the direction of the changing current in order to oppose it. The back emf lowers the overall voltage supplied to electrical loads connected after the inductor. Changing current is caused by a circuit turning off and on, with current changing between I_0 and I_{max}.

The emf or voltage formed can, therefore, be related to the inductance of the conductor, a constant referred to as L, and the change in current across the conductor. The negative sign indicates the emf produced is a back emf, based on Lenz's Law.

$$\mathcal{E} = -L\frac{dI}{dt} \qquad (1)$$

The magnetic field created when current flows through a conductor has a particular amount of magnetic flux or Φ. The SI unit for magnetic flux is the Weber (Wb). The changing magnetic field based on the changing current through the inductor also causes a change in the magnetic flux. It also can be related to emf produced by the changing current to give equation 2.

$$\mathcal{E} = -\frac{d\Phi}{dt} \qquad (2)$$

Relating the inductance L to the magnetic flux, based on the change in current gives equation 3.

$$L = \frac{\Phi}{I} \text{ or } \Phi = LI \qquad (3)$$

Inductance is a constant for a particular inductor based on its geometric shape and surrounding material. For a solenoid, it is magnetic flux density, *B*, which can be related to Ampere's Law, giving equation 4.

$$B = \mu_0 \frac{N}{l} I \qquad (4)$$

where μ_0 is the magnetic constant or the permeability of free space, with units of Henry per meter (H/m), *N* is the number of turns of wire in the solenoid and *l* is the length of the solenoid.

The SI unit for magnetic flux density is the Tesla (T) or Wb/m^2. Magnetic flux Φ relates to the magnetic flux density by equation 5; however, for a solenoid, the number of turns, N, must also be taken into consideration, giving equation 6.

$$\boldsymbol{\Phi = BA} \qquad \textit{(5)}$$

$$\boldsymbol{\Phi = NBA} \qquad \textit{(6)}$$

where A refers to the magnetic vector potential. Combing equation 4 and 6 together in terms of magnetic flux creates equation 7, the magnetic flux found within an inductor.

$$\boldsymbol{\Phi = N\left(\mu_0 \frac{N}{l} I\right) A = \frac{\mu_0 A N^2}{l} I} \qquad \textit{(7)}$$

Finally, relating magnetic flux to inductance (equation 3):

$$L = \frac{\frac{\mu_0 A N^2}{l} I}{I} = \frac{\mu_0 A N^2}{l} \qquad \textit{(8)}$$

This equation shows how inductance is a constant for a particular conductor, so long as the conductor's geometric shape is not affected in any way, as seen by $\frac{AN^2}{l}$, and the permeability, μ, of the material around the inductor does not change.

Permeability is the ability of a material to support a magnetic field forming within the material. μ_0 is the permeability of free space, or the magnetic constant, referring to the ability of a vacuum to support a magnetic field.[10] The permeability of air is typically considered to be μ_0. When a magnetic material is used in an inductor, the permeability is changed relative to the permeability of the magnetic material. This new permeability is called relative permeability, μ_r, and replaces μ_0 in equation 8 to give the inductance of a solenoid containing a magnetic material.

$$L = \frac{\mu_r A N^2}{l} \qquad \textbf{(9)}$$

The permeability of the magnetic material is an intrinsic property of the material itself, relating to the maximum magnetic field density, B_{sat}, of the material, and the magnetic field (H) supplied to the material.

$$\boldsymbol{\mu = \frac{B}{H}} \qquad \textbf{(10)}$$

$$\text{where } \boldsymbol{\mu_r} = \frac{\boldsymbol{\mu}}{\boldsymbol{\mu_0}} \qquad \textbf{(11)}$$

In a magnetic material, the magnetic flux density increases as the magnetic field, *H*, applied to the material increases, until B_{sat} is reached. At this point, the permeability of the material can be considered at maximum. Further increasing the magnetic field (*H*) will lead to no more increase in magnetic flux density past B_{sat}, and μ will become μ_0, effectively causing μ_r to decrease to 1, meaning the inductor is no longer benefitting from the magnetic material. Inductors, therefore, typically discharge the stored energy before the magnetic flux density reaches B_{sat}.

Inductance (L) is used to calculate the Q-Factor (Q) of an inductor, a key-value which helps to explain the overall efficiency of an inductor at a particular frequency by a ratio of the inductance and AC resistance of the device.

$$\boldsymbol{Q = \frac{w_0 L}{R}} \textbf{ (12)}$$

where W_0 is the frequency, L is inductance & R is the AC resistance of the inductor. This resistance refers to the resistance of the copper coil, relating to its thickness, length and number of turns. Typical Q-factors of ~25 at 100 MHz and >20 at 10 MHz have been seen at Tyndall [11, 12], with commercial foundries typically producing Q-factors of 10-15 at 10-40 MHz [13, 14].

The higher the Q-Factor, the more the inductor acts with the behaviour of an ideal inductor. By increasing inductance and decreasing AC resistance at a particular frequency, the Q-Factor increases, therefore, increasing the device's efficiency. It should also be noted that by decreasing the AC resistance, core losses also decrease.

The equation for calculating the resistivity is shown below:

$$\boldsymbol{R = K\frac{VT}{I}} \quad \textbf{\textit{(13)}}$$

where ρ (R) is electrical resistivity (μΩcm), T is the thickness of the deposited material, K is measured sheet resistance correction factor of the sample size (4.53 for 4-inch wafers), & V and I are voltage and current, respectively [15].

1.1.3 – Magnetic Core Properties

Materials that are wrapped around by the conducting wires of the inductors are considered cores. For inductors with no magnetic material, they are considered to have an air-core. The magnetic properties of the soft magnetic material used as the core are key to influencing the effectiveness of the inductor and are explained below:

Magnetic Flux Density Saturation

A higher saturation flux density (B_{sat}) allows the inductor to handle more current before the core reaches saturation. A higher B_{sat} also means a higher permeability as shown by Equation 10, and therefore a higher inductance. Overall, this allows the inductor to fit into a small footprint as now it can work at a higher frequency.

Permeability

A high permeability, $\mu_{r,}$ affects inductance and magnetic saturation, increasing both. This property is therefore vital in ensuring an inductor can work at a higher frequency, by maintaining a high power density.

Coercivity & Hysteresis

Coercivity or H_c refers to the amount of force required to fully demagnetise a particular material containing remanent magnetisation (B_r). The units used are Oersted (Oe) or A/m. A low H_c is required to ensure low *hysteresis losses*, allowing the device to work at higher frequencies. As previously mentioned, a material with a hysteresis of H_c = <10 A/m is referred to as an "ultrasoft" material.

Fig 3 shows a hysteresis loop for a typical ferromagnetic material [16]. Magnetic hysteresis refers to the remanent magnetisation (Point B in Fig 3) that remains after an external magnetic field was used to align the magnetic dipoles within a ferromagnetic material.

When the external field is removed, some of the dipoles remain aligned and are therefore permanently magnetised. An opposing magnetic field is required to demagnetise the material, with force from the field required to demagnetise the material known as H_c (Point C in Fig 3). The work done to demagnetise wastes electrical energy, and this lost energy is referred to as the *Hysteresis Loss*. Soft magnetic materials have little magnetic remanence and therefore have a low H_c while hard magnetic materials are designed to stay magnetic, and have a high B_r and H_c. Coercivity is dependent on the thickness of the magnetic material, with larger thicknesses giving a more significant H_c.

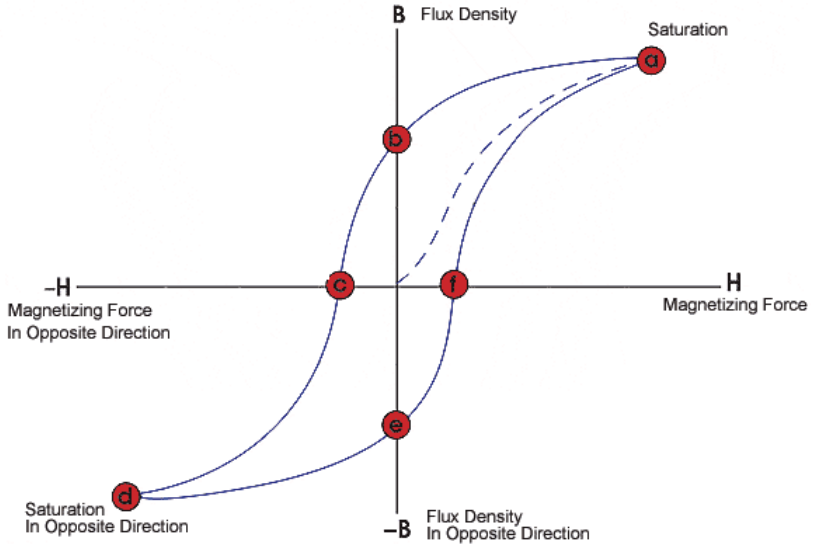


Figure 3 - Hysteresis Loop of a typical ferromagnetic material

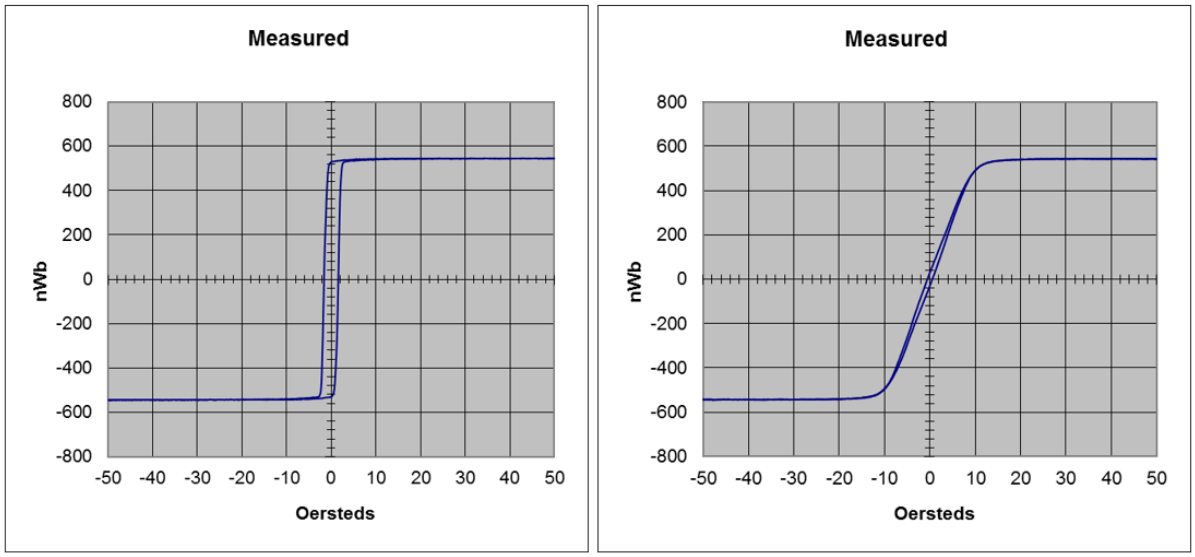


Figure 4 - Hysteresis loop of the easy axis (left) and hard axis (right) of anisotropic $Ni_{45}Fe_{55}$

Anisotropic Field (H_k)

The crystalline structure of the ferromagnetic magnetic material gives way to two axes of magnetisation, one easier than the other to magnetise along. These axes are known as the easy and hard axis, as shown in Fig 4. The easy axis is the more favourable axis and allows for instantaneous magnetisation, i.e. the magnetic dipoles of the material quickly align parallel to this axis even with a small field. The hard axis is perpendicular to the easy axis and requires a stronger field, or the anisotropy field, in order to fully align the dipoles in this direction.

The magnetic material should have a high anisotropy field (H_k) in order to allow the magnetic flux density to increase slowly as the magnetic field is increased. This allows H_k to withstand a larger magnetic field than the easy axis.

Resistivity & Eddy Currents

The electrical resistivity of the magnetic material must be high in order to reduce eddy current loss, thus allowing the device to work at higher frequencies. Eddy current is produced by a changing magnetic field, based on Faraday's law of induction and effects not only the core but other surrounding material. This current expends itself by creating a magnetic field which opposes the changing magnetic field (Lenz's law) as well as producing heat, which therefore affects the core properties as well as other nearby material. Overall, the eddy current produced is energy lost from the inductor, and therefore must be kept to a minimum. Eddy current can also be reduced by the use of a magnetic lamination core, which reduces the skin effect of the overall core, see Fig 5 [17].

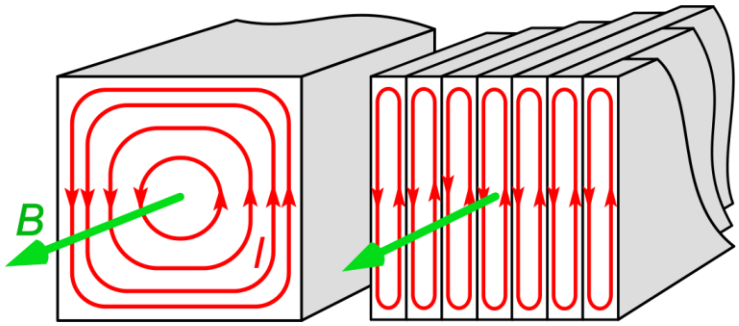


Figure 5 - Skin effect of single thickness core (left) and laminated core (right)

1.2 – Power Supplies

1.2.1 – Introduction

Modern technology strives for continuous improvement with increased device functionality and power efficiency. Despite the challenging nature of these improvements, there is an increasing demand for these reduced circuit size and cost. These factors all relate to the More than Moore (MtM) approach, referring to silicon technology, such as power supplies, that do not scale with Moore's Law. [18, 19]

Moore's Law is reaching its physical limitation, with microelectronics now in the nanoscale, the further miniaturisation of electronics must be done by integrating other vital parts of electronics. Micro inductors and capacitors which are used in power supplies are examples of micro-devices that are currently being combined with other electronic components into a single package or ideally onto a single chip, which in itself also creates challenges.

These challenges are being met with the fabrication of Power Supply in Package (PwrSiP) and Power Supply on Chip (PwrSoC) devices, which are now being integrated into current and future technologies [20]. PwrSoC refers to an entire power supply, such as a switch-mode DC power supply, commonly found in many electronic devices such as mobile phones, integrated onto a single silicon die. PwrSiP refers to the power supply having its components, such as its switches and controller being integrated across multiple dies in the same package, with the components such as the inductors being external.

Unlike other electronic components, such as CMOS (memory) or processing circuitries, power supplies do not follow typical Moore's Law scaling and instead, depend on the improvement of design and materials for increased efficiency and decrease in scale. The inductor component is a crucial device of power supplies that must decrease in size for overall electronic circuits to become smaller. However, the reduced size requires an increase in the working frequency of the inductor, and typical magnetic materials used in macro-scale inductors will not work at these high frequencies.[21, 22]

This project focuses on the micro-inductor components of the power supply and the optimisation of new magnetic materials for use in the ever-decreasing scale of these devices.

1.2.2 – Power Supplies

Micro power-supplies refer to the devices that supply the electrical load components with the correct power by converting incoming power from the mains or battery. This conversion

involves converting the voltage, current and frequency for the many different loads found within a single electronic device. Examples of power supplies include AC to DC power supplies, found inside smartphone chargers, linear converters & switch-mode power supplies; found in the smartphones themselves.[23, 24]

Linear converters are one of the simplest power conversion circuits available, known for their small costs and size. They contain active components, such as a variable resistor, to convert power. However, these devices can only decrease voltage/current and are extremely energy inefficient (<35%), [23, 24] with the circuit converting electrical energy into heat, to reduce the power, which can then affect other circuitries nearby.

A switch-mode power supply is a standard power supply circuit found in nearly all electrical devices today. It allows for AC currents from the mains or DC from a battery to be converted to the correct DC required by a load. An inductor is a primary component of such a device. Unlike the linear converters, these circuits can increase and decrease current/voltage and are highly energy-efficient (90%). Fig 6 below shows an example of a switch-mode power supply, known as a Buck converter.

Buck and boost converters are examples of switch-mode power supplies and are used to convert input voltages to the necessary voltage of the output load. Buck lowers the input voltage to the required voltage of the output, while the boost increases the voltage.

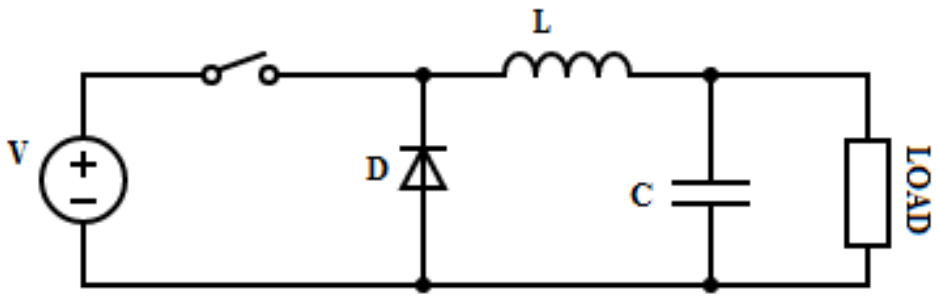


Figure 6 - Circuit diagram for a simple buck converter

Theory of Operation of a Buck Converter

As an example, the method of operation behind the buck converter is as follows: During the On-State (Fig 7 (a) [25]), the switch is closed for the DT_s period, where D refers to the duty cycle of the switch. During this time, the power supply, at voltage V_{HV}, (indicating that the input is at a higher voltage), is directly supplying current to the load while passing a current through the inductor.

As explained in Section 1.1, the inductor produces an opposing voltage due to the change in current across itself, which in turn lowers the voltage supplied to the load. V_{LV} refers to this lower output voltage. The difference between V_{HV} and V_{LV} is the back *emf* or voltage across the inductor, V_{IND}.

Using Faraday's Law, we can relate the inductor's back *emf* to the change in the inductor's current, where $\boldsymbol{i_{IND}(t)}$ refers to the change in inductor current.

$$\boldsymbol{V_{IND} = L\frac{di_{IND}(t)}{dt}}$$

The change in inductor current is caused by the inductor storing energy by creating a magnetic field during the DT_s period. Fig 8 (a) shows the DT_s period in which the voltage across the inductor is V_{IND}, while (b) shows the increasing current of the inductor as it charges up by creating magnetic fields [24]. Typically, a buck converter also contains a capacitor which stores energy in electric fields. These are used as further voltage filters to smooth out the voltage received by the output.

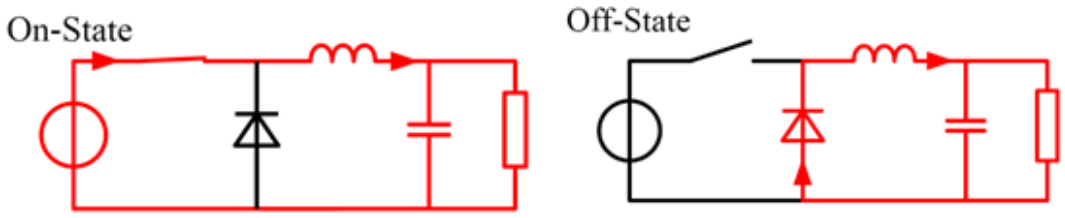


Figure 7 - ON (a) & OFF (b) State of a buck converter

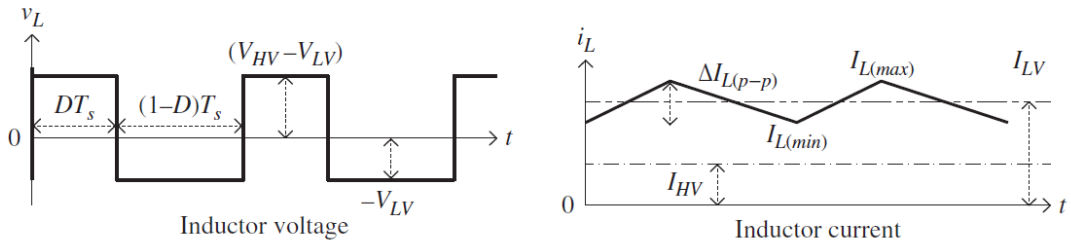


Figure 8 - Graph of inductor's voltage (a) and current (b)

As the current continues to flow, the inductor will continue to charge until it is saturated. As the inductor becomes saturated, its resistance to the change in current and, in response, the opposing voltage from the inductor would also decrease. To ensure the voltage supplied to the load is constant, the circuit will then change to an Off-State before the inductor reaches saturation.

During the Off-State (Fig 7 (b) [25]), the switch is now open for a period of $1 - DT_s$, but the load is still supplied with current and the correct voltage thanks to the inductor and diode. As shown in Fig 8 (a), the inductor creates a voltage ($-V_{LV}$) as the current across the inductor has once again changed. However, this voltage is now in the opposite direction, hence the negative V_{LV} value, which supplies voltage to the output. Fig 8 (b) shows the decrease in the inductor's current as the energy stored in the inductor's magnetic field is discharged to supply the output. During the Off state, the diode is now used as a conduction path for the new circuit path while the capacitor further supplies current as well as continuing to filter the outgoing voltage.

By alternating between the On and Off states, the load will always be supplied with the correct voltage. As seen in Fig 8 (b), the current provided to the output (I_{LV}) is the average between $I_{L(max)}$, the max current the inductor stores during the On state and $I_{L(min)}$, the minimum current in the inductor after discharging in the Off state.

This example uses the Continuous Conduction Mode (CCM), whereby the buck converter is constantly supplying current. In this case, the inductor never reaches saturation or is completely depleted, i.e. $I_{L(max)} < I_{L(Saturation)}$ and $I_{L(min)} > 0$. Other modes include Discontinuous Conduction Mode (DCM), whereby the inductor is allowed to completely deplete during the Off-State, leading to a period within this state where no current or voltage is being supplied to the output. This mode is useful for extremely light loads (low current and voltage needs).

1.2.3 - PwrSoC / PwrSiP

Within a single electronic device, such as a smartphone, they are multiple loads, all requiring varying voltages and currents. These loads can be grouped into power domains based on their power requirements, to which each domain has a DC/DC converter that supplies the necessary power. By combing all of these DC/DC converters, including its switches, inductors, as well as other discrete power supply components together onto a single silicon die, a Power Supply on Chip (PwrSoC) system is made, as shown in Fig 9.

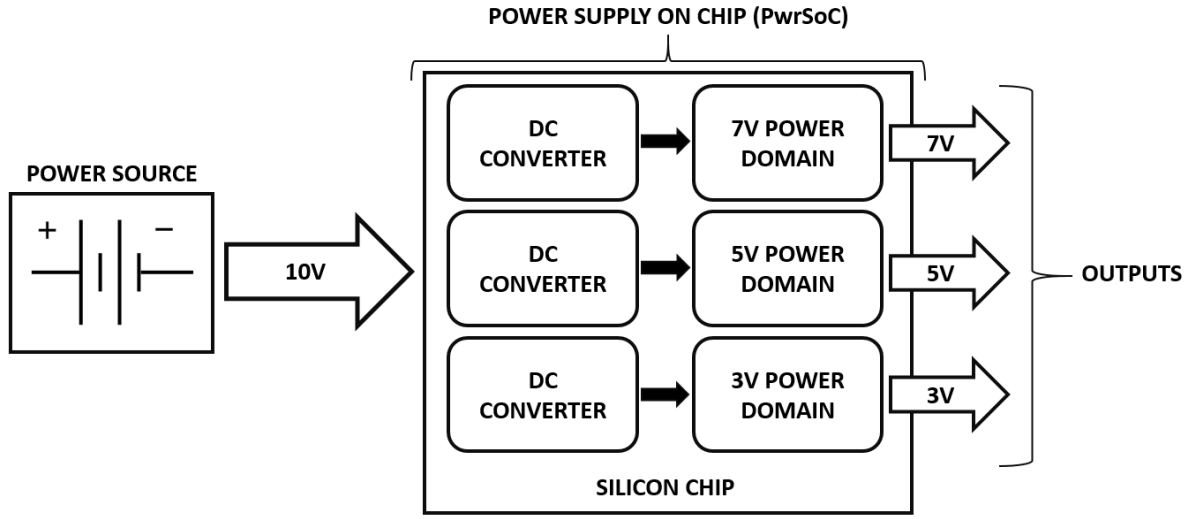


Figure 9 - Example of PwrSoC circuit setup

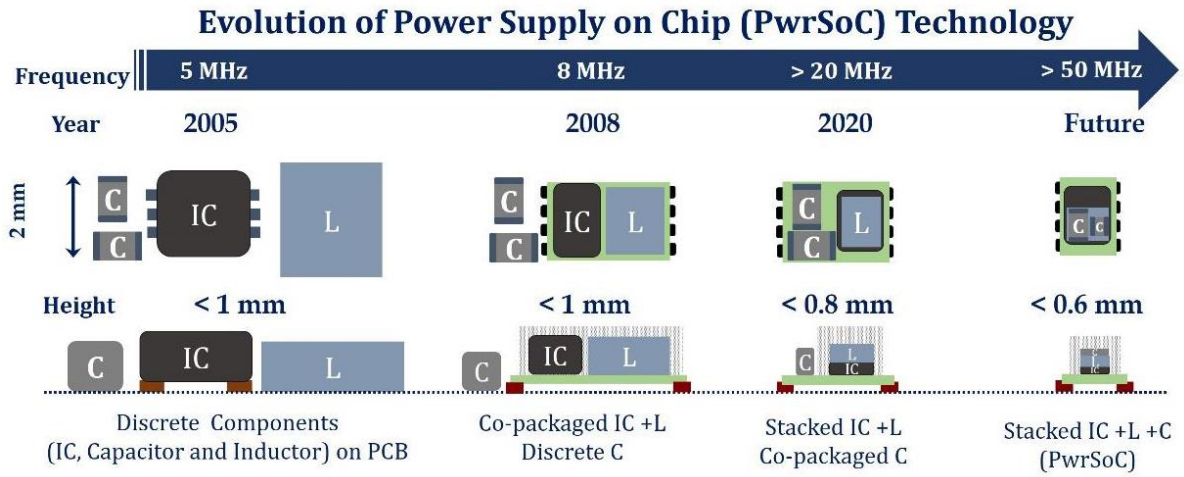
However, some of these discrete components, such as the inductor, cannot be reduced in size without increasing their working frequency. Inherent properties of inductors, such as inductance and capacitance, are inversely proportional to operating frequency as well as being affected by the load-current specifications. For PwrSoC technology, the switching frequency would be in the 10-100 MHz range; however, current inductors only work, functionally, at 0.5-0.8MHz.[26]

Until the inductor's properties can be kept constant or improved when their size is reduced, inductors must instead be built as large components, typically externally to the rest of the power supply on another silicon die. This set-up is referred to as Power-IC (PwrIC). Separating each discrete component of a power supply onto separate dies in a single package with an external inductor creates what is known as a Power Supply in Package (PwrSiP) system. [20]

Knowing this, the current technological advancements in the area of MtM are pushing towards moving the components of power supplies together onto a single die, i.e. PwrSiP → PwrIC / PwrSoc. However, the inductor is one of the most significant, yet largest components of a power supply and therefore must be reduced in size dramatically before being placed onto the same die containing other components.

With micro-power supplies, there are two types of size reductions, both of which must be taken into consideration. Footprint size refers to the 2D footprint area the overall device takes up [26] Volume size refers to the total 3D volume of the entire device. PwrSiP has the largest footprint size, with components spanning over multiple dies with other components external to the whole package. PwrSoC sees the footprint decrease to the size of a single silicon die, due to the monolithic design of integrating components on top of one another, as well as volume decrease due to the decrease in size of the individual components. Fig. 10 shows the evolution of PwrSoC technology [26].

Figure 10



1.2.4 – Integrated Magnetics

Today, the need to move away from traditional power-supply manufacturing, involving discrete power supplies' components being constructed separately, is required. Emphasis must now be put on micro-electronics technologies such as integrated magnetics in order to construct PwrSiP or PwrSoC technology.

The integration of thin-film magnetic material onto the silicon substrate referred to as *integrated magnetics technology* is used to fabricate micron-sized inductors or micro-inductors components. Research in this area is focused on two fronts: The fabrication of new or improved magnetic material capable of operating at a high frequency & suitable integration techniques [27]. Integration techniques include techniques needed for the microfabrication of micron-sized inductor metal cores and the conductive windings onto silicon. There are two current methods of creating micro-inductors: Enclosing the planar conductive coils with magnetic material (racetrack) or fabricating the coils around the planar magnetic core using multi-layered construction, i.e. a solenoid.

With the decrease in size of inductors, micro-inductors will be working at frequencies from 10-100 MHz. This requires the integrated magnetic materials to show an increase in its saturation flux density, permeability, resistivity and the anisotropy field, and showing a decrease in magnetostriction, coercivity and overall core lose. However, currently, no single material has all of these required properties in order to be integrated as the core in micro-inductors for all power supply applications.

Integrating/depositing the magnetic core typically uses one of two techniques; sputter deposition or electrodeposition. Sputter deposition has seen the integration of cores such as FINEMET [28] & laminated CZT (Co, Zr, Ta) / SiO_2 cores [29]. Electrodeposition has seen the deposition of cores such as laminated $Ni_{80}Fe_{20}$ cores [30] and $Ni_{45}Fe_{55}$ cores [31, 32]. More information on the advantages and disadvantages of these deposition methods can be found in Section 1.4 – Core Deposition.

Laminated cores are used order to limit eddy currents, which become an increasingly difficult problem at high frequencies, using nanoscale dielectric lamination films (SiO_2) between the cores, thus keeping the magnetic film laminations below the skin depth at the required frequency. [33]

Ferrites cores are typically used in low frequency (1 MHz) applications. They offer low saturation flux and permeability but extremely high resistivity, allowing millimetre thick cores

with little eddy current losses at these thicknesses. However, these materials are difficult to integrate into microfabrication processes as they cannot be sputtered or electroplated.

NiFe and other high flux density alloys with low coercivity are used for higher frequencies (>5 MHz). These materials can be easily electroplated, a typically inexpensive process and compatible with numerous microfabrication processes. Metal magnetic alloys, unfortunately, offer limited resistivity as a trade-off for higher permeability and flux density. The addition of non-metallic elements such as boron, oxygen and phosphorous to these metallic alloys can increase the resistivity, but in doing so, sacrifice the high flux and permeability.

CZT or more recently, CZTB (Co, Zr, Ta, B) cores [34] have seen use at extremely high frequencies (>10 MHz) due to their high inductance at these frequencies. The material has found the balance between metal and non-metal elements, offering high magnetic flux and permeability, with a laminated core further increasing the core's resistivity. However, currently, this material can only be sputter deposited. While sputter deposition is compatible with current microfabrication technologies and processes, the process is considered expensive, and the need for laminations further increases the cost and complexity of manufacturing these cores.

Therefore, there is a demand for integrated magnetics research into more cost-effective magnetic materials for use in high-frequency micro-inductors for power supply applications. Electroplating is the more cost-effective method of depositing the magnetic material; however, integrating non-metallic elements into a predominantly metal only process is complicated.

This project will see the integration of non-metallic elements into electroplated ferromagnetic material using a new, novel post-deposition technique, in order to increase the material's magnetic properties. These new materials will then be integrated into micro-inductors for magnetic and electrical testing, with the goal that these materials will increase the working frequency when compared to their conventional, as-deposited counterparts.

1.3 - Microfabrication

1.3.1 – Introduction

Microfabrication is the construction of micrometre or smaller sized devices, typically onto silicon-based substrates, using a wide variety of well-defined technologies such as photolithography and electroplating. While the exact method of fabrication depends on the manufacturers, at Tyndall, state of the art photolithography and metal deposition techniques/technologies are used to create the micro-devices. These techniques/technologies will each be described individually for the overall steps in the device fabrication. Details on the metal deposition techniques used throughout the fabrication process can be found in Section 1.4 – Core Deposition.

1.3.2 – Photolithography

Photolithography is the process in which a pattern, typically from a photomask, is transferred onto light-sensitive compounds, known as photoresists, which cover a wafer's surface. [35] Using a photomask's pattern, regions of a photoresist layer are selectively exposed to UV light, chemically altering these select areas of the photoresist. These regions in the photoresist layer are either (semi-) permanent polymer structures or easily removable regions that dissolve in a solvent known as a developer. After exposure, the removal of the soluble regions of photoresist leaves behind an etched pattern in the photoresist layer, as shown as in Fig 11. Following this, processes such as etching the now exposed material underlying the photoresist, or deposition of material into the pattern can occur.

Photolithography is, therefore, one of the most crucial steps in microfabrication as it allows for the construction of devices using etching or deposition techniques with the patterned photoresist as the guide [36]. Multiple steps of photolithography allow for the 3D device to be fabricated by layering multiple 2D layers on one another, made up of deposited and etched polymer-based material and metals. There are two main techniques used to create patterned material layers: etching and lift-off. Fig 12 shows the necessary steps behind these techniques [37].

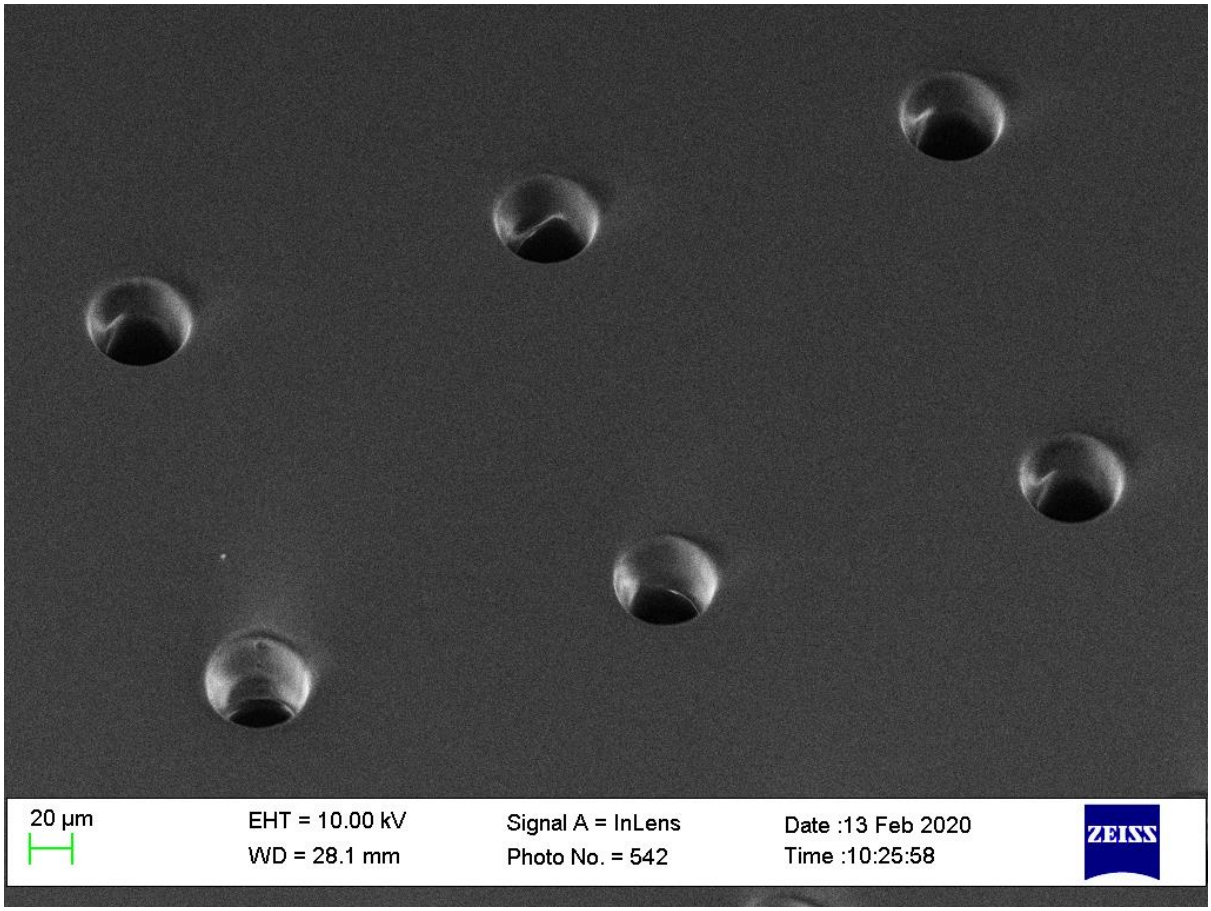


Figure 11 - Patterned and developed photoresist layer containing via holes

Credit to Daniel Smallwood 2020 ©

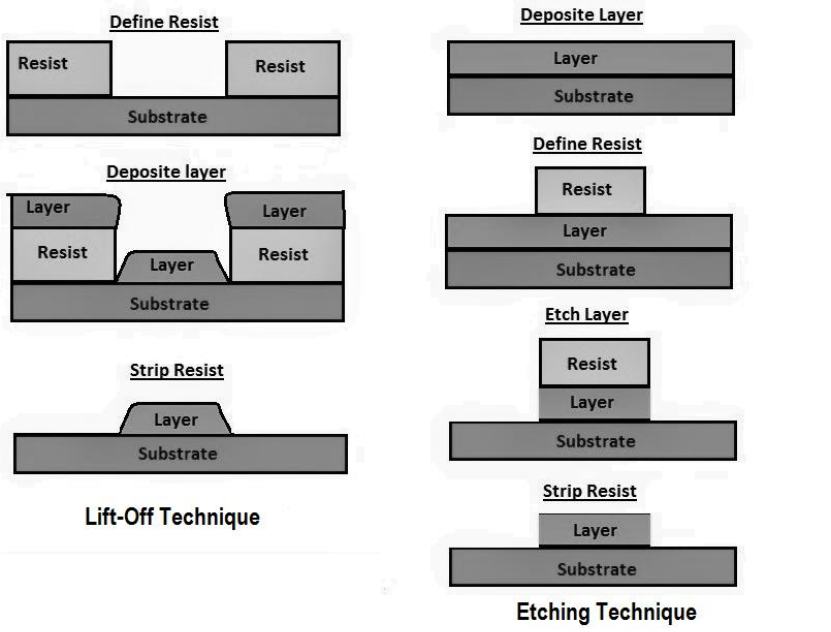


Figure 12 – Lift-off & Etch Photoresist techniques

Lift-off uses a photoresist layer to create a pattern, to which materials, such as metals can be deposited into. The material does not have to be guided to deposit into any particular area and can instead be blanket deposited across all the entire wafer. After the material is deposited, the photoresist layer is removed, removing any material deposited on top of it with it. The pattern from the photoresist is, therefore, successfully transferred to the new material.

Etching involves having the material already deposited onto the substrate to which a photoresist layer is then spun onto. This resist is then exposed and developed, leaving a patterned photoresist layer that is to cover specific areas of the deposed material and protect it from being etched. After etching any exposed material, the photoresist is removed, leaving behind a now etched and patterned layer of the deposited material.

With photolithography, during developing of photoresist or etching of deposited metal, only certain areas of these materials are to be removed by the use of developer or chemical etchants. However, these chemicals can still dissolve the remaining areas at a slower rate. Etch resistance is a key property for any material used in photolithography as it controls how quickly the now permanent exposed negative resist, semi-permanent unexposed positive resist or deposited metals layers takes to dissolve. Typical patterns in photoresists offer a etch margin where etching of these regions can occur without affecting the device functionality.

For the microfabrication of devices, the need for high-quality photolithography is paramount and is affected by a few broad specifications: *photoresist profile control, overlay, downstream compatibility and manufacturability*.[35]

Photoresist profile control refers to the ability to produce a patterned photoresist layer to the correct specifications of the design. These specifications include the linewidth, sidewall angle, resist thickness of the patterned photoresist.[38] Linewidth, also known as the critical dimension, refers to the smallest dimension on the pattern that must be controlled. If this dimension can be controlled and correctly patterned, then any similar sized or larger dimensions in the pattern can be too. Sidewall angle refers to the angle of the photoresist after exposure (Fig 13). Too low an angle and the photoresist may collapse later on in the fabrication process of the device, while too high of an angle may stop the photoresist from being fully developed.[39] The depth of focus of photolithography is therefore referred to the focus range over a specific exposure range, that allows the desired resist profile or a specific feature within the given specifications.

The resist thickness at the start of the processing and the final thickness is usually compared for any resist loss. The thickness of the photoresist typically decreases during processing, as solvents in the photoresist are removed during heating, and as the photoresist itself is chemically altered once exposed.

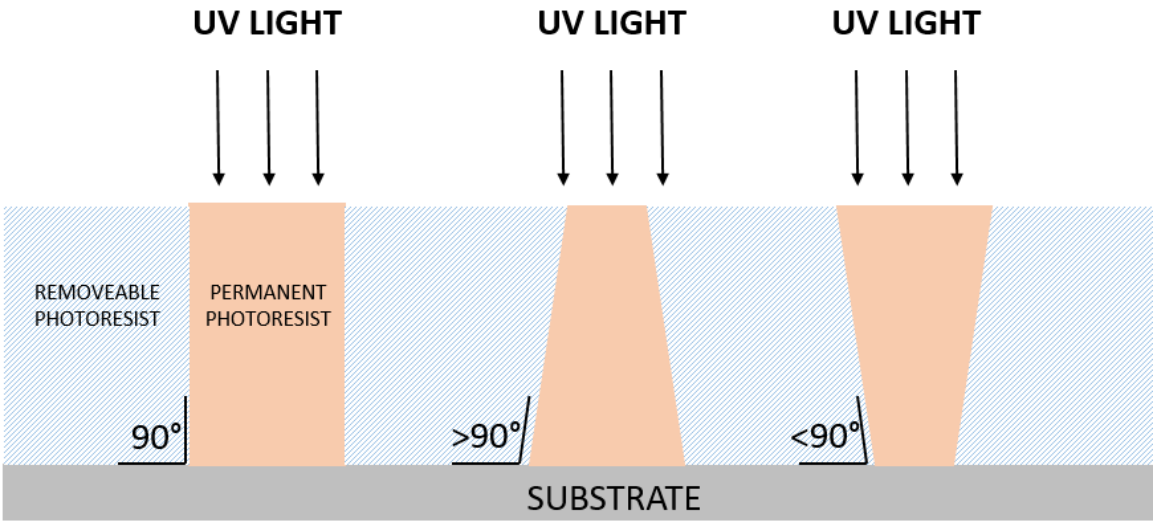


Figure 13 - Left: Sidewall of 90° Centre: Sidewall of >90° Right: Sidewall of <90°

Resolution refers to the smallest feature of a device that can be patterned with a specific depth of focus. [40] Using photoresists designed for high-resolution patterning, along with corresponding methods of exposure and fabrication processing, allows for smaller sections of a device to be fabricated successfully; increasing the resolution. The need to increase resolution is an ongoing challenge in the field of micro-fabrication and photolithography, as it is one of the deciding factors in producing smaller devices.

Overlay refers to the ability to correctly layer the next pattern of photoresist onto the previously completed layer. A typical micro-device design has multiple photomasks that produce the various patterns for the layers required to build it. These masks also have alignment marks which align to inscribed alignment markings or “blocks” on the wafer surface which ensures proper alignment of each layer (Fig 14). Mask aligners are used to ensure proper alignment, and many can also expose the wafer once it has been aligned. Section 1.3.4 explains this process in more detail.

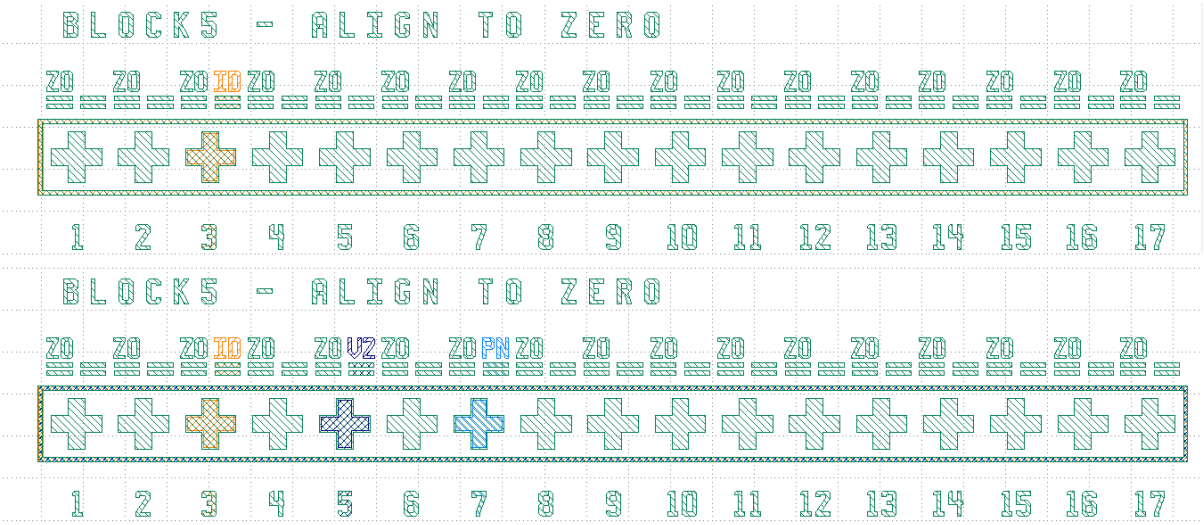


Figure 14 - Alignment marks. The block is patterned first, allowing for following alignment marks to line up to the block.

Downstream Compatability refers to the compatibility of the pattern in other process steps, such as metal deposition. A photoresists physical adhesion, chemical and thermal compatibility and etch-resistance are examples of factors that affect downstream compatibility.

Manufacturability refers to the cost of the photolithography processes. It takes into consideration all costs (machinery, chemicals) as well as the defectivity per production run. Combining the manufacturability of the photolithography processes with the manufacturability of other processes allows for the calculation of the total cost and possible loss (defective devices) of a microfabrication run.

1.3.3 – Photoresists

Photoresists are light-sensitive polymer materials that are spread across a wafer and processed to fabricate patterned polymer coatings on the wafer surface and are chemically altered once exposed to UV light. Photoresists typically have three main ingredients: the polymer resin, the photoactive compound and the solvent.[41, 42] Photoresists can be split into two groups, *positive and negative*, referring to whether the inscribed pattern in the photoresist is a positive or negative copy of the photomask pattern, (See Figure 15)[43]. Processing refers to heating or "baking", exposure and development of the photoresist, producing the patterned coating. Both positive and negative photoresists are used in this work.

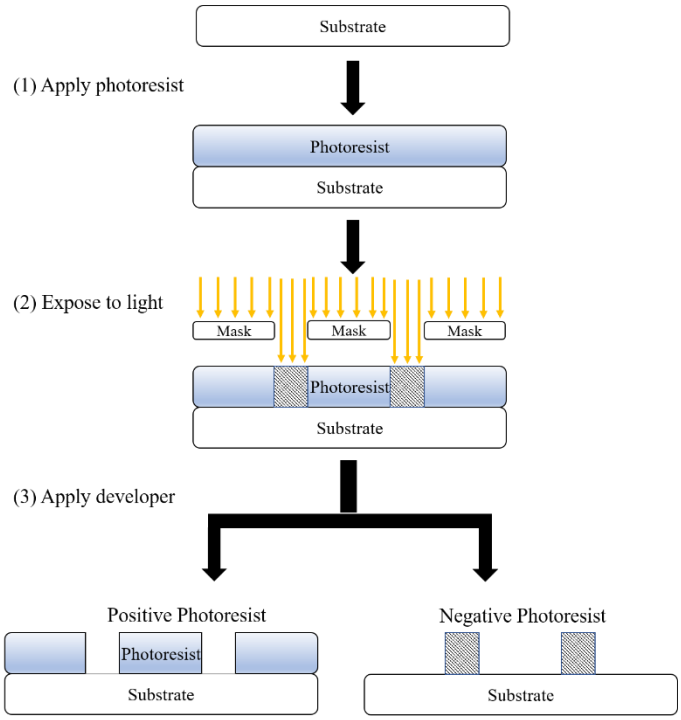


Figure 15 – Photolithography of positive and negative photoresists and their resulting pattern

A positive photoresist is a photoresist that dissolves in developer once exposed to UV light. Unexposed regions of the positive photoresist remain insoluble. These photoresists typically contain an alkaline soluble novalac based polymer, acting as the resin (Fig 16)[44]. Manufactures produce derivatives of the novalac polymer, creating brands of positive photoresist based on individual photolithography needs. The photoactive compound, typically a derivative of Diazonaphthaquinone (DNQ), acts as a dissolution inhibitor, blocking the novalac based polymer from dissolving in the alkaline developers. The solvent is typically propylene glycol methyl ether acetate (PGMEA) or an equivalent, which allows for the photoresist to be dispensed as a liquid onto the wafer and uniformly spread across its surface.

The solvent's volatile nature allows it to slowly evaporate or be removed by heating, solidifying the photoresist on the wafer's surface. [41, 42]

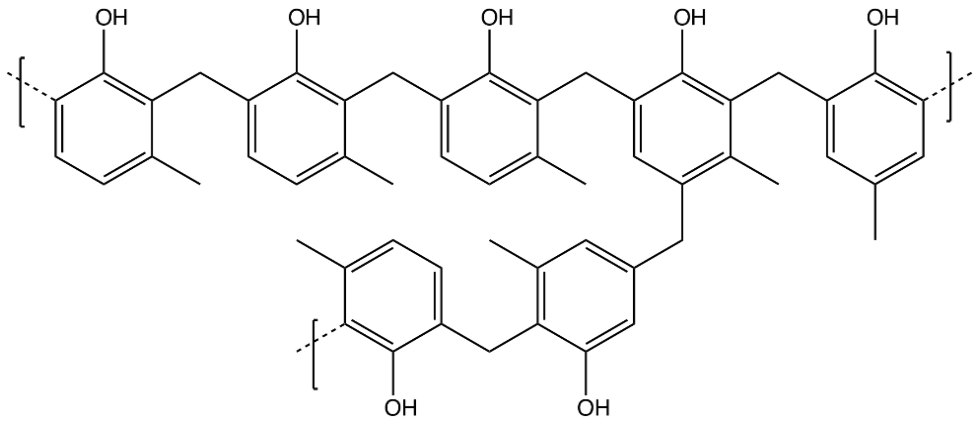


Figure 16 - Example of a novalac derivative polymer chain

DNQ acts as a dissolution inhibitor, blocking the hydroxide groups of the novalac resin, hindering its solubility in alkaline solutions, such as the photoresist's developer. When exposed to UV light, the DNQ is chemically altered, releasing N_2 and thus forming a carbene. This carbene undergoes a Wolff rearrangement, forming an intermediate indene ketene which, when reacted with water, forms the indene carboxylic acid (Fig 17). This carboxylic acid product is incapable of inhibiting the novalac resin from dissolving in the developer. [45, 46]

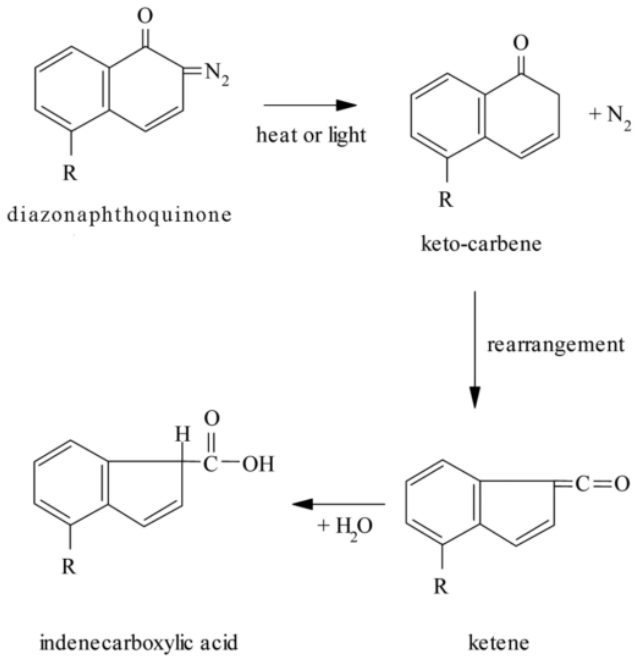


Figure 17 - Diazonaphthoquinone's reaction mechanism to form an indene carboxylic acid

With the unexposed insoluble regions remaining, this creates a pattern in the photoresist coating. Unexposed regions can be eventually removed by acetone after the patterned coating is no longer required. The relative ease of removing patterned positive photoresist makes it ideal for the fabrication of temporary patterns or moulds, allowing for the electrodeposition of new metal structures using these patterns.

A negative photoresist is a photoresist whose monomer resin crosslinks into polymers once exposed to UV light. Unexposed regions remain as monomers and are easily dissolved in developer. Much like positive photoresists, negative resist has a resin, photoactive compound and a solvent.

These resists used an isopropene based monomers resin, a biz-azide derivative-based photoactive compound and an organic solvent. UV exposure would cause the biz-azide to begin cross-linking using free-radical based reactions with the isopropene monomers, producing the insoluble polymer chain. Developers would include a variety of organic solvents, capable of dissolving unlinked monomers. A strong organic stripper would be required to remove the patterned coating once it was no longer needed. More modern negative photoresists include epoxy-based monomers like SU-8. Their photoactive compound is an acid-generator which catalyses the polymerisation of the epoxy monomers. The solvents used include gamma-butyrolactone or cyclopentanone.

BCB is a negative photoresist used throughout the current fabrication process (Fig 18). Once exposed, biz-azide chemistry allows for monomers to begin crosslinking as it is thermally cured. The monomers undergo a Diel-Alder reaction, crosslinking a monomer's four-ring system with the vinyl double bonds of the divinylsiloxane (DVS) section of the BCB (Fig 19). [47]

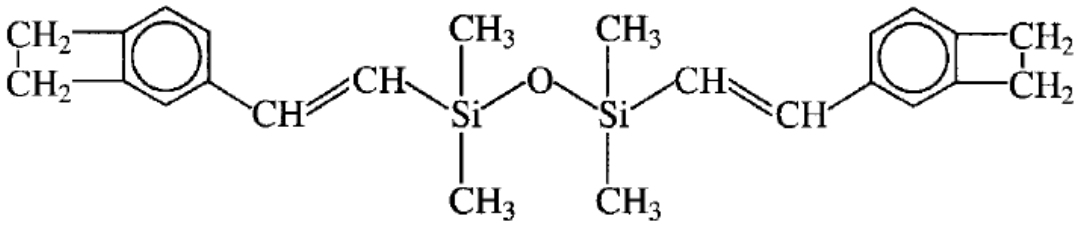


Figure 18 - DVS BCB molecule

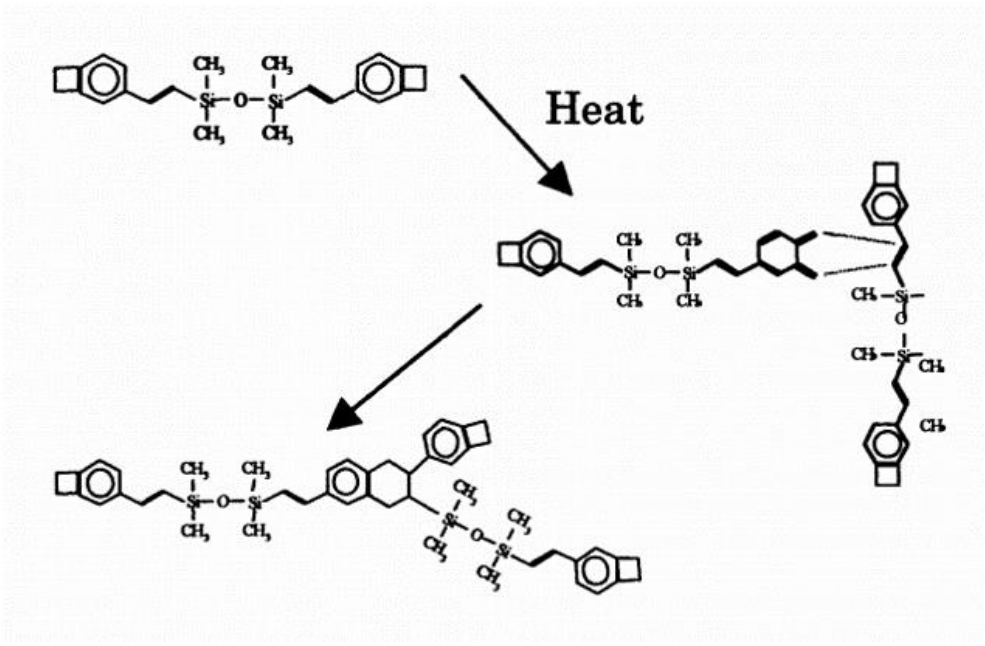


Figure 19 - DVS BCB polymerisation

The polymerised nature of exposed negative photoresist makes it ideal for permanent structures in devices, typically used as a dielectric layer to separate two metal sections in devices. [48] However, the polymerisation of these photoresists can cause problems when a new layer of metal is to be deposited on top, as the adhesion between the polymer and the new metal layer can be too weak, leading to delamination; the peeling of deposited layers off the wafer.

To mitigate this, before a new seed layer is deposited onto the surface of the polymerised resist, it is first subjected to argon-ion treatment. Ar^+ ions are fired at the smooth surface of the resist, breaking apart the surface polymers. Ar^+ treatment of BCB, for example, destroys the surface polymer aromatic rings, causing loss of conjugation and electron delocalisation, and the formation of carbon radicals. Furthermore, the DVS portions of the polymer are torn apart, causing silicon and oxygen radicals to form, although the silicon radicals typically react to form Si-H_n bonds. [49, 50]

With the surface roughened and radicals available to react, the metal seed layer can be deposited. Typical seed layers first involve the deposition of titanium, as an adhesive layer between the photoresist or silicon oxide surface of the wafer and the next layer of the seed layer. Titanium deposits into the micro-grooves of the roughened polymer surface, creating micromechanical interlocking and further secured by the formation of Ti-C and Ti-O bonds between the layers. Titanium bonds readily with other metals, meaning the next layer of the seed layer, typically $Ni_{80}Fe_{20}$ or copper, adheres easily to the wafer surface.

1.3.4 – Photomasks & Mask Aligners

A photomask is a glass plate containing opaque and transparent sections that combine to produce a pattern. This pattern is transferrable on a photo-sensitive compound (photoresist) by shining light through the photomask. This pattern, once developed, will allow for the selective etching, lift-off and metal deposition processes in select areas of the wafer surface.

In the design and fabrication of micro-devices, a set of photomasks are created in order to produce each 2D layer of the build in order to fabricate the 3D device. Starting with the base layer of a build, an alignment block is etched onto the build. This alignment block contains numerous marks, typically crosses, which overlap and align with alignment marks on photoresists.

Each photomask in a set contains a specific alignment mark that is to align with a specific mark in the block to ensure that the photomask properly aligns with the previously patterned build layer. Failure to precisely align can lead to entire device wafers, typically containing over 100 devices to fail. Failures can include lack of electrical connections (top and bottom windings not connecting), device collapse (core misplacement), over-etching (core not protected by photoresist) and many more issues.

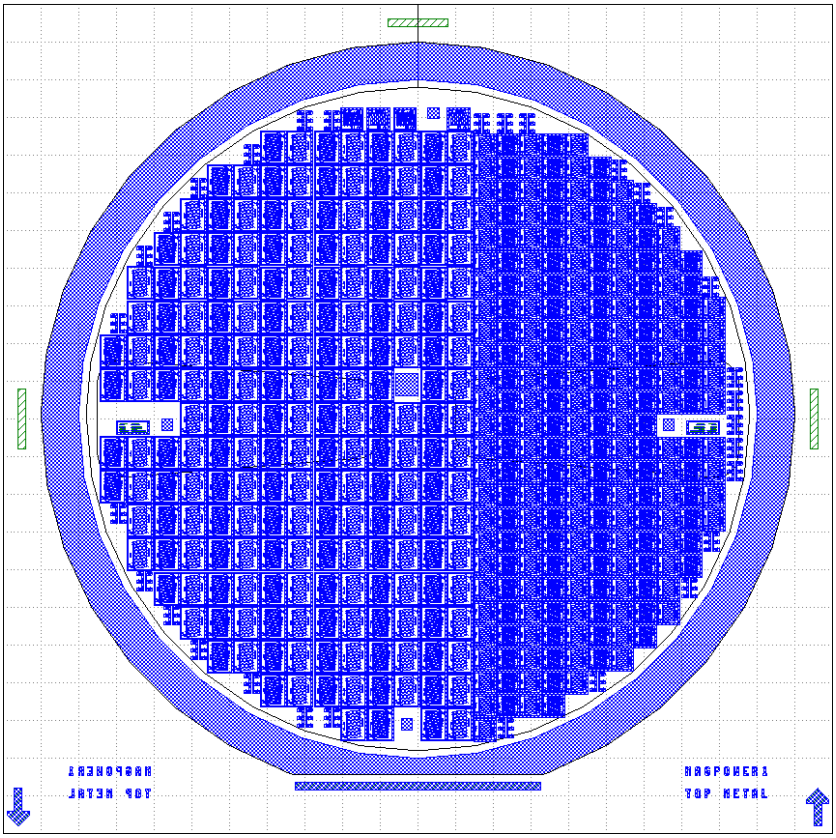


Figure 20 – The top metal winding photomask design used in this project

In the case of the current devices, there are six photomasks in the set that are used to create the device. Fig 20 shows the *Top Metal Windings* Photomask, used for the patterning of an AZ 9260 layer in order to deposit copper to create the top copper windings. Appendix A shows all six of the photomask designs used.

To ensure the proper alignment of photomasks to the substrate wafers, a mask aligner is used to precisely align the photomask with the underlying alignment block on the wafer surface as well as allowing the photoresist to be exposed once aligned. With photolithography, as light passes through the transparent openings of a photomask, it is subject to various forms of light diffraction, including Fresnel, Kirchhoff and Fraunhofer diffraction [51], as shown in Fig 22 [35]. Due to this, any small distance between the mask and the wafer surface can affect the resulting pattern as the UV light scatters as it passes through the mask. Mask aligners offer modes of contact that allow for different distances between the wafer surface and photomask, as shown in Fig 21 [35].

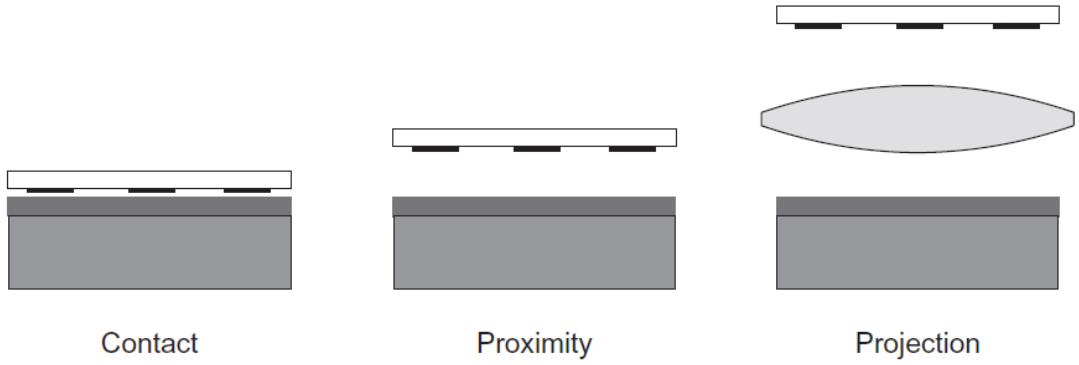


Figure 21 - Modes of contact for photolithography

Hard-contact forces the photomask and wafer surface to be pressed against one another at a particular pressure (*60 psg set on PLA600F optical mask aligner* [52]), while soft-contact presses the mask and wafer together with less force (*20 psg*). These contact modes limit the amount of light diffraction, with hard contacting offering better resolution in patterning.

Depending on the circumstances, the use of excessive pressure to contact the mask and a wafer may damage the underlying fabricated layers on the wafer or the photomask itself.

In some cases, the photoresist on the wafer may be adhesive whereby contact would cause the wafer to adhere to the mask, or that the use of pressure is too great a risk to the fabricated layers or mask, thus making any hard- or soft-contact methods unsuitable. In these cases, the proximity-contact mode can be used to transfer the pattern. In proximity mode, the wafer and

photomask are not in contact, but due to diffraction of the UV light, the resolution of the pattern is severally decreased.

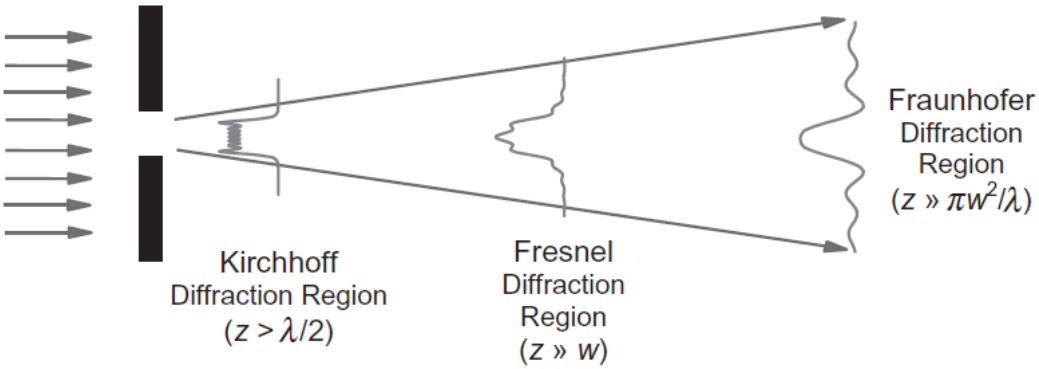


Figure 22 - Forms of diffraction seen in photolithography

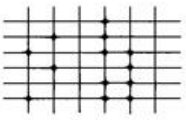
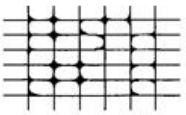
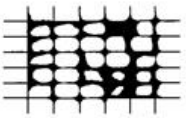
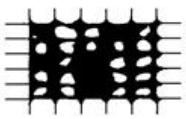
In industry, the need to protect the devices and mask while maintaining the resolution is vital; therefore, projection printing is used mostly in industry. In this mode, a series of lenses are used between the mask and wafer to project the pattern onto the photoresist layer. These lenses produce near-perfect patterns, sacrificing little resolution, with only small defects in the pattern caused by lens defects.[35, 53]

1.3.5 – Adhesion

Throughout a fabrication process, the adhesion between every layer, for photoresists, deposited metals and any other material, must be strong enough to ensure the overall device is durable and resistant to wear and tear. Lack of adhesion of any layer during fabrication can cause it to delaminate, destroying the device. It is therefore vital that the adhesion of each layer is thoroughly tested and additional processes put in place to improve adhesion, for example, the Ar^+ treatment of BCB for adhesion to the Ti seed layer.

Adhesion can be tested with a simple *Tape Test* (Fig 23) [54]. These tests involve making incisions through the newly adhere surface to create a criss-cross pattern. A small portion of transparent tape is placed on the pattern with a loose end available to pull off the tape when ready. After a minute, the tape is rapidly pulled off, and the criss-cross pattern is examined to determine the adhesion rating.

Figure 23 - Tape Test classification sheet

Classification	Surface of cross-cut areas from which listing has occurred. (Example for six parallel cuts.)	Rate of adhesion
5B	None	The edges of the cuts are completely smooth; none of the squares or the lattice are detached.
4B		Small flakes of coating are detached at intersections; less than 5% of the area is affected.
3B		Small flakes of coating are detached along edges and at intersections of cuts. The area affected is 5 to 15% of the lattice.
2B		The coating has flaked along the edges and at parts of the squares. The affected area is 15 to 35% of the lattice.
1B		The coating has flaked along the edges of cuts in large ribbons and entire squares have detached. The area affected is 35 to 65% of the lattice.
0B	Flaking and detachment in excess of 65%.	

A rating or classification of 5B or 4B is considered adequate for adhesion. The fabrication process can continue on this new surface with little worry of the material delaminating. A rating of 3B may be suitable for top layers of a device; however, any classification lower shows that the adhesion will need to be improved. Fig 24 shows an example of complete delamination of a metal core material during this project.

In order to improve adhesion, the following methods can be used: the use of alternative surface cleaning and material deposition methods, use of adhesion promoters & pre-adhesion treatments, and as a last resort, the use of alternative materials. [48, 50, 55]

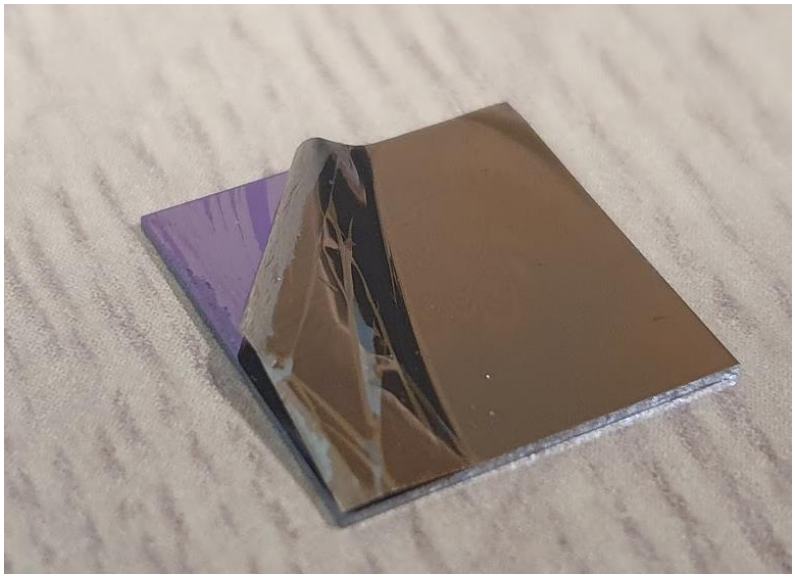


Figure 24 - Delamination of NiFe from the silicon substrate

1.4 – Core Deposition

1.4.1 – Introduction

Metal deposition in this project refers to the various methods of producing metal thin film layers on top of a specific substrate. A thin film refers to a material layer ranging from nanometre to micron-scale thickness. They are multiple methods of depositing thin films, each with their specific use, pros and cons. These methods can be broadly split into two categories, chemical or physical, based on the process behind the deposition.

Chemical deposition techniques involve chemical reactions, typically in a liquid or gaseous medium to which the reaction occurs at a substrate surface, forming a solid thin film of material. Such techniques include electroplating, electroless plating, chemical vapour deposition (CVD) and atomic layer deposition (ALD). Specifically, electroplating is the crucial chemical deposition technique used in this project. Due to the liquid or gaseous medium of these techniques, the deposition of the thin film typically occurs across all of the exposed substrate surfaces, producing a conformal deposit.

Physical deposition techniques involve physically covering a substrate with the material, in terms of mechanical, electromechanical or thermodynamic means. Generally, the material to be deposited is physically changed to a gaseous state or vapour, thus requiring large amounts of energy. Physical vapour deposition (VPD) is one of the most common over-arching physical deposition techniques, which encompasses the technique known as sputter deposition, which is the primary physical technique used in this project. These techniques can create a very conformal deposit, but unlike their chemical counterpart, these techniques typically cannot be directed to deposit in specific areas of a substrate. Sputter deposition and electroplating were the two deposition methods used to deposit various thin films of metals throughout this project.

1.4.2 – Sputter Deposition

Sputter deposition involves bombarding a substrate surface with particles of a material. These particles originate from a "target" which themselves are bombarded with highly energised gas or plasma, with the target itself made up of the material that is to be sputtered. In bombarding the target with plasma or energised gas, the material in the target is ejected, causing it to impact any available surface, including the substrate. [56] Sputtering is especially useful as the material never changes state, meaning that high-melting-point material can be deposited with ease. Fig 25 shows a schematic of the magnetron sputter operation. [57].

.

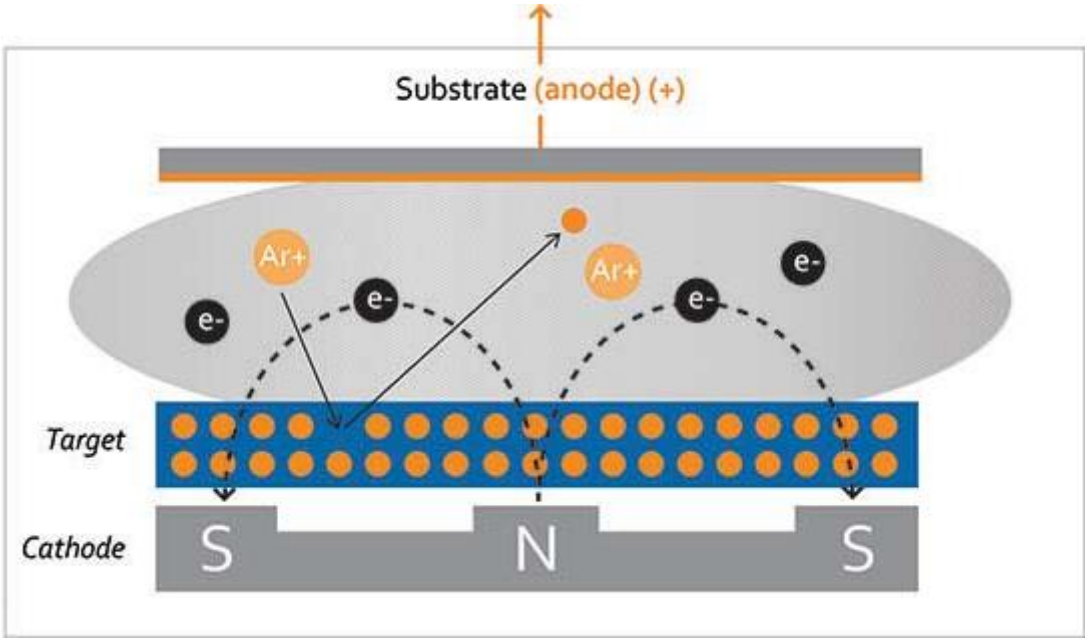


Figure 25 - Diagram of a Magnetron Sputter Deposition System

Sputter deposition often employs the use of magnetrons in order to generate the plasma, created from positively charged ions, at low pressure and in vacuums.[58-60] Alongside the magnetrons, potentials are supplied to the targets and substrate to form a cathode and anode respectively.

The cathode target uses the magnetron to form an electric field within a region around the cathode's target surface and also produces a magnetic field, trapping electrons within this region. This leads to the creation of a highly saturated, electron-filled area, localised around the target surface, which improves the efficiency of the ionisation of argon.

Thanks to this, less argon is used in the sputtering process, reducing the number of background gases in the sputterer. These gases interfere with the sputtering process by colliding with ejected target atoms; removing their energy, altering their trajectory and overall slowing the deposition rate of the target material, as well as incorporating themselves as contaminants in the deposited film.

Any argon atom that enters the electron-filled field is positively ionised with potentials ranging from hundreds to thousands of electron volts (eV), accelerating the newly formed positive ions towards the negatively charged cathode. The energy supplied to the argon ions dislodges and ejects a target atom when the ion bombards the target surface. Ejected target atoms travel in a straight line, with a trajectory based on the angle of impact of the argon-ion, towards the opposing side of the sputterer which contains the anode surface.

The target atoms impact and condense on any available surface, which includes the sputterer's internal walls, the substrate (wafer) holder and the substrate surface itself. This impact typically causes the target material to slightly embed itself into the substrate surface, promoting excellent adhesion between the newly formed thin film and the underlying substrate.

Sputtering does not require any form of heat in order to work as the use of the magnetron allows the creation of plasma at low pressure and temperatures, ensuring that heat-sensitive material on the substrate is not damaged. Furthermore, the substrate does not have to be conductive in order for deposition to occur, meaning plastics (photoresists) can be covered with a metal layer with excellent adhesion.

Overall, a very uniform thin film of material is deposited over the entire substrate surface. However, this can also be considered a disadvantage as the ejected atoms of the target material cannot be directed to avoid certain areas of the substrate. Specific micro-fabrications techniques, such as lift-off that require the removal of the photoresist layer after metal deposition can become more difficult to achieve after sputtering, as every surface, both vertical and horizontal, are covered with the target material. This leaves the photoresist encased in the metal, with no exposed photoresist which can react and dissolve using the photoresist stripper solution, hindering the lift-off process. (Fig 26) [61].

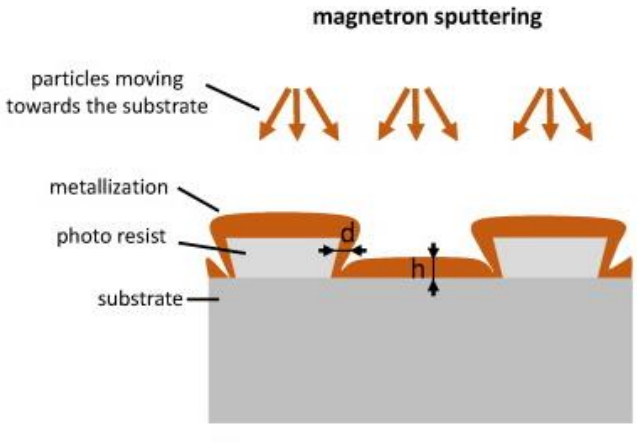


Figure 26 - Sputter deposition for lift-off technique

Other disadvantages include the amount of target material that is wasted as it condenses onto surfaces other than the substrate. Combined with expensive targets, sputtering is not considered the most efficient PVD technique. The rate of sputter deposition, despite the integration of magnetrons, is also slow in comparison to other PVD techniques, and considerably slower than other techniques.

Sputtering is typically used for nanometre-scale thick seed layers, typically titanium, as an adhesive layer, followed by copper or $Ni_{80}Fe_{20}$ as the conductive layer. These seed layers can be sputtered over silicon wafers to allow electroplating on silicon or over other non-conductive layers of material (photoresist), which is useful in microfabrication. For example, in integrated magnetics; core material like CZTB can be directly sputtered onto previously fabricated layers, or a seed layer can be deposited allowing for a NiFe or CoNiFe core to be deposited using electrodeposition. Producing thick deposits of material using sputtering is possible and is used for sputtering core material like CZTB, which cannot be deposited by chemical means, although this process is slow and expensive.

The deposited magnetic material can also interfere with the magnetron's created magnetic field, decreasing the deposition rate. Sputterers that are used to deposit magnetic material contain extremely strong hard earth-magnets in order to reduce the interference from the deposited material.

1.4.3 – Electrolysis Theory

Electrolysis is the use of electrical current to drive chemical reactions, particularly in non-spontaneous pathways. Electroplating is a form of electrolysis and consists of an electrochemical cell containing a solution of metal ions which are non-spontaneously reduced onto a substrate surface using an external power source. The theory behind electrolysis is summarised below, describing the potential required for electroplating to occur and how this potential relates to the current. The current flowing through the electrochemical cell is dependent on numerous factors including overpotential, metal/ion interphases and electric double layers. [62, 63]

Metal / Ion Interphase

When a metal is placed into a solution containing ions of that metal, there is an exchange of ions between the solid metal, containing metal atoms *M*, and the solution, containing the metal ions M^{Z+}. The metal can be considered to be made of a crystal lattice, to which *M* may leave the lattice, forming a positive cation M^{Z+} (oxidation) as it enters the solution. In doing so, the atom has left behind an electron in the lattice. M^{Z+}ions may also enter the crystal lattice, forming an atom *M* (reduction).

With M atoms forming M^{Z+} ions, the metal now has an excess of electrons, giving it a negative charge, while the newly formed cations form a positive charge around the surface of the metal. These charges form an equilibrium interphase at the metal surface, as shown in equation 12 and Fig 27 [62, 63], and results in a potential forming between the metal and solution as shown in equation 13, where q_M and q_s are the charges of the metal and solution respectively.

$$\boldsymbol{M \rightleftharpoons M^{Z+} + Ze^{-}} \textbf{ (12)} \qquad \boldsymbol{q_M = -q_s} \textbf{ (13)}$$

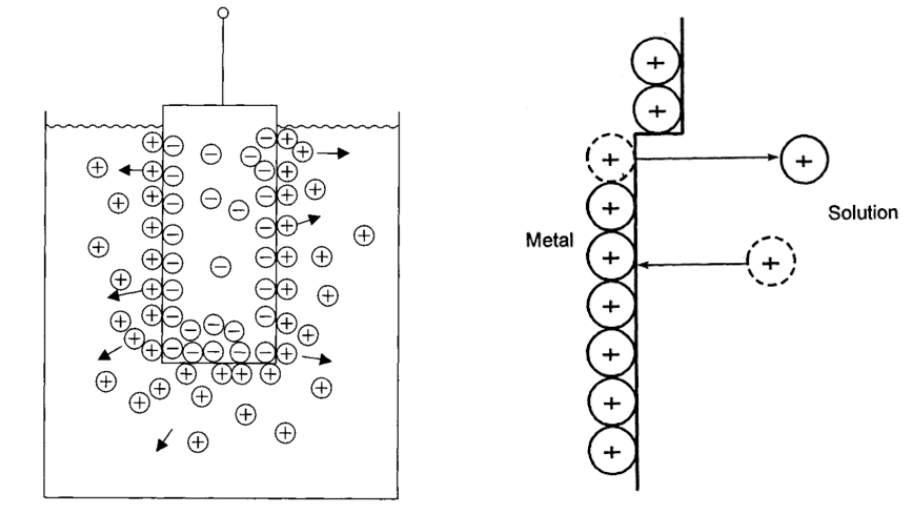


Figure 27 - Metal - Ion interphase

With the dissolution of M into solution and deposition of M^{Z+} onto the metal at equilibrium, the potential between these two phases cannot be measured on their own. Another interphase is required and by connecting two interphases, an electrochemical cell is formed.

Standard Electrode Potentials

Using a standardised interphase, whose potential is already known, the potential of the other interphase can be measured. Each metal/ion interphase can be referred to as an electrode, and the standard hydrogen electrode (SHE) is an electrode which has a potential of 0 V by convention.

By using the SHE or any electrode whose potential is known, in conjunction with the other electrode whose potential is unknown, the potential difference between the two electrodes can be used to calculate the unknown potential. This potential is referred to as the standard electrode potential ($\boldsymbol{E^0}$), at 298.15 K and 1 atm. Table 1 lists the $\boldsymbol{E^0}$ of metals used throughout this project.[64]

Metal	***Reaction (Interface)***	***E^0 (V)***
Co	$Co^{2+} + 2e^- \rightleftharpoons Co$	-0.280
	$Co^{3+} + e^- \rightleftharpoons Co^{2+}$	+1.920
Cu	$Cu^{+} + e^- \rightleftharpoons Cu$	+0.521
	$Cu^{2+} + e^- \rightleftharpoons Cu^{+}$	+0.153
	$Cu^{2+} + 2e^- \rightleftharpoons Cu$	+0.342
	$Cu^{3+} + e^- \rightleftharpoons Cu^{2+}$	+2.400
Fe	$Fe^{2+} + 2e^- \rightleftharpoons Fe$	-0.447
	$Fe^{3+} + 3e^- \rightleftharpoons Fe$	-0.037
	$Fe^{3+} + e \rightleftharpoons Fe^{2+}$	+0.771
Ni	$Ni^{2+} + 2e^- \rightleftharpoons Ni$	-0.257

Table 1 - E^0 of various metals interphases

Nernst Equation

This standard potential, $\boldsymbol{E^0}$, can be used to calculate the reduction potential, $\boldsymbol{E}$, of a particular electrochemical half-cell reaction (examples are shown above), at non-standard conditions using the Nernst equation:

$$\boldsymbol{E = E^0 - \frac{RT}{nF} lnQ} \quad \textbf{(14)}$$

Where ***R*** is the universal gas constant, ***T*** is temperature, ***n*** is the number of electrons transferred in the cell reaction or half-reaction, ***F*** is Faraday's constant and ***Q*** is the reaction quotient. The reaction quotient refers to the overall activity of the ion in the half-cell reaction and comprises of the concentration and the activity coefficient (*a*) of the ion.

Overpotential

When the electrode is used in an electrochemical bath, a power supply supplies an external voltage across the circuit, tilting the equilibrium reaction (Eq. 12) in one direction. This forces an imbalance in charges at the interphase, forcing the electrode to become either electron-rich or electron-deficient. As $\boldsymbol{M \rightarrow M^{Z+} + Ze^{-}}$, the electrode is electron-rich and is considered an anode. As $\boldsymbol{M^{Z+} + Ze^{-} \rightarrow M}$, the electrode is electron-deficient and is considered a cathode. Connecting the anode and cathode via the power supply creates a closed circuit, and currently begins to flow.

The actual potential (***E***) of an electrode required for the reaction to proceed in a particular direction as current flows are different from the standard theoretical potential ($\mathbf{E^0}$). This difference is referred to as the overpotential, η, as shown in equation 15. [63, 65]

$$\boldsymbol{\eta = E - E^0} \quad \textbf{(15)}$$

As the overpotential increases, the current density at the electrodes increases and thus, the rate of reaction increases. Depending on which direction the reaction is forced, the overpotential can be classified as either anodic η_a or cathodic η_c.

Potential & Current Relationship – Electrical Charge Transfer

Current density (*i*), is the specific amount of current that flows through a particular area (SI Units = $A.m^2$) and controls the electrochemical cell rate of reaction. Current density helps define one of the most fundamental kinetic equation of an electrochemical bath:

$$\boldsymbol{i_c = -i^0 . e^{\left(\frac{((1-\alpha)nF)}{RT}\eta\right)}} \quad \textbf{or } \boldsymbol{i_a = i^0 . e^{\left(\frac{(\alpha nF)}{RT}\eta\right)}} \quad \textbf{(16)}$$

Where i_c is the cathodic current density, i_a is the anodic current density, i^0 is the exchange current density, and α is the activity coefficient. Fig 28 shows the change in current density as overpotential changes, in terms of the anode and cathode [62].

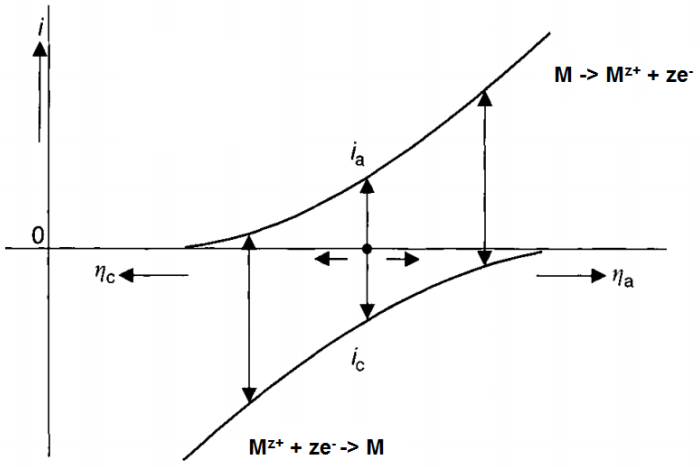


Figure 28 - Polarisation plot showing the rates of both the anodic dissolution and cathodic metal deposition as a function of potential

As the overpotential increases, anodic dissolution and cathodic deposition increases as more current is flowing, increasing the current density. However, this relationship is under the assumption that the charge transfer reactions ($M \rightleftharpoons M^{Z+} + Ze^-$) are the rate-determining steps of the electrochemical cell. The transport of M^{Z+} ions limits this relationship and is another crucial factor in electroplating. There are three main modes of transport for ions in solution, migration, diffusion and convection.

Migration

Migration is the movement of ions through the solution by electrostatic attraction to electrodes. When supplied with potential, these electrodes produce an electric field between them. The ions begin to move at a velocity determined by the potential gradient across the solution between the electrodes. Anions are attracted to the anions and cations are attracted to the cathode. These velocities are typically far too slow and considering impending collisions with other ions and molecules in solution, migration's effect on ion transfer is considered negligible.

Convection

Convection is the movement of the bulk solution. Through thermally induced convection (convection currents) or forced convection (physical stirring), the ions, solvent molecules, electrolyte are all moved around in solution. This ensures fresh solution comes into proximity to the electrodes, although the effect of convection at the electrode surfaces is negligible due to the diffusion layer of the electric double layer of the electrodes. Movement through the diffusion layer is controlled by diffusion, although the thickness of this layer is dependent on convection, with an increase in convection decreasing the diffusion layer thickness.

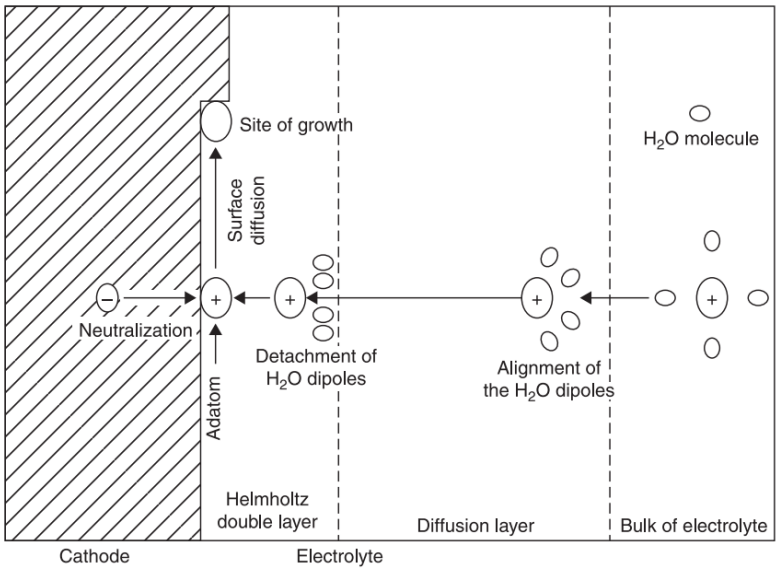


Figure 29 - Movement of ions through the bulk electrolyte, diffusion layer and double layer

As shown in Fig 29 [66], the bulk of the electrolyte is controlled by convection. The movement through the diffusion layer is controlled by diffusion and the movement through the Helmholtz double-layer is through migration (electrostatic attraction).

Diffusion

The movement of the ions through the diffusion layer contributes to the concentration gradient that forms when the electrical circuit is complete. In this electroplating electrochemical cell, the cathode is reducing cations from solution, effectively removing the ion from solution as it is deposited onto the cathode surface. The anode may be resupplying the cations via anodic dissolution or simply removing anions from solution by oxidation to maintain the charge balance. The lack of cations at the cathode surface creates the gradient, causing cations from the bulk solution to move into the diffusion layer, towards the electrode surface.

Effect of Transfer Mechanics on Current

The diffusion layer may be defined to have a thickness of δ and is dependent on the convection of the bulk solution. The bulk solution has a concentration of cations of C_b, up to the diffuse layer, which has a varying concentration gradient. The cations must then travel from the bulk across a distance of δ, through the diffusion layer to the electrode, which has a concentration of cations of C_e.

Assuming at a current density of i_L, the charge transfer mechanics **($M^{Z+} + Ze^- \rightarrow M$)** at the cathode are instantaneous, then the concentration of cations at the electrode, $C_e = 0$. Thus, the rate of deposition is limited by the transfer mechanism of the cation (M^{Z+}). The current density

i_L is considered the limiting, or maximum current density this electrochemical cell can achieve. The Nernst-Planck equation can be used to show the relationship of i_L to the movement of M^{Z+} through the diffusion layer, as shown in Equation 17. Further increasing the potential supplied to the cell will no longer increase the current until the potential reaches a point where an alternative reaction can occur.

$$\boldsymbol{i_L = \frac{nFD}{\delta} C_b} \quad \textbf{(17)}$$

It should be noted that proceeding with the reaction at i_L will lead to a powdered deposit in practice. The current density of the cathode should, therefore, be kept below i_L to ensure a well adhered functional deposit.

Faraday's Law

Faraday's law of electrolysis can be used to calculate the amount of material deposited onto the cathode surface. Equation 18 shows that the amount of material deposited depends on the amount of electricity utilised and that the amount deposited is proportional to the atomic weight or mass of the material.

$$\textbf{Mass deposited} = \frac{WQ}{nF} = ZQ \qquad \textbf{(18)}$$

where *W* is the atomic weight or mass of the material that was deposited, *Q* is the quantity of electric charge passed through the cell, *n* is the number electrons required to reduce the metal (i.e. valency) *F* is Faraday's constant and Z is the electrochemical equivalent of the species being deposited. Faraday's constant shows that 96,487 C is required to deposit one mole of the material.

Deposit Thickness

Using the Faradays equation, the time required to achieve a certain thickness of the deposited material can also be estimated. First, the thickness can be related to the volume of the deposit over the surface area (*a*). Using the weight (*w*) and density (*d*) of the deposited material, Equation 19 is formed.

$$\boldsymbol{h = \frac{w}{ad}} \qquad \textbf{(19)}$$

Relating this to Faraday's law of electrolysis:

$$\boldsymbol{h = \frac{ZQ}{ad} = \frac{ZIt}{ad}} \qquad \textbf{(20)}$$

where h is the height of the deposited metal in cm, I is current supplied to the electrode and t is the time in seconds.

Current Efficiency

Finally, the weight of the material deposited can be used to calculate the current efficiency of the electroplating process. An efficiency rating of 100% means that the current supplied to the cathode is only being used to deposition reaction ($M^{Z+} + Ze^- \rightarrow M$). The plating bath solution contains numerous other ions and reactants that can react at electrodes causing parasitic reactions. These parasitic reactions lower the current efficiency for that electrochemical cell. Examples of such parasitic reactions include near avoidable reactions such as hydrogen and oxygen evolution and the cathode and anode surface, respectively.

Comparing the calculated weight of material deposited against the actual weight deposited, the current efficiency can be calculated, as shown in Equation 21.

$$\boldsymbol{Current\ Efficiency} = \frac{\boldsymbol{w_{deposited}}}{\boldsymbol{w_{calculated}}} \quad \textbf{(21)}$$

1.4.4 – Electroplating

Electroplating, a form of electrolysis, is the process of reducing cations of the desired metal in solution with the use of an electrical signal to produce a metal coating. At its most basic, an electroplating setup contains a metal bath solution, electrodes and a power supply. Fig 30 shows a diagram of a basic electroplating set-up [62].

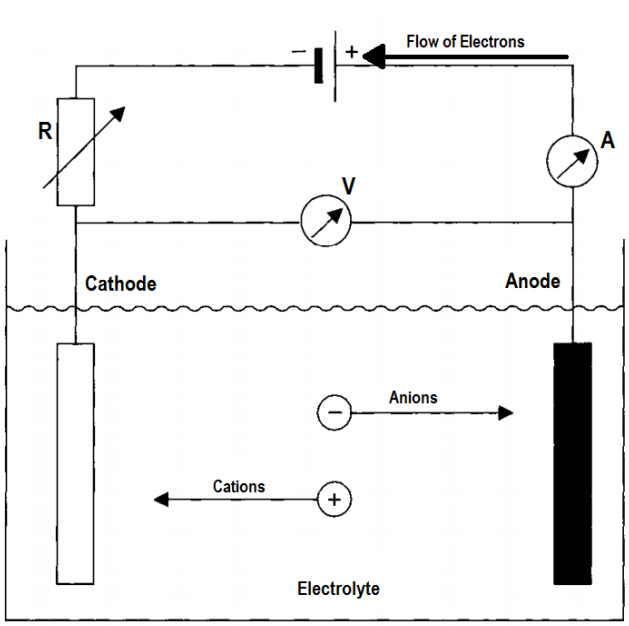


Figure 30 - Diagram of a basic electroplating setup

Electrodes

An electrode is any conductive material that is immersed in the bath solution. The most basic electroplating set-ups require only two electrodes, an anode and cathode. When connected to a power supply, the anode attracts anions in solution and oxidises them by removing their electrons, while the cathode attracts cations in solution and reduces them by giving them electrons. Therefore, the cathode is where the metal deposition occurs, with metal ions at the surface of the cathode reduced into their metal atom form.

In a closed circuit, the power supply supplies a potential to the electrodes, moving electrons from the anode to cathode, while ions in solution move to their respective electrodes, supplying or receiving electrons in redox reactions. This movement of electrons through the circuit and ions through solution constitutes the *current* in electroplating.

The cathode is the main focus in metal and alloy electroplating, as this is the substrate the metal ions will be deposited onto. Naturally, the electrode itself must be conductive in order for electroplating to occur. With substrates like plastic (photoresists), the material will first need to be sputtered with a conductive layer allowing them to act as cathodes. Wafers sputtered with a conductive seed layer, are used throughout this project as the cathode surface. These wafers are held in specially designed wafer holders that ensure a uniform electrical connection and current density to the wafer's surface.

The anode's most basic function is to complete the closed circuit and allow the flow of current. Since metal cations are being consumed at the cathode surface as they deposit onto the metal, the anode must also remove anions from solution to maintain the charge balance of the metal bath and supplying electrons to the circuit. These anodes are typically made of inert materials that will not react in the electroplating process. If the anode is made of the metal being deposited, the anode can also supply electrons to circuit and metal cations to the solution by slowly dissolving into solution via oxidation. In this case, this anode is referred to as a "sacrificial anode". This method ensures the metal ion concentration in the bath is kept constant.

The anode surface area must be equal or greater than the cathodes surface area to ensure that it can keep up with the demand of the system. Too small an anode and the current flow through the system is restricted, due to a decrease in oxidation occurring at its surface, limiting electron flow. This cause an increase in voltage across the system, affecting the electroplated layer and increases the likelihood of unwanted side reactions at both the electrode surfaces.[67]

Metal Bath - Overview

The metal bath solutions all contain an electrolyte made of metal salts as well as additional ions and additives, dissolved in a compatible solvent, typically water. An electrolyte allows the movement of current through the solution by ionic movement towards an electrode, based on charge. For individual plating baths, typically containing a single metal, the metal cation concentration can be kept constant with the dissolution of a sacrificial metal anode. For plating alloys, inert anodes are typically used, and the metal-ion concentrations slowly deplete over time. Routine composition tests must be run on the plated materials from these baths to ensure the metal composition is correct. The incorrect metal composition indicates that a metal ion concentration in the bath has dropped below a minimum threshold level to which it can no longer produce the required alloy composition. At this point, these baths may be regenerated by the addition of the lacking metal salts to the bath; however, if after the addition the composition is still incorrect, a new bath must be created. A plating bath's lifespan, therefore heavily depends on their usage.

Agitating the metal bath is key to ensuring the electrode surfaces are supplied with fresh solution. Without agitation, the potential of the cell increases, allowing for alternative reactions to occur at the electrode surface. Multiple methods of agitation are used throughout this project, including rotating disk electrodes (RDE), paddle and jet impingement systems. Magnetic stirrers cannot be used during the electroplating of magnetic materials due to adverse effects the stirrer would have on the material's magnetic properties.

Throughout the plating process, specific parasitic reactions will occur at the electrode surfaces. Examples of such reactions include hydrogen and oxygen evolution from the electrodes, although these reactions are near unavoidable. However, other parasitic reactions must be avoided in order to maintain a high plating rate, produce the required material composition and stop precipitation of bath constituents. The current density, plating voltage and additional bath compositions are therefore carefully chosen to decrease the chances of these other parasitic reactions occurring.

Metal Bath – Additives

Bath parameters such as pH and conductivity as well as metal deposition parameters, such as stress and grain size, are all affected by the additional chemicals known as additives which are added to the bath. The pH of the bath must be kept within a specific range, depending on the metal bath. For example, the NiFe bath has a pH at 2.5. Too low a pH can cause too many protons to be reduced, forming hydrogen gas, which leads to pitting (small craters in the plated

surface). Too high of a pH will cause additional parasitic reactions in the bath and the precipitation of metal ions [67]. pH buffers are therefore used in order to keep the pH of the bath in the required range.

Plating stress refers to the internal stress within the plated material. Stress is affected by the elctrocrystallisation process as well as the addition of impurities to the material. Tensile stress causes the plated material to contract, while compressive stress causes the material to expand. These stresses lead to delamination of the plated material or in extreme cases, the cracking of the entire plated wafer. Additional chemicals referred to stress reducers are added to the bath to reduce these stresses, typically by depositing as an impurity in the deposited material and disrupting the crystalline structure of the plated material [68]. Additional chemicals are also added to reduce the grain size of the material, which also decreases stress.

Hydrogen evolution at the cathode surface is a typical side reaction in any plating bath and can form hydrogen bubbles on the cathode surface. These bubbles cause pit marks to form on the deposit surface, creating an uneven surface. Wetting agents are added to the bath to reduce the bath's surface tension. This reduces the ability for bubbles to form on the electrode surfaces [68].

The anomalous deposition is a phenomenon seen when plating alloys, whereby the less noble metals are preferentially deposited [69]. Therefore, complexing agents are also added to baths. These agents help by moving specific ions through the solution towards electrode surfaces and by hindering certain metals from reducing at the cathode surface, promoting the creation of specific alloy compositions.

Power Supply

The power supply used for electroplating can vary, depending on the plating method chosen. DC plating is one of the most common plating methods, using a single current or current density output. An example of the diffusion layer at the cathode surface was shown in Section 1.4.3 – Electrolysis Theory. Pulse DC plating involves the rapid pulsing of DC, typically between an ON state of current i_c, for a period of T_{on}, and an OFF state with no current for a period of T_{off}. During the ON state, plating occurs and the cathodic diffusion layer forms, however, when in the OFF state, plating stops allowing the cathodic diffusion layer to begin to relax, and the resupply of metal ions to the vicinity of the cathode surface. Pulse DC may also involve a positive current, rather than simply an OFF period. The duty cycle, γ, shows how much time the system is on over a single cycle and can be expressed by the equation:

$$\gamma = {T_{on}}/{T_{on} + T_{off}} \quad (22)$$

Pulse DC is used to increase the limiting current density, decrease additive concentration required, improve deposit distribution across the substrate surface and alter crystalline morphologies. Fig 31 shows the waveform for Pulse DC.

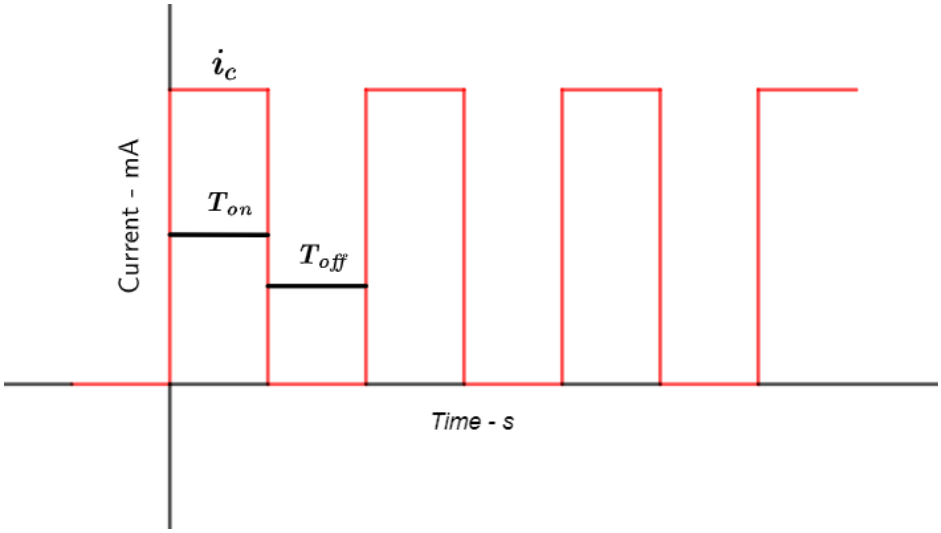


Figure 31 - Pulse DC waveform

Pulse reverse plating (PRP) combines the use of pulse DC, with a current, $i_{forward}$, for a period $T_{forward}$, with the uses of reverse current, $i_{reverse,}$ for a period, $T_{reverse}$. This reverse pulse causes the dissolution of plated material at high current density areas of the plate. These high current density areas are typically uneven areas of the plate. Thus, PRP helps to control thickness build-up in certain areas of the wafer and promotes uniform deposition. [70] Fig 32 shows the waveform for PRP.

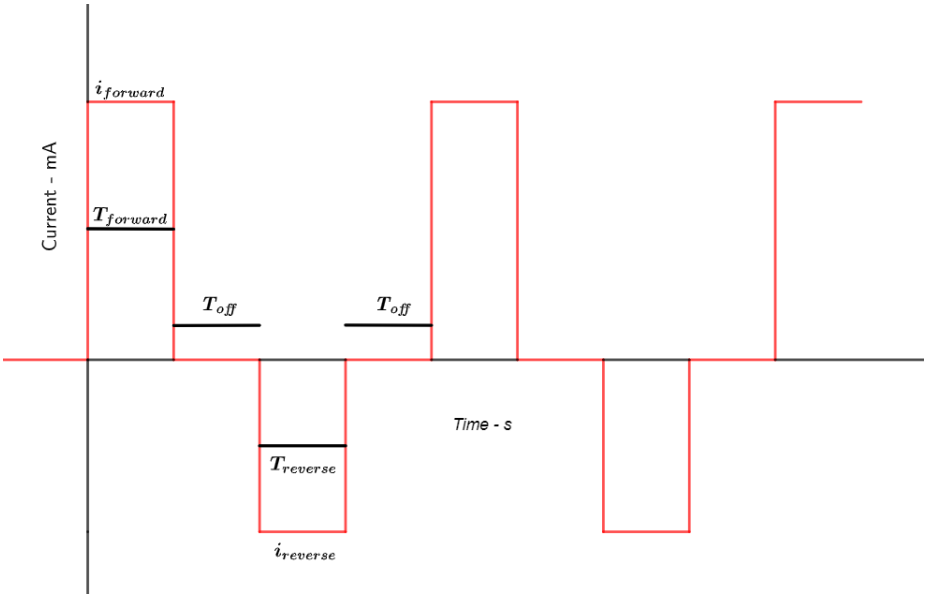


Figure 32 - Pulse reverse waveform

Magnets

The deposition of magnetic material, such as NiFe & CoNiFe, for use in inductors, requires an anisotropic field. This can be achieved by the alignment of the metal dipoles as they deposit, creating a distinct hard and easy magnetic field axis within the metal. Strong, rare-earth metals magnets, such as neodymium are used on either side of the bath cell during the electrodeposition of magnetic materials to align the dipoles during electroplating.

The magnets are typically aligned perpendicular to the cathode, creating the anisotropic field with the hard axis passing perpendicular to the magnetic material and the easy axis running along parallel, as shown in Fig 33 [71].

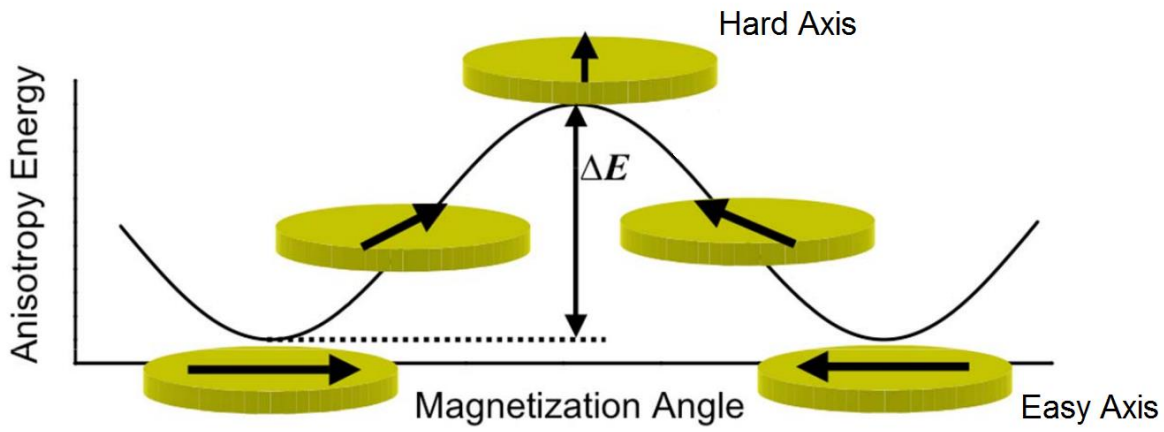


Figure 33 – Anisotropy energy relative to the magnetization angle

1.5 - Soft Magnetic Metals

1.5.1 - Introduction

As explained in Section 1.1.3, soft magnetic material in inductor cores can be used to reduce energy loss and improve the overall functionality of the inductor. However, there are numerous other properties that affect materials usefulness as a core material, such as resistivity and corrosion resistance.

Depending on the desired use of the inductor, the soft magnetic metal can vary, however as explained in Section 1.2, with the ever-increasing demand for decreased inductor size, comes the increase in working frequency for these inductors. Typical soft ferromagnetic materials such as NiFe or CoNiFe have been used extensively in low-frequency devices, with research now focusing on creating new materials for high-frequency devices.

"Ultrasoft" materials (which can be defined as those for which H_c = <10 A/m) are essential for these high-frequency applications, with decreased core lose and improved device efficiency. CZTB is an example of such material that has shown ultrasoft magnetic properties at high frequencies. However, a disadvantage to these materials is that currently, none of these materials can be electrodeposited, which has been the low-cost method for metals deposition in the micro-fabrication industry.

Table 2 shows the magnetic and electrical properties of numerous types of soft NiFe and CoNiFe alloys and the ultrasoft magnetic CZTB material.

Material	**B_{sat} (T)**	**H_C (A/m)**	**ρ (μΩ-cm)**	**μ_r**	**Thickness (μm)**	**Crystal Structure**	**Ref**
Sputtered $Ni_{80}Fe_{20}$	1.3	-	20	2000	4	fcc	[72]
Electroplated $Ni_{80}Fe_{20}$	0.79	-	20	2000	10	fcc	[73]
$Ni_{78}Fe_{22}$	1.08	4	-	8000	-	fcc	[10]
Anisotropic Electroplated $Ni_{45}Fe_{55}$ (Hard Axis)	1.6	192	45	-	0.390	fcc	[74]
Electroplated $Ni_{45}Fe_{55}$	1.5	102	45	300	3.5	fcc	[75]
Anisotropic Electroplated $Co_{59}Ni_{13}Fe_{28}$ (Hard Axis)	1.8	95	24	450	-	fcc-bcc	[76]
Electroplated $Co_{65}Ni_{12}Fe_{23}$	2.1	95	21	600	1	fcc-bcc	[77]
CZTB	1.25	**40**	-	500	250nm laminations with 20nm AlN	Amphorous	(Tyndall)

Table 2 - Magnetic & electrical properties of various soft magnetic metals

1.5.2 – NiFe

Nickel-Iron alloys are one of the most common and versatile nano-crystalline magnetic alloys, with a wide array of alloy composition, creating materials with high permeability, magnetic saturation and electrical resistance, as shown in Fig 34.[10, 78]

Permalloy or $Ni_{80}Fe_{20}$ is a widely used NiFe alloy due to the permeability of NiFe being highest at 80% nickel and the alloy having near-zero magnetostriction. This is due to the fcc (111, 200) orientated crystalline material having a relatively high anisotropic magnetoresistance, with an anisotropic constant near zero. Coercivity is generally < 25 A/m for NiFe alloys, however for Permalloy; the coercivity may be as low < 8 A/m.

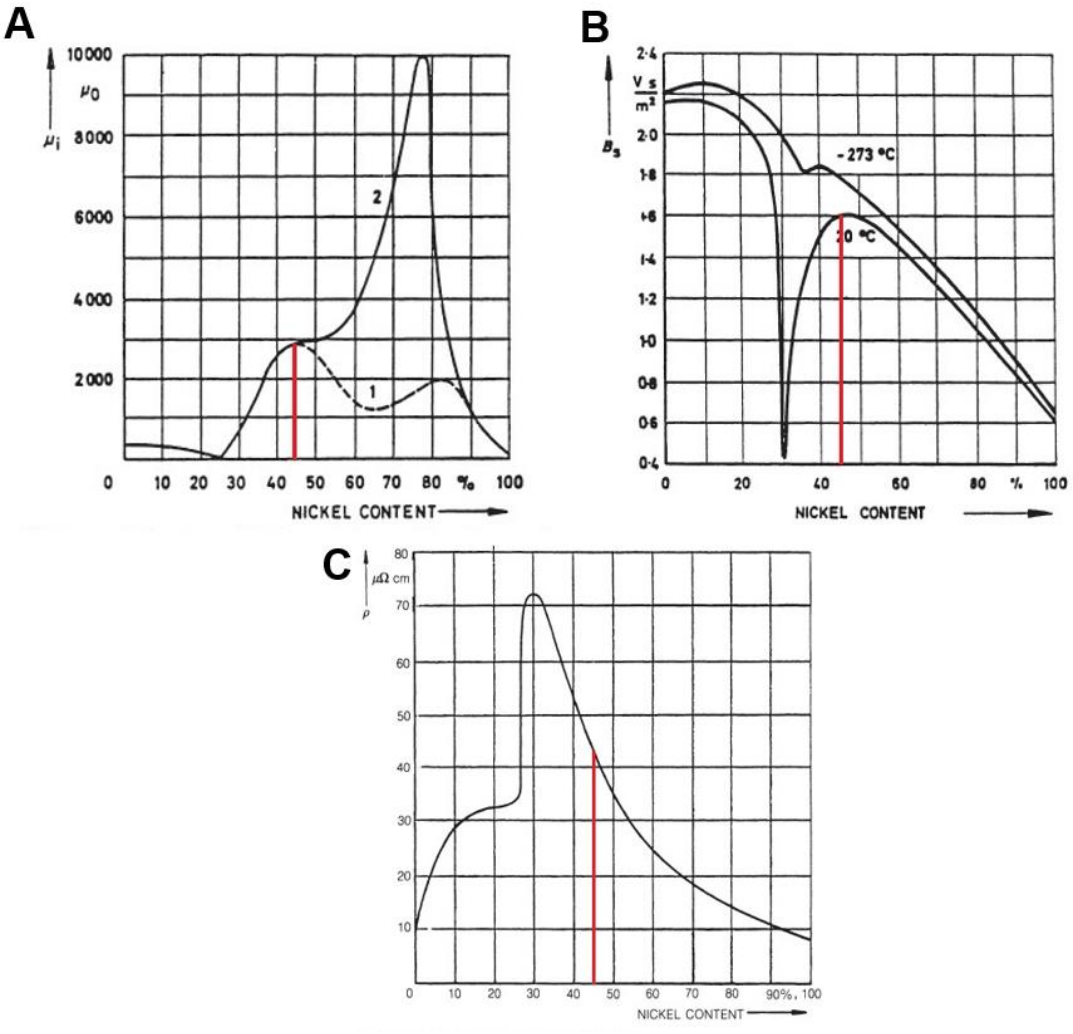


Figure 34: A - Permeability B - Saturation magnetic induction C - Electrical resistance of Ni alloys

Permalloy, unfortunately, has a lower magnetic saturation and electrical resistance than its larger iron-content counterparts. However, below 35% nickel content, the NiFe material may undergo crystal lattice alterations at different temperatures, making it unsuitable for use as inductor cores. Overall, Permalloy is typically replaced by its $Ni_{45}Fe_{55}$ counterpart for use in

low-frequency inductor cores, although Permalloy is still used in electromechanical actuators and transformer laminations.

The $Ni_{45}Fe_{55}$ composition has been highlighted by a red line on Fig 34 (A-C). While $Ni_{45}Fe_{55}$ has a higher coercivity of ~ 150 A/m, and lower permeability than Permalloy, this is a necessary trade-off in order to increase the magnetic saturation and electrical resistance.

As shown in Fig 34 (B), between 30-90% nickel content range, the material peaks in magnetic saturation at 45%; approx. 1.5 higher than Permalloy, at > 1.5 T. Furthermore, with this composition, there is a substantial increase in electrical resistance in comparison to Permalloy at > 40 μΩ-cm. The material also falls into a smaller yet relatively high peak for permeability at Ni - 45%.

With $Ni_{45}Fe_{55}$, the crystalline structure is no longer an fcc predominant alloy with the loss of the fcc (200) phase, which was characteristic of iron contents < 55%. Instead, the material now shows mixed crystal phases between bcc (110) and fcc (111), to which the material's magnetic properties owes its improvements. The mixed phases also allow for decreased grain size, reducing the stress in the deposit.[79]

1.5.3 – CoNiFe

The addition of cobalt to NiFe offers increased corrosion resistance and decreased stress without causing detrimental effects to the magnetic properties of the alloy. Corrosion resistance refers to the durability of the film and is a critical factor for downstream compatibility in photolithography and device fabrication. Devices with low corrosion resistance have extremely limited usages, despite their other properties.

CoNiFe shows a mixed crystalline phase between fcc (111) and bcc (110), although the move towards bcc>fcc mixtures have shown to improve the magnetic properties of the alloy. Previous work has shown that the use of Pulse DC allows for specific fcc-bcc ratios to be produced depending on the duty cycle used while plating [69]. Overall, the presence of the bcc crystalline phase gives CoNiFe alloys a magnetic saturation (B_{sat}) of > 2.0 T, while the fcc phase offers a low coercivity (H_c) of ~ 100 A/m. The material also has extremely low magnetostriction and moderate electrical resistivity and exceptionally high permeability at a range of high frequencies.[76] Overall, the properties of CoNiFe make it useful for use as magnetic cores in a wide range of applications.

1.5.4 – Magnetic Oxides

Ni-Fe oxide has been used as an anode due to its electro-catalytic nature in the evolution of oxygen. [80-82] This NiFe oxide is known as the NiFe layered double hydroxide (LDH). Due to the high iron content in $Ni_{45}Fe_{55}$, it is believed that once oxidised; the $Ni_{45}Fe_{55}$ LDH would contain nickel oxides and iron hydroxides, which may change the alloy's magnetic and electrical properties. This material is hereby referred to as *"Oxidised"* NiFe, or Oxi-NiFe

Initial tests from previous research conducted at Tyndall National Institute have shown, using the Oxi-NiFe as a magnetic material, that there was an improvement in the magnetic and electrical properties of the material [83]. Table 3 shows the results of these initial tests.

Table 3 - Magnetic properties of the various forms of $Ni_{45}Fe_{55}$

Material Properties	Units	As-Deposited $Ni_{45}Fe_{55}$	Oxi-NiFe
Thickness	*µm*	1.65	1.65
Coercivity	*A/m*	32	2
Resistivity	*µΩ cm*	47	70
Saturation flux density	*T*	1.4	1.4
Anisotropy field	*A/m*	735	900
Initial relative permeability	-	650	550
Cut-off frequency (calculated)	*MHz*	67	120

The NiFe LDH can be synthesised by several methods, including precipitation by a solvothermal (hydrothermal) reaction, liquid-phase exfoliation electrodeposition or redox of the NiFe alloy.

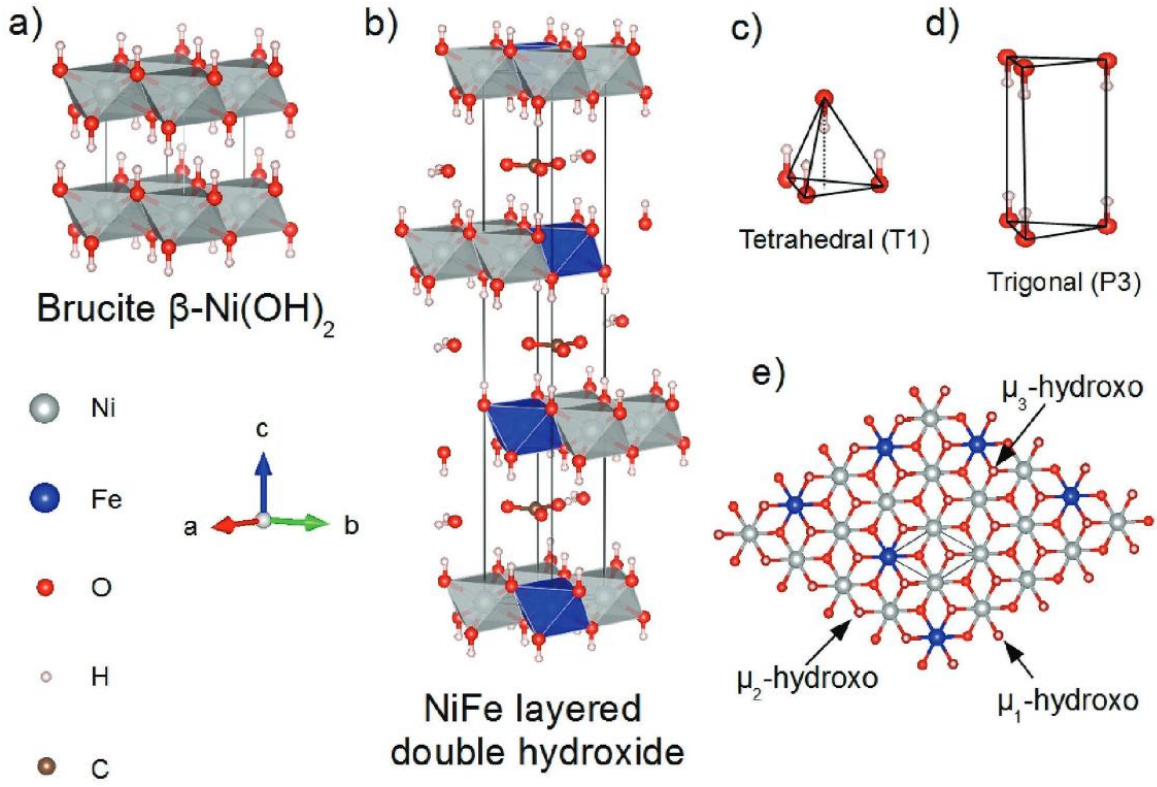
Solvothermal methods [84] involve the use of pre-cursors (Ni^{+} & Fe^{+}) dissolved in a solvent (aqueous or non-aqueous) alongside other chemicals. This solution is held within a closed system where the temperature is brought above the solvent's boiling point. Unfortunately, the NiFe LDH precipitates over a long period, typically over 24 hours, making it unsuitable for this project.

Liquid phase exfoliation [85] is a method that allows the creation of nanosheets of various LDH's, such as $Ni(OH)_2$ and $Co(OH)_2$ [86, 87]. Metal oxide powders are dissolved in a suitable solvent and sonicated in order to cause the formation of the nanosheet LDH. The solvent used depends on its surface energy, which must match with the LDH's crystals that are to be formed. The sonication of the mixture causes the formation of microbubbles. These microbubbles eventually become unstable and collapse, providing high energy which forces the formation of single or a few layered nanosheets of the LDH. This process can produce large quantities of LDH; however, the need for the formation of alloy-based NiFe LDH directly onto a silicon material has to be attempted.

Electrodeposition is a method in which the LDH is directly formed by depositing onto the cathode substrate. Previous work has seen LDH formed from baths containing iron and nickel salts in an acidic medium. However, these layers are typically thin layers of approx. ~40 nm thick [88], making it unsuitable for this research. Other work [89] showed the formation of a NiFe LDH (~250 nm layer) through electroplating using a simple iron and nickel salt solution, with no pH adjustment.

Non-oxidised Ni-Fe alloy ($Ni_{45}Fe_{55}$) can quickly be deposited up to large thickness (> 3 μm) via electrodeposition. A standard *"Post-Processing"* method was utilised at Tyndall to anodise the NiFe alloy into the Oxi-NiFe via cyclic voltammetry (CV) in an alkaline medium. Using CV allows for the redox cycling of NiFe to continuously occur, at any particular rate. Furthermore, with an alkaline medium, oxidation of the NiFe can occur beyond the monolayer, resulting in a thick, hydrated and porous layer of NiFe LDH. The subsequent reduction of the NiFe would allow for a highly disordered layer of metal atoms to form, forming an amorphous NiFe LDH layer or *Oxi*-NiFe [83].

The crystalline structure of LDH has been estimated to be trigonal crystal symmetry with rhombohedral lattices (3R polytype) and space group R-3m, with (003) & (001) crystal planes. [82]



Other than $Ni_{45}Fe_{55}$, this *Post-Processing* method has yet to be tested on other soft-magnetic alloys, such as CoNiFe. This research aims to test the properties of the Oxi-NiFe material further, to test the viability of the *"Post-Processing"* technique with other soft alloys in producing an oxidised counterpart, and test these new oxidised materials within inductor devices as magnetic cores.

1.6 – Cyclic Voltammetry

1.6.1 – Introduction

Cyclic voltammetry (CV) is an electrochemical technique employed to investigate the oxidation and reduction processes of a particular material [90-92]. This technique is a three-electrode set-up, requiring a working electrode (WE), a counter electrode (CE) and a reference electrode (RE). Fig 35 shows a classic electrochemical cell set-up [90]. The material or analyte that is under test is typically in solution, known as the electrolyte solution.

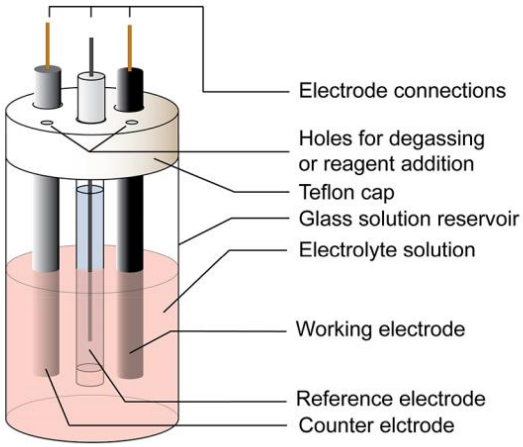


Figure 35 - Electrochemical cell set-up

The WE carries out the redox reaction of the material under investigation, supplying or removing electrons from the solution species or from the WE itself. A RE is used as a reference point to define the potential range of the reactions. RE's have a stable, fixed electrochemical half-cell reaction that produces a standard reduction potential (E^0). Since the potential is being applied between the WE and RE, a CE is also needed to complete the electrical circuit. This CE should be as inert as possible to avoid reacting and forming by-products, which in turn produces a recordable current. Furthermore, the CE should also have a larger surface area than the WE to ensure that kinetics of the reactions occurring at the CE does not interfere with the analyte's reaction kinetics occurring at the WE.

The current produced in an electrochemical cell as the potential is varied over a specific range is recorded on a voltammogram, as shown below in Fig 36 [90]. For clarification, this voltammogram is a US formatted version, showing a potential decrease from left to right. All resulting voltammograms from this research follow the IUPAC format, where potential increase from left to right. It should be noted that the potential supplied to the cell can be negative and positive, can be within any potential range specified and that the CV can start at

any potential within that range. The potential supplied can either move in the positive potential direction, known as the anodic trace or in the negative direction, known as the cathodic direction. This example shows the well-studied redox of Ferrocene or in general, the equation: $X^+ + e^- \rightleftharpoons X$.

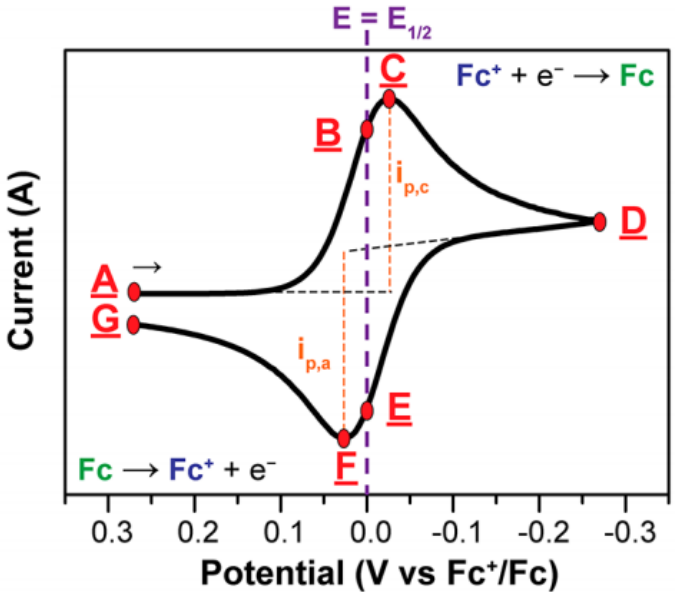


Figure 36 - Voltammogram of Ferrocene ($X^+ + e- \rightleftharpoons X$)

Point A is the starting point of this CV as it moves cathodically. The peak at point C is cathodic and shows the current produced when the material being tested is reduced, in this case, X^+ to X. As the analyte reacts, a diffusion layer of X molecules builds up, and the current is recorded. As the potential moves further negative, the diffusion layer for X^+ continues to grow into the solution, and the reduction occurs at a higher rate until it reaches a peak or the diffusion-limited current. Point C shows the peak current produced, which depends on the diffusion coefficient of the species in solution.

As the potential moves further negative past point C, the diffusion layer of X at the WE surface continues to grow, the surface concentration of the X+ species is zero, and the current is diffusion-limited and decreases proportionally to the square root of the sweep rate. At the lower potential limit the sweep direction is reversed towards the original starting potential As the potential sweeps back, the WE begins to oxidise the abundant X back into X^+ creating the anodic peak that leads to point F, indicating the maximum amount of X is diffusing through the now created X^+ diffusion layer. The anodic peak begins to decrease before reaching point G. Moving from A to G is considered a cycle.

1.6.2 – Metal Oxide Growth

If the working electrode is made of a material that can react during cyclic voltammetry, then it will do so, undergoing redox reactions depending on the potential range selected. Previous research was used to define the potential range required for the oxidation of $Ni_{45}Fe_{55}$ and the CoNiFe alloys, and to assist with the peak assignments during the *Post-Processing* technique. It should be noted that the peaks shown for the single metals will vary when combined with other metals to form alloys. The intensity of each metal's peak will most likely decrease due to the decrease in each of the metal's quantity within the alloy (< 100%). Overlapping of peaks may also make it difficult to distinguish between the redox reactions of the differing metals.

Cobalt

Cobalt metal undergoes rapid oxidation at room temperature when exposed to air, forming a thin 8-10 Å film of $Co(OH)_2$ [93]. When cobalt is subjected to electrochemical studies, using cyclic voltammetry in an alkaline medium, the metal and hydro-oxide layer undergoes numerous reactions, depending on the potential range selected. Fig 37 shows the cyclic voltammogram of cobalt in a 0.2M KOH alkaline medium between -1.2V and +0.6V vs Ag/AgCl. [94]

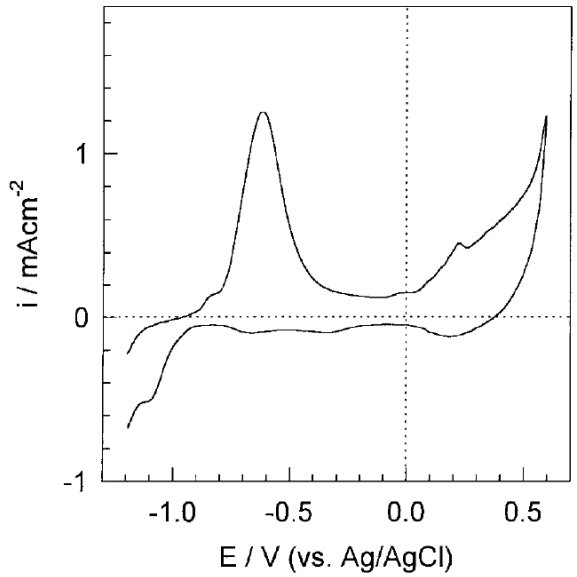


Figure 37 - Voltammogram of cobalt in 0.2M KOH between -1.2V and +0.6V

At -600 mV, cobalt metal undergoes dissolution and passivation in alkaline solutions.[94, 95]

Dissolution: $\mathbf{Co + 2OH^- \rightleftharpoons CoOOH^-_{(aq)} + H^+ + e^-}$ **(23)**

Passivation: $\mathbf{Co + OH^- \rightleftharpoons CoO + H^+ + 2\ e^-}$ **(24)**

$\mathbf{Co + 2OH^- \rightleftharpoons Co(OH)_2 + 2e^-}$ **(25)**

These reactions are dependent on the abundance of the OH^- ions, therefore the more alkaline the solution, the larger the peak seen at -600 mV. The formation of CoO and $Co(OH)_2$ was confirmed by XPS analysis.

At +200 mV vs. Ag/AgCl, the $Co(OH)_2$ layer at the oxide-solution interphase undergoes a reaction, forming Co(II)/Co(III) compounds [94, 96]

$\mathbf{Co(OH)_2 + OH^- \rightleftharpoons CoOOH + H_2O + e^-}$ **(26)**

$\mathbf{3Co(OH)_2 + 2OH^- \rightleftharpoons Co_3O_4 + 4H_2O + 2e^-}$ **(27)**

Additionally, at high concentrations of OH^- ions (high pH), Co_2O_3 can form at 250 mV vs. Ag/AgCl via the following reaction:

$\mathbf{2Co(OH)_2 + 2OH^- \rightleftharpoons Co_2O_3 + 3H_2O + 2e^-}$ **(28)**

With these reactions in mind, the oxidation of cobalt metal into an oxide/hydro-oxide solution requires a highly alkaline solution, with the potential range between -500 mV and 400 mV vs. SHE. Within this range, the oxidation of cobalt and $Co(OH)_2$ would take precedence, showing large anodic peaks. Therefore, it is necessary to ensure the reduction of Co(III) back to $Co(OH)_2$ or CoO is given sufficient time, in order to allow the build-up of an oxide/hydro-oxide layer on the electrode. Reduction of oxides back to cobalt metal is difficult in alkaline solutions.

Iron

The electrochemical behaviour of metallic iron is well documented, particularly in alkaline solutions with a consensus that the formation of $Fe(OH)_2$ is the primary oxidation product in alkaline solutions. [97-100]

$\mathbf{Fe + 2OH^- \rightleftharpoons Fe(OH)_2 + 2e^-}$ **(29)**

The redox reactions between metallic Fe, $Fe(OH)_2$ and FeOOH are easily definable on voltammograms, as shown in Fig 38 [101], although the reduction of $Fe^{2+} \rightarrow Fe^0$ is known to blend with peaks corresponding to the reduction of water and hydrogen evolution. At high pH, positive potentials beyond -700 mV vs. SCE yield no more peaks until 500 mV vs. SCE, due

to the passivation of the iron electrode.[101] At 500 mV, water oxidation and oxygen evolution occur at iron electrodes.

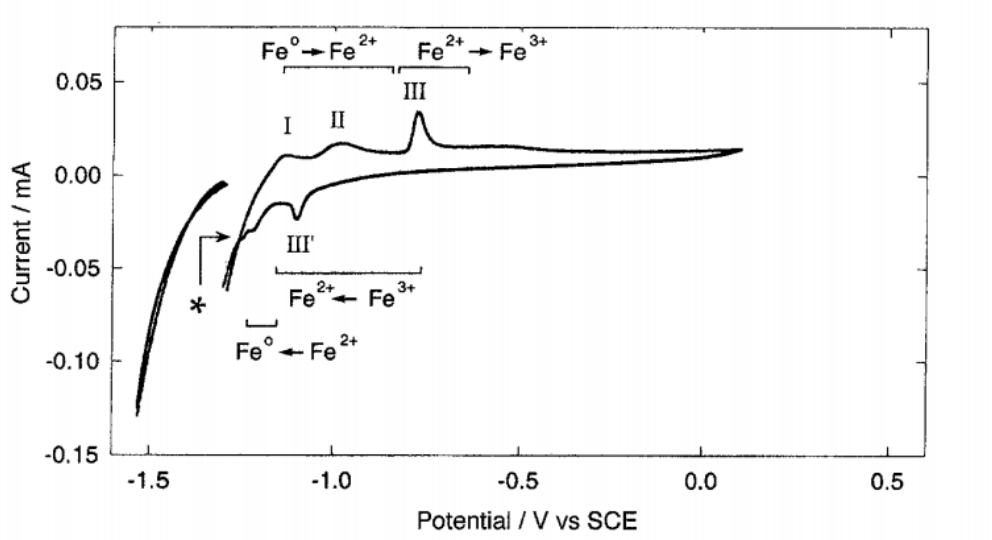


Figure 38 - Voltammogram of iron in 1M KOH between -1.275V and >0V

Starting with the anodic peaks, metallic iron would undergo oxidation between -1.2 V to -0.9 V, with Peak II (-0.95 V vs. SCE) involves the formation of $Fe(OH)_2$, along with stepwise formation of metastable intermediates such as $Fe(OH)_{ads}$ & $Fe(OH)^+_{ads}$ [97]. The formation of $Fe(OH)_2$ was confirmed by infrared spectroscopy [102, 103]. Due to the lack of a corresponding cathodic reduction peak, Peak I (-1.15 V vs. SCE) may be considered the formation of the unstable intermediate $HFeO_2^-$ or simply the adsorption of hydrogen onto the iron electrode.[101] Peak III (-0.75 V vs. SCE) is the oxidation of Fe^{2+} to Fe^{3+} by the oxidation of $Fe(OH)_2$ to FeOOH. The FeOOH produced was confirmed by IR spectroscopy to be predominantly α-forms, with δ and δ' formed at high pH [102, 103]. These FeOOH ions can then undergo rearrangement to form Fe_2O_3, a more stable iron ion complex [104].

$$\mathbf{Fe(OH)_2 + OH^- \rightleftharpoons FeOOH + H_2O + e^- \ (30)}$$

With the cathodic peaks, the reduction of Fe^{3+} to Fe^{2+} occurs over a wide range from -0.7 V, with low gradual peak, to the well-defined peak at -1.1 V vs. SCE. More negative than this potential and the reduction of water and evolution of hydrogen begins, although the reduction of Fe^{2+} to Fe^0 does occur here, though slowly. Fig 38 shows the voltammogram at 2 mV/s, with faster scan rates pushing the water and Fe^{2+} peak further negative, beyond -1.5 V vs. SCE.

It is therefore recommended that for the oxidation of a metallic iron electrode at a scan rate of ≥ 50 mV/s, the potential range should be -1.6 V to -0.75 V vs. SCE. To ensure the formation

of the required oxidation products of iron, the electrode must also be in an alkaline solution. However, the aqueous alkaline solution would be subjected to water reduction/hydrogen evolution due to the overlap with iron's reduction range within the selected potential range.

Nickel

There have been conflicting electrochemical studies on the anodic behaviour of nickel, particularly with the oxidation products and the absorption of hydrogen into the nickel. [105] The products seem to be dependent on the potential range and electrolyte medium selected.

It has been reported that nickel is first oxidised to NiO before forming Ni_3O_4, although this was at near low alkaline pH [106], while at higher pH, the oxidised material formed is NiO and $Ni(OH)_2$ with additional reactions to form a third oxide, NiOOH [107-109]. The formation of $Ni(OH)_2$ was confirmed by later research using coupled ellipsometry, showing the hydroxide was in its β form.[110]

The continuous potential cycling in alkaline solutions allows for the build-up of nickel oxides, as shown in previous research [111, 112]. With a broad potential range, -1.2 V to +0.6 V vs. SCE, as shown in Fig 39 [105], two anodic peaks occur. The anodic peak at -0.7 V vs. SCE is due to the oxidation of Ni to $Ni(OH)_2$ and the peak starting at +0.4V vs. SCE is the further oxidation of $Ni(OH)_2$ to NiOOH[105]. The long, flat current plateau seen from -0.6 V to 0.3 V vs. SCE has also been shown to be the transformation of α-$Ni(OH)_2$ into β-$Ni(OH)_2$ [111]. The peak at +0.6 V vs. SCE indicates the start of oxygen evolution.

$$\mathbf{Ni + 2OH^- \rightleftharpoons Ni(OH)_2 + 2e^-} \quad \mathbf{(31)}$$

$$\mathbf{Ni(OH)_2 + 2OH^- \rightleftharpoons NiOOH + H_2O + 2e^-} \quad \mathbf{(32)}$$

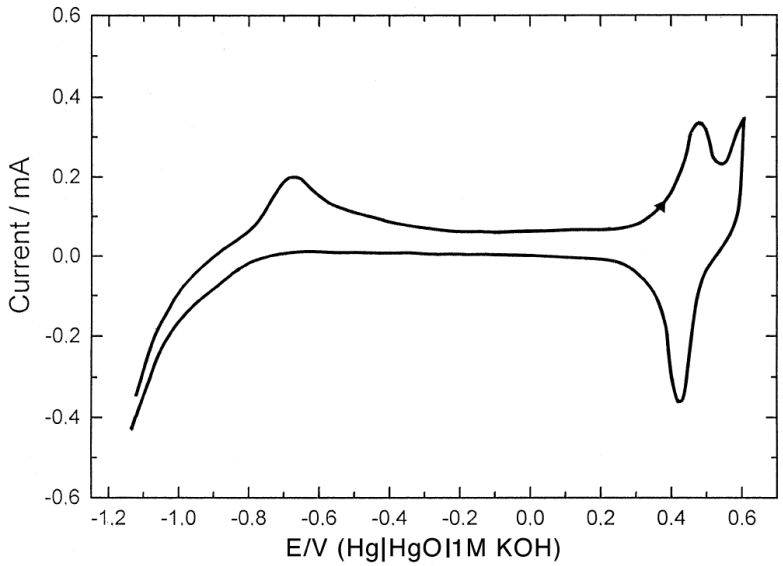


Figure 39 - Voltammogram of nickel in 1M KOH between -1.15V and +0.6V

This first anodic peak is due to the formation of $Ni(OH)_2$, which is then difficult to reduce. This layer of $Ni(OH)_2$ passivates the electrode, limiting further oxidation, hence the lack of anodic peak during further cycles. In order to reduce $Ni(OH)_2$, hydrogen evolution is required, as hydrogen is known to dissolve nickel oxides. [105]

The anodic peak for the reduction of $Ni(OH)_2$ is difficult to identify due it blending with the broad anodic peak caused by the water reduction/hydrogen evolution range (-1.2 V - -0.7 V vs. SCE). The anodic peak at +0.45 V vs. SCE is the redox coupled reaction of $Ni(OH)_2$ / NiOOH.

Overall, for the continuous formation of nickel oxides, the range should be broad, with the lower potential set in the water reduction/hydrogen evolution range and the higher potential range just entering the water oxidation/oxygen evolution range. This ensures the complete formation of β-$Ni(OH)_2$ as well as NiOOH. To avoid the formation of Ni_3O_4, the electrolyte medium must also be considerably alkaline, giving a high pH.

Chapter 2 – Experimental

2.1 – Fabrication Chemicals & Equipment

Details on the step-by-step fabrication process of the inductor devices can be found in Section 3.1 – Device Fabrication Process.

2.1.1 – Process Chemicals

The following list of chemicals was used throughout the device fabrication process:

Photoresists & Developers

- *AZ 9260 photoresist* (Microchemicals GmbH)[113] is a thick, positive, high-resolution photoresist that offers thicknesses of up to 20 μm. A 1 : 3 AZ 400K developer: DI ratio, using manual agitation in puddle mode (i.e., the wafer in solution in a glass petri dish), was used to develop the photoresist by removing exposed areas of the photoresist. Acetone was used to entirely remove patterned AZ, followed by IPA and DI, to ensure all traces of photoresist were removed from the wafer surface.
- *BCB 4026-46* (Dow Chemicals)[48] is a negative insulating dielectric layer, surrounding the core and copper vias and windings. An Ar^+ gun treatment was required on the BCB's surface if there was to be a metal layer sputtered on top, in order to promote better adhesion. DS2100 Developer in puddle mode was used to remove the unexposed photoresist. Exposed BCB is polymerised and is extremely difficult to remove.

Bath Solutions

Details on the specific chemicals found within these baths can be found in Section 3.2 – Metal Deposition.

- *Bright Copper ACG 8* [114] is a commercial solution produced by Schlötter GmbH that is used in the plating of copper. Details on the composition and plating method for this bath can be found in Section 3.2.2 – Copper Deposition.
- *Tyndall's in-house NiFe bath solution* was used to plate the NiFe cores. Details on the composition and plating method for this bath can be found in Section 3.2.3 – NiFe Core Deposition.
- The *CoNiFe bath*, used to plate the CoNiFe cores for this build, was created using a combination of numerous plating methods detailed in various publications, including previous work in Tyndall. Details on the formation of this bath, it's final composition and plating method can be found in Section 3.2.4 – CoNiFe Deposition.

Additional Chemicals

- *Acetone* was used to wash away exposed positive photoresist as well as any additional organic residue and particulates from the device wafers.
- *IPA* was used to wash away acetone to ensure no traces amounts of the solvent are left on the device wafers. IPA can then be washed away with DI to ensure a clean wafer surface.
- *Hydrofluoric acid (HF) or BOE Etchant* was used to remove unused Ti seed layers. 100 ml of the solution in puddle-mode was used, followed by several washings with water to remove trace amounts of the acid.
- *Nitric Acid* was used to remove unused copper or NiFe seed layers. Combined with water in a 1:2 ratio, a puddle mode wash was used, followed by several washings with water to remove trace amounts of the acid.
- *1M Hydrochloric Acid (HCl)* was used for pH adjustment in the in-house NiFe Bath
- *1M Sulfuric Acid (H_2SO_4)* was used for pH adjustment in the CoNiFe Bath
- *1M Sodium Hydroxide (NaOH*) was used for pH adjustment in both the NiFe & CoNiFe Baths.
- *Deionised Water (99%)* was used throughout the fabrication process for cleaning the device wafers and creating solutions. The DI Water must be sufficiently deionised as certain ions such as chloride can affect the various plating baths used throughout this fabrication.

2.1.2 - Process Equipment

The following list of machinery & equipment were used throughout the device fabrication process.

- A *Quorum Q300T D Plus Sputter tool* was used with Ti, Cu and $Ni_{80}Fe_{20}$ targets to deposit the required seed layers. This sputter tool also was used to deposit the CZTB cores in the comparison devices.
- *A Digital Matrix SA/1B Plating System* was used in the plating of copper. This instrument was supplied by Digital Matrix. Details on this equipment can be found in Section 3.2.2 – *C*opper Deposition.
- A *custom made pulse waveform generating power supply (Tech Mu Inc.)* was used for plating of both NiFe and CoNiFe. This system is capable of numerous plating methods, including DC, pulse DC & pulse reverse DC. The system has customizable settings for plating such as the required current, both forward ($I_{forward}$) and reverse ($I_{reverse}$) as well as the timeframe for these currents ($T_{forward}$ / $T_{reverse}$) and off-periods (T_{off}). The system is also programmable, in that up to 4 plating methods can be set-up to run within one plating session.
- A *Cascade 700 LV, 3052-0000 Pump* was used to pump bath solutions from the bath container into the jet impingement system while plating NiFe. The pump was submerged into the bath and was connected to the perforated Teflon pipe, which causes a jet of the bath solution to stream out of these perforations towards the cathode (wafer) surface.
- A *DC power supply (Wayne Kerr Electronics LS 30-10)* was used to power the clockwise motor in the jet impingement & paddle agitation system when plating NiFe and CoNiFe. This clockwise motor moves the perforated Teflon pipe left and right parallel to the cathode/anode surfaces. Combined with the pump, this completes the *Jet Impingement system*.
- An *IJ Cambria 660B electrochemical workstation* was used as a potentiostat to oxidise the core material using cyclic voltammetry.
- A *Laurell spin coater* was used for the spinning of various photoresists across wafer surfaces. This programmable device aids in the fabrication of a photoresist layer of a thickness, by creating a program of multiple, timed spin steps at a particular RPM.
- A Cannon *PLA600F optical mask aligner* and the accompanying photomasks was used for the precise alignment and exposure of photoresist covered wafers for the fabrication of patterned photoresist layers.

- An *IKATRON ETS-D 4 fuzzy magnetic stirrer with hotplate* was used for mixing bath solutions and the baking of wafers during the fabrication of photoresist layers.
- A *digital multimeter* was used to test the electrical connection between the wafer's surface and its electrical connection to the plating systems. Poor quality connections between the wafer and the plating systems are shown by a resistance of 1-1.4 Ω and voltage of 1.4 V, which should decrease below 1.4 V as plating occurs. Allowing plating to occur with such a connection will lead to an increase in current and potential range, affecting the bath chemistry and therefore the resulting plate in terms of composition, appearance, morphology and thickness. Such connections are typically caused by unclean/oxidised metal contacts that connect to the wafer.
- A calibrated *Jenway 3310 pH meter* was used to test the pH of both the NiFe and CoNiFe baths.
- *Nitrogen guns* were used for the drying of wafers.

Additional Help

- Mechanical dicing of wafers into large sections (>2cm) was completed in-house by Dr Paul Tassie.
- Laser dicing of wafers into small sections (<2cm) was completed in-house by Dr Ann Foley.

2.2 - Characterisation Tests

2.2.1 – Composition Characterisation

Deposit Thickness

Varnish marks were used on wafers when the thickness of deposited material or the plating rate of the bath was required. For device wafers, dummy wafers were first electroplated with varnish marks to determine the time required to deposit the device-specific core thickness.

These varnish marks were placed at least in the north, south, east, west and centre of the wafer, as shown in Fig 40. The varnish prevents metal deposition at these locations, and once the varnish was removed using acetone, micron-sized holes in the deposit exposing the original, underlying metal seed layer were left behind.

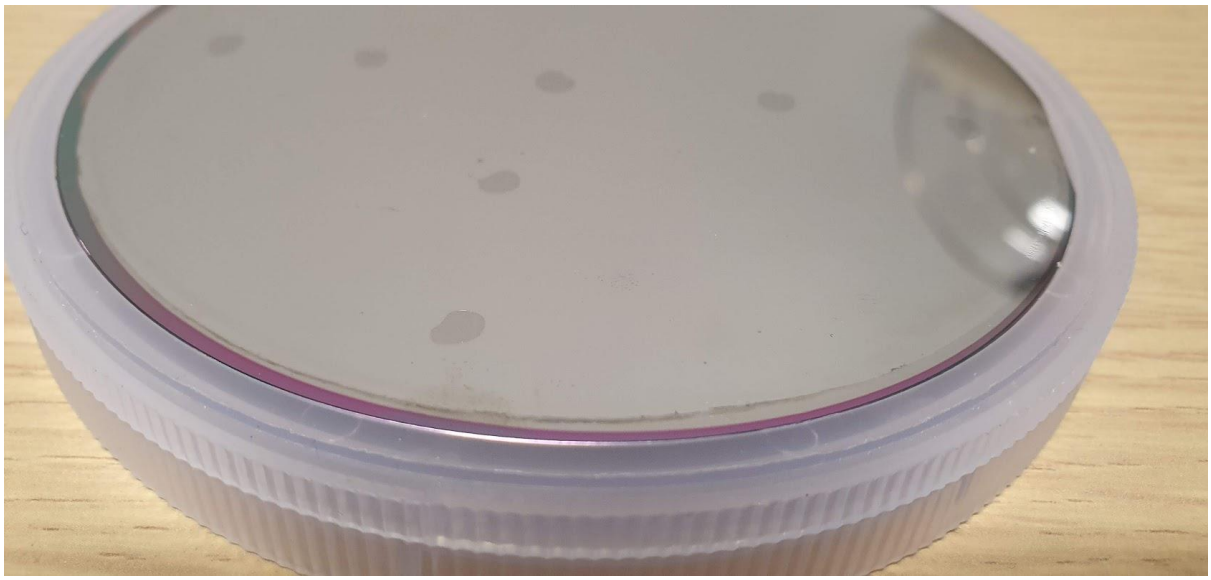


Figure 40 - Varnish Marks on the wafer after electroplating

Using a Tencor P10 stylus-based surface profilometer, the height between the surface of deposit and the seed layer, i.e. the thickness of the deposit, can be measured. The profilometer's stylus is next to the varnish mark and beings to move along the surface of the wafer towards the varnish mark. As the stylus reaches the edge of the varnish mark, it falls down and onto the underlying surface of the original sputtered metal layer, recording the difference in height.

For accurate measurements, the stylus was placed in at least five varnish marks spread across the wafer, and the thickness at each mark was measured twice. Based on the electroplating method, the thickness measurements taken at any of the five varnish marks should be similar, although minute fluctuations in thickness across the wafer were expected. Dissimilar

thicknesses across the wafer can be caused by numerous factors, with improper current density distribution being one of the most common.

Deposit Roughness

The profilometer's stylus can also be used to measure its surface roughness. The deposited material should also show a smooth surface, with little to no roughness, although nanometre scale bumps and ridges are typical of electroplated deposits. The Tencor is capable of detecting roughness to a minimum range of 1-2nm. Nanoscale roughness is too small to affect the shiny appearance or more importantly, the magnetic properties of the deposit.

Any larger scale roughness, such as the roughness formed from "burning", can have a detrimental effect on both the electrical and magnetic properties, such as eddy current loses and coercivity.

Surface Imaging & Thickness

The Quanta FEG650 scanning electron microscope (SEM) & Zeiss Supra 40 SEM were used in order to image the surface of the deposited material. For rough deposits, the SEM typically shows the appearance of nanoscale bumps on the surface of the deposit. These bumps are indicative of burning, typically caused by too high of an overpotential used while electroplating. Decreasing the current used while electroplating decreases the overpotential and the chance of burning, leading to a smoother deposit.

The SEM can also be used to confirm the thickness of the metal deposit by calculating the height of the deposited material at varnish & etch marks, while the sample is at an angle. This is extremely useful when combined with the EDX, as the composition and thickness of a layered deposit can be determined.

Deposit Composition

The Quanta FEG 650 SEM (Fig. 41) & Zeiss Supra 40 SEM also house an Oxford X-Max EDX System (Fig.60), which was used for testing the composition of metal deposits. The composition of the resulting deposits from electroplating baths were tested regularly with the use of dummy wafers, particularly before the deposition of metal for use as a core in a device. All EDX results were collected with the EDX & SEM power at 20.0 keV.

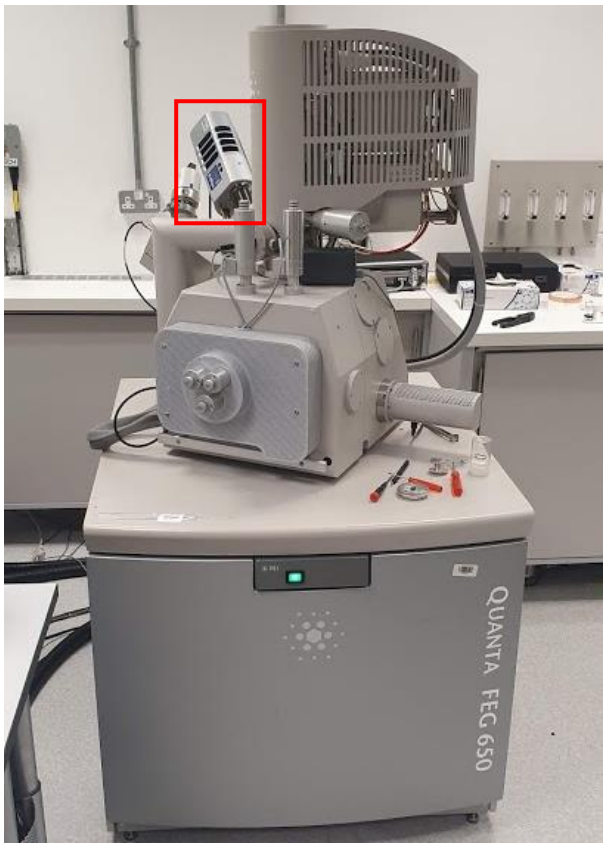


Figure 41 - Quanta FEG 650 SEM with Oxford X-Max EDX System (Red Box)

Deposit Crystallography

A Jeol JEM 2100 TEM system, with selective area electron diffraction (SAED), operated by Dr Michael Schmidt at Tyndall, and the image analysing program ImageJ, was used to identify and image the crystalline structure of the metal deposits. Pure metal deposits ($Ni_{45}Fe_{55}$) typically show a nanocrystalline morphology, while oxides can show amorphous morphology..

Grain Size

The deposits grain size can also be calculated using the TEM system. Using precise TEM imaging of individual grains within a deposit, and the analysis of the images using ImageJ, the size of the grains in the core materials was calculated.

2.2.2 – Magnetic & Electrical Characterisation

BH Looper – Coercivity, Saturation Flux Density, Retentivity & Anisotropy Field

A MESA HF200P BH loop tracer from SHB Instruments (Fig. 42) was used to measure the static magnetic properties of the deposited materials. These properties, such as coercivity (H_c), saturation flux density (B_{sat}) magnetic retentivity (B_r) and anisotropy field (H_k) were all measured along the hard axis of the material.

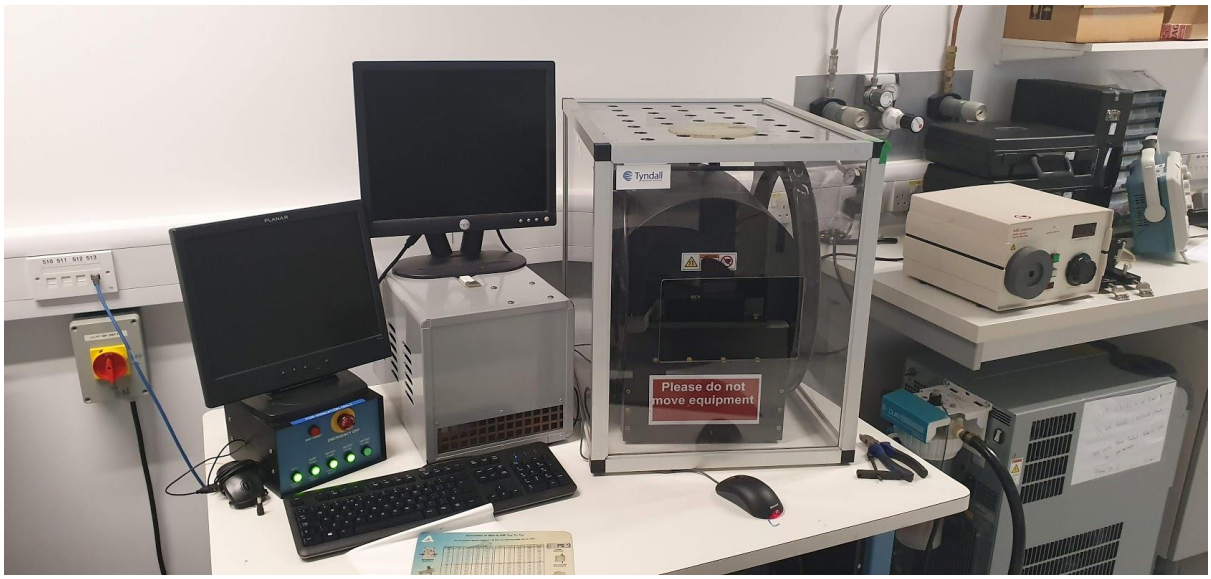


Figure 42 – Tyndall' MESA HF200P BH Looper system

Permeameter – Permeability, Loss Tangent & Material Q-Factor

A PMM 9G Permeameter from Ryowa Electronics was used to measure the permeability of the materials, with loss tangent and Q-Factor calculated by the Permeameter using the measured permeability's. The tests were performed at room temperature, using a broad range of frequencies (1MHz – 1GHz). This piece of equipment was operated by Dr Pranay Podder at Tyndall.

Inductance, AC Resistivity & Device Q-Factor

Inductance (L) & Electrical Resistivity (R) of the produced devices were measured using Formfactor ACP 100 RF probes with the Cascade Attoguard Probe System, a DC source & an Agilent E5071C network analyser. Q-Factor of the devices were then calculated using the values of inductance and resistivity. Fig 43 – 44 show the testing of a device wafer. These pieces of equipment were operated by Dr Pranay Podder at Tyndall.

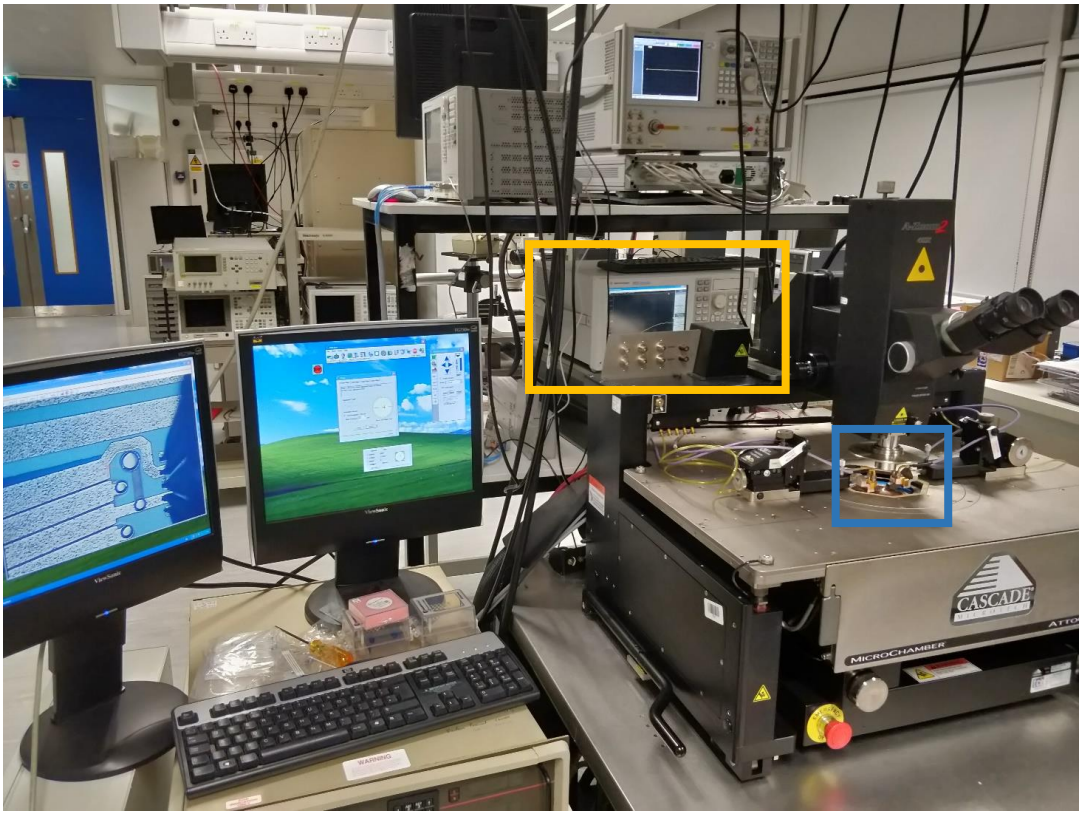


Figure 43 - Probe Station for testing of devices on a device wafer. Orange Box indicates the Network Analyser and the Blue Box indicates the RF Probes and device wafer holder.

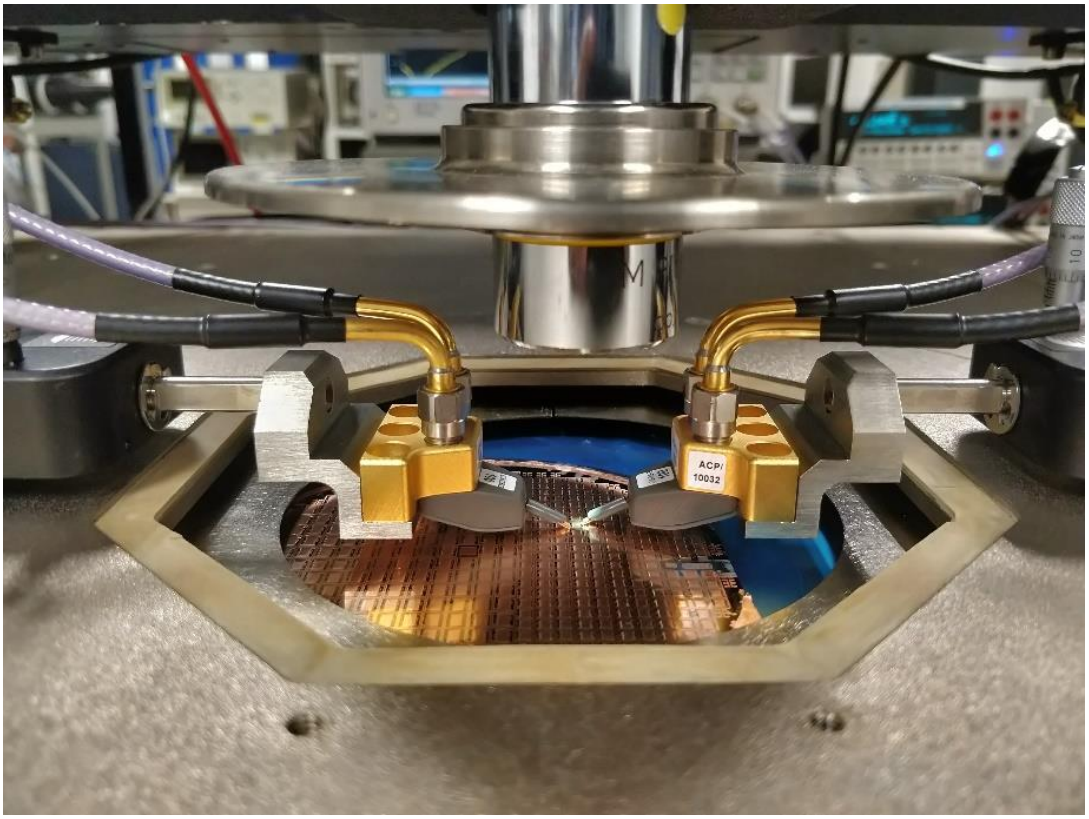


Figure 44 - Testing of a device at the wafer level. The device was contacted by the Formfactor ACP 100 Rf Probes in order to create a circuit.

Chapter 3 – Results & Discussion

3.1 –Device Fabrication Process

3.1.1 - Introduction

The devices were fabricated using a micro-inductor design referred to as the 'ultrasoft design.' The design itself consists of four different inductors (MS1, MS2, MC1, MC2) on each wafer, for use with different power conversion circuit topologies. MS1 & MS2 were single inductors while MC1 & MC2 were coupled inductors. Table 4 shows the parameters of these devices, while Figures 45-48 show the design of each device. Device width and length include a small perimeter around the main core which contains the device design code and electrical connections.

Design	Core Width (µm)	Core Length (µm)	Number of Turns (Per Phase)	Copper Track Width (µm)	Winding Pitch (µm)	Via Diameter (µm)	Device Width (µm)	Device Length (µm)
MS1	1700	3800	8.5	380	400	100	3440	4400
MS2	1400	2400	7.5	260	280	100	3440	4400
MC1	1700	3800	8.5	180	200	100	2940	3000
MC2	1400	2400	6.5	140	160	100	2940	3000

Table 4 - Each of the four devices and their parameters

The inductor designs were rectangular solenoid types, with a magnetic metal core embedded between the bottom and top copper tracks, connected through inline copper vias. A dielectric insulator was used to insulate the core from the copper tracks and vias. The entire device was created layer by layer utilising a combination of Tyndall's in-house, state of the art microfabrication techniques. Four full device wafers were fabricated in total; two as-deposited NiFe and CoNiFe core devices and two with their oxidised counterparts.

The majority of the production steps, as shown in Section 3.1.3, were completed in Tyndall's fabrication clean room, by Tyndall's Fabrication Team. Other steps, such as electroplating were completed in the Plating Lab by Dr Declan Casey and/or personally.

The ultrasoft design is similar to a previous design used in Tyndall, in which a 4 µm CZTB core was deposited. Based the desired magnetic and electrical properties of the ultrasoft devices, (which in turn are based on the device's planned usage) and the properties of NiFe, 3.3 µm was chosen as the NiFe thickness to achieve the desired device properties. Once

measured, these properties would act as the baseline in which the results post-oxidation could be compared to, as well as the use of other ferrite-based materials, such as CoNiFe and their oxidised forms.

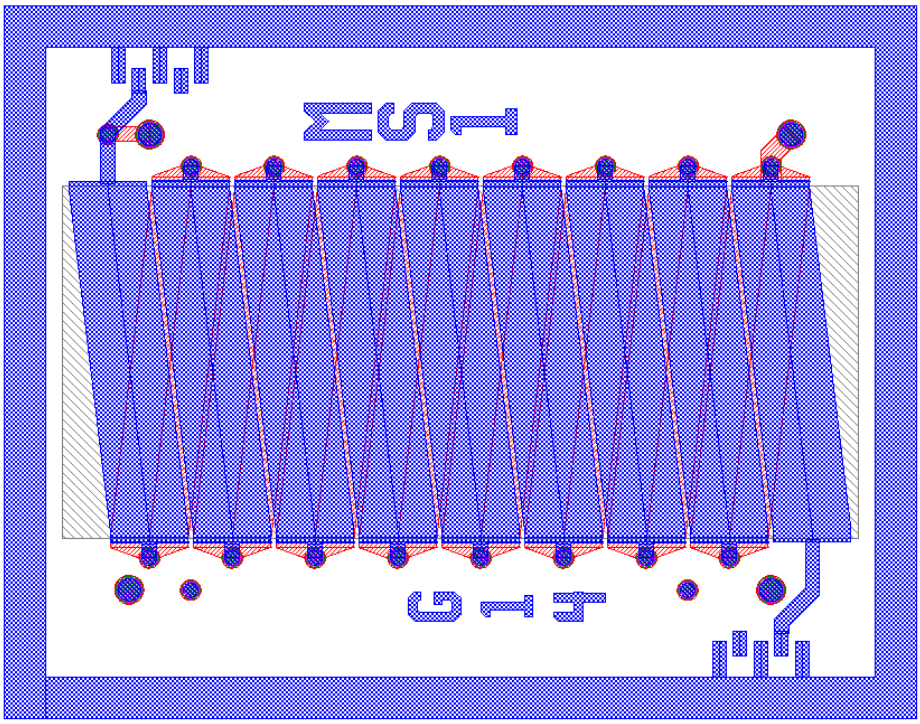


Figure 45 - MS1 Inductor Design

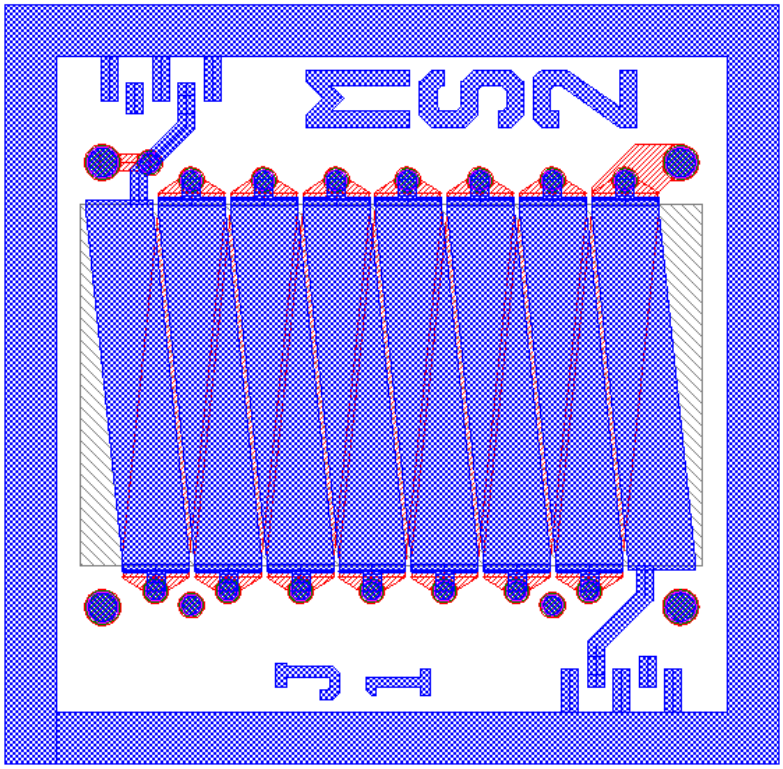


Figure 46 - MS2 Inductor Design

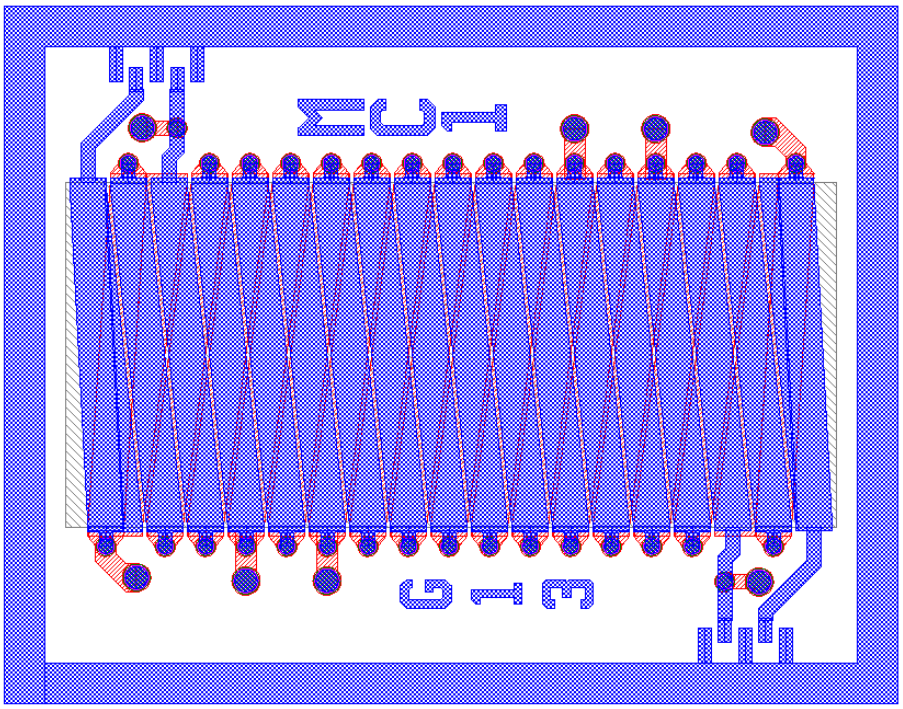


Figure 47 - MC1 Inductor Design

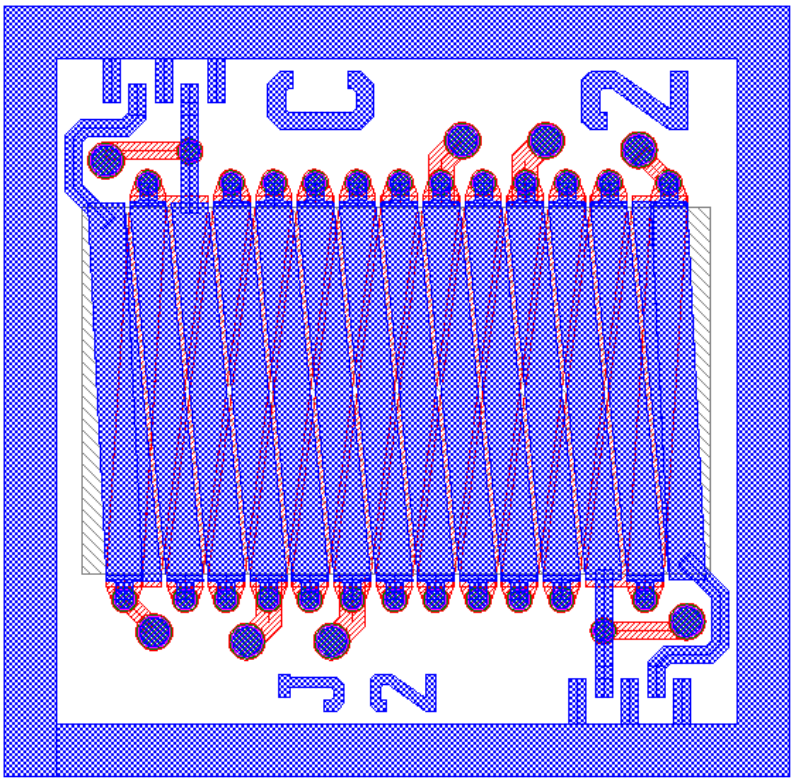
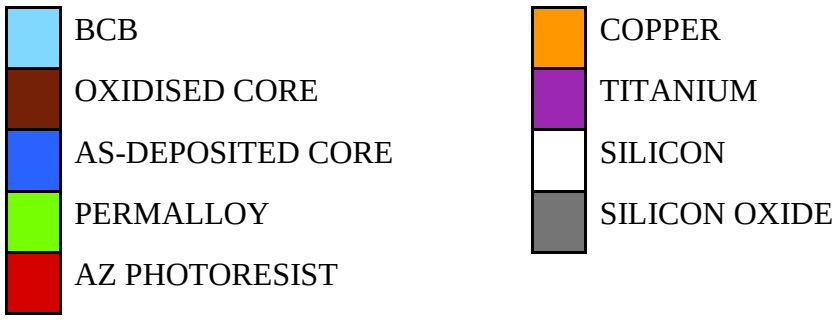
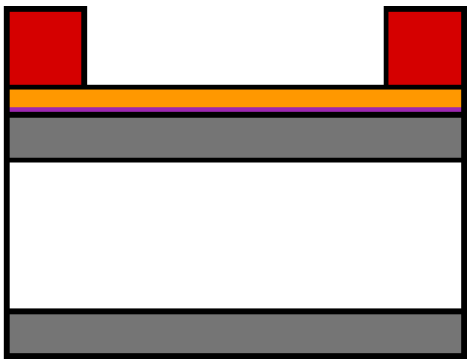


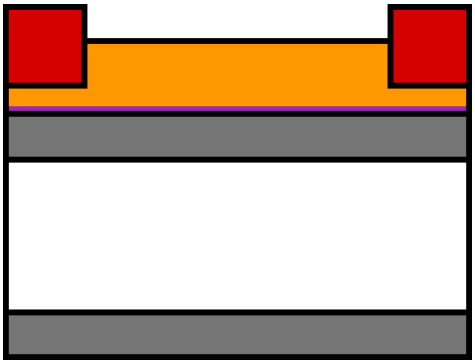
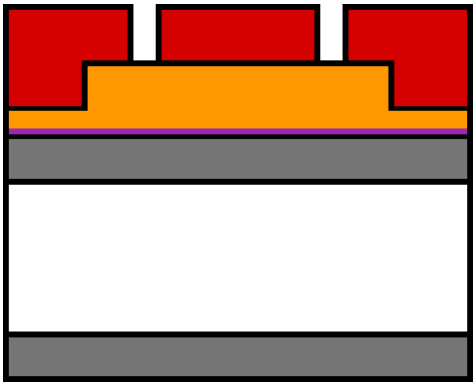
Figure 48 - MC2 Inductor Design

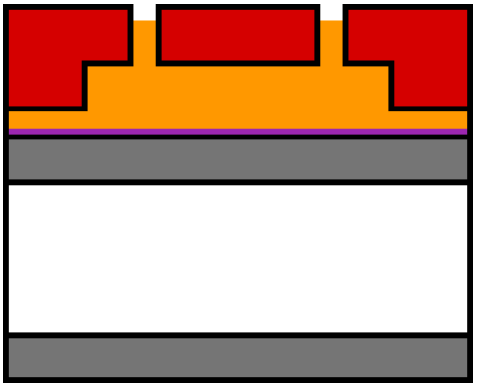
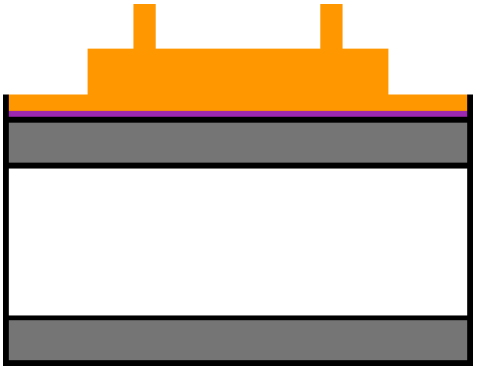
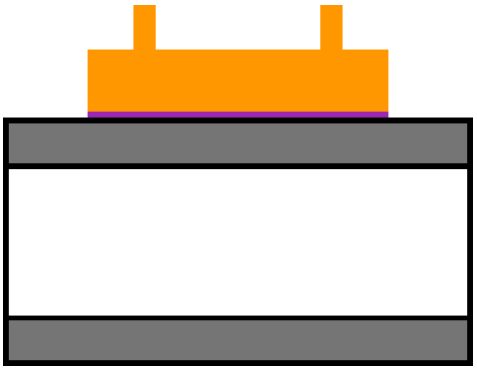
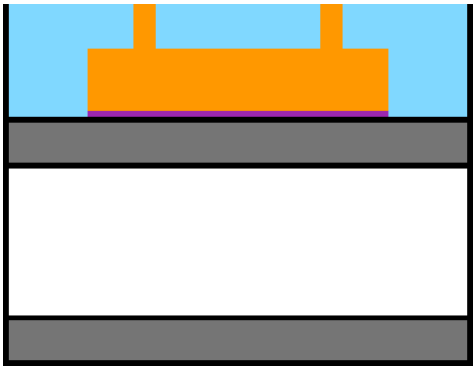
3.1.2 – Fabrication Procedure: Legend/Key

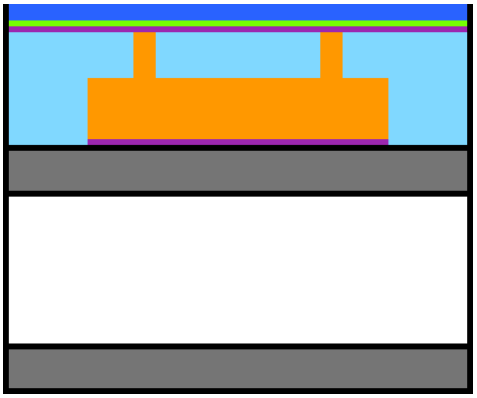
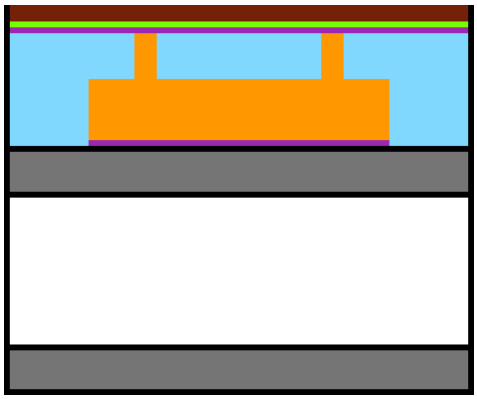


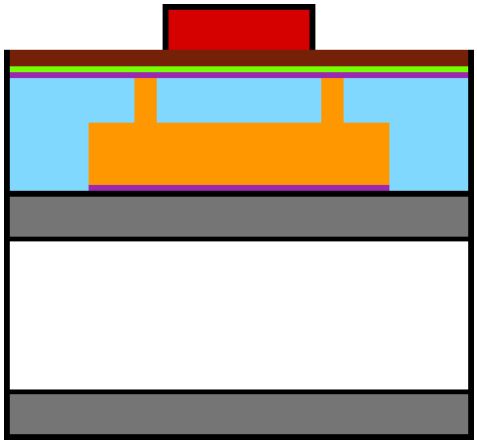
3.1.3 – Fabrication Procedure: Device Construction

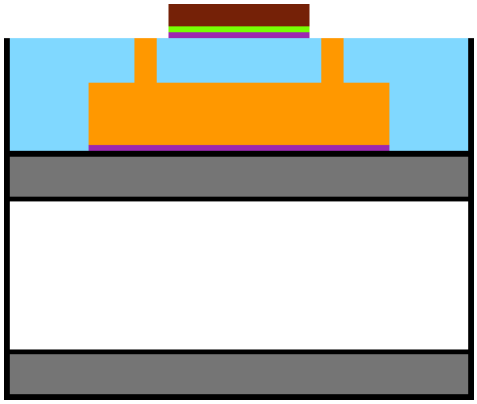
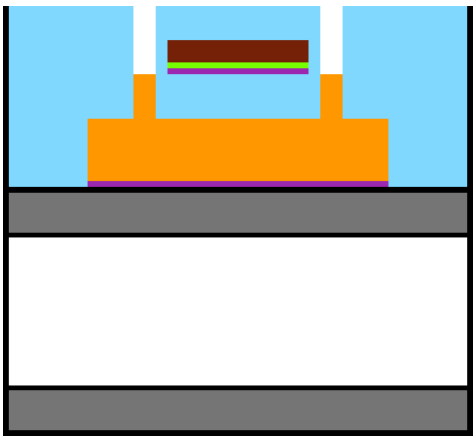
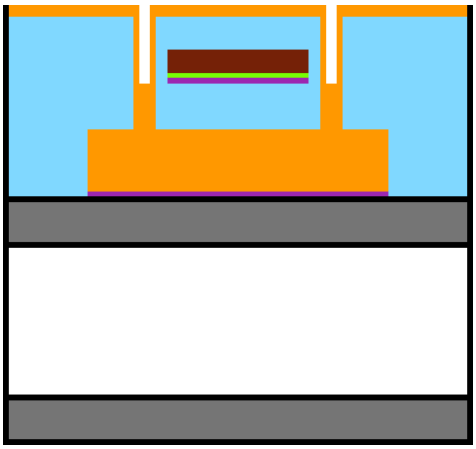
Step	Diagram	Description
1 Wafer oxidation & Seed Layer Deposition		- 100 mm silicon wafers were thermally oxidized to grow 1 µm SiO_2. - Ti (20 nm) seed layer was sputtered deposited onto the wafer. - Cu (200 nm) seed layer was sputtered onto the wafer. - **Completed in Fabrication Room by Fab Team**
2 **Fabrication of Bottom Copper Pattern**		- 20 µm of AZ 9260 (AZ) photoresist was spun onto the wafer, and soft baked. - AZ was patterned using mask aligner and Bottom Copper Mask. - AZ developed using manual agitation in the developer. - Wafer washed with DI and dried with N_2 gas. - AZ pattern optical microscope inspection. - **Completed in Fabrication Room by Fab Team**

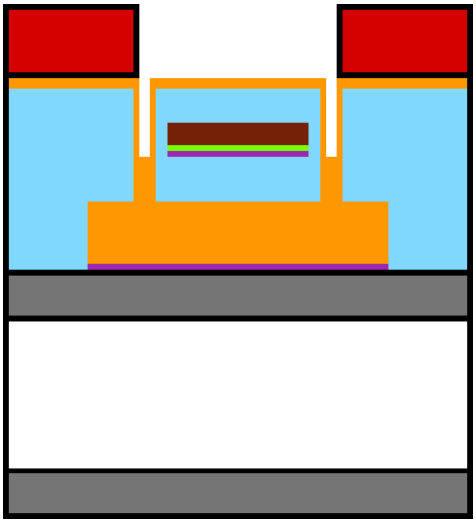
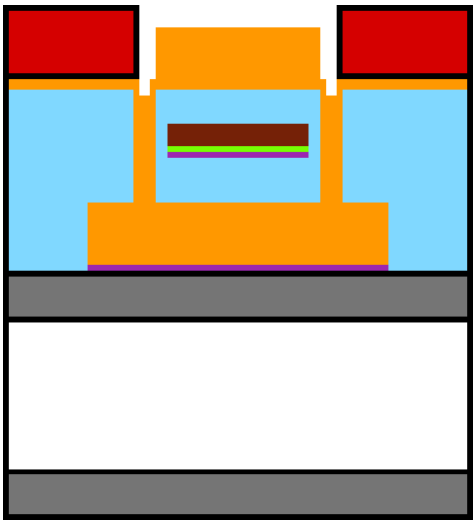
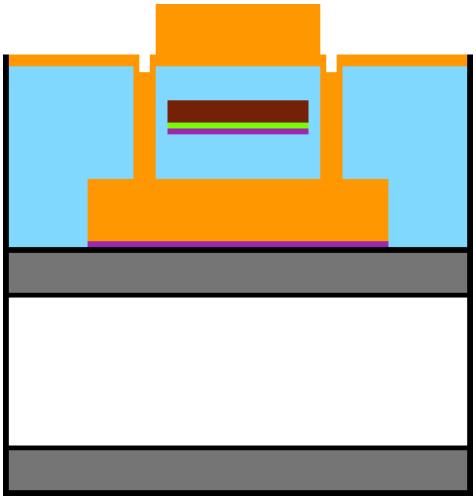
3 Bottom Copper Winding Layer Deposition		- Exposed copper cleaned of any oxide layer, washed with DI and dried with N_2. - Wafer cleaned using O_2 plasma asher at 100 W for 2 minutes. - 15 µm of copper electroplated using Digital Matrix copper plating system. - Wafer washed and dried - **Completed by Dr Declan Casey in Plating Lab**
4 Bottom Copper Pattern Removal		- The AZ bottom copper pattern was removed using Acetone. - Acetone cleaned with IPA. - - Wafer washed and dried - **Completed in Plating Lab**
5 Fabrication Of Bottom Copper Via Pattern		- 20 µm of AZ was spun and soft baked. - AZ was patterned using mask aligner and Copper-Via Mask 1. - AZ was developed using manual agitation in the developer. - Wafer washed and dried - Pattern optical microscope inspection. - **Completed in Fabrication Room by Fab Team**

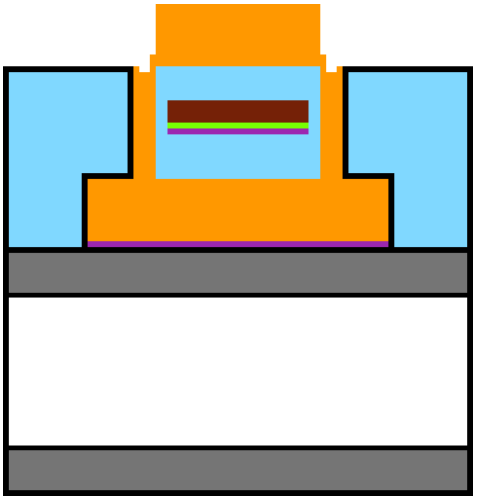
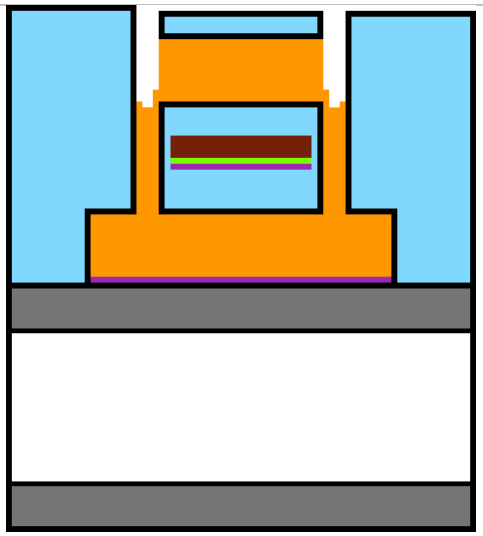
6 Bottom Copper Via Deposition		- Exposed copper cleaned of any oxide layer, washed and dried with N_2. - Copper vias (5 µm) electroplated using in-house plating system. - Wafer washed and dried - Copper vias optical microscope inspection. - **Completed by Dr Declan Casey in Plating Lab**
7 Bottom Copper Via Pattern Removal		- AZ pattern removed using Acetone. - Acetone cleaned with IPA. - Wafer washed and dried - **Completed in Plating Lab**
8 Ti/Cu Seed Layer Removal		- The exposed seed layer (Ti/Cu) removed using hydrofluoric acid (HF). - Wafer washed and dried - Optical microscope inspection. - **Completed by Dr Declan Casey**
9 Fabrication of Bottom Dielectric Layer		- 20 µm BCB photoresist / dielectric layer was spun onto the wafer and soft baked. - BCB patterned using mask aligner and BCB Core Mask. - BCB was developed using manual agitation in DS2100 developer (Dow Chemicals). - BCB surface treated with an Argon ion gun. **(Completed in Fab)**

11 Magnetic Core Deposition		- $Ti/Ni_{80}Fe_{20}$ (20 nm/200 nm) seed layer sputter deposited onto the wafer - Wafer cleaned using O_2 plasma asher at 100 W for 2 minutes. - 3.3 µm core metal (NiFe / CoNiFe) was electroplated using an in-house plating solution. - Wafer was washed and dried - **Completed in Plating Lab**
12 Core Oxidation		- Wafer was submerged and oxidised using the 'Post-Processing' technique. - Wafer washed and dried - **Completed in Plating Lab**

13 Fabrication of AZ Core Pattern		- 20 µm of AZ photoresist was spun onto the wafer and soft baked. - AZ patterned using mask aligner and AZ Core Mask. - AZ developed using manual agitation in the developer - Wafer washed and dried - Pattern optical microscope inspection. - **Completed in Fabrication Room by Fab Team**

14 **Core Etch**		- Core etched using a nitric acid solution. - AZ removed using Acetone - Acetone cleaned with IPA - Wafer washed and dried - Magnetic core optical microscope inspection. - **Completed in Fabrication Room by Fab Team**
15 **Fabrication of Top Dielectric Layer**		- 20 µm BCB photoresist / dielectric layer was spun onto the wafer and soft baked. - BCB patterned using mask aligner and BCB Core Mask. - BCB was developed using manual agitation in DS2100 developer (Dow Chemicals). - Wafer washed and dried. - **Completed in Fabrication Room by Fab Team**
16 **Top Seed Layer Deposition**		- Exposed copper cleaned of any oxide layer, washed and dried with N_2. - Ti/Cu (20 nm/200 nm) seed layer sputter deposited onto the wafer - **Completed in Fabrication Room by Fab Team**

17 Fabrication of AZ Top Copper Pattern		- 20 µm of AZ photoresist was spun onto the wafer and soft baked. - AZ patterned using mask aligner and AZ Top Copper Mask. - AZ developed using manual agitation in the developer. - Wafer washed in DI and dried with N_2 gas. - Pattern optical microscope inspection. - **Completed in Fabrication Room by Fab Team**
18 Deposition of Top Copper Windings		- Exposed copper cleaned of any oxide layer, washed with DI and dried with N_2. - Wafer cleaned using O_2 plasma asher at 100 W for 2 minutes. - 15 µm of copper electroplated using in-house copper plating system - Wafer washed and dried - Windings optical microscope inspection. - **Completed by Dr Declan Casey in Plating Lab**
19 Removal of AZ Top Winding Pattern		- AZ pattern removed using Acetone. - Acetone cleaned with IPA. - Wafer washed and dried - **Completed in Plating Lab**

20 **Top Seed Layer Etch**		- Exposed seed layer removed using hydrofluoric acid (HF). - Wafer washed and dried. - Optical microscope inspection. - **Completed by Dr Declan Casey in Plating Lab**
21 **Fabrication of BCB Passivation Layer**		- BCB passivation layer spun onto the wafer, soft-baked, patterned and developed. - Expected height of final device = 60 µm - **Completed in Fabrication Room by Fab Team**

3.2 – Metal Deposition

3.2.1 – Introduction

Throughout the fabrication process, copper and one of the core material metals were electroplated onto the surface of the device wafers. Each metal has its own plating method and set-up, which is described in the sub-sections below. In total, each device wafer had five separate plating sessions; 4 copper plating sessions, creating the top/bottom windings, along with the connecting vias, and one for the magnetic core material, NiFe or CoNiFe.

Using the average thickness across an electroplated wafer, the deposition rate (µm/min) of a bath can be calculated. It should be noted that the deposition rate calculated for a specific bath is not a constant and will vary based on the type of bath, its age and previous usage. Therefore it was necessary when specific thicknesses are required, i.e. for depositing cores, that the deposition rate was first calculated, typically by first electroplating a dummy wafer with varnish marks. Section 2.2.1 – Composition Characterisation describes the method of determining the thickness of a deposit.

3.2.2 – Copper Deposition

Copper was plated using the Digital Matrix Copper SA/1B plating system [115] via DC Current (operated by Dr Declan Casey), using the commercial Bright Copper ACG 8 bath solution [114]. Bright Copper ACG 8 is a highly stable, commercial solution produced by Schlötter GmbH. Table 5 below shows all the necessary chemicals stated in ACG 8 instructions for creating this bath.

Table 5 - Chemicals required for a 100 L Bright Copper ACG 8 bath.

Chemical	Quanity	Units	Supplier
Copper Salt FG	24	kg	Schlötter GmbH (030401)
Sulphuric Acid (99% Pure)	3.3	L	Supplied by User
Hydrochloric Acid (99% Pure)	19	mL	Supplied by User
Starter ACG 8	0.4	L	Schlötter GmbH (030300)
DI Water	Up To 100	L	Supplied by User

If the copper content of the bath falls below optimum quantity, the brightness, plating rate and levelling rate of the plate will decrease. Sulphuric acid & hydrochloric acid provide the

optimum acidic conditions (<1 pH) for the bath. The sulphuric acid also acts as a supporting electrolyte, as well as contributing to throwing and covering power.

Hydrochloric acid supplies chloride ions to the bath. These ions help with the conductivity of the bath, allowing for an increase in the achievable current density and decreasing the chances of burning during plating. Too high of a chloride content will decrease the brightness of the plated material and in some cases may cause anode polarisation. Starter ACG 8 is a commercial solution produced by Schlötter helps creates softer plates and promotes better plating at higher thicknesses, with factors such as increased brightness and levelling. Once all the chemicals have been added to the bath, additional DI water was added to bring the bath to 100 L.

The Digital Matrix System requires phosphorous copper rounds, containing 0.04-0.06% phosphorous for use as anodes in the anode basket, in order to replace the Copper ions lost in solution while plating. These rounds also increase the anode surface area, which must be larger than the cathode surface area to ensure adequate and uniform current density to the cathode surface.

The optimum temperature for the bath was approximately 20-30 °C, to which the laboratory's controlled room temperature (25 °C) falls within. When not in use, the bath was stored in plastic containers to reduce sediment build-up within the Digital Matrix, which was capable of either pumping in or draining out the solution when required. It should be noted that even when the Matrix is full, additional solution is found within the storage containers. During use, the Digital Matrix filters and pumps out the solution in the plating chamber, and pumps in stored solution, ensuring fresh solution regularly enters the bath.

The Digital Matrix uses a rotating cathode arm to hold the wafer during plating securely. In rotating the arm during plating, uniform thickness on the wafer was also achieved as well as keeping the plating solution sufficiently mixed and homogenous around the wafer surface and in the bath as a whole. The arm also contains an O-ring that ensures the electrical connection to the wafer is isolated from the bath. By controlling the cathode arm turning speed and the DC amp-hour supplied to the cathode, the plating speed can be controlled. Furthermore, due to the stable nature of this bath and plating method, the plating rate of the bath is found to be near linear throughout most of the plating timeframe.

3.2.3 – NiFe Core Deposition

The $Ni_{45}Fe_{55}$ alloy was plated using a pulse-reverse plating (PRP) system along with an in house plating bath at room temperature. Firstly, the wafer's surface must be sputtered with a metal adhesive layer, a 20 nm Ti and 100 nm Permalloy seed layer. The wafer was then secured in the specially designed wafer holder. The holder has a metal O ring, allowing for uniform electrical connection along the circumference of the wafer.

A rectangular plating cell was used to hold the bath, with two neodymium magnets on each side creating the external magnetic field (300 mT in the centre of the wafer). Using the wafer holder, the wafer was fully submerged in the bath and positioned so that it was parallel to the external magnetic field and facing the counter electrode. The counter electrode was a solid plate of $Ni_{45}Fe_{55}$. Both the wafer and CE were connected to the TecNu pulse reverse power supply system.

To ensure a uniform composition and thickness during the plating, the bath must be sufficiently agitated throughout the procedure, with fresh solution contacting the wafer's surface; thus, a jet impingement system was used. This system worked by using a Teflon tube, with a perforated side facing the submerged wafer, to stir the solution. Meanwhile, a Jebao AP355 pump was placed into the bath and was connected to the Teflon pipe. The pump ensures that a constant jet of the plating bath was pumped out of the holes of the perforated pipe and at the wafer's surface as it moves across its surface. A Tenma power supply system and a standard clockwise motor were used to move the Teflon pipe back and forth.

The overall plating time per wafer was split into two equal periods, between which the wafer was removed from the bath and rotated 180° to ensure uniform composition and thickness further. Previous work has led to the optimised PRP parameters, as shown in Table 6.

Table 6 - NiFe PRP Parameters

Step	Current / A	Time / ms
$I_{Forward}$	0.55	18.4
T_{Off-1}	-	0.5
$I_{Reverse}$	3.85	06
T_{Off-2}	-	0.5

Dummy wafers are periodically used to test the bath and before electroplating sample wafers, in order to calculate plating rates and to test the composition of plated NiFe with the use of EDX. The plating rates of the bath heavily depend on bath usage and age. A new NiFe bath had an approximate plating rate of 73 nm/min or 4.38 μm/hr.

The NiFe composition has an acceptable range of (45%:55%) ±2%. If that composition is not achieved additional nickel and iron salts can be added to the bath to correct the composition. The NiFe bath's acceptable lifetime is heavily dependent on its usage and age. The bath's pH must be kept at 2.5, with 1M HCl and 1M NaOH used to adjust the pH when necessary.

In order to prepare this bath, a 5 L beaker with a magnetic stirrer is used to mix the constituents. Each constituent is added to bath once the previous constituent has fully dissolved into solution. Once everything has been added and dissolved, the bath is made up to 3 L with additional DI water, pH adjusted and then filtered into its storage container. The constituents of the plating bath can be found in Table 7 below.

Table 7 - Constituents of the $Ni_{45}Fe_{55}$ Bath

Constituents	Seller	Quantity / g
DI Water	N/A	3 L
$NiCl_2.6H_2O$	Sigma Aldrich	450 (0.70M)
$FeCl_2.4H_2O$		26 (0.05M)
Boric Acid		75 (0.45M)
Saccharin		15 (0.03M)
1, 3, 6- Naphthalene Trisulphonic acid		12
Sulfosalicyclic acid		15
Triton X		1.5

The nickel and iron chloride salts supply the metal ions required for the correct nickel:iron 45:55 ratio, although it should be noted that the concentration of the salts in the solution is actually 14:1. This skewed bath concentration is based on the chemistry (diffusion coefficient, ionic attraction, migration, electrochemical potential) behind both these ions plating in the correct composition. However, it should be noted that because of the low iron content in the bath, during a bath's life cycle, the iron content will most likely decrease below optimal conditions, affecting the composition of the plated material. Additional iron salt may be added to the bath based on the plate's current composition in order to regenerate the bath.

Furthermore, both the iron and nickel salts supply small quantities of chloride ions. HCl, which in itself is added to adjust the bath's pH, also provides chloride ions to the bath. The role of these chloride ions is the same as their role in the copper bath. Boric acid is used a pH buffer solution in order to keep the pH of the bath within a range of the optimum pH (2.5), although the addition of HCl or NaOH may be required for precise pH adjustment.

Saccharin is also used as a stress reducer as well as an adhesion promoter between the seed layer and deposited metal layer. Saccharin is known to reduce tensile stress, caused by coalescence. Saccharin inhibits nickel reduction, pushing the nickel's reduction peak to a higher potential. A higher potential causes an increase in the number of nucleation sites formed, which in turn also causes finer grain sizes. In promoting smaller, finer grain sizes of electroplated metal, the adhesion between the plated film and seed layer substrate also increases. [116, 117]

1, 3, 6-Naphthalene Trisulphonic acid is used as a compressive stress reducer, i.e. reducing stress caused by compressive stress factors (lattice mismatch, capillary stress, interstitial incorporation, etc.). In general, the acid reduces the grain size of the material by allowing the internal crystalline structure of the plated metal more time to effectively relax into a stable structure, thus reducing the internal stress. In reducing stress, the plated film will also have better adhesion to the seed layer substrate. [118, 119]

Sulfosalicyclic acid is used as a complexing agent.[120, 121] This acid complexes with the metal ions, effecting their movement through the cathodic diffusion layer. This complex ensures that the correct composition of Ni:Fe (45:55) is achieved by promoting the plating potential to move towards the less noble iron, rather than nickel. This ensures that the abundant concentration of nickel does not off-set the composition, i.e. Ni content >45%.

Finally, Triton X (Polyoxyethylene octyl phenyl ether) is a non-ionic polymer surfactant which acts as a wetting agent. This agent will see to that the cathode's surface is adequately wetted by reducing the bath's surface tension.[122] This ensures that the entire cathode surface is always in contact with the solution, ensuring that no hydrogen bubbles stick to the surface and cause the formation of pores on the newly plated surface. Triton X is also shown to act a stress reducer.

3.2.4 – CoNiFe Core Deposition

The CoNiFe bath used in this project was based on the analysis of many baths from multiple papers [69, 76, 123-126] after initial tests showed unfavourable compositions of the alloy were being formed using earlier baths. The target composition of CoNiFe alloy was an approximate composition of 60:20:20, although the final composition achieved in this project was $Co_{64.5}Ni_{16.5}Fe_{19}$.

Although there is research published that uses chloride metal salts when preparing the CoNiFe bath [123], numerous papers have used sulphate based salts as an alternative. Due to the abundance and cost-effectiveness of Co, Ni, and Fe sulphate salts, the CoNiFe bath in this project was a sulphate based. Other constituents such as boric acid, ammonium chloride and sodium dodecylsulphate (SDS) (sodium lauryl sulphate) were used in all cited research. Table 8 shows the constituents of the CoNiFe bath.

Table 8 - CoNiFe Bath Constituents

Constituents	Seller	Quantity / g
DI Water	N/A	3.5 L
$CoSO_4.7H_2O$	Sigma Aldrich	59 (0.060M)
$NiSO_4.7H_2O$		184 (0.20M)
$FeSO_4.7H_2O$		14.6 (0.015M)
Boric Acid		86.56 (0.40M)
Ammonium Chloride		52.42 (0.280M)
Sodium dodecylsulphate (SDS)		0.035
Saccharin		1.2

However, a point of contention between papers was the use of another organic sulphur additive, saccharin. Saccharin is known to reduce the deposition stress and promote better adhesion of the deposited material but adversely reduces the coercivity of the material [126]. Numerous papers did not use saccharin and achieved good adhesion between the CoNiFe and small samples of copper foil and Si wafers with a copper seed ($5x5cm^2$) [69, 76], however, in large scale tests (4-inch wafers) performed in this work, the CoNiFe showed little to no adhesion with the wafer and subsequently delaminated. Other research has seen the use of low concentrations of saccharin (<5 g/L)[124, 125]. Initial tests using saccharin at 5 g/L, as per the

NiFe bath, showed a 5B adhesion rating, although the deposit was grey, indicative of deposit burning.

Tests using lower concentrations of saccharin were completed in order to find a suitable concentration for the finalised CoNiFe bath, as shown in Table 9. 0.4 g/L of Saccharin was found to cause minimal burning across the wafer, while still maintaining a good adhesion rating from the tape test.

Table 9 - Saccharin adhesion tests

Saccharin (g/L)	Adhesion Rating	Deposit Appearance
0	0B	Smooth and shiny – delaminated easily
5	5B	Grey colouration – typical of deposit burning
1	5B	Shiny plate with grey patches
0.5	5B	Smooth and shiny, slight burning on edges of the wafer
0.25	3B	Smooth and shiny – moderate delamination
0.4	4-5B	Smooth and shiny, no burning, no delamination

Another round of tests were performed in order to finalise the anode for electroplating CoNiFe. In electroplating NiFe, a $Ni_{45}Fe_{55}$ anode with a small dissolution factor is used. This anode was found to electroplate CoNiFe at a low voltage, approx. 1.6-1.9 V, however, the resulting compositions were found to be unfavourable, approx. $Co_{66}Ni_{22}Fe_{12}$. It is believed that anomalous co-deposition of these noble metals is affected by the NiFe anode metal plate and its dissolution.

Inert platinised titanium mesh anodes were tested as a replacement for the NiFe slab. The mesh increases the surface area of the anode, with the material allowing current densities up to 75 A/dm^2. [127] It was found that the Pt/Ti surface area must be more than double the cathode to ensure that the anode does not limit the cathode reaction and thus maintain a low electroplating voltage.

The mesh used from CM Scientific Ltd. had a length & width of 10 x 6 mm and strand width & thickness of 1.5 x 0.75 mm, with a 2.5 μm coating of platinum. It was found that a single sheet of mesh, the approximate size and shape of a 4-inch wafer, gave a voltage of > 2.5V, which was unacceptable. Therefore, three mesh foils, each the size and shape of the wafer were

stacked and clamped together and used as the finalised anode. This inert anode allowed the voltage to stay low at 1.7-1.9V, similar to the NiFe metal plate. Figure 55 shows a single mesh. The stacked Pt/Ti meshes are also used in the metal oxidation step.

The electroplating process was also chosen based on previous experimental data and tests. PRP was used in previous research in electroplating CoNiFe in Tyndall [76]. The PRP system used was the same as the one used to electroplate $Ni_{45}Fe_{55}$, with strong mechanical stirring as agitation for the bath to produce a composition of $Co_{59.4}Ni_{12.8}Fe_{27.7}$. This version of CoNiFe showed coercivity of 1.2 Oe and a magnetic saturation flux of 1.8 T. Osaka 1999 [69] used Pulse DC at varying duty cycles in order to alternate the bcc/fcc crystalline structure of the resulting deposited CoNiFe. The fine-grain size was known to be achieved while electroplating CoNiFe by obtaining a mixed-phase boundary between fcc and bcc structures [77, 128]. Magnetic flux density (B_{sat}) was also known to increase with a bcc majority phase for CoNiFe [129, 130]

A pulse period of 0.1 s and a duty cycle of 0.5 was found to give the CoNiFe a bcc majority structure, and 10 mA cm^{-2} was found to keep the plating voltage low and limit deposit burning while also supporting an effective plating rate. The agitation method was the use of a rotating disk electrode (RDE) at 1000 rpm. Osaka's final composition was $Co_{63}Ni_{11}Fe_{26}$, with a coercivity of 1.2 Oe but with a magnetic saturation density of 2.1 T. Based on these results, Osaka's Pulse DC plating method was chosen, with minor changes such as the agitation method and bath composition, which was expected to affect the final composition.

The use of the jet impingement system produced a smooth, shiny plate, as did the use of just the paddle system. However, the use of the jet impingement system was detrimental to the composition of CoNiFe deposit, increasing the nickel content to >20% while decreasing the iron content <20%. The composition of cobalt stayed constant, at 64-66%. The jet of solution directed at the cathode surface affected the convection process at the cathode surface and the anomalous co-deposition, thus limiting the preferential deposition of iron over nickel.

Table 10 - CoNiFe Pulse DC Parameters

Step	Current / mA	Time / ms
T_{on}	10	50
T_{off}	0	50

The bath composition is shown in Table 8 Pulse DC at 10 mA cm^{-2} (T_{on} = 0.05 s T_{off} = 0.05 s), a layered Pt/Ti mesh anode, and a paddle agitation system, to deposit the CoNiFe used in this project. Table 10 shows the plating steps programmed into Tech Mu Inc's power supply. A fresh CoNiFe bath electroplated at 2.2 μm/hr.

3.3 – Oxidation of Metal Cores

3.3.1 – Introduction

Once the NiFe or CoNiFe core was electroplated onto the wafer during step 11 of the fabrication procedure, step 12 involved the oxidation procedure to oxidise these alloys. The oxidation procedure involved cyclic voltammetry, with wafers submerged in an alkaline solution, connected to IJ Cambria 660B electrochemical workstation. The potential range that was selected for the CV depended on the metal alloy that was to be oxidised. Once the oxidation was completed, the wafers continued on to the next step of the fabrication procedure. By oxidising, the core material, the composition, structural and crystalline morphology, colour, and its magnetic properties change. Based on previous work on this material [83], it was believed that the magnetic properties of this material would improve once oxidised.

3.3.2 – Oxidation Method

The CV process was performed in a custom-made Teflon rectangular cell, containing a 2.5 L of 1M NaOH bath (pH 13). The potential limits used for the CV range were -1.5 V to +0.65 V for NiFe and -1.55 V to +0.85 V for CoNiFe, versus a mercury oxide (Hg/HgO) RE.

Previous in-house research in this laboratory [83], determined the ideal scan rate to be 50mV/s, in order to give adequate time for the metal in each alloy to oxidise and form the amorphous material. Fig 49 shows the coercivity values of NiFe, at different thicknesses, taken after a range of scan cycles. The number of cycles required to oxidise the NiFe layer entirely was based on its thickness (e.g. 300 cycles = 1.5 μm). Therefore, it was extrapolated that a core thickness of 3.3 μm would take approx. 450 cycles for NiFe and CoNiFe.

Pt/Ti wire mesh was used as both the counter electrode (CE) and as a specially designed wafer holder, as shown in Fig 50. The holder comprised of the Pt/Ti wire mesh with Teflon screws that prevented the wafer and CE making contact. A sufficient gap was left between the wafer and CE, allowing the RE to sit between the two. This holder could then be securely placed into the Teflon box or "cell" containing the NaOH bath. Since crocodile clips were used to connect all three electrodes to the CHI660B workstation, a small portion of the wafer was therefore left unsubmerged in the bath to allow for the connection to the CHI potentiostat.

The resulting voltammograms produced from the oxidation of these metals is shown below (Fig. 51) with assigned peaks, corresponding to the different metals in the alloys.

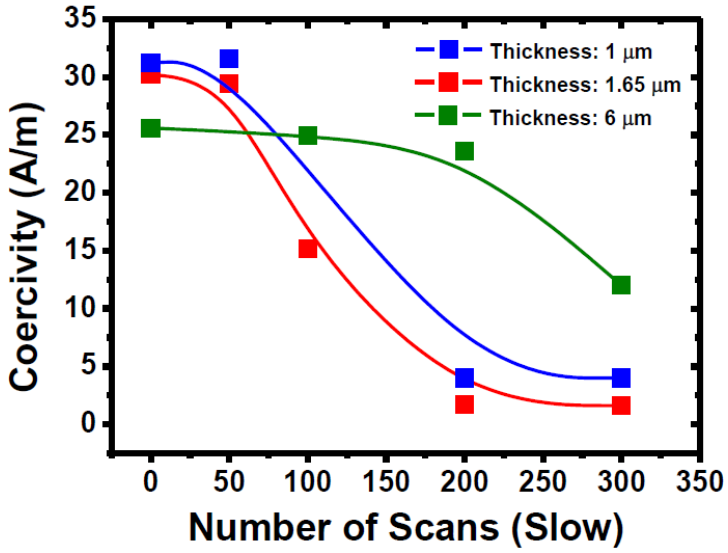


Figure 49 – Coercivity measured at different stages of post-processing (slow cycles) for different film thickness



Figure 50 - Metal oxidations set-up: Pt/Ti mesh with Teflon holders securing a wafer. Hg/HgO electrode held between the wafer and mesh

3.3.3 - NiFe Oxidation

The voltammogram of NiFe can be seen in Fig 51, Based on previous research into the separate reactions iron and nickel electrodes, each peak will be complex due to the overlap of multiple reactions from both metals. In general, the formed oxide/hydroxides seem to match up with the

individual metal's oxide reactions as explained in Section 1.6.2 – Metal Oxide Growth, as well as literature on the formation of NiFe LDH. [89]

Anodic Peaks

The broad Peak I at -0.6V, was the oxidation of both iron and nickel. With iron, two reactions occur sequentially, blending into one peak; $Fe^0 \rightarrow Fe^{2+}$, forming $Fe(OH)_2$, followed by $Fe^{2+} \rightarrow Fe^{3+}$, forming FeOOH. This is a stark contrast to the two distinct peaks shown in Fig 38. With nickel, the oxidation of Ni^0 to Ni^{2+} forms α-$Ni(OH)_2$. This peak also increases in size as the cycling continues, proving the slow increase in oxide formation per cycle. This was due to more of the iron and nickel deposit beginning to react as the deposit becomes more porous and the oxide extends deeper into the film. The large anodic plateau from -0.3 V to +0.4 V was the slow transformation of α-$Ni(OH)_2$ to β-$Ni(OH)_2$ and FeOOH slowly rearranging to form Fe_2O_3.

Peak II starts as two distinct peaks at the beginning of the oxidation process; The oxidation of β-$Ni(OH)_2$ to NiOOH, and the oxidation of water/oxygen evolution. The rearrangement of FeOOH to Fe_2O_3 was also believed to occur here at a faster rate. As the cycles continue, the two peaks blend into one due to the step-wise increase of the NiOOH formation peak, further proving the slow increase in oxide formation per cycle.

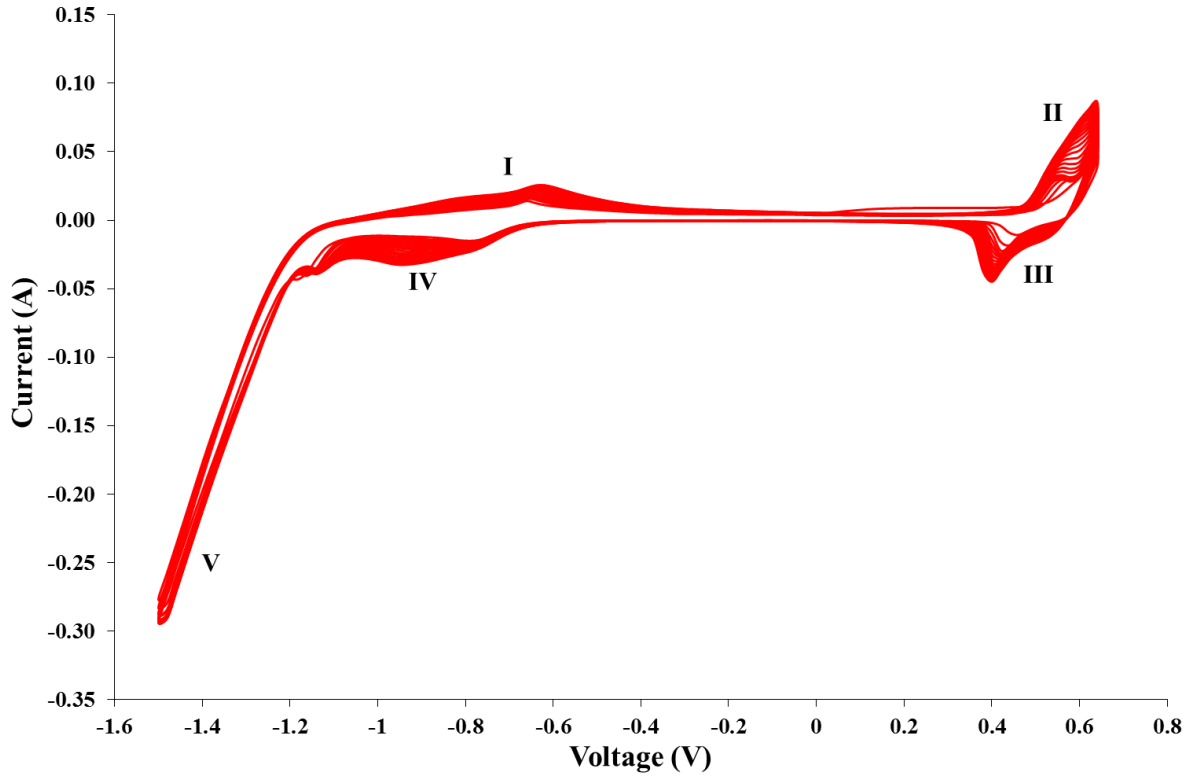


Figure 51 - Voltammogram of the $Ni_{45}Fe_{55}$ electrode

Cathodic Peaks

Peak III shows the reduction of NiOOH back to $Ni(OH)_2$. This peak was initially small but grew as the cycling continues, as more oxide was available for reduction. Between Peak III and IV, a plateau trails approximately along 0 mA, showing little or no reactions were occurring during this period, although the rearrangements of iron and nickel oxides are still occurring. Peak IV shows the reduction of the Fe^{3+} ion mixture of Fe_2O_3 & FeOOH to Fe^{2+} or $Fe(OH)_2$. Again, this peak grows as the amount of oxide capable of being reduced increases.

Feature V is predominantly the reduction of water/hydrogen evolution; however, hydrogen evolution was required for the reduction of $Ni(OH)_2$, or Ni^{2+} to Ni^0. Along with the reduction of nickel, Fe^{2+}, in the form of $Fe(OH)_2$, was also reduced to Fe^0 within this peak.

Colouration

The oxidation procedure also changes the colour of the deposit, producing an iridescent film, meaning that the film alters colouration based on the angle of light. Fig 52 below shows the silver colour of the as-deposited (AD) NiFe on the left, and the iridescent film of the oxidised NiFe on the right, which alternates between a red-brown & green colouration. This colouration is believed to be caused by the colouration of the metal oxide/hydroxides formed. Fe_2O_3 is known to be a red-brown coloured oxide, while $Ni(OH)_2$ is known to be green [64].

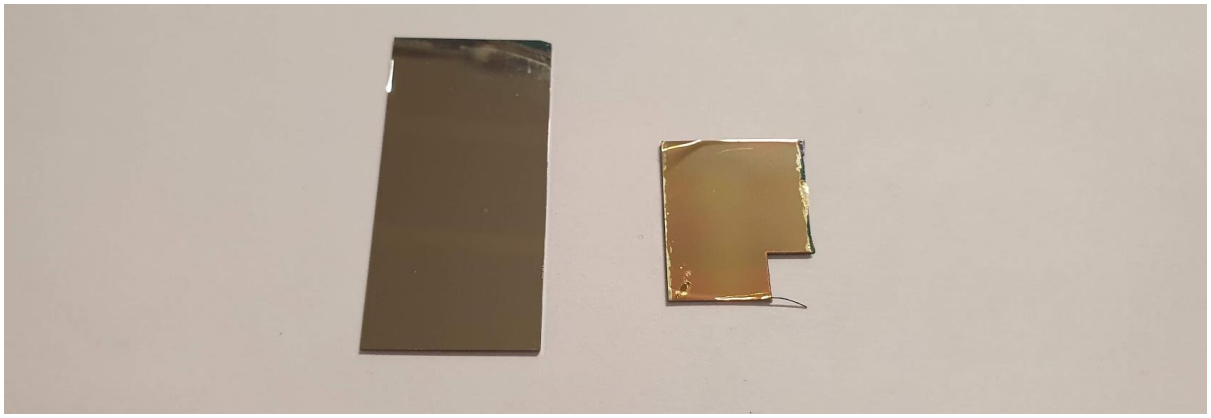


Figure 52 - AD NiFe (Left) & Oxi-NiFe (Right)

3.3.4 – CoNiFe Oxidation

The voltammogram of CoNiFe can be seen in Fig 53, with each of the anodic and cathodic peaks labelled I to VII. As previously stated with NiFe, research into the separate reactions cobalt, iron and nickel electrodes, allows each peak to be discerned, although the peaks will be an amalgamation of multiple reactions from all three metals.

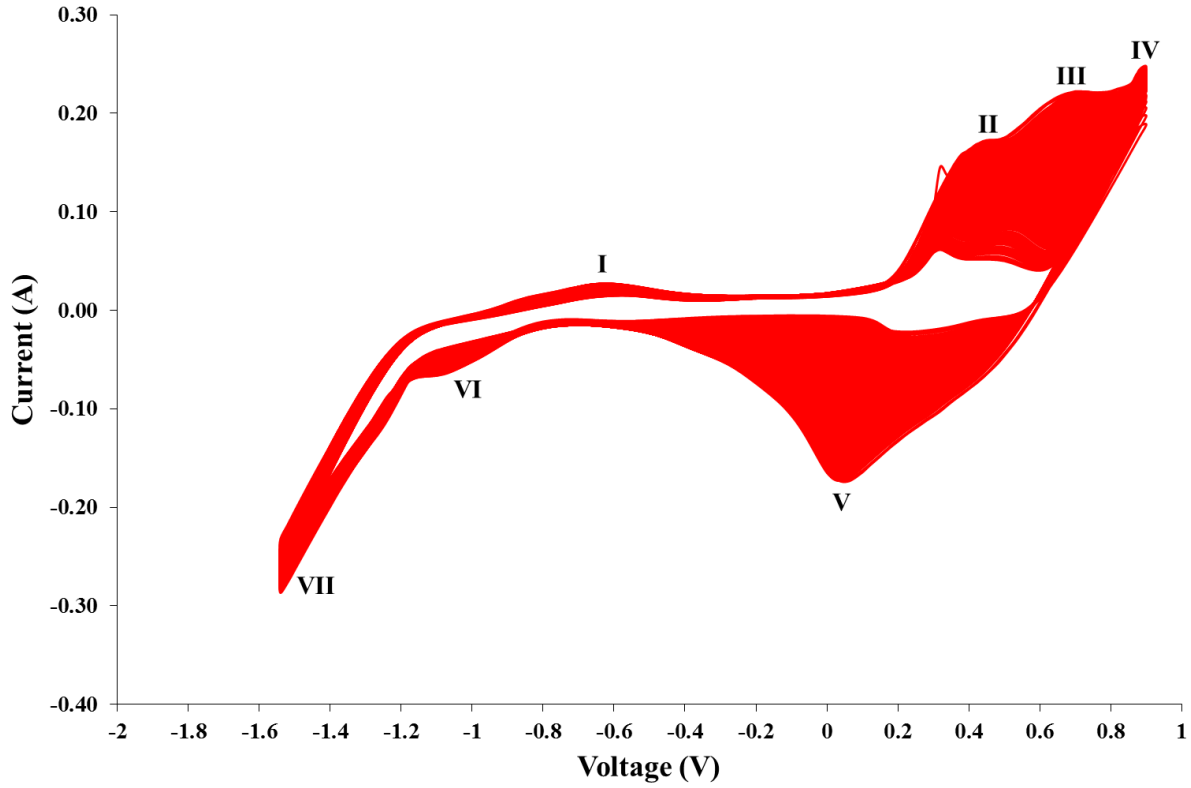


Figure 53 – Voltammogram of CoNiFe Electrode

Anodic Peaks

Peak I was similar to Peak I on the NiFe voltammogram, with the nickel and iron reactions. However, this peak also includes cobalt metal (Co^0) oxidising to Co^{2+}, forming products such as CoO and $Co(OH)_2$. This peak was smaller than the NiFe counterpart due to the passivation caused by the formation of CoO and $Co(OH)_2$ and the decreased concentration of Fe and Ni in the CoNiFe alloy (≥20%) in comparison to NiFe (≈50%).

The plateau between Peak I and Peak II was the slow transformation of α-$Ni(OH)_2$ to β-$Ni(OH)_2$ and FeOOH slowly rearranging to form Fe_2O_3. Peak II refers to the reaction of Co^{2+} in the form of $Co(OH)_2$ oxidising to Co^{3+} in the form of CoH, Co_3O_4 & Co_2O_3.

Peak III was the oxidation of β-$Ni(OH)_2$ to NiOOH and the further rearrangement of FeOOH to Fe_2O_3. Both Peak II and III increase in size as cycling continues due to the slow increase in oxide content. Further beyond Peak III was the beginning of the water oxidation/oxygen evolution range as seen by Peak IV.

Cathodic Peaks

The broad Peak V was the combination of the reduction of NiOOH back to $Ni(OH)_2$ and the numerous Co^{3+} forms back to Co^{2+} . This peak also increases in size as cycling continues, proving that the oxidation build-up, beyond the single monolayer, was possible with other metallic alloys.

Peak VI was the reduction of the Fe^{3+} forms to Fe^{2+} in the form of $Fe(OH)_2$. Finally, feature VII is water reduction/hydrogen evolution, however the reduction of $Ni(OH)_2$, $Fe(OH)_2$, CoO and $Co(OH)_2$ to their metallic forms with the help of hydrogen.

Colouration:

The oxidation procedure also changes the colour of the deposit, and much like the NiFe oxidation produces an iridescent film of Oxi-CoNiFe. Fig 54 below shows the silver colour of the AD-CoNiFe and the red/green iridescent colouration of the oxidised CoNiFe. Much like Oxi-NiFe, the colouration of the Oxi-CoNiFe is believed to be due to the mixture of oxides and their colours. $Ni(OH)_2$ and $Fe(OH)_2$ give the red/green colouration. Although CoO, Co_2O_3 and Co_3O_4 are typically grey/black coloured, $Co(OH)_2$ is known to be a green crystalline material. [64]

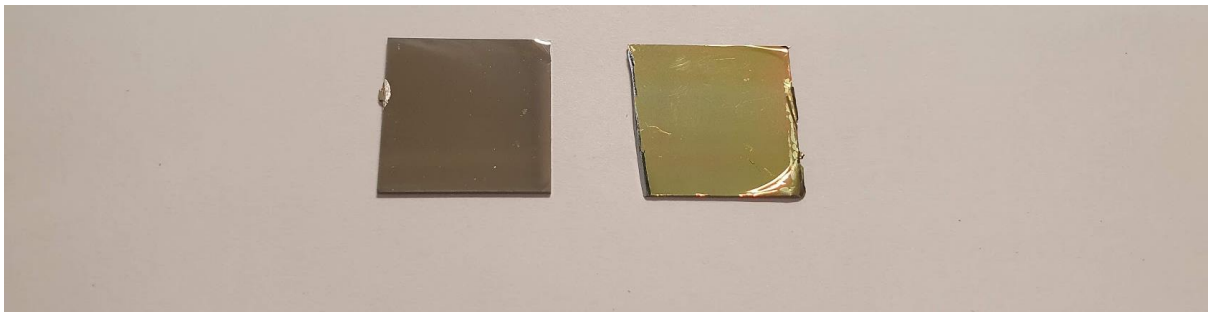


Figure 54 - AD-CoNiFe (Left) & Oxi-CoNiFe (Right)

Peak II starts as two distinct peaks at the beginning of the oxidation process; The oxidation of β-$Ni(OH)_2$ to NiOOH, and the oxidation of water/oxygen evolution. The rearrangement of FeOOH to Fe_2O_3 was also believed to occur here at a faster rate. As the cycles continue, the two peaks blend into one due to the step-wise increase of the NiOOH formation peak, further proving the slow increase in oxide formation per cycle.

3.4 - NiFe Cores Properties

3.4.1 – NiFe Cores Composition Properties

Thickness & Roughness – Tencor & SEM:

As-Deposited NiFe

The appearance of the electroplated NiFe was a typical shiny deposit, confirmed to have little to no roughness by the Tencor surface profilometer, with 5nm being the minimum roughness range that Tencor can determine. A Typical electroplated NiFe wafer should be within this range. Unfortunately, surface profiling was not able to determine the thickness of the deposited NiFe on the inductor devices due to the design and layout of the device wafers.

To remedy this, a dummy wafer with varnish marks was electroplated before the device wafer, using the same deposition process to estimate plating rates and the methods overall thickness. The dummy wafer measured the thickness of approximately 3.2-3.4 µm; an acceptable thickness and within the estimated thickness range of the selected electroplating period.

The AD NiFe device wafer was then electroplated, with the core's thickness capable of being confirmed later after the devices were completed by cross-section analysis of some of the completed devices using SEM. The thickness from these devices was measured to be 3.3 µm.

Oxidised NiFe

Much like the AD NiFe, the Tencor was only capable of measuring the surface roughness of the Oxi-NiFe on the inductor wafer; however, based on previous tests, the oxidation procedure typically has a negligible effect on the thickness of the NiFe cores. The Oxi-NiFe showed roughness range in the >100nm.

The surface of the Oxi-NiFe was known to be rougher in comparison to the AD-NiFe, as shown visually by the SEM. This was due to the change in crystalline structure from the typical nanocrystalline structure to the amorphous, needle-like structures, as shown by the TEM images below (Page 105). However, this roughness was still within the nanometre range, although magnetic properties such as coercivity will still be affected by this change in roughness. Fig 55 shows the SEM Images of the Oxi-NiFe surface.

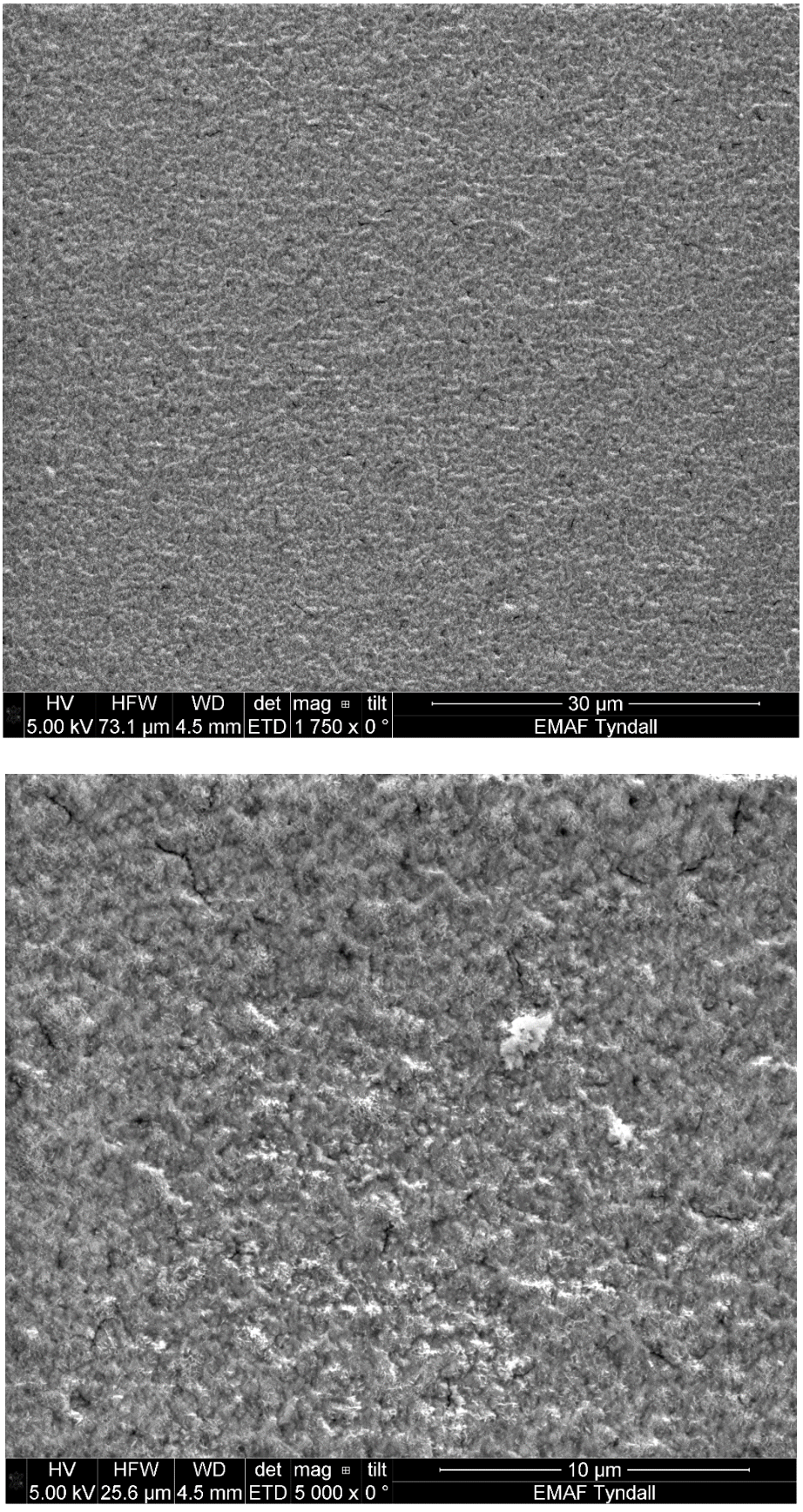


Figure 55 – Oxi-NiFe Surface – 1750x Mag (Top) & 5000x Mag (Bottom)

Composition - EDX:

AD NiFe

For the as-deposited core and the pre-oxidised core, it was paramount that the NiFe bath deposited the correct composition of NiFe required for the device fabrication. Composition analysis of the deposited NiFe was therefore completed using EDX before the wafers continued with the fabrication process. Failure to produce the correct composition would require the NiFe layer to be removed via chemical etching and the deposition of a new NiFe layer.

The composition was recorded in weight percent before being converted to atomic percent, with $Ni_{45}Fe_{55}$ having an acceptable atomic percent range of ±2%. Table 11 and Fig 56 show the composition & spectrum of the AD NiFe.

Element	Weight %	Weight % (Corrections)	Atomic %
Iron	53.42	0.2	**54.66**
Nickel	46.58	0.2	**45.34**
Total:	100	-	100

Table 11 - EDX Analysis of AD NiFe

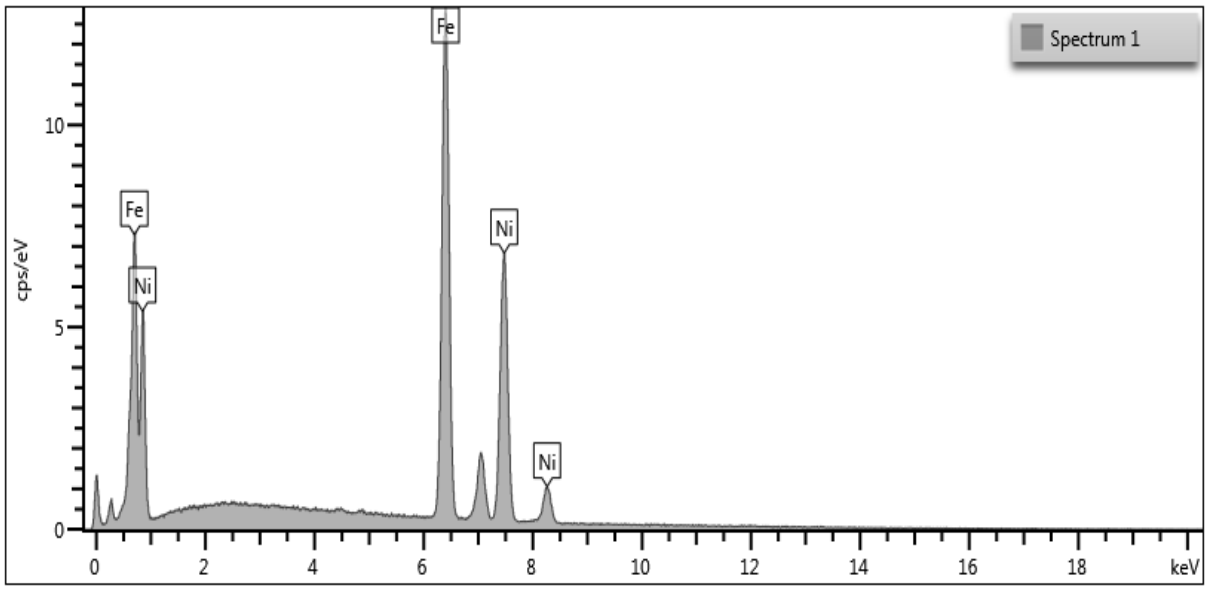


Figure 56 - EDX Spectrum of AD NiFe

Oxidised NiFe

Once the NiFe core material was deposited and oxidised, the material was analysed by EDX to determine its composition before the fabrication process continued. Table 12 and Fig 57 show the EDX analysis & spectrum of the Oxi-NiFe. The composition was recorded in weight percentage before being converted to an atomic percentage.

The percentage composition of oxygen in the Oxi-NiFe varied marginally depending on the thickness of the Oxi-NiFe layer. It was found that areas of the deposit with a larger thickness (>300nm), in comparison to the wafer's typical thickness, showed a decrease in oxygen content in these areas. This was due to the presence of remaining AD NiFe under the Oxi-NiFe. Therefore, it was essential to ensure that the thickness of the deposited material across the wafer was <300 nm to allow for full oxidation of the deposit.

Element	Weight %	Weight % (Corrections)	Atomic %
Iron	42.87	0.24	**31.37**
Nickel	41.59	0.26	**28.95**
Oxygen	15.54	0.18	**39.68**
Total:	100		100

Table 12 - EDX Analysis of Oxi-NiFe

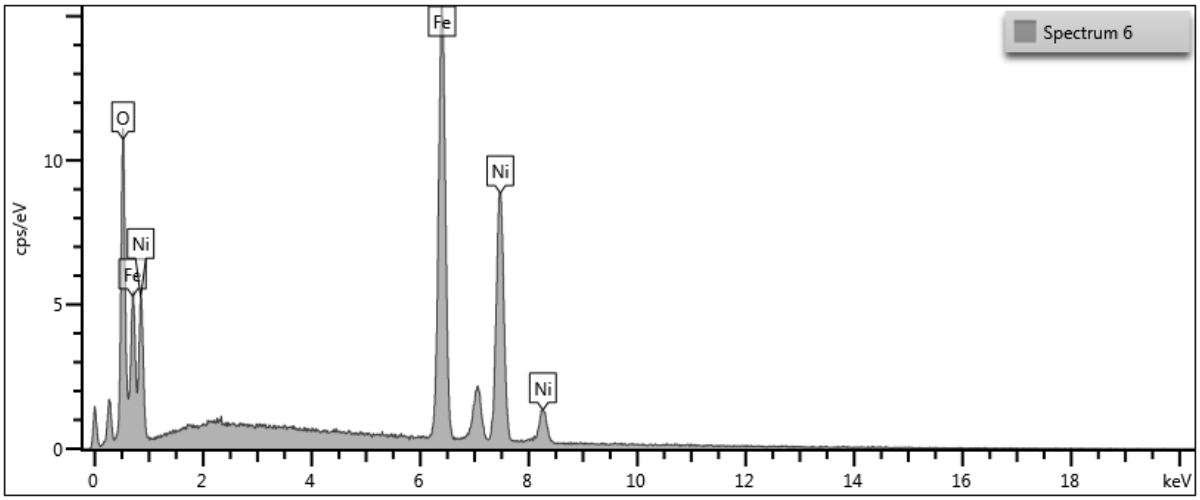


Figure 57 - EDX Spectrum of Oxi-NiFe

Mass Composition & Density Calculations:

AD NiFe:

The density of 100 g of AD NiFe was approximated to be 8.324g.cm^{-3} using the weight percentage from the EDX and the density of the individual elements of the alloy, iron and nickel.

$$\boldsymbol{Fe}: \frac{\mathbf{53.42}\boldsymbol{g}}{\mathbf{7.874}\boldsymbol{g.cm^{-3}}} = \mathbf{6.784}\boldsymbol{cm^3} \qquad \boldsymbol{Ni}: \frac{\mathbf{46.58}\boldsymbol{g}}{\mathbf{8.908}\boldsymbol{g.cm^{-3}}} = \mathbf{5.229}\boldsymbol{cm^3}$$

$$\boldsymbol{NiFe}: \mathbf{6.784}\boldsymbol{cm^3} + \mathbf{5.229}\boldsymbol{cm^3} = \mathbf{12.013}\boldsymbol{cm^3}$$

$$\boldsymbol{Density} = \frac{\mathbf{100}\boldsymbol{g}}{\mathbf{12.103}\boldsymbol{cm^3}} = \mathbf{8.324}\boldsymbol{g.cm^{-3}}$$

Using the 3.3 µm thickness or height of the AD NiFe, and the approximate area of the 4" inch wafer (area of a circle) which was 81.07 cm^2, the volume of NiFe was calculated using the volume of a cylinder equation. The volume was calculated as 2.68 x 10^{-2} cm^3.

$$\boldsymbol{Volume} = \boldsymbol{\pi r^2 h} = \mathbf{3.142}(\mathbf{25.806}\boldsymbol{cm^2})(\mathbf{3.3}\boldsymbol{x}\mathbf{10^{-4}}\boldsymbol{cm}) = \mathbf{2.676}\boldsymbol{x}\mathbf{10^{-2}}\boldsymbol{cm^3}$$

Using the newly calculated volume and density, the mass of the as-deposited NiFe was calculated as 0.233 g. Furthermore, using the weight percentage of the iron and nickel in the alloy, the mass of each element was also calculated.

$$\boldsymbol{Mass} = \boldsymbol{DxV} = \mathbf{2.676}\boldsymbol{x}\mathbf{10^{-2}}\boldsymbol{cm^3}(\mathbf{8.324}\boldsymbol{g.cm^{-3}}) = \mathbf{0.223}\boldsymbol{g}$$

$$\boldsymbol{Fe}: \mathbf{0.223}\boldsymbol{g}\left(\frac{\mathbf{53.42}}{\mathbf{100}}\right) = \mathbf{0.119}\boldsymbol{g} \qquad \boldsymbol{Ni}: \mathbf{0.223}\boldsymbol{g}\left(\frac{\mathbf{46.58}}{\mathbf{100}}\right) = \mathbf{0.104}\boldsymbol{g}$$

Oxi-NiFe:

The density of the Oxi-NiFe could be not be calculated as the density of oxygen within the oxidised material could be determined. Based on the porous nature of the material via the TEM and the fact, the thickness did not change during the oxidation process; the oxidised material was most likely less dense than the as-deposited material.

Crystalline Structure - TEM:

TEM results show the crystalline structure of the AD NiFe & Oxi-NiFe materials. The crystalline structure of the NiFe was altered when the material was oxidised, moving from a predominantly nanocrystalline structure to that of a predominantly amorphous nature.

The following TEM results were accompanied by selected area electron diffraction (SAED) images in order to calculate the crystalline nature of the material. Below are the TEM & SAED images of AD NiFe & As-Deposited NiFe. Single crystal grains & points of interest have been highlighted in red in the TEM images.

AD NiFe:

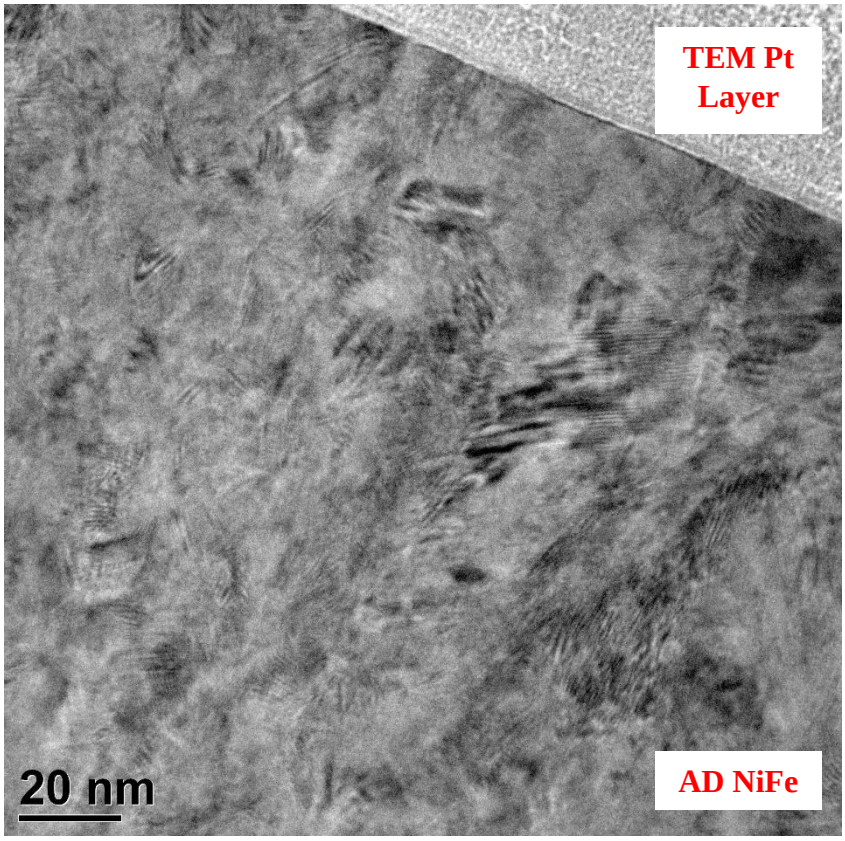


Figure 58 – Top Section of AD NiFe layer, with Sputtered Pt Layer for TEM Analysis

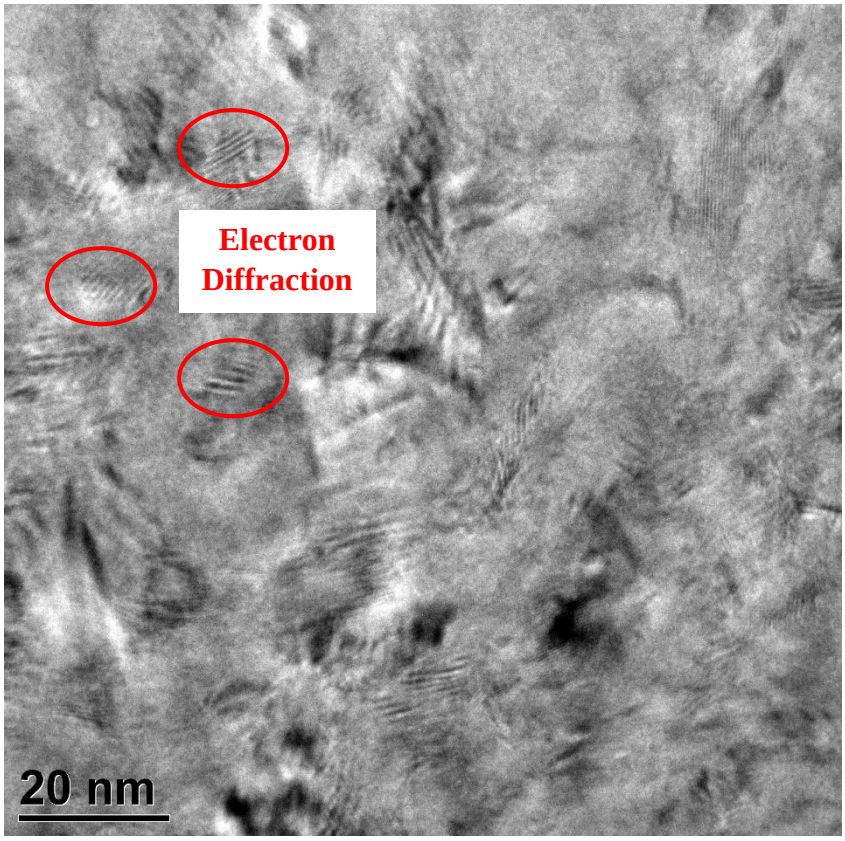


Figure 59 – Large portion of nanocrystalline AD NiFe grains

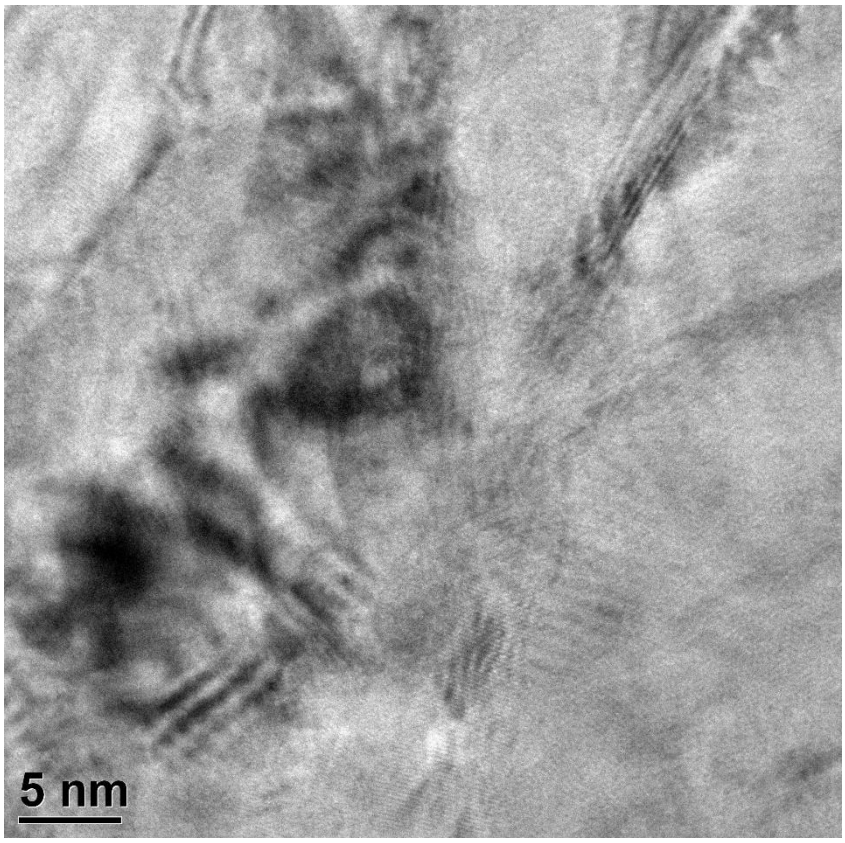


Figure 60 – Individual AD NiFe grain

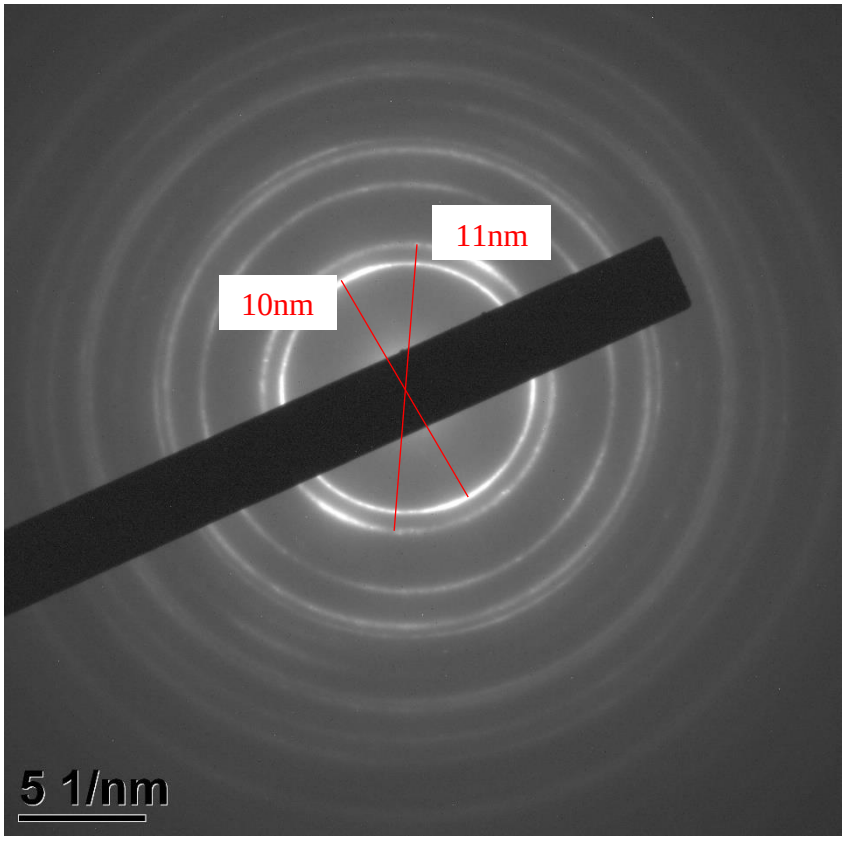


Figure 61 – SAED of AD NiFe with selected area aperture

For AD NiFe, due to electron diffraction through two or more crystals, it was difficult to discern a single crystal of the poly-nanocrystalline AD NiFe material. The lattice mismatch causing the diffraction was clearly seen in Figure 59.

Based on the images, the average grain size was estimated to be 5-20 nm (length and width) via image analysis, although due to the distinct lack of visible crystal shapes, this estimation was highly subjective. The SAED image, encompassing a 200 nm diameter area, and penetrating a 50 nm thickness contains approximately 1000-2000 crystals, and due to the presence of small heterogeneous rings, it was clear that the material was predominately poly-nanocrystalline.

Using the SAED images (Fig. 61) and the radius of the rings, the d-spacing of the AD NiFe can also be measured. The first ring was 10nm in diameter, giving a d-spacing of approximately 2Å, while the 2nd ring was 11 nm in diameter, giving a d-spacing of 1.8 Å.

$$\mathbf{d-spacing} = \frac{\mathbf{1}}{\mathbf{r}}\mathbf{nm}\ \ (\mathbf{1}\text{Å} = \mathbf{0.1nm})$$

Using the d-spacing and X'PERT^3 XRD Analysis Program, the crystalline structure of AD NiFe was estimated to be a face-centred cubic lattice (Fm-3m space group, O_h point group) in nature, with the 1st d-spacing relating to a (111) crystal plane and the 2nd relating to (200) crystal plane, as shown in Fig. 62 [131, 132]. It should be noted that the SAED images have an error bar of ± 5%.

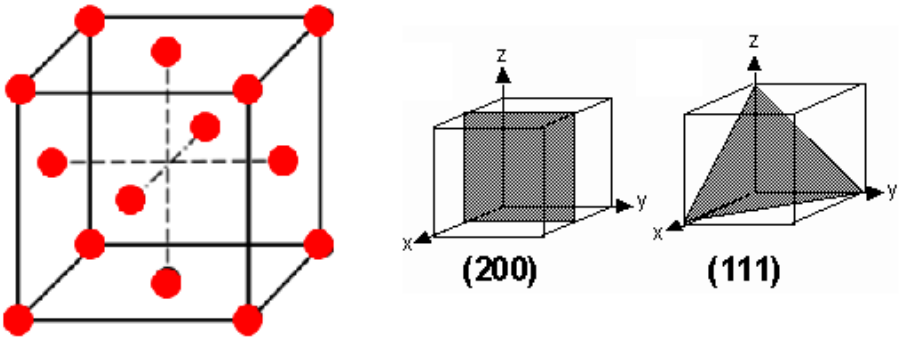


Figure 62 - Face centred cubic lattice, with (200) & (111) crystal planes

Oxi-NiFe:

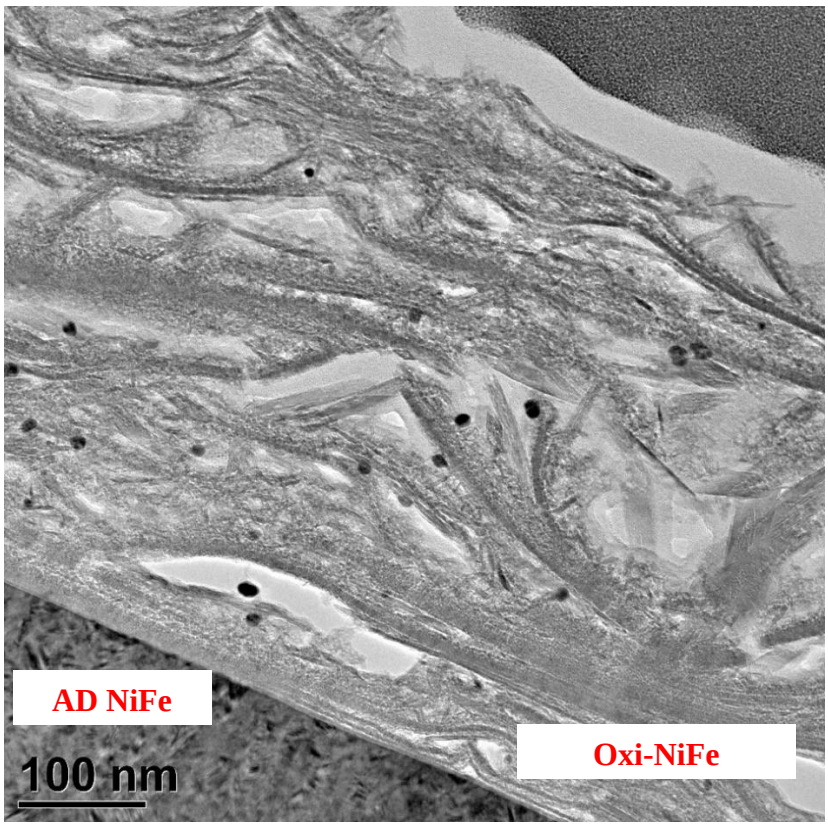


Figure 63 – 100nm scaling showing a 1um thick layer of Oxi-NiFe on top of AD NiFe

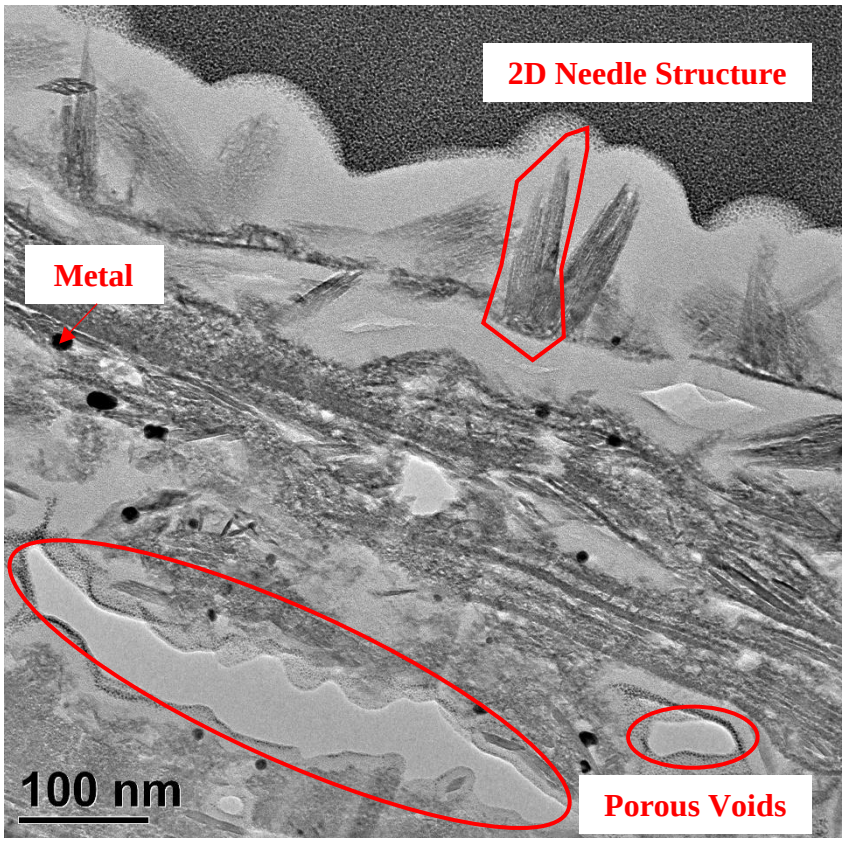


Figure 64 – 100nm scaling, showing the surface of Oxi-NiFe & the needle-like grains

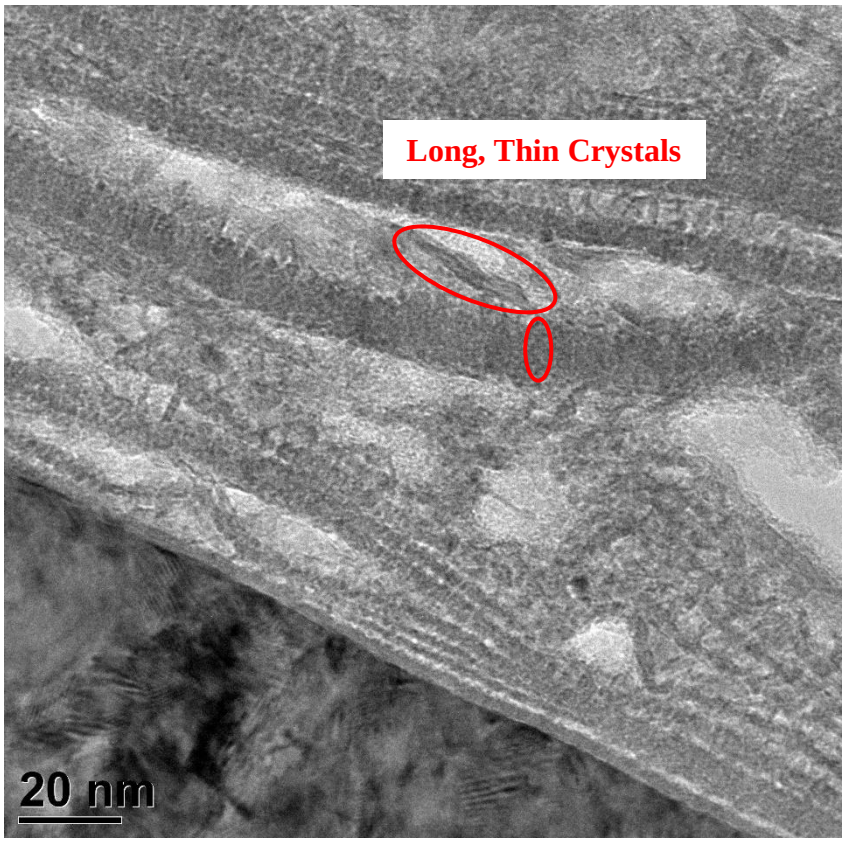


Figure 65 – 20nm scaling, showing the interphase between the two NiFe materials

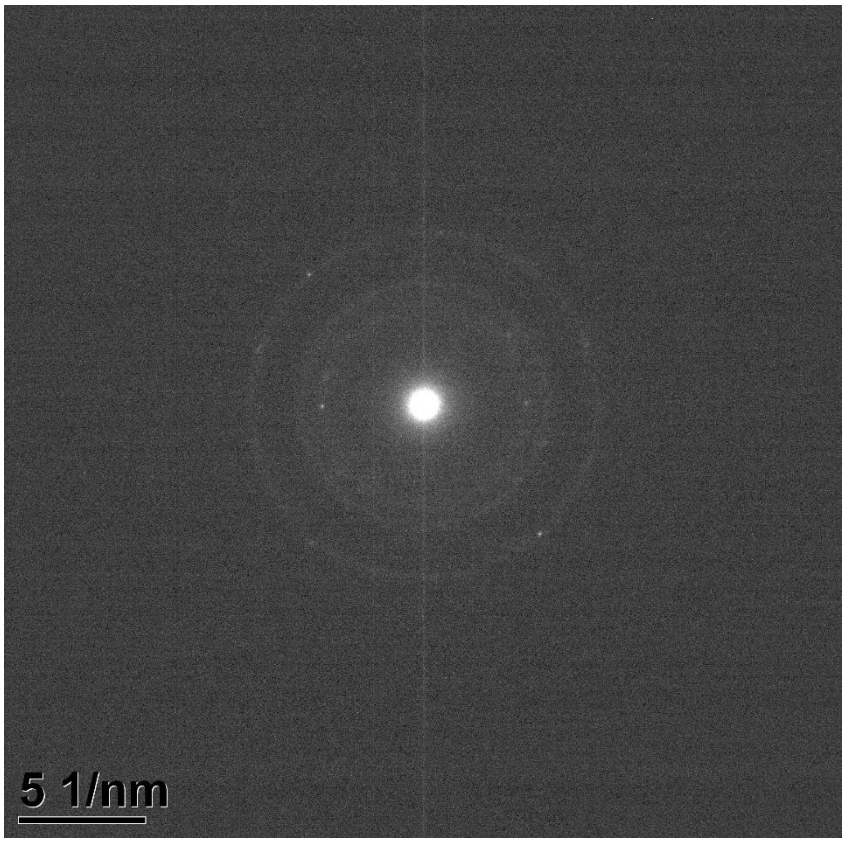


Figure 66 – SAED 1 of Oxi-NiFe

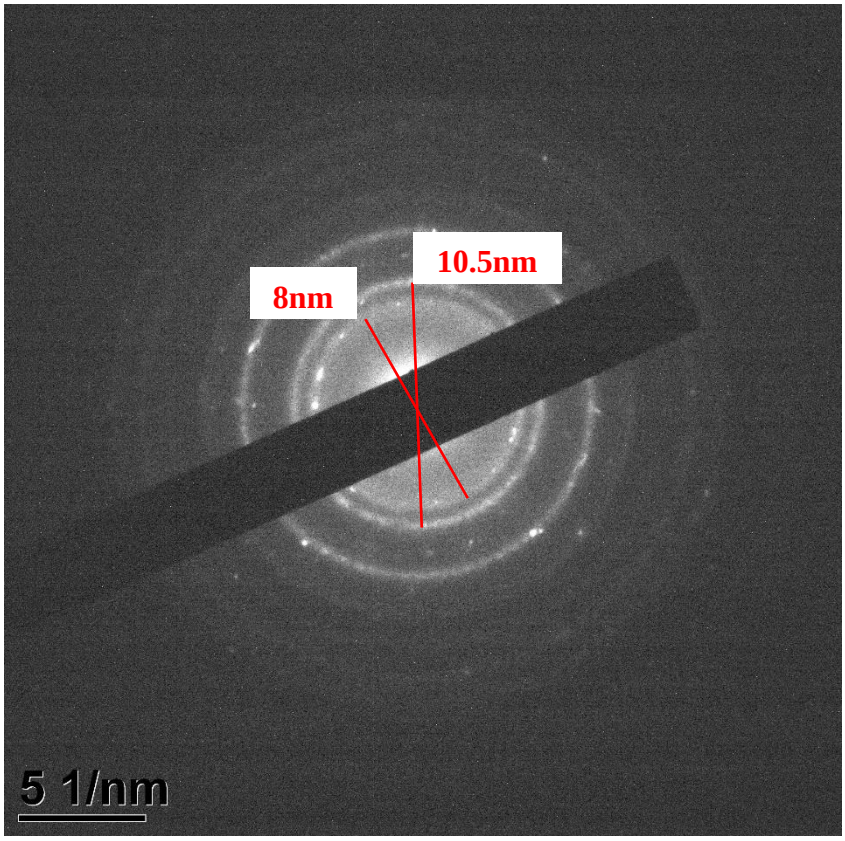


Figure 67 – SAED 2 of Oxi-NiFe with a selected area aperture

For Oxi-NiFe, the TEM showed that with an original 3.3 µm AD NiFe sample, only 0.5µm had been oxidised. This material was cycled for the standard 450 cycles. This indicates that despite the expanded oxidation period, not all of the NiFe was oxidised, contrary to previous estimations. The interface between AD NiFe & Oxi-NiFe was a straight, distinct interface. This was most likely due to the nature of the oxidation process, with the CV of the AD NiFe oxidising and reducing the material, layer by layer.

Single crystals of Oxi-NiFe were easily discernible due to the lack of electron diffraction and were labelled in Fig 63-65. These long needle-like crystals range from lengths of 2-20 nm with 2-5 nm widths. It was also noticeable in Fig 64 the presence of voids, indicating the porous nature of the material, another process caused by the nature of the CV -process. The vertical needle-like structures at the surface of the Oxi-NiFe seems to be constructed of many 2D needle crystal grains, of significant length. Black dots were also present in the Oxi-NiFe layers. These black dots were believed to be dense metal centres of AD NiFe. The reason behind the presence of these black metal centres is currently unknown.

Using the SAED images (Fig 66-67), the 1st and 2nd d-spacing was calculated to be 2.5Å & 1.9Å, respectively. Due to the presence of diffusion rings and thicker rings, it was also clear

that this material was more amorphous than its AD counterpart, although the SAED clearly shows some crystalline structures remaining. Based on the d-spacing and XPERT, the crystal structure of Oxi-NiFe was estimated to be a trigonal crystal lattice symmetry (R-3m space group, D_{3d} point group). This correlates with the NiFe LDH crystal structures explained in Section 1.5.4, in previous cited researched [82].

3.4.2 – NiFe Cores Magnetic Properties

Magnetic Saturation, Retentivity, Coercivity - BH Looper:
Magnetic testing of the AD NiFe 4-inch wafers using the MESA BH Looper showed magnetic properties typical to that of electroplated NiFe alloys. These samples were then oxidised and tested once more. In general, it was hoped that with oxidation, Magnetic Saturation (B_{Sat}) & Anisotropy Field (Hk) increases while Magnetic Retentivity (Br) and Coercivity (Hc) decreases.

Table 13 shows these properties for the NiFe test wafer samples (A-C) as well as the inductor device wafer sample. Each oxidised sample underwent 450 cycles during the oxidation process. The oxidised sample's values are highlighted in green and red, indicating an improvement or worsening of the properties respectively, in comparison to the As-deposited counterparts. Figure 68-69 shows the hysteresis loops for these materials.

Sample	Thickness (µm)	B_{Sat} (T)	Br (mT)	Hc (A/m)	Hk (A/m)
AD NiFe Sample A	3.3	1.49	138	65.04	755.09
Oxi-NiFe Sample A	3.3	**1.36**	**97.2**	**56.37**	**811.69**
AD NiFe Sample B	1.7	1.54	127	61.54	715.48
Oxi-NiFe Sample B	1.7	**0.86**	**41.2**	**35.58**	**774.93**
AD NiFe Sample C	3.3	1.62	91	42.29	781.61
Oxi-NiFe Sample C	3.3	**1.56**	**77.6**	**36.80**	**787.18**
AD NiFe Inductor Sample	3.3	1.62	62	26.09	703.62
Oxi-NiFe Inductor Sample	3.3	**1.38**	**47.5**	**24.03**	**731.64**
Average AD NiFe	**3.3**	**1.57**	**104.50**	**48.74**	**738.95**
Average Oxi-NiFe	**3.3**	**1.29**	**65.88**	**38.20**	**776.36**

Table 13 - NiFe BH Looper results - Sample A = 1.5x1.5cm square - Sample B = 4-inch wafer - Sample C = 4-inch wafer

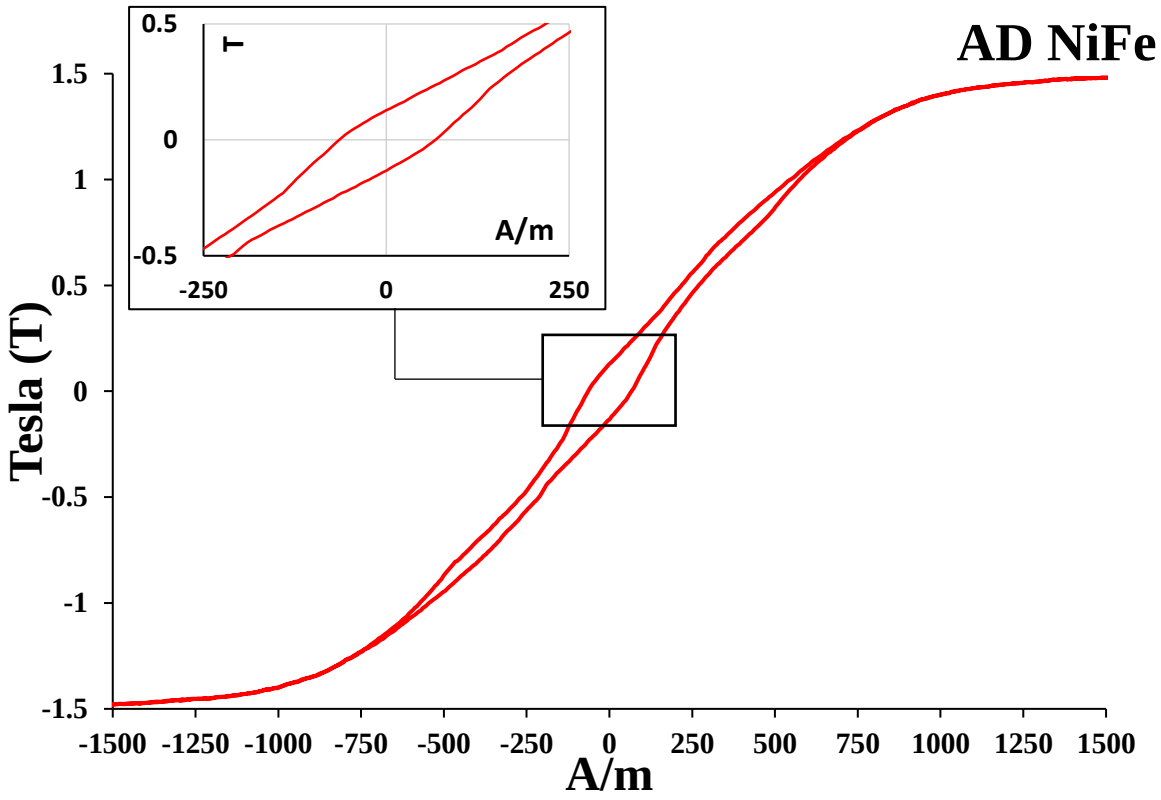


Figure 68 - Hysteresis Loop of 1.5cm x 1.5cm AD NiFe

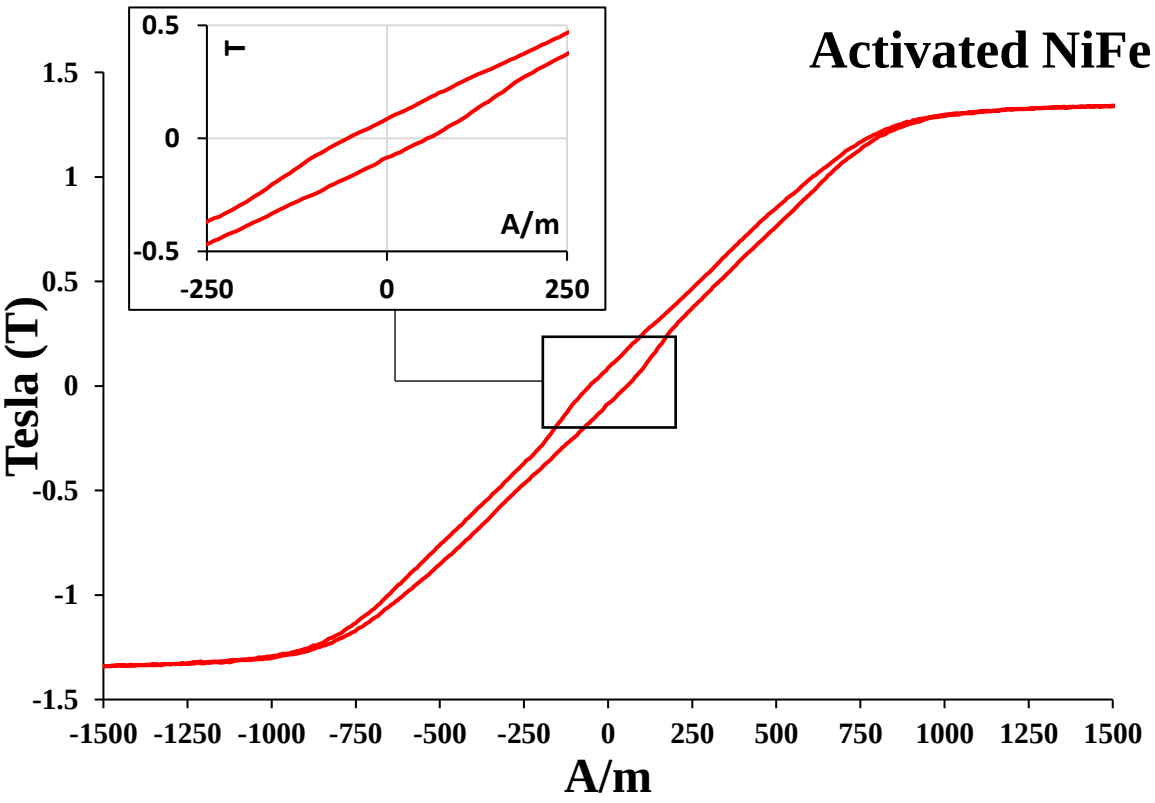


Figure 69 - Hysteresis Loop of 1.5cm x 1.5cm sample of Oxi-NiFe

Table 14 below is a small summary table showing the average results for the Oxidised versions of the NiFe material. The up and down arrows show whether the magnetic properties in Table 13 have, on average, increased or decreased after oxidation. The colouration of these arrows indicates whether the increase or decrease was an improvement (green) or diminishing (red) of the property. Further to this, the table also shows the average percentage increase/decrease in the Oxidised sample's properties in comparison to the As-deposited (AD) counterpart.

Material Properties	*Oxidised Material*	*% Increase (+) OR Decrease (-)*
Thickness	-	-
Saturation Flux Density	↓	**-18%**
Retentivity	↓	**-37%**
Coercivity	↓	**-22%**
Anisotropic Field	↑	**+5%**

Table 14 - % Increase / Decrease in the properties of Oxi-NiFe in comparison to AD NiFe.

While there was a decrease in the magnetic flux density saturation of approx. 18%, the other magnetic properties of the Oxi-NiFe have seen an increase in comparison to the AD counterpart. Magnetic retentivity showed the most substantial improvement, with a 37% decrease, which in turn caused the improvement of coercivity by 22%. This was due to the decreased magnetic field the material holds once the external field has been removed and therefore the energy required to remove the remaining field held by the Oxi-NiFe. The Anisotropy of the material saw a small but noticeable improvement, increasing by 5%, meaning the material now requires a stronger magnetic field to become magnetically saturated.

Permeability - Permeameter:

Using the A PMM 9G permeameter, the permeability of seven, 3.3 µm thick, 1.5x1.5 cm sized diced wafer samples of AD & Oxi-NiFe were measured at 10 MHz. It was expected that with oxidation, the permeability would decrease and therefore also causing a decreasing in the loss tangent. The loss tangent refers to the ratio of electromagnetic energy being dissipated. The energy is predominantly dissipated in the form of heat.

The relative (**μ_r**), real (**μ_r'**) & imaginary (**μ_r''**) permeabilities are listed below in Table 15, along with the material's **Q-Factor** & loss tangent (**tan(δ)**), to 4 significant figures. The median and average are listed for both materials. The median was calculated due to the presence of outliers in the results. The percentage increase/decrease was also calculated between the As-Deposited & Oxidised samples. Standard deviation (STD%) was calculated based on the median results.

As shown by the results in Table 15, there was a definite improvement with the oxidation of the NiFe material. The permeability (real, relative and imaginary) of Oxi-NiFe decreased in comparison to AD, which was as expected due to the increase in the anisotropic field.

While this was considered to be negative, when taking the permeability values in terms of its Q-Factor$\left(\frac{\mu r'}{\mu r''}\right)$, there was a substantial improvement in the materials Q-Factor. This 50% increase on average shows the material overall soft magnetic efficiency was higher than that of the AD NiFe. The loss tangent also was calculated and showed an improvement, with a decrease of -33%, which proves that the material loses less electromagnetic energy, a critical factor in decreasing core lose when the material was integrated into the inductor devices.

Sample Type	Sample Number	μr 10 MHz	μr' 10 MHz	μr" 10 MHz	Q-Factor @ 10MHz	tan(δ) 10 MHz
As-Deposited NiFe	1	847.7	836.6	136.3	6.140	0.1629
	2	867.7	855.8	142.9	5.989	0.1670
	3	825.3	815.5	127.1	6.417	0.1558
	4	795.9	786.6	121.4	6.479	0.1543
	5	862.9	851.7	138.6	6.144	0.1628
	6	817.8	806.7	134.3	6.009	0.1664
	7	869.3	858.6	135.9	6.317	0.1583
	Median	**847.7**	**836.6**	**135.9**	**6.144**	**0.1628**
	Average	**840.9**	**830.2**	**133.8**	**6.214**	**0.1611**
	STD %	**3.4**	**3.3**	**5.3**	**3.2**	**3.1**
Oxidised NiFe	1	780.5	775.4	89.0	8.717	0.1147
	2	830.4	824.8	96.1	8.587	0.1164
	3	800.4	795.3	90.2	8.819	0.1134
	4	634.9	631.5	65.5	9.636	0.1038
	5	799.0	794.1	89.0	8.925	0.1120
	6	755.6	751.7	76.8	9.792	0.1021
	7	574.6	572.1	53.5	10.701	0.0934
	Median	**780.5**	**775.4**	**89.0**	**8.925**	**0.1120**
	Average	**739.3**	**735.0**	**80**	**9.311**	**0.1080**
	STD %	**12.3**	**12.3**	**17.5**	**8.6**	**7.5**
% Increase / Decrease Δ (Oxidised – Non-Oxidised)	**Median**	**-7.92%**	**-7.32%**	**-34.55%**	**+45.28%**	**-31.20%**
% Increase / Decrease Δ (Oxidised – Non-Oxidised)	**Average**	**-12.08%**	**-11.47%**	**-40.21%**	**+49.92%**	**-32.96%**
Improvement / Worsening		↓	↓	↓	↑	↓

Table 15 - Relative, Real & Imaginary Permeability & Loss Tangent of AD & Oxi-NiFe.

3.4.3 – NiFe Device Imaging

Light Microscope

Throughout the fabrication process, the wafers were regularly imaged using a light microscope to assess the processing of the devices. The metal via holes were checked regularly before the vias were deposited to ensure all photoresist within the holes had been removed. Failure to remove all the photoresist can lead to over-plating and the creation of void holes. The core of the devices were also checked after core etching to ensure that they have not been over-etched.

Fig 70 shows the imaging of the vias and cores of the oxidised and as-deposited NiFe devices. The vias on both devices had been constructed without issue, although the as-deposited devices were showing minute core over-etching.

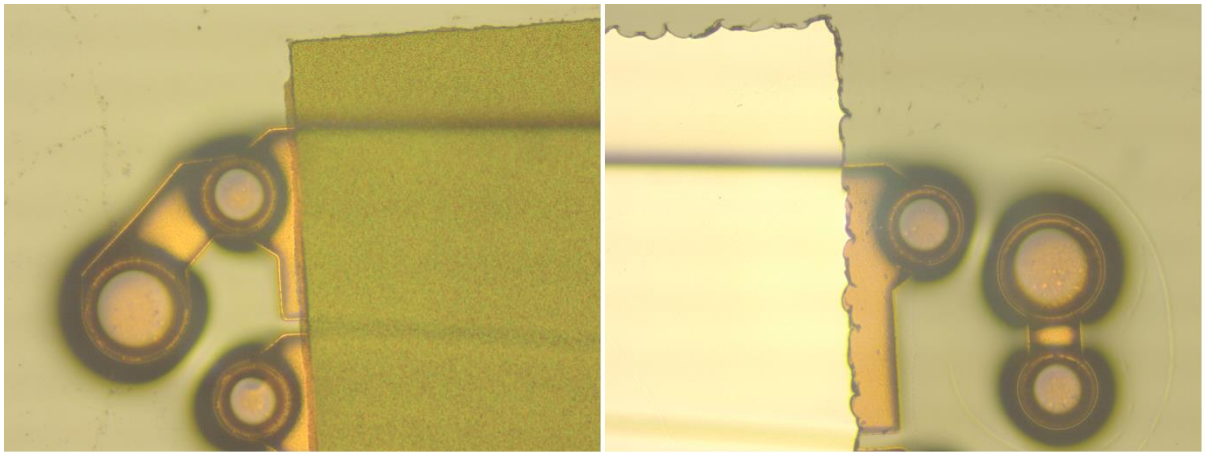


Figure 70 - Light microscope image of the vias and cores of the oxidised devices (left) and as-deposited devices (right)

SEM

Once finalised, the devices were imaged using the SEM. The dimensions of the various devices were measured and labelled on these images. Below are the photos of a finalised MC1 coupled inductor (Fig 71) and MS1 single inductor (Fig 72), along with the device's overall length and width as well as their via length and width.

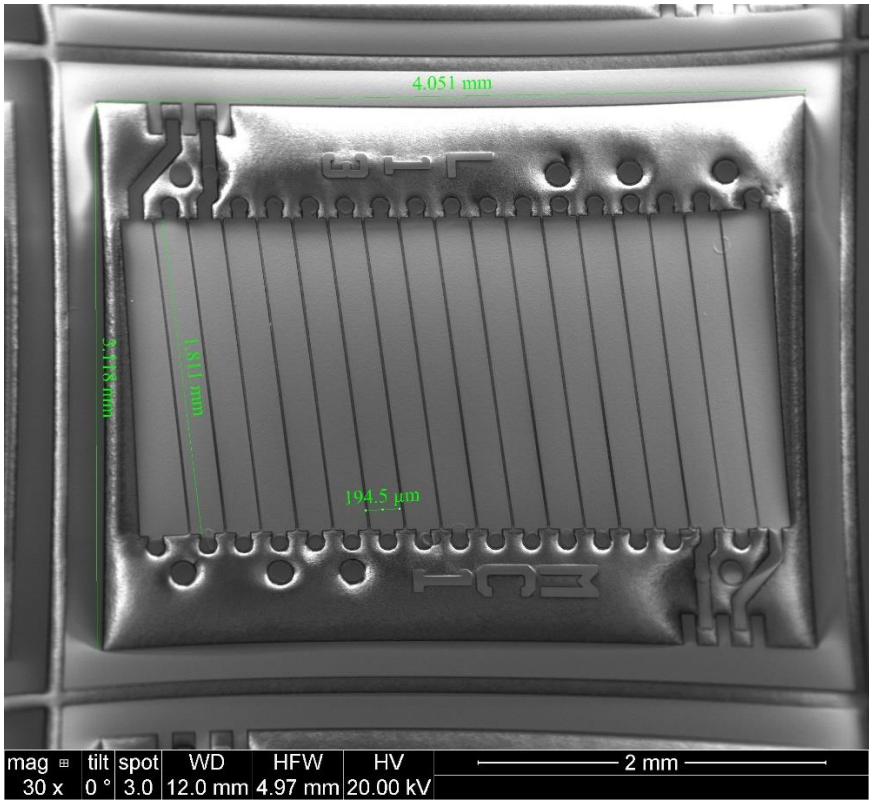


Figure 71 – MC1 coupled inductor with measurements

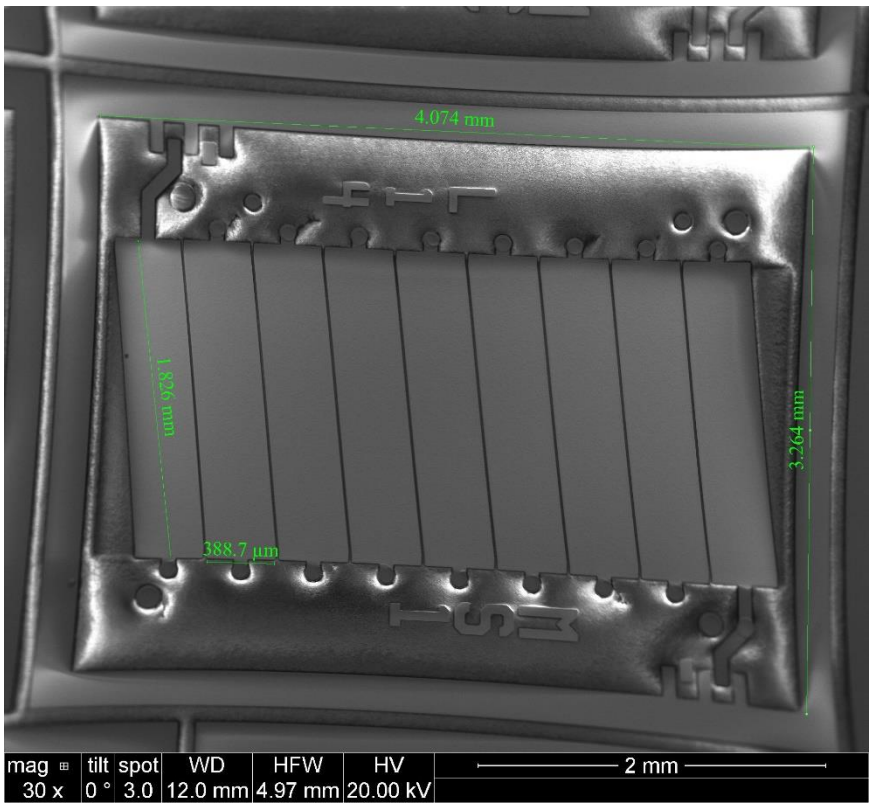


Figure 72 – MS1 single inductor with measurements

3D X-Ray

Additional 3D X-Ray imaging of the devices were also taken to show the design of the inductor devices further and inspect in a non-destructive manner that there were no open or short circuits within the devices. Fig 73 shows the X-ray imaging of the copper windings in the devices, with Fig 73 (D) showing the thickness of the inductor in comparison to the Si substrate.

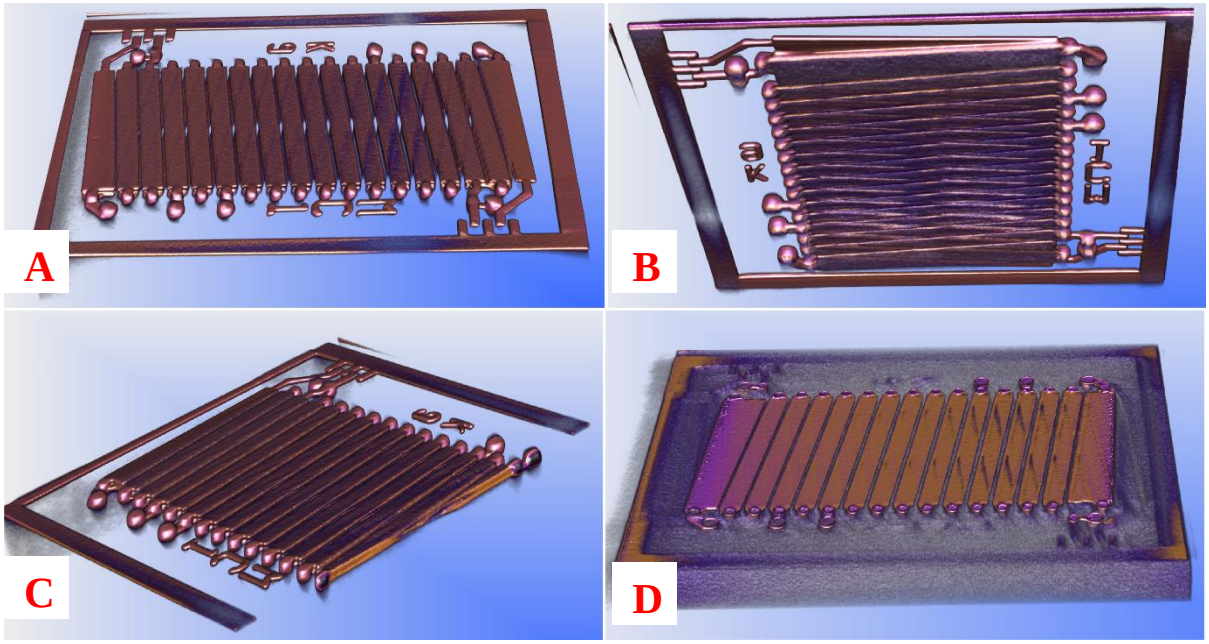


Figure 73 - 3D X-Ray Images of MC1 Inductor

Camera

Additional images (Fig 74-78) were also taken throughout the device fabrication process using a standard camera.

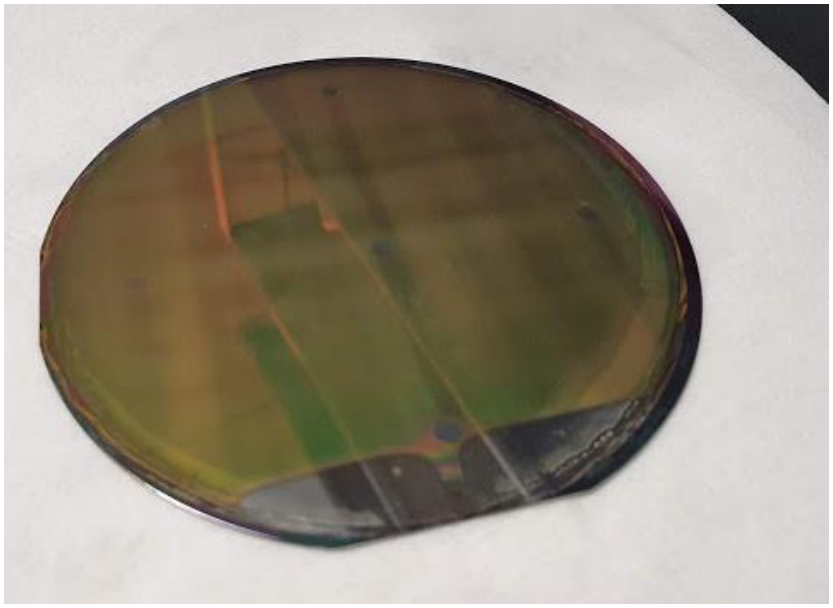


Figure 74 - NiFe wafer after oxidation, showing the iridescent colouring of Oxi-NiFe. Note the bottom of the wafer is AD NiFe - This area was not submerged in the bath and was used as the electrical connection point

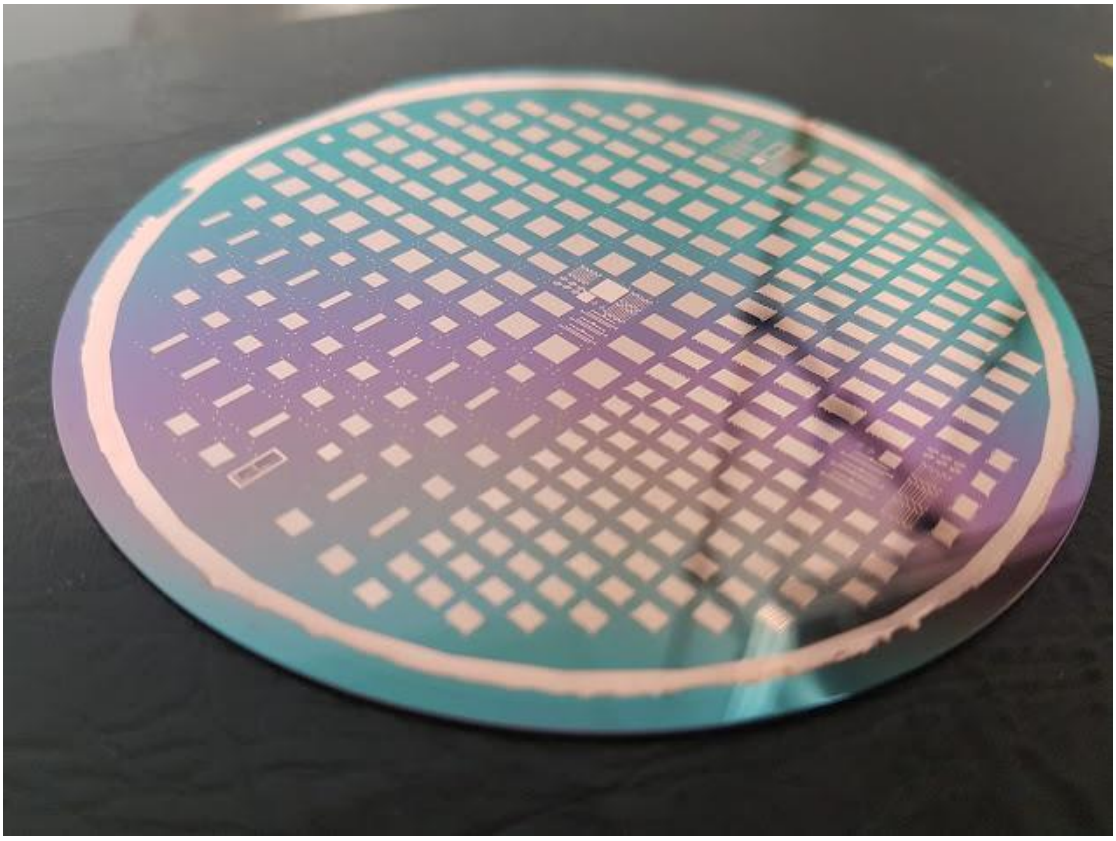


Figure 75 - Device Wafers with bottom windings and vias built

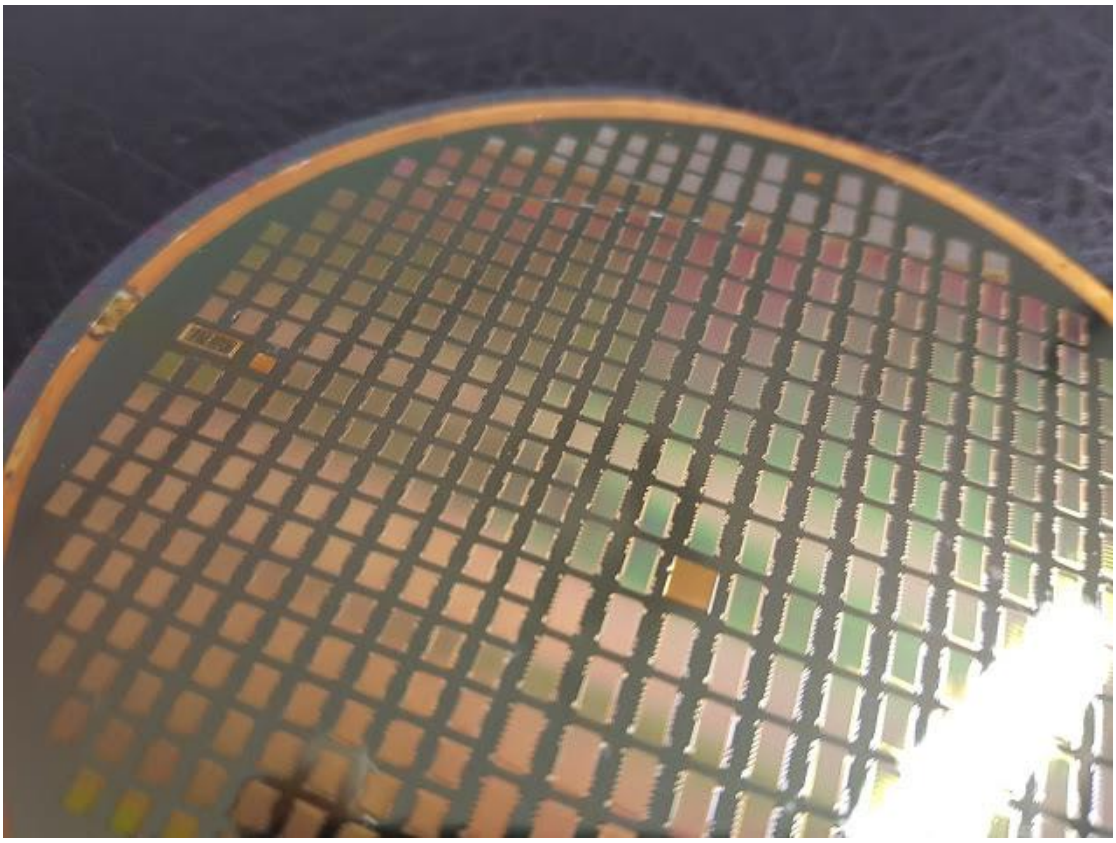


Figure 76 - Oxi-NiFe Wafer after Core Etching. Cores show the iridescent colouration.

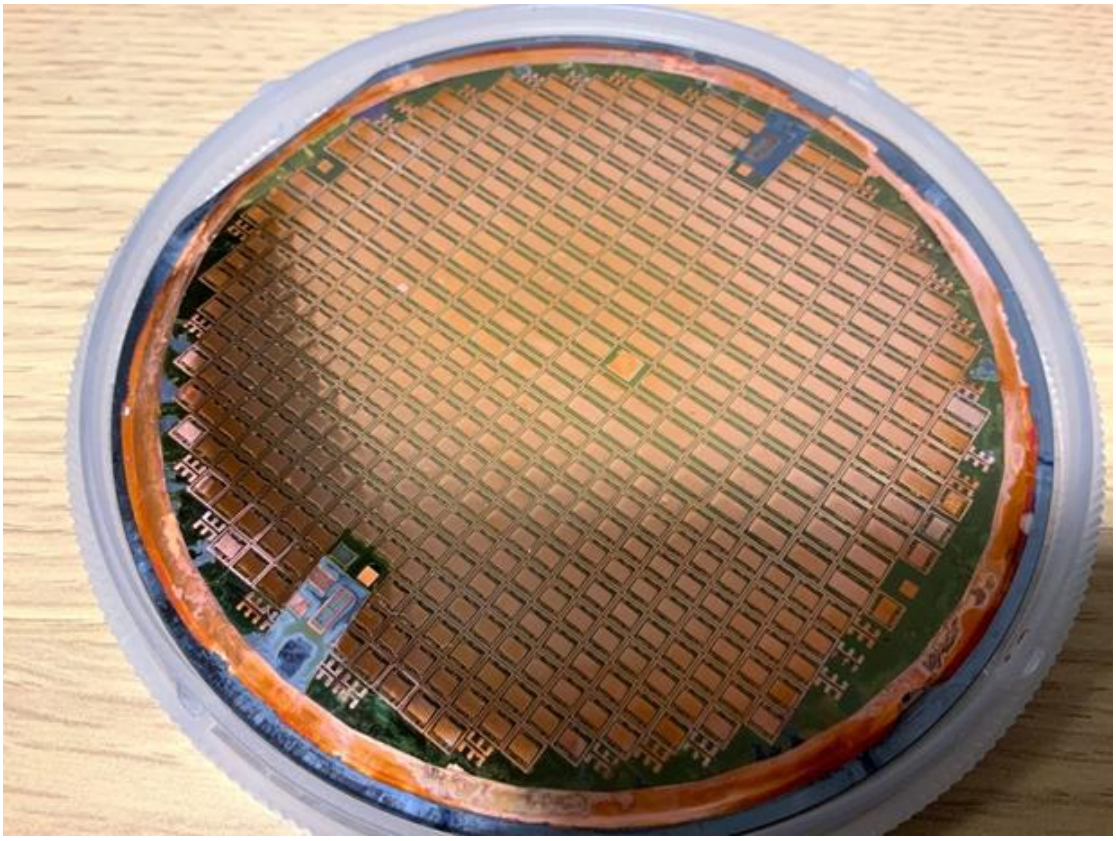


Figure 77 – Fully Constructed Oxi-CoNiFe Device Wafer

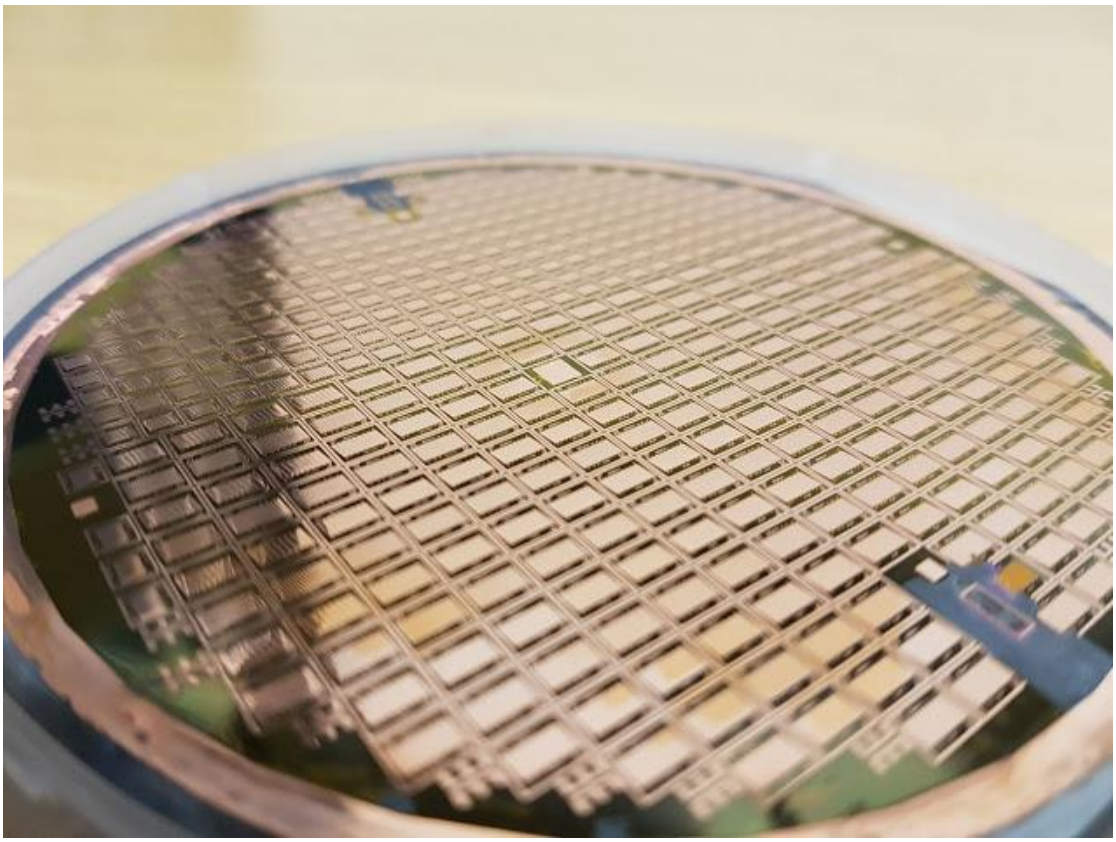


Figure 78 - Fully Constructed AD NiFe Device Wafer

3.4.4 – NiFe Devices Properties

Each of the four inductor designs (MS1, MS2, MC1, MC2) were fabricated on each device wafer, allowing the comparison of the AD NiFe & Oxi-NiFe versions of each design. Inductance, & AC Resistance was measured using the Cascade Attoguard Probe System and thus allowing for the calculation of the Q-Factor of each of the inductor designs. Peak efficiency was found to be at 4 MHz; therefore, all electrical parameters were considered at such.

Below in Figures 79-90, show the inductance (L11), AC resistance (R11) & Q-Factor (Q11) of each of the four designs for both the AD NiFe (NiFe_NAct) and Oxi (NiFe_Act) cores. From this, it should be seen that Oxi cores perform better than the AD cores (i.e. NiFe_Act should be higher in all plots.) Table 16 shows the overall results for each design for both NiFe materials. The 11 after L, R and Q was given as the sample batch number on the day of testing by the Probe System and was not removed in error.

NiFe MS1 Inductor:

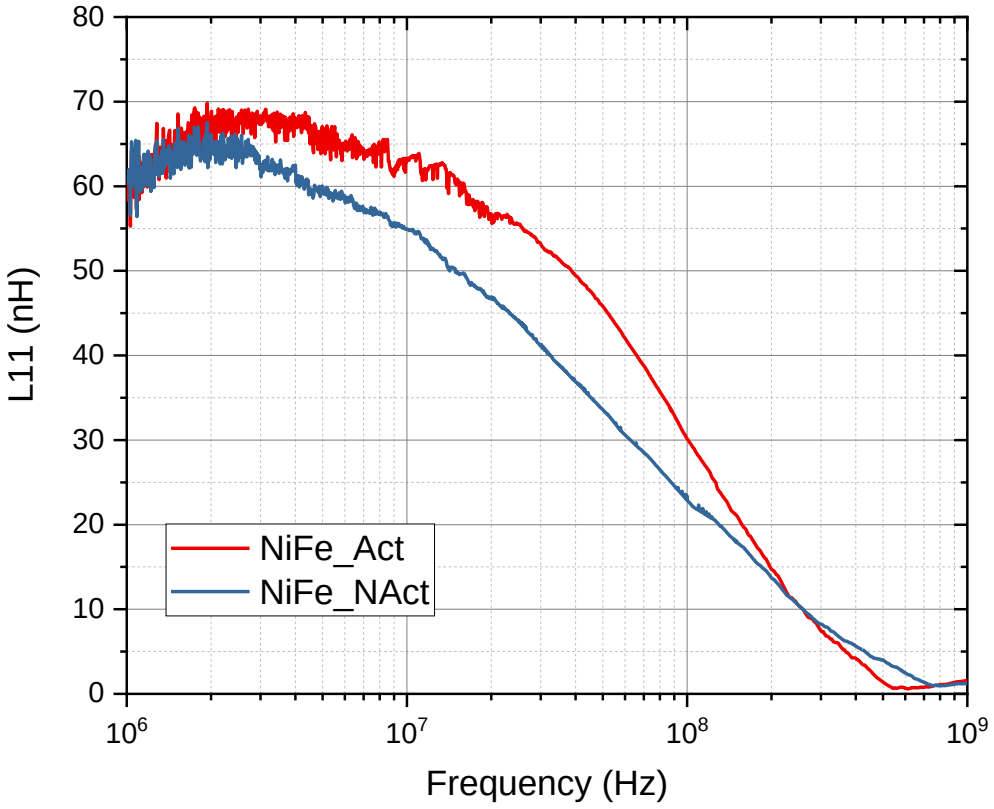


Figure 79 - Inductance of NiFe MS1 Inductor Devices

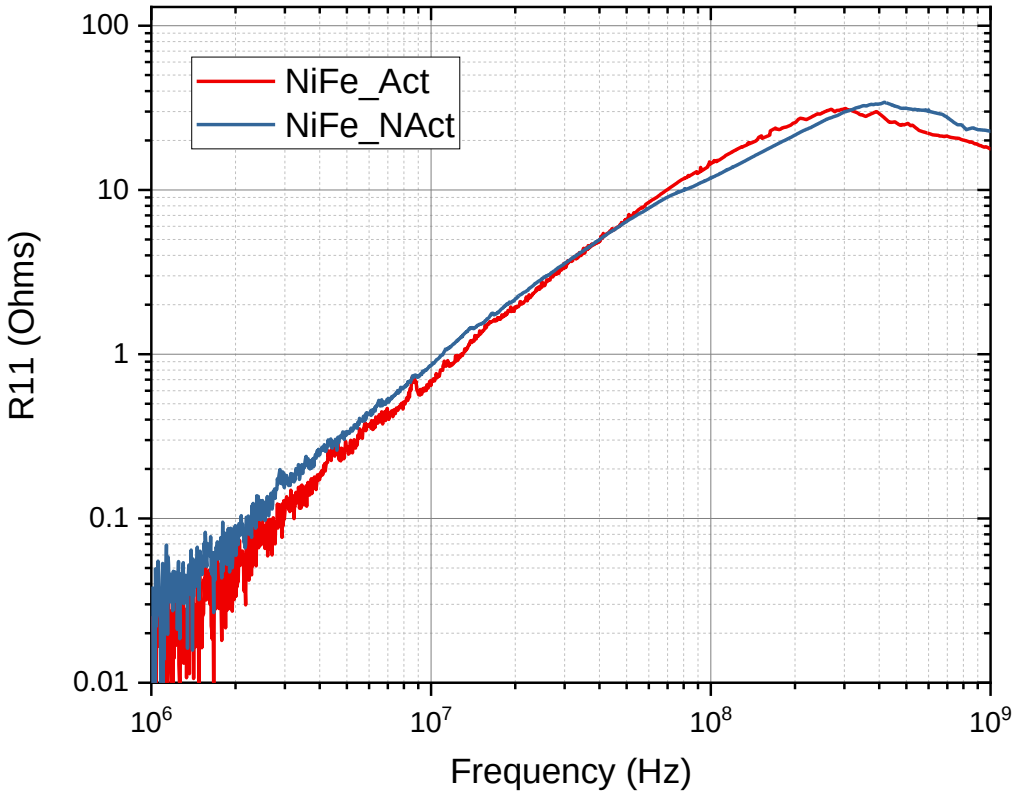


Figure 80 - AC Resistance of NiFe MS1 Inductor Devices

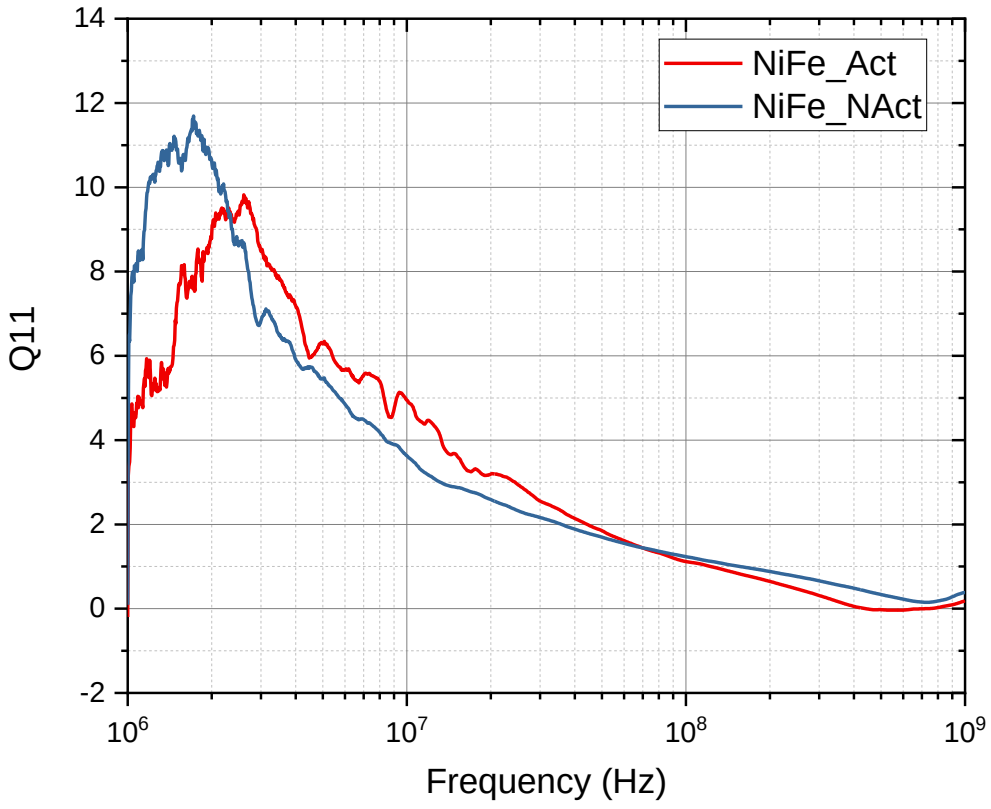


Figure 81 - Q-Factor of NiFe MS1 Inductor Devices

NiFe MS2 Inductor:

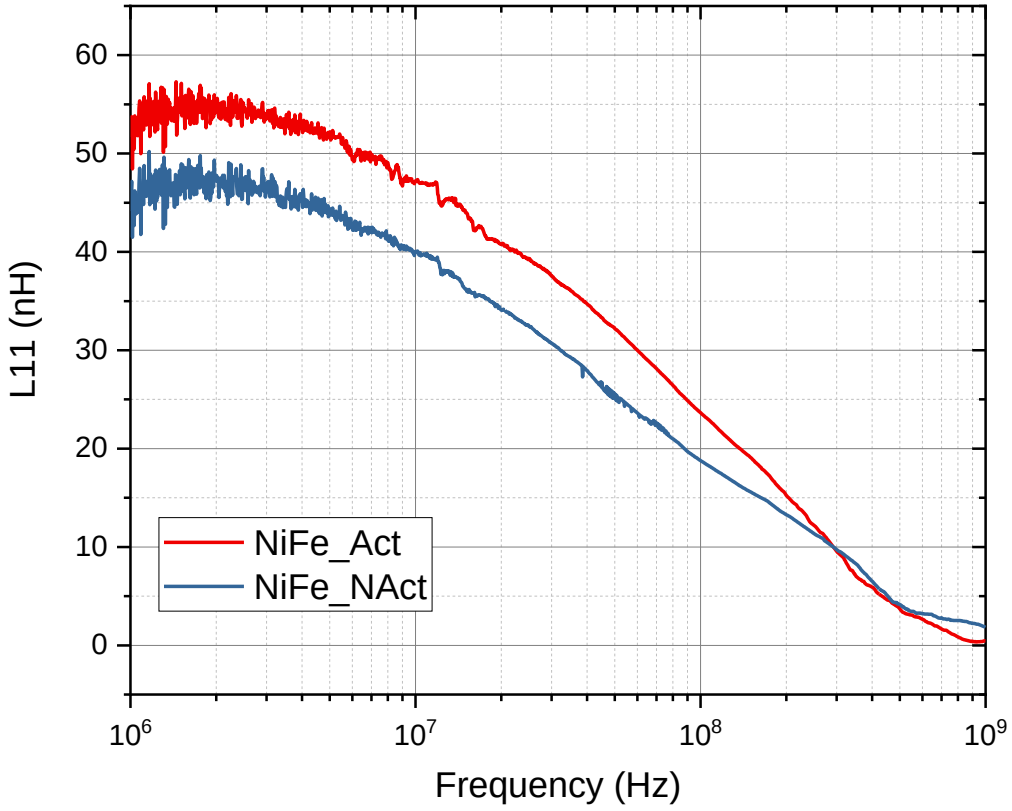


Figure 82 - Inductance of NiFe MS2 Inductor Devices

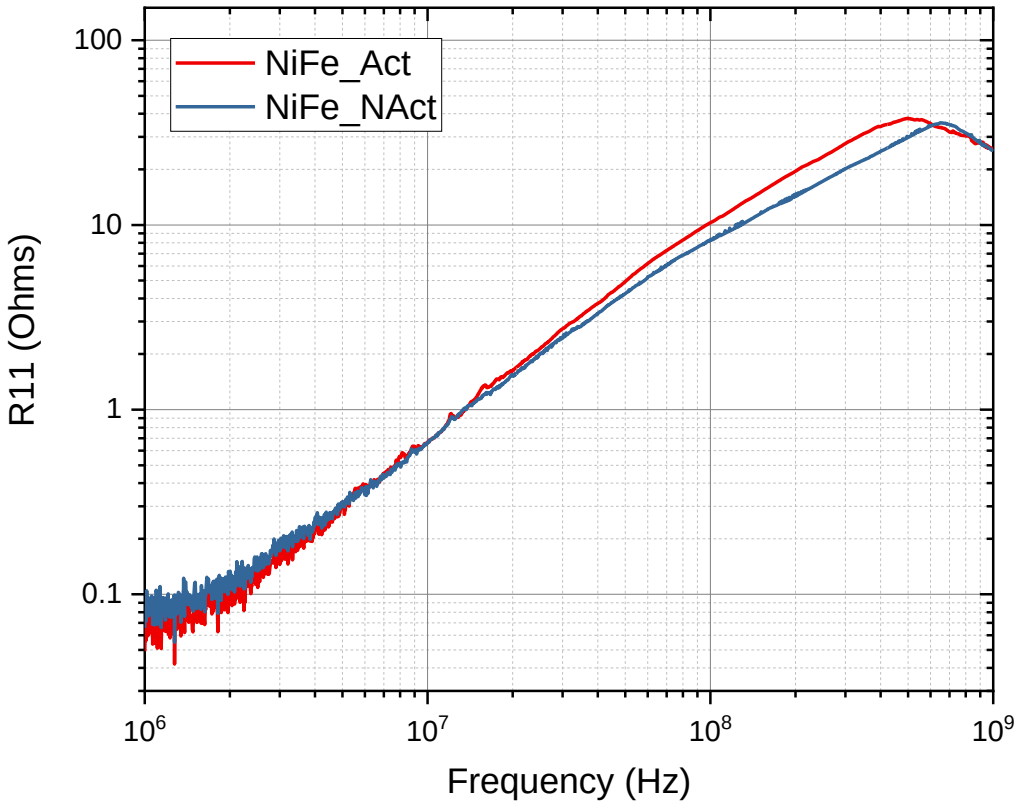


Figure 83 - AC Resistance of NiFe MS2 Inductor Devices

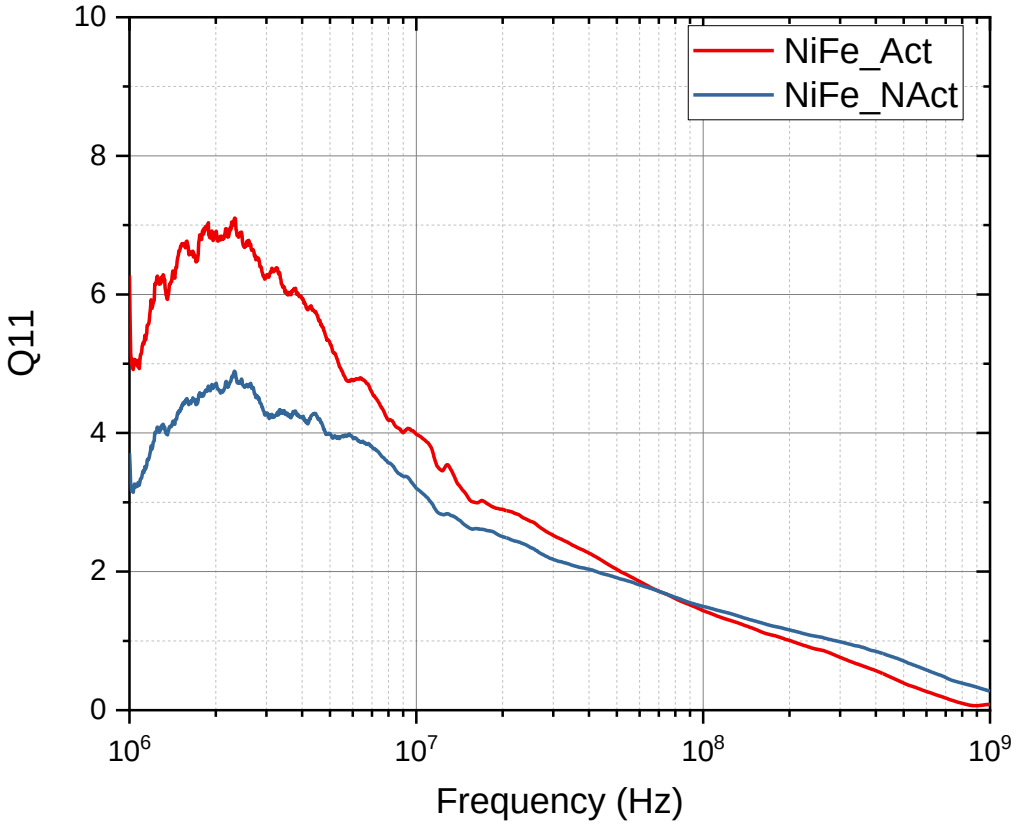


Figure 84 - Q-Factor of NiFe MS2 Inductor Devices

NiFe MC1 Inductor:

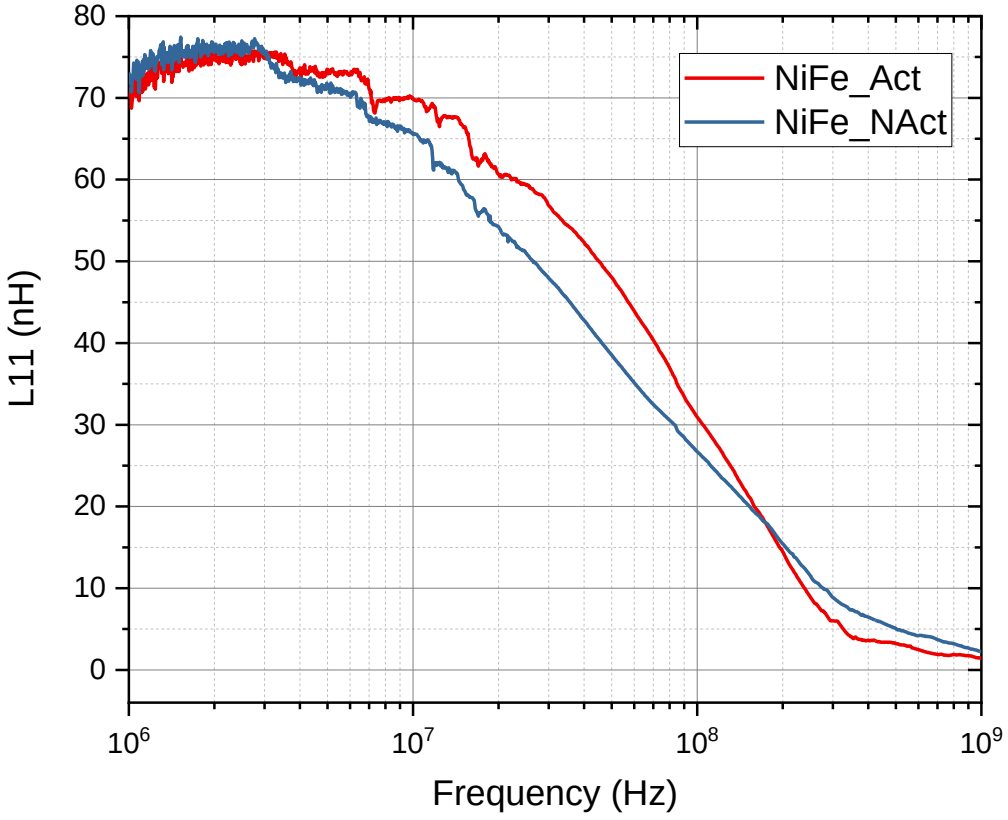


Figure 85 - Inductance of MC1 Inductor Devices

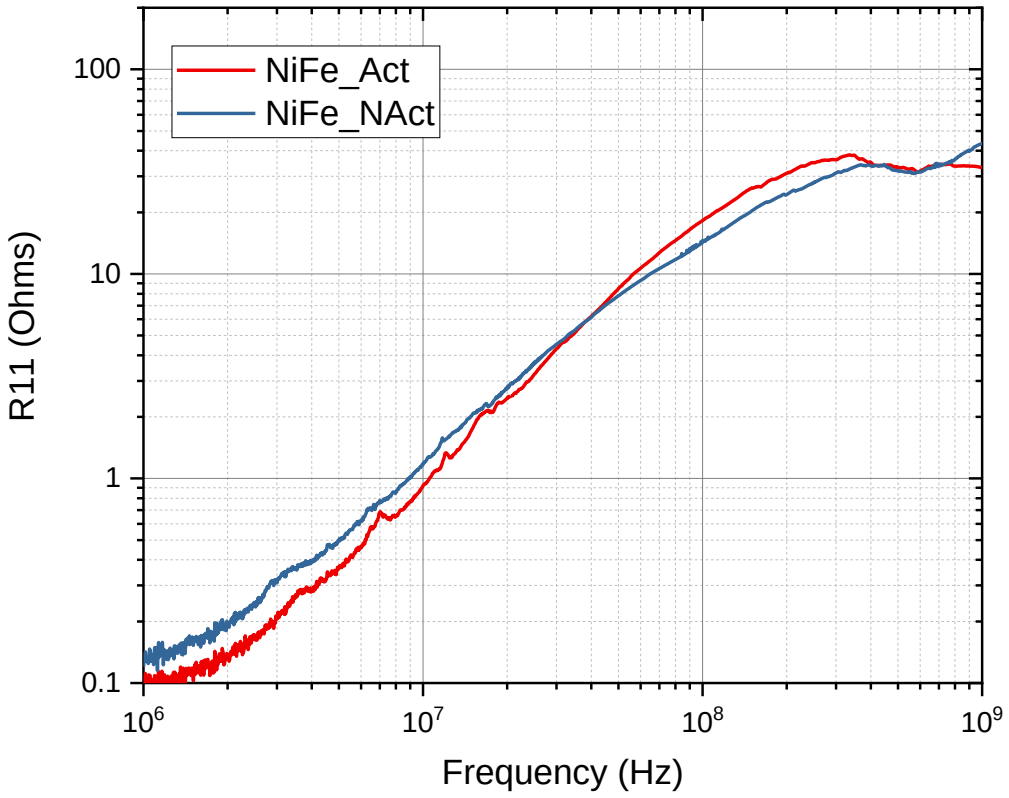


Figure 86 - AC Resistance of NiFe MC1 Inductor Devices

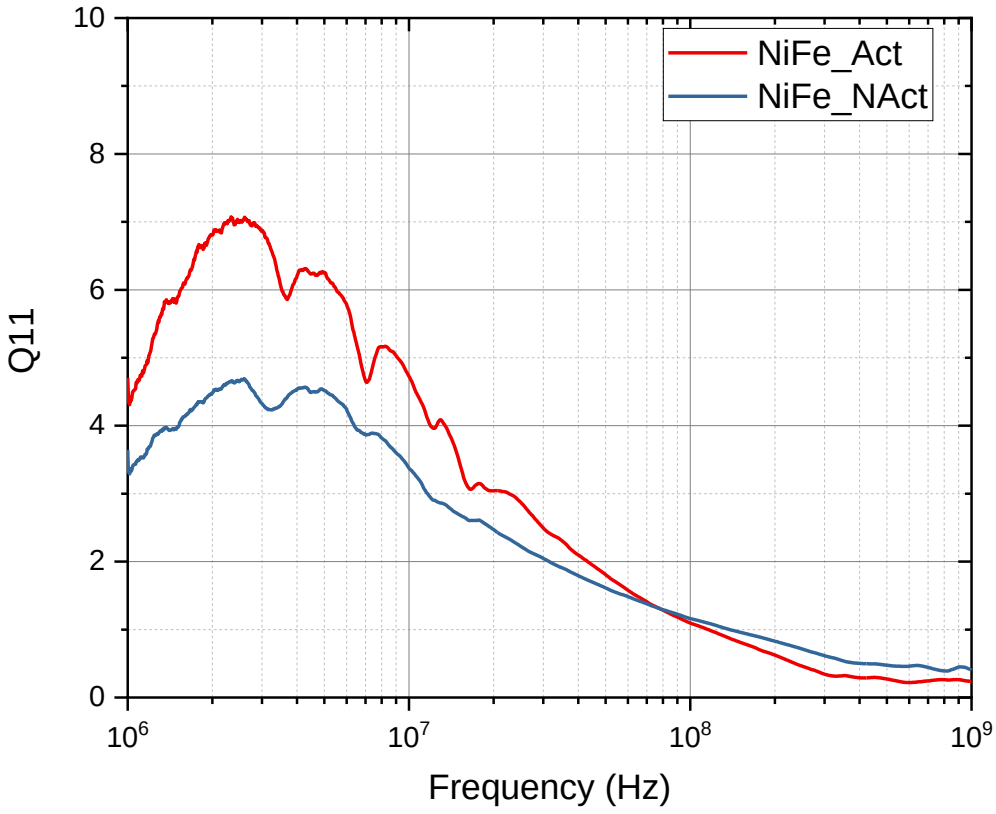


Figure 87 - Q-Factor of NiFe MC1 Inductor Device

NiFe MC2 Inductor:

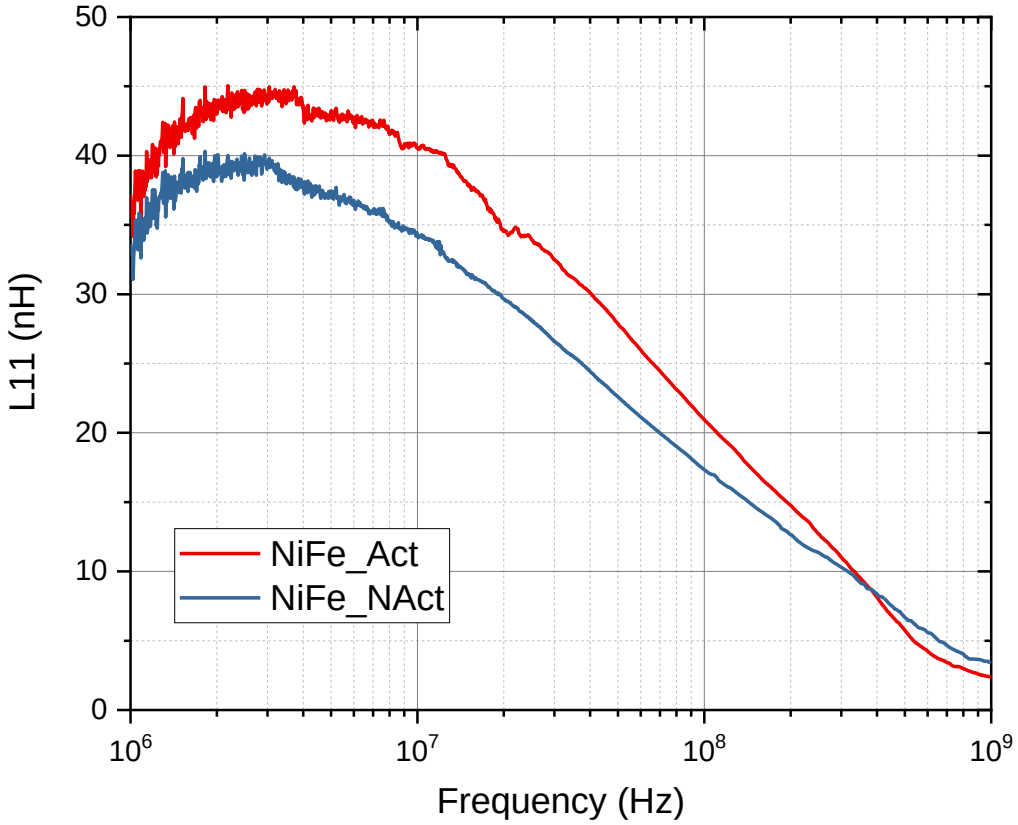


Figure 88 - Inductance of NiFe MC2 Inductor Devices

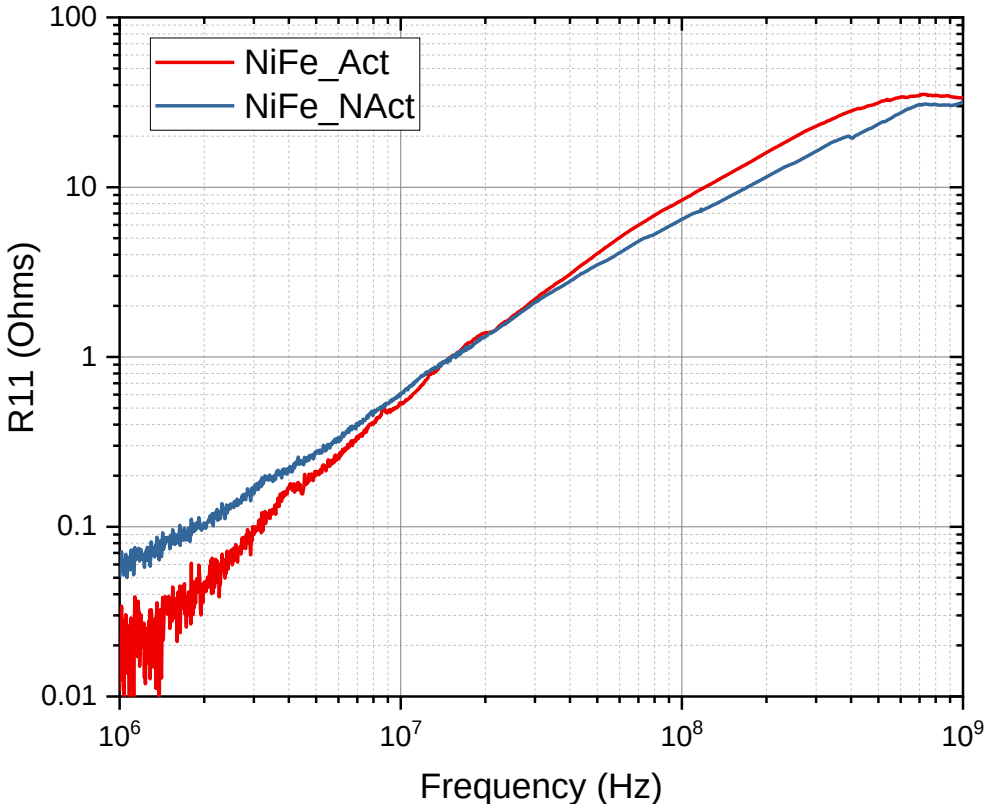


Figure 89 – AC Resistance of NiFe MC2 Inductor Devices

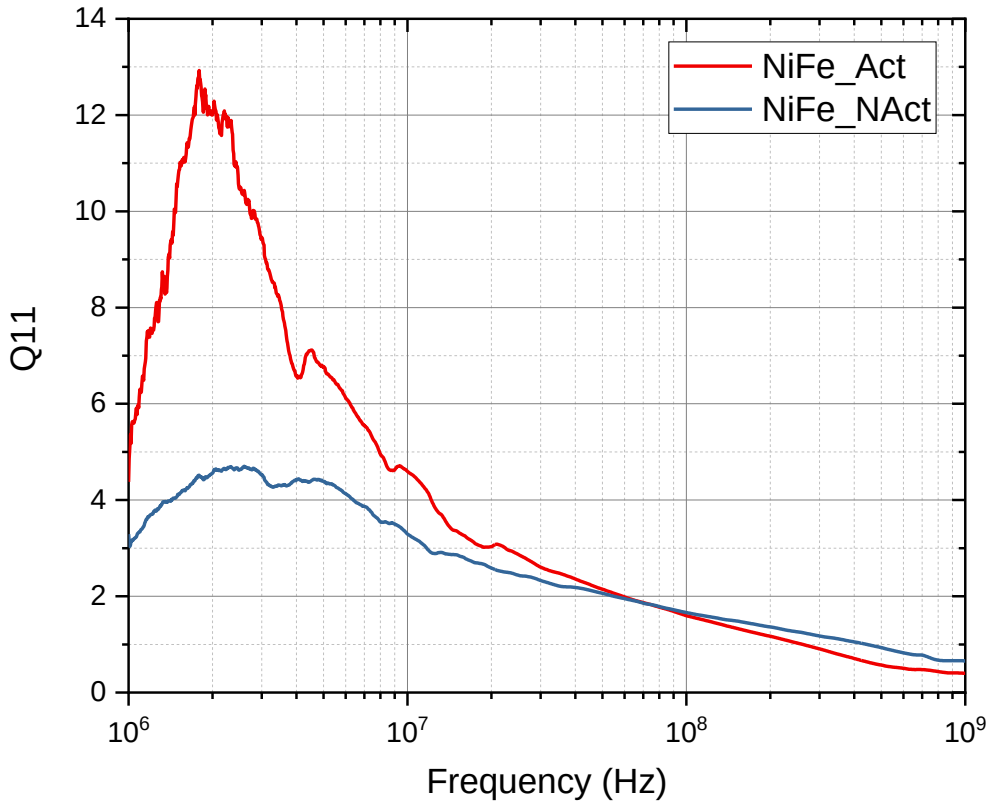


Figure 90 - Q-Factor of NiFe MC2 Inductor Devices

Total Results:

Type	Property	MS1	MS2	MC1	MC2	Average
Non-Oxidised NiFe	L11 (nH)	62.51	45.79	72.31	38.07	**54.67**
	R11 (Ω)	0.24	0.26	0.39	0.22	**0.28**
	Q11	6.13	3.79	4.59	4.50	**4.75**
Oxidised NiFe	L11 (nH)	67.55	52.72	73.68	43.59	**59.39**
	R11 (Ω)	0.17	0.24	0.29	0.17	**0.22**
	Q11	7.72	5.39	6.23	6.26	**6.4**
% Increase Δ (Oxidised – Non-Oxidised)	L11 (nH)	8.07	15.14	1.91	14.50	**9.91**
	R11 (Ω)	-29.12	-9.00	-27.03	-21.93	**-21.77**
	Q11	25.93	42.16	35.79	39.33	**35.80**
Improvement or Worsening (Oxidised vs Non-Oxidised)	L11 (nH)	↑	↑	↑	↑	↑
	R11 (Ω)	↓	↓	↓	↓	↓
	Q11	↑	↑	↑	↑	↑

Table 16 - Inductance, AC Resistance & Q-Factor of the MS1, MS2, MC1 & MC2 devices with AD & Oxi-NiFe

Discussion:

The results of L, R & Q for each device were the average results of all the devices tested. However, not every device on the wafers was tested, due to a device failure, typically caused by an electrical failure (short circuit) or other fabrication errors (overlay failure). However, device failure was rare for this fabrication due to the industrial manufacturability required of these devices.

As expected, the oxidation process caused a decrease of AC resistance of the device by 22%, resulting in lower core loss. This correlates with the decrease in loss tangent & increase in Q-Factor as seen in the permeability results. The inductance of the device also saw an improvement, with a 10% average increase across all devices. Combined, these two results lead to an increase in the Device's Q-Factor of 36%, averaged across all the devices, proving that the NiFe devices had substantially improved with the integration of the oxidised core. $Ni(OH)_2$ has been shown to have paramagnetic properties

In terms of the individual devices, it should be noted that the MS2 design saw the highest percentage improvement in Q factor once oxidised (42%), followed by MC2, MC1 and MS1. However, MS1 saw the highest Q factor for both AD & Oxidised Core devices, while MS2 saw the lowest in both. MS2 also showed the smallest improvement in AC Resistance, at only a -9% decrease, in comparison to the rest of the devices which had a -30 – -20% decrease. Despite the inefficiencies in the designs, the results clearly show an improvement in the cores once oxidised, for all the properties, in each design. Evidently, as shown by the results, even before oxidation the MS2 design was the least effective out of all four devices, while MS1 was the most effective device, while MC1 & MC2 were near equal in-between.

As mentioned in Section 3.1.1, the ultrasoft design was based on a previous design that was fully optimised for a 3.3 µm laminated CZTB cores. Inductor designs are typically designed around the core material, whereby the material is chosen based on the thickness of the core required and the magnetic and electrical properties the material will have at that thickness. While the thickness of the new NiFe cores remained at 3.3 µm, the material itself was different and may not have been entirely optimised for the designs. As stated in Section 1.1.2, Q-Factor is based on inductance (L) vs resistance (R), with inductance based on the permeability (µr) and resistance based on the thickness of the material and addition of laminations. Since the magnetic permeability and electrical resistance vary from material to material and the NiFe not being laminated, it is clear that the NiFe core would, therefore, have varying inductance and resistance and therefore Q-Factor in comparison to a laminated CZTB core.

3.6 – CoNiFe Cores Properties

3.6.1 –CoNiFe Cores Composition Properties

Thickness & Roughness – Tencor & SEM:

AD CoNiFe

After the numerous tests with the CoNiFe bath and plating methods, the CoNiFe plating system produced deposits with a smooth and shiny appearance and adequate plating rate (2.2 μm/hr), despite it being considerably slower deposition rate in comparison to NiFe (4.38 μm/hr).

Fig 91-94 are SEM images of the CoNiFe surface. Using the profilometer, the roughness of the CoNiFe surface was found to be in the nanometre range (>50 nm). Surface blemishes or small protrusions on the deposit's surface appeared sparsely and were approximately 100 nm-500 nm high. These can be caused by numerous factors, such as surface contamination before deposition, creation of new nucleation sites or deposition onto a rough surface.

Oxi-CoNiFe

In oxidising CoNiFe the thickness of the material was found to be 3.3 μm. While the thickness of the Oxi-CoNiFe could not be measured using a profilometer during the fabrication stage, it was measured using a cross-section analysis of a fully constructed device using an SEM.

Typical of the oxidation procedure, the roughness of the CoNiFe' surface increased once oxidised. Tencor analysis showed that roughness of the Oxi-CoNiFe was in an average range of (>200nm), though large protrusions due to cracks could be as high as 500nm.

Fig 93-94 shows the SEM images of the Oxi-CoNiFe surface. Cracks in the surface of the Oxi-CoNiFe can be seen in Fig 93-94, which speculates the now porous nature of the material. The surface also visually appears to be rougher than typical CoNiFe, which was caused by the large grains of the oxidised CoNiFe forming during oxidation.

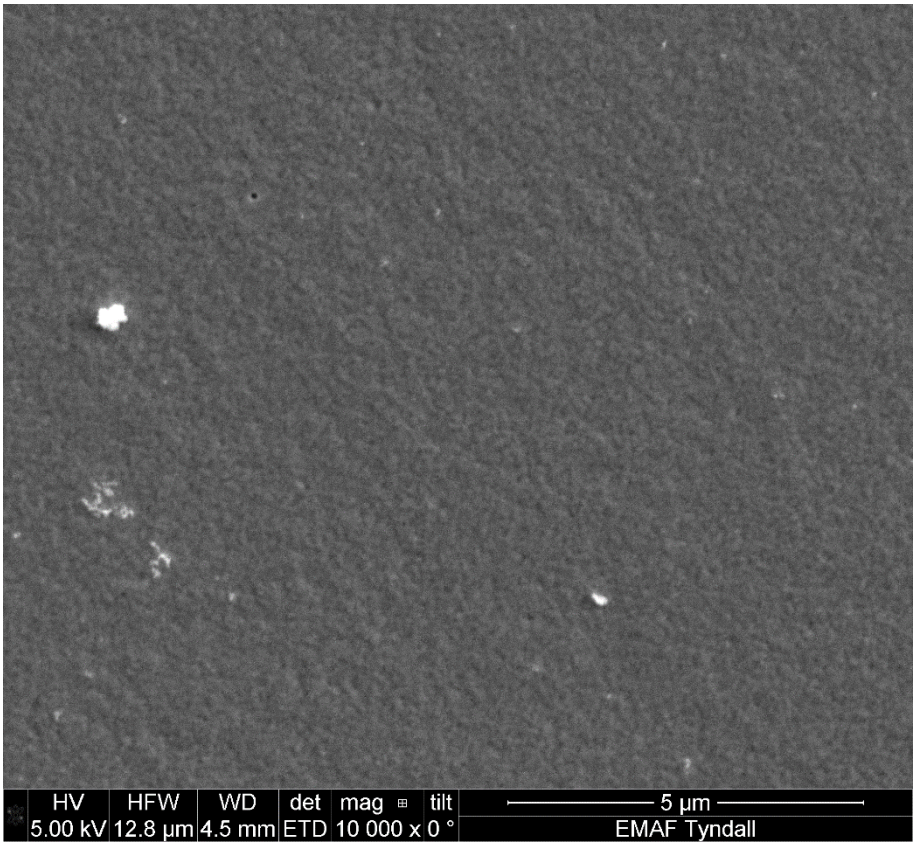


Figure 91 - AD CoNiFe Surface (Top-Down View)

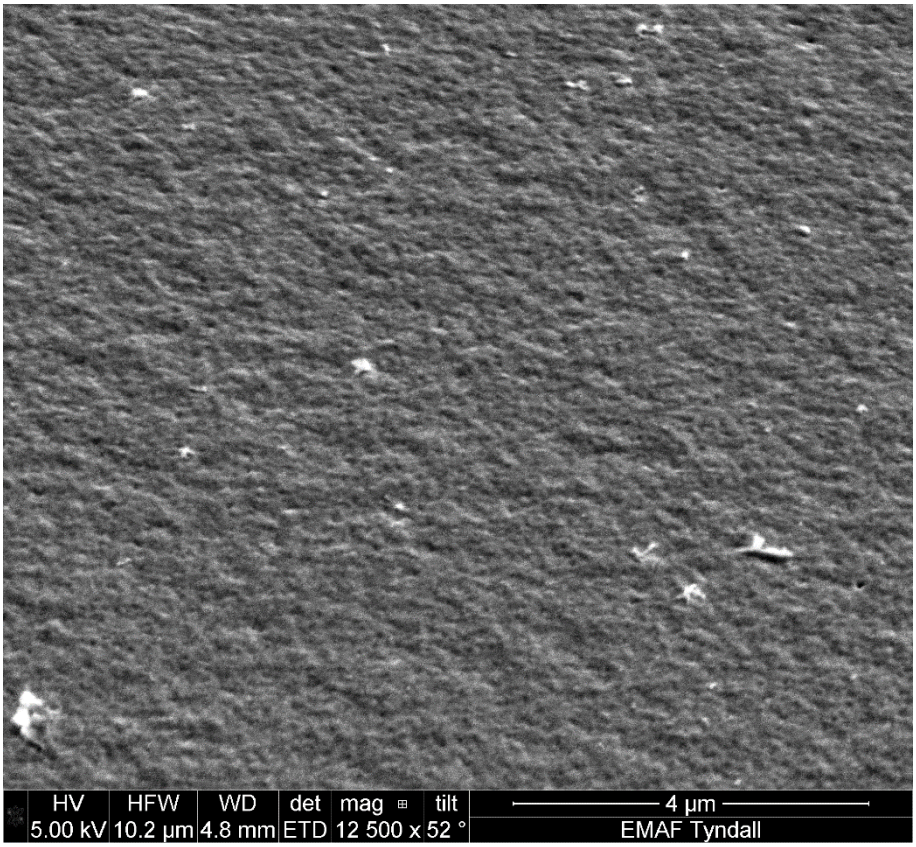


Figure 92 - AD CoNiFe Surface (58° Angle)

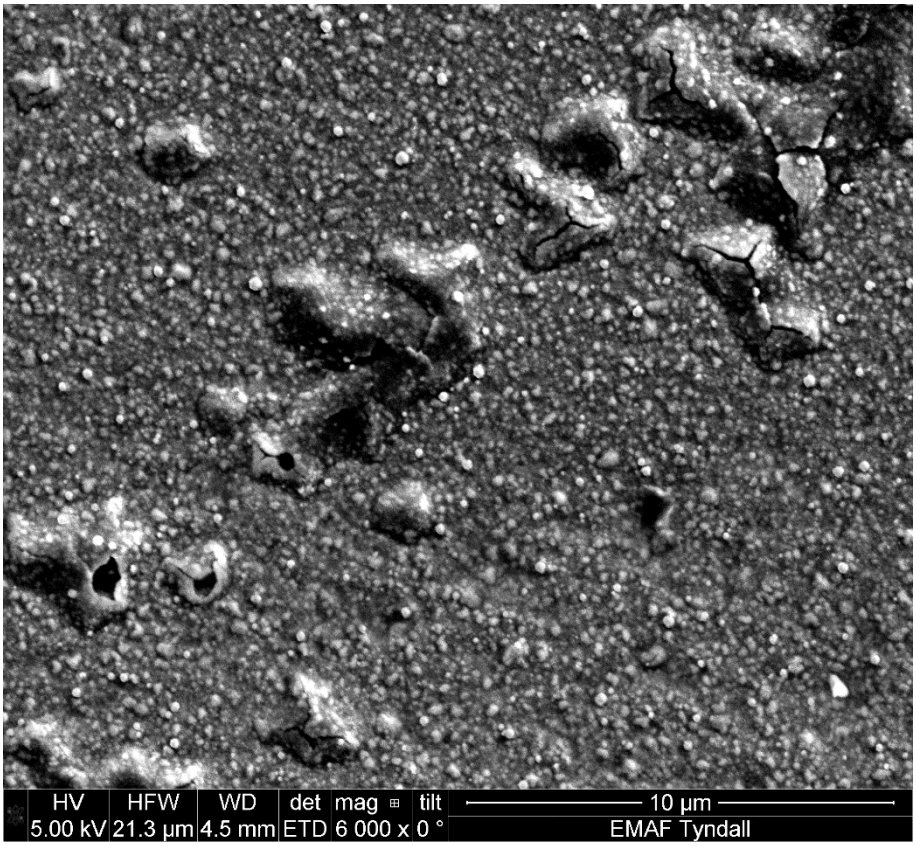


Figure 93 - Oxi-CoNiFe Surface (Top-Down Viewing)

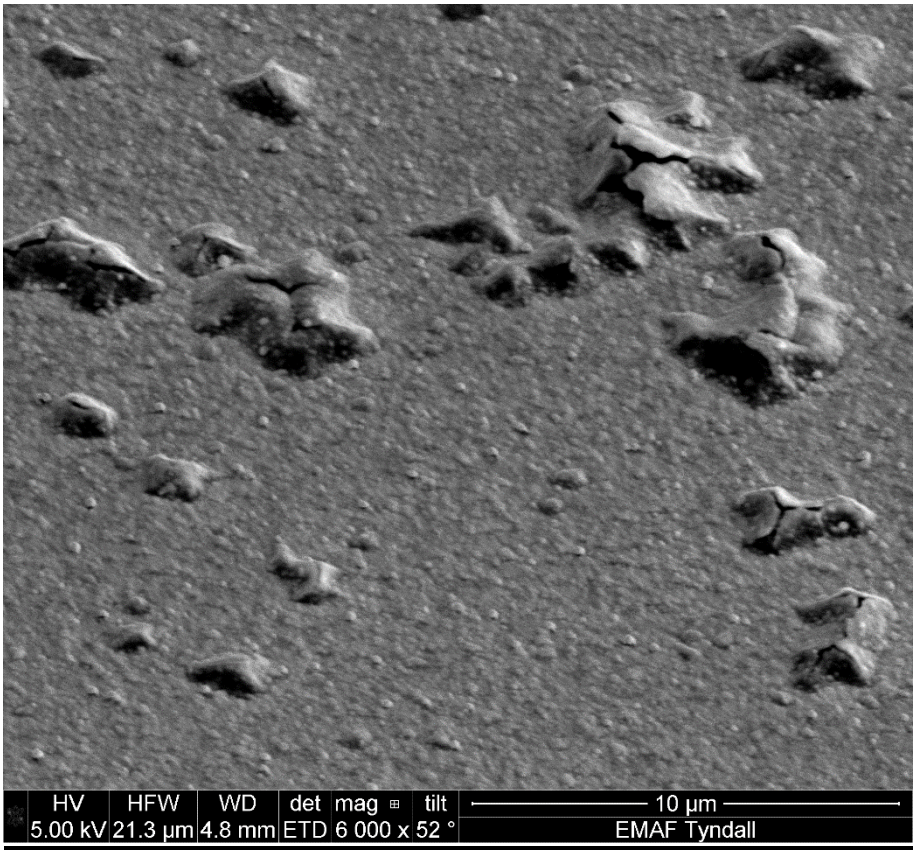


Figure 94 - Oxi-CoNiFe Surface (52° Angle)

Composition - EDX:

AD CoNiFe

Much like NiFe, it was essential that the CoNiFe bath deposited the correct composition of CoNiFe required for the as-deposited and pre-oxidised cores. Composition analysis of the $Co_{64.5}Ni_{16.5}Fe_{19}$ using EDX was completed before the wafers continued with the fabrication process.

However, unlike NiFe, failure to produce the correct composition would lead to a problematic removal of the deposited CoNiFe layer. The addition of cobalt increases the chemical resistance of the alloy, which could cause a delay in the etch time. This delay could allow for the inadvertent etching of other materials deposited on the wafer, leading to the destruction of the device. Therefore, it was necessary to ensure the bath was producing the correct composition using a dummy wafer before the deposition of the CoNiFe onto the device wafers.

The composition was recorded in weight percentage before being converted to an atomic percentage, with the CoNiFe composition having an acceptable atomic percentage range of ±2%. Table 17 shows the composition of the AD CoNiFe.

Element	Apparent Concentration	Weight %	Weight % Sigma	Atomic %
Cobalt	62.24	64.12	0.29	**63.39**
Iron	20.36	19.83	0.22	**20.69**
Nickel	15.59	16.05	0.26	**15.92**
Total:		100		100

Table 17 - EDX Analysis of AD CoNiFe

Oxi-CoNiFe

EDX composition analysis of the Oxi-CoNiFe took place after the oxidation procedure and before the wafers were processed further.

The oxygen content in Oxi-CoNiFe varied slightly (±1%) across the samples however unlike Oxi-NiFe, these fluctuations in percentages were most likely caused by the slight differences (±1%) in the composition of the AD CoNiFe across the wafer, rather than thickness differences. Table 18 and Fig 95 show the composition and spectrum of the Oxi-CoNiFe sample.

Element	Apparent Concentration	Weight %	Weight % Sigma	Atomic %
Cobalt	9.44	56.75	0.23	**41.06**
Iron	2.69	15.27	0.15	**11.66**
Nickel	2.37	14.08	0.19	**10.23**
Oxygen	3.64	13.9	0.16	**37.05**
Total:		100		100

Table 18 - EDX Analysis of Oxi-CoNiFe

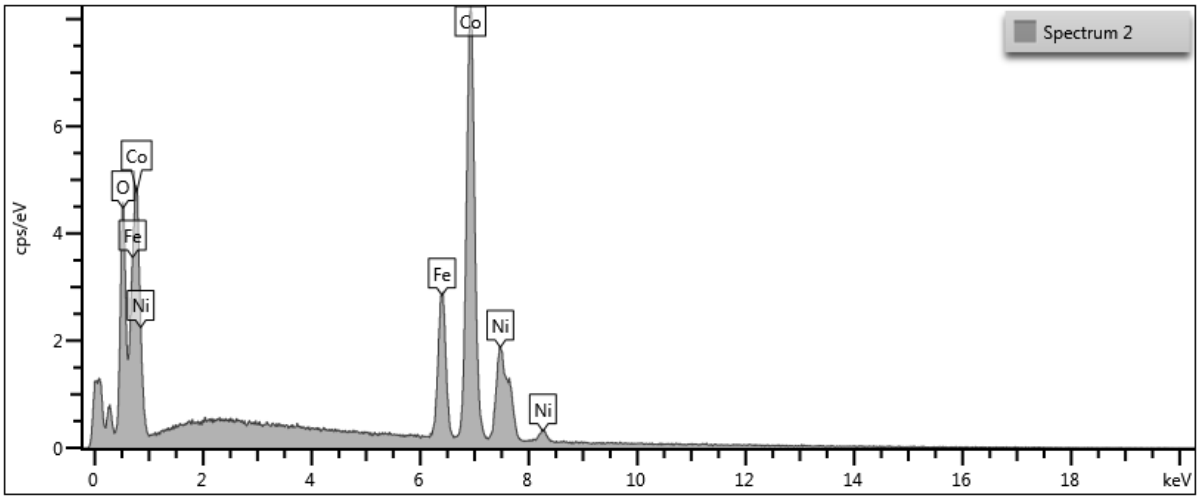


Figure 95 - EDX Spectrum of Oxi-CoNiFe

Mass Composition & Density Calculations:

AD CoNiFe:

The density of 100 g of AD CoNiFe was calculated to be 8.678 g.cm^{-3} using the weight percentage from the EDX and the density of the individual elements of the alloy, cobalt, iron & nickel.

$$\boldsymbol{Co}: \frac{\mathbf{64.12}\boldsymbol{g}}{\mathbf{8.900}\boldsymbol{g}.\boldsymbol{cm}^{-\mathbf{3}}} = \mathbf{7.204}\boldsymbol{cm}^{\mathbf{3}} \quad \boldsymbol{Fe}: \frac{\mathbf{19.83}\boldsymbol{g}}{\mathbf{7.874}\boldsymbol{g}.\boldsymbol{cm}^{-\mathbf{3}}} = \mathbf{2.518}\boldsymbol{cm}^{\mathbf{3}}$$

$$\boldsymbol{Ni}: \frac{\mathbf{16.05}\boldsymbol{g}}{\mathbf{8.908}\boldsymbol{g}.\boldsymbol{cm}^{-\mathbf{3}}} = \mathbf{1.802}\boldsymbol{cm}^{\mathbf{3}}$$

$$\boldsymbol{CoNiFe}: \mathbf{7.204}\boldsymbol{cm}^{\mathbf{3}} + \mathbf{2.518}\boldsymbol{cm}^{\mathbf{3}} + \mathbf{1.802}\boldsymbol{cm}^{\mathbf{3}} = \mathbf{11.524}\boldsymbol{cm}^{\mathbf{3}}$$

$$\boldsymbol{Density = \frac{100g}{11.524cm^3} = 8.678g.cm^{-3}}$$

Using the 3.3 µm thickness or height of the AD CoNiFe, and the approximate area of the 4" inch wafer (area of a circle) which is 81.07 cm^2, the volume of CoNiFe was calculated using the volume of a cylinder equation. The approximate volume was calculated as 2.676 x 10^{-2} cm^3.

$$\boldsymbol{Volume = \pi r^2 h = 3.142(25.806cm^2)(3.3x10^{-4}cm) = 2.676x10^{-2}cm^3}$$

Using the newly calculated volume and density, the mass of the as-deposited CoNiFe was calculated as 0.232 g. Furthermore, using the weight percentage of the cobalt, iron and nickel in the alloy, the mass of each element was also calculated.

$$\boldsymbol{Mass = DxV = 2.676x10^{-2}cm^3(8.678g.cm^{-3}) = 0.232g}$$

$$\boldsymbol{Co: 0.232g\left(\frac{64.12}{100}\right) = 0.149g \quad Fe: 0.232g\left(\frac{19.83}{100}\right) = 0.046g}$$

$$\boldsymbol{Ni: 0.232g\left(\frac{16.05}{100}\right) = 0.037g}$$

Oxi-CoNiFe:

Much like the Oxi-NiFe, the density of the Oxi-CoNiFe could be not be calculated due to the presence of oxygen, with an unknown density, but based on the porous nature of CoNiFe, its density was estimated to less than that of the oxidised compound.

Crystalline Structure - TEM:

TEM results show the crystalline structure of the AD & Oxi-CoNiFe materials. The crystalline structure of the CoNiFe was altered when the material was oxidised, moving from a predominantly nanocrystalline structure to that of a nanocrystalline/amorphous mixture.

The following TEM results are accompanied by selected area electron diffraction (SAED) images in order to calculate the crystalline nature of the material. Below are the TEM & SAED images of AD CoNiFe & As-Deposited CoNiFe. Single crystal grains & points of interest have been highlighted in red in the TEM images (Fig 96-100).

AD CoNiFe:

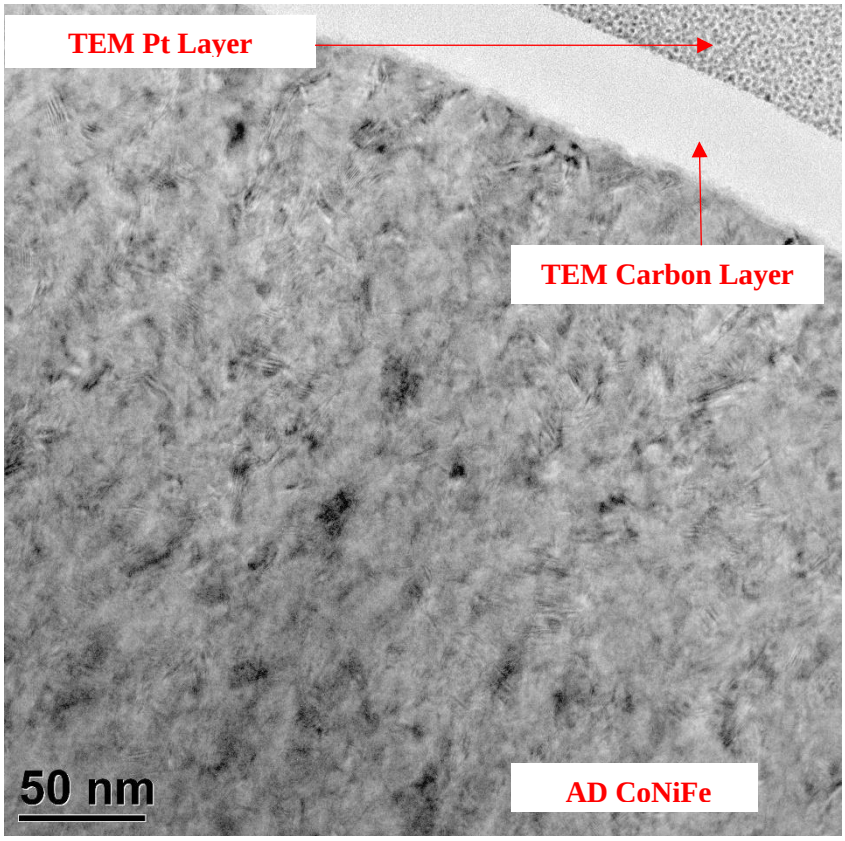


Figure 96 - Top surface of the AD CoNiFe & Pt / Carbon Layer

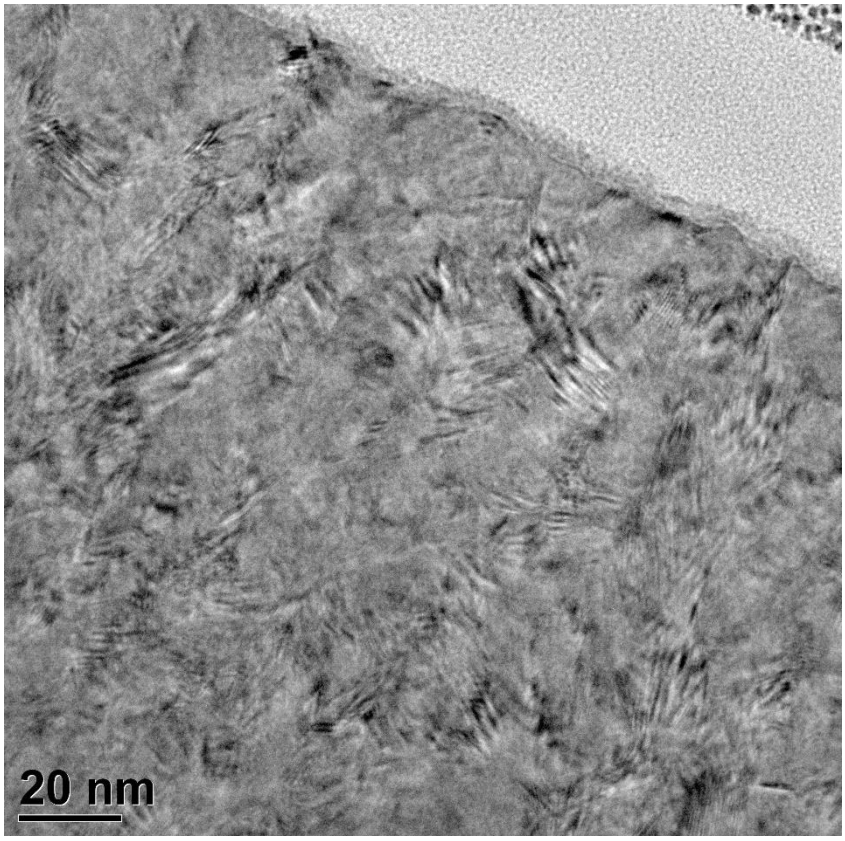


Figure 97 - 20nm scaling of the top surface of AD CoNiFe

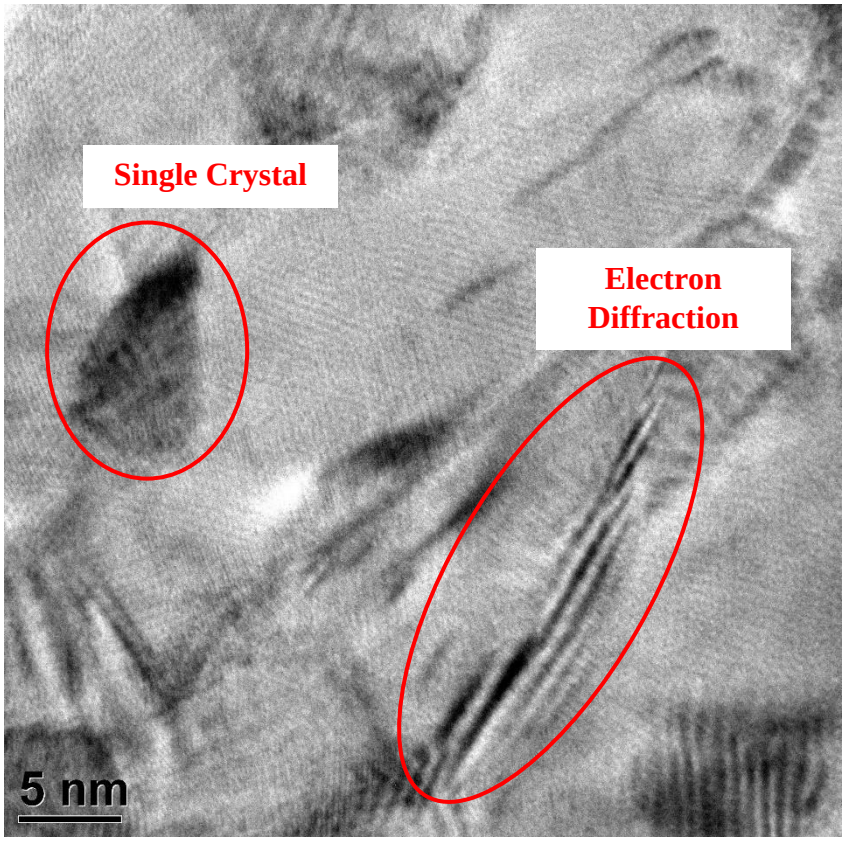


Figure 98 - Individual Grain of AD CoNiFe

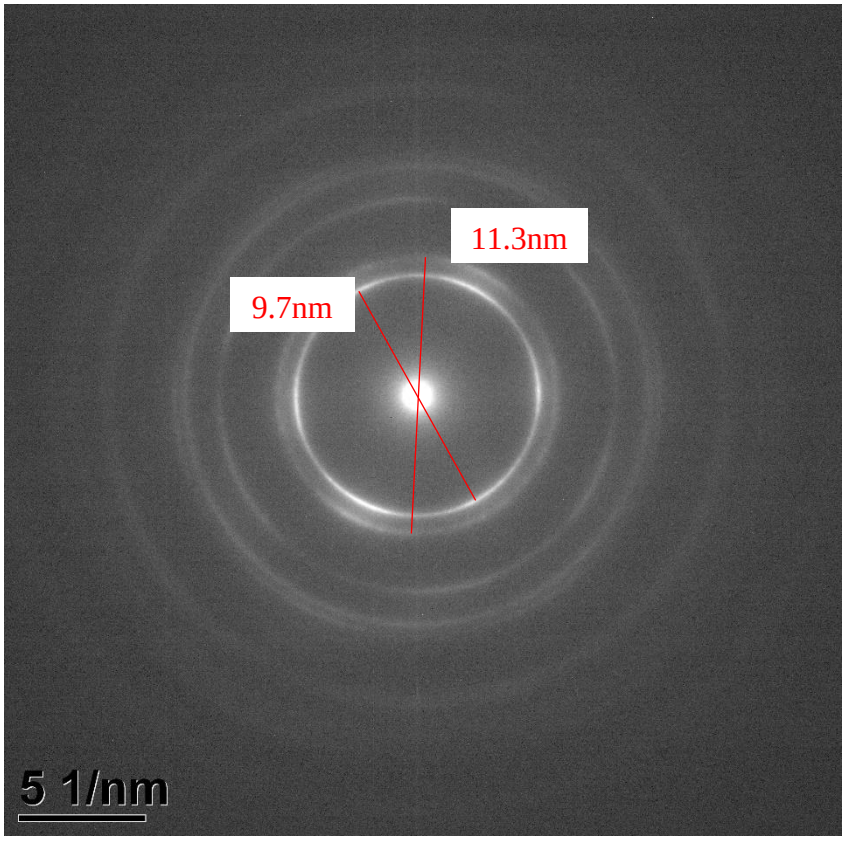


Figure 99 - SAED of AD CoNiFe

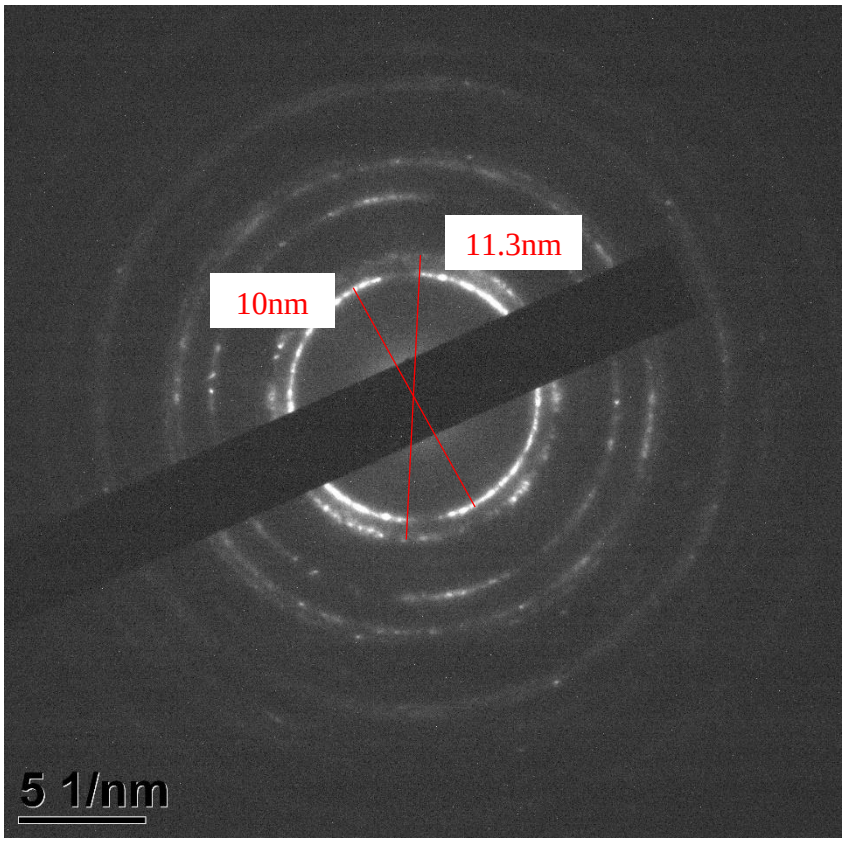


Figure 100 - SAED of AD CoNiFe with Selected area aperture

Electron diffraction refers to the wave nature of electrons as they scatter when impacting a solid material (crystals, molecules, atoms). The metal crystal lattice of the CoNiFe (or NiFe) material acts as a diffraction grating, scattering the electrons in a manner that helps identify the crystal lattice itself, as well as single crystals within the lattice.

While electron diffraction did occur in the CoNiFe sample, unlike NiFe, single grains were more pronounced and therefore easier to identify. Figures 96-97 shows the nano-polycrystalline structure of the material, including an individual grain as well as the electron diffraction patterning. The CoNiFe material also showed crystal twinning, with the average size of the crystal measured to be 5-20 nm (length & width).

The SAED images encompassed a 200 nm diameter wide area, and by scanning 50 nm deep, it was calculated that there were approximately 1-2 thousand crystals within the SAED. Based on the SAED images, the 9.7 nm & 11.3 nm diameter rings gave a d-spacing of 2.06 Å & 1.8 Å respectively. Using the X'PERT^3 and the d-spaces, the crystalline structure of CoNiFe was face-centred/body-centred cubic lattice mix (Fm-3m space group, O_h point group).

Oxi-CoNiFe:

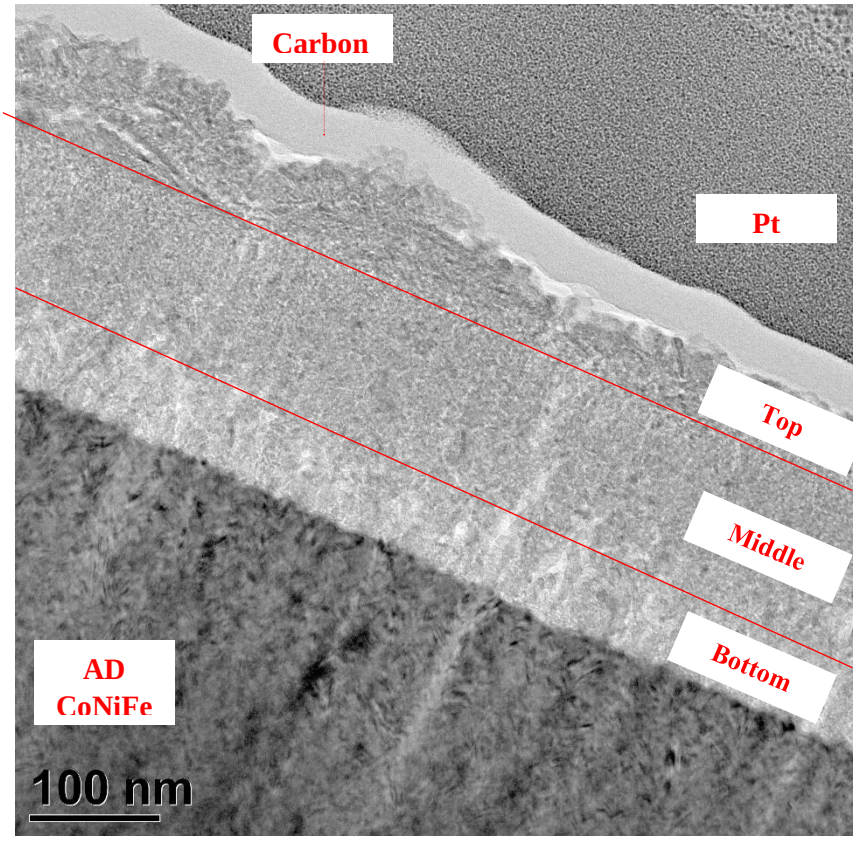


Figure 101 - 0.5µm Oxi-CoNiFe & its interphases between AD CoNiFe & TEM Pt / C Layers

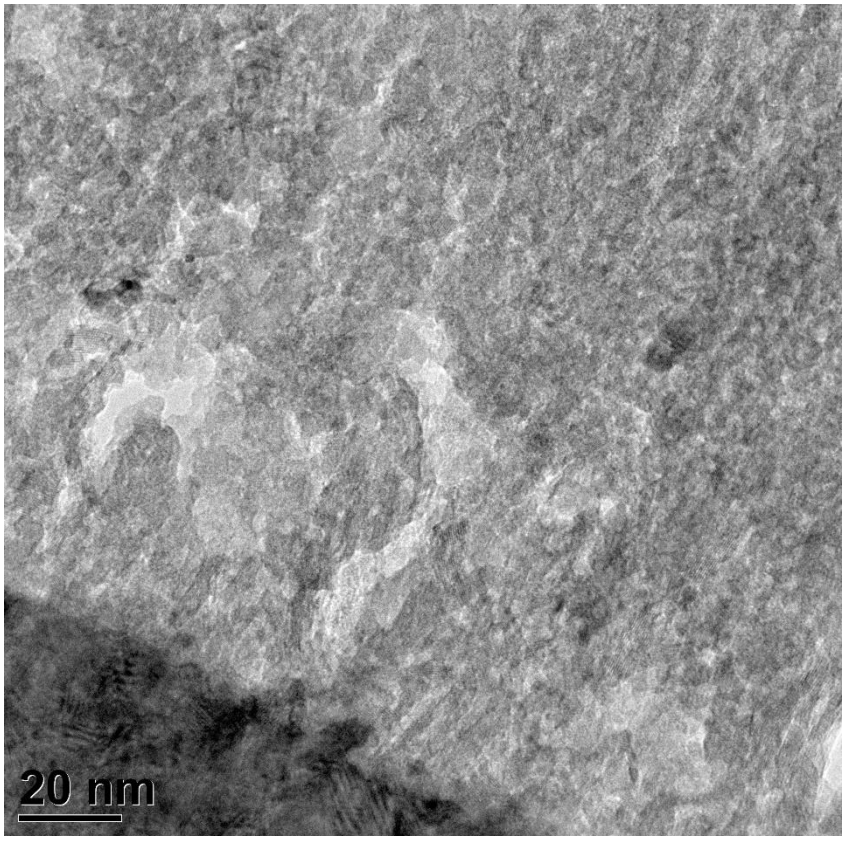


Figure 102 - Interphase between AD & Oxi-CoNiFe.

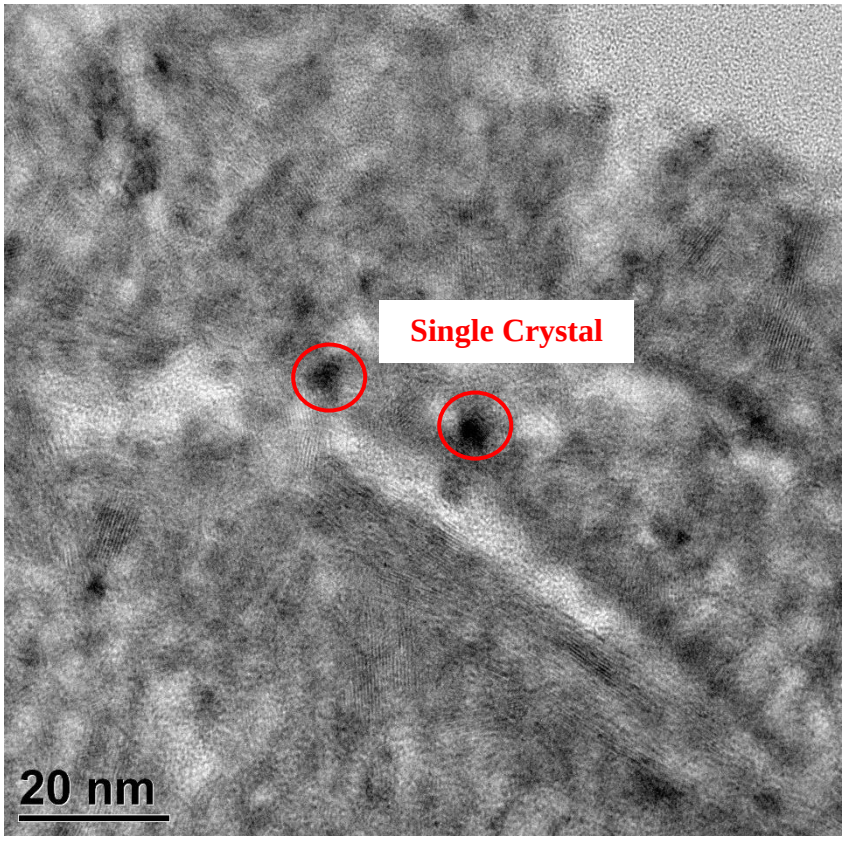


Figure 103 - Oxi-CoNiFe Grains

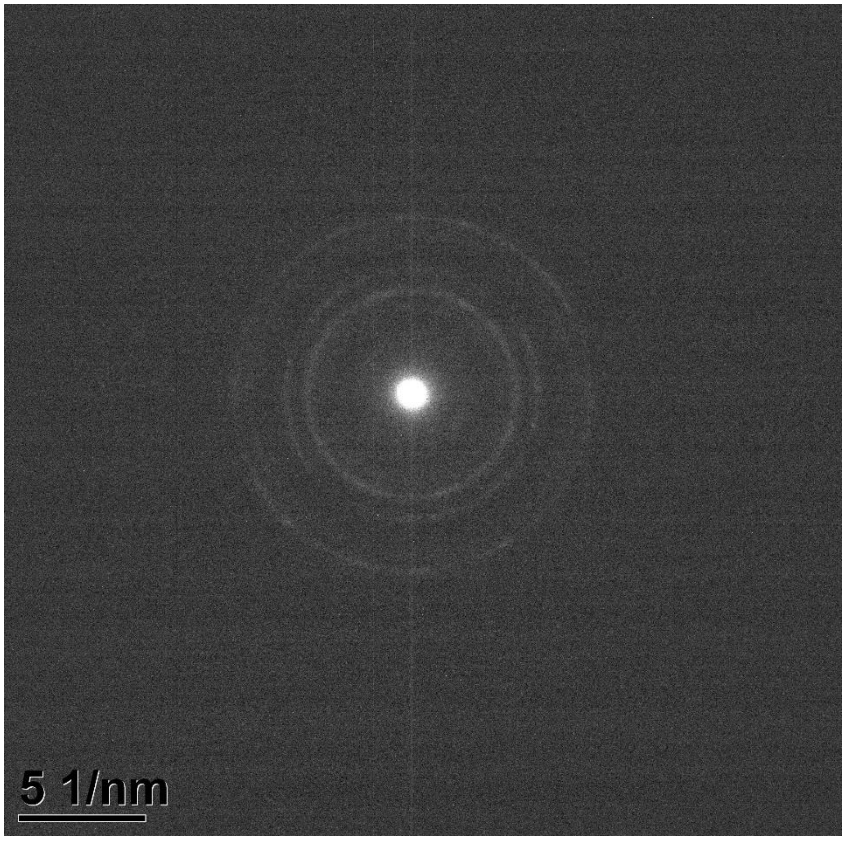


Figure 104 - SAED of Oxi-CoNiFe

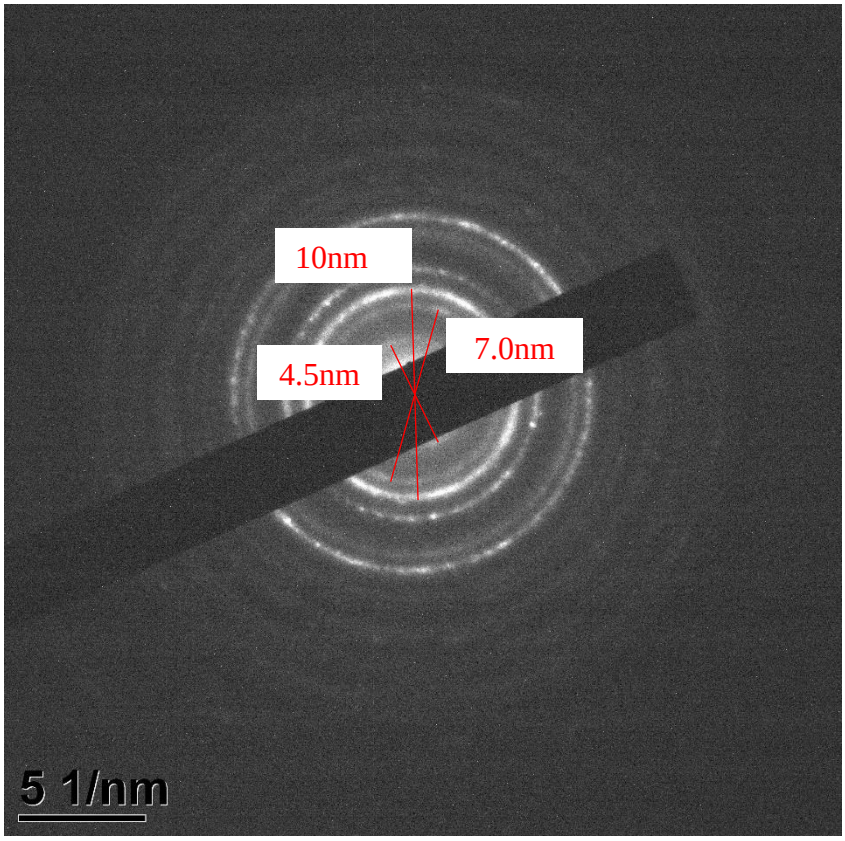


Figure 105 - SAED of CoNiFe with selected area aperture

Figure 101-102 shows the AD & Oxi-CoNiFe interface, along with the Pt/C TEM layers on top. From the image, the oxidised layer was measured to be 250 nm in thickness. Much like the NiFe, the 450 CV cycles did not fully oxidise the 3.3 μm sample; however, based on the increased chemical resistance of CoNiFe, it was expected that the material would require more cycling than NiFe.

Unlike Oxi-NiFe, the Oxi-CoNiFe layer shows three distinct crystal layers, with the crystals altering their orientation as the material moves away from the AD CoNiFe interface. At the bottom interface section, the crystals show a dendritic pattern, with long, thin crystals of 10nm length and 2nm width, in a vertical pattern. In the middle section of material, the crystals are dense and are believed to be changing orientation to the structures seen on the top section, which shows the long, thin crystals, now in a horizontal orientation, in distinct stacked layers.

This change in the structure of the crystals was believed to be due to stress. During crystal formation at the interphase, the newly formed crystals are most likely under stress, due to the proximity and connection to the AD CoNiFe crystals. This stress was alleviated as the interphases move down due to more of the CoNiFe being oxidised and new crystals forming. The original crystals, no longer in proximity with AD CoNiFe, begin to alter their orientation, as shown by the dense middle section before eventually reaching a level of minimum crystalline stress as the crystals now lay flat, as shown on the top section.

The porous nature of CoNiFe can be seen in Figure 100-102, with the presence of void holes. Figure 103 shows two single crystals in the middle section as they are changing orientation.

Using the SAED images (Fig. 104-105), the oxidised material was shown to be amorphous than the AD counterpart, with rings showing diffusion. However, the material does still show a predominant polycrystalline nature. In comparison to AD CoNiFe, the Oxi-CoNiFe's SAED shows two new rings before the 10nm ring (2Å d-spacing); a 4.5 nm & 7 nm ring, giving a d-spacing of 4.3 Å & 2.9 Å respectively. Using X'PERT[3] and the d-spaces, the crystalline structure was estimated to be an fcc/bcc cubic symmetry structure (Fd-3m space group, O_h point group), with the 4.3 Å & 2.9 Å d-space referring to a (111) & (220) crystal plane.

3.6.2 – CoNiFe Cores Magnetic Properties

Magnetic Saturation, Retentivity, Coercivity - BH Looper:

Magnetic testing of the AD & Oxi-CoNiFe wafers was completed using the MESA BH Looper. The CoNiFe samples were first created (As-Deposited Samples), tested using the BH Looper before being oxidised and tested once again. As stated, the oxidation process was hoped to increase (B_{Sat}) & (Hk) while decreasing (Br) and (Hc).

Table 19 shows these properties for the 1.5x1.5 cm^2 samples of 3.3 µm AD & Oxi-CoNiFe. These samples came from 4" wafers, which contained the Ti/NiFe seed layer, with CoNiFe electroplated onto it. Once the AD CoNiFe measurements were taken, the wafers were oxidised and measured again. The oxidised sample's values are highlighted in green and red, indicating an improvement or worsening of the properties respectively, in comparison to the As-deposited counterparts. Figure 106 & 107 show the hysteresis loops for the 1.5x1.5cm samples of AD & Oxi-CoNiFe.

Sample	Thickness (µm)	B_{Sat} (T)	Br (mT)	Hc (A/m)	Hk (A/m)
AD CoNiFe Sample A	3.3	1.65	54.61	31.47	1417.51
Oxi-CoNiFe Sample A	3.3	**1.52**	**69.02**	**28.80**	**1214.90**
AD CoNiFe Sample B	3.3	1.46	12.57	15.33	1206.92
Oxi-CoNiFe Sample B	3.3	**1.02**	**21.86**	**23.05**	**1245.21**
AD CoNiFe Sample C	3.3	1.56	43.35	28.31	1317.00
Oxi-CoNiFe Sample C	3.3	**1.33**	**52.51**	**38.54**	**1308.23**
AD CoNiFe Sample D	3.3	1.38	21.61	11.42	1373.64

Oxi-CoNiFe Sample D	3.3	**1.12**	**21.24**	**20.32**	**1161.45**
AD CoNiFe Sample E	3.3	1.58	15.82	13.09	1370.45
Oxi-CoNiFe Sample E	3.3	**1.15**	**40.78**	**24.02**	**1085.67**
Average AD CoNiFe	**3.3**	**1.56**	**29.592**	**19.924**	**1337.104**
Average Oxi-CoNiFe	**3.3**	**1.228**	**41.082**	**26.946**	**1203.092**

Table 19 - NiFe BH Looper results - Sample A = 1.5x1.5cm square - Sample B = 4-inch wafer - Sample C = 4-inch wafer

Table 20 below is a small summary table showing the average results for the Oxidised versions of the CoNiFe material. The up and down arrows show whether the magnetic properties in Table 20 have, on average, increased or decreased after oxidation. The colouration of these arrows indicates whether the increase or decrease was an improvement (green) or diminishing (red) of the property. Further to this, the table also shows the average percentage increase/decrease in the Oxidised sample's properties in comparison to the As-deposited (AD) counterpart.

Material Properties	*Oxidised Material*	*% Increase (+) OR Decrease (-)*
Thickness	-	-
Saturation Flux Density	↓	**-19.5%**
Retentivity	↓	**+39%**
Coercivity	↑	**+35%**
Anisotropic Field	↓	**-10%**

Table 20 - % Increase / Decrease in the properties of Oxi-CoNiFe in comparison to AD CoNiFe.

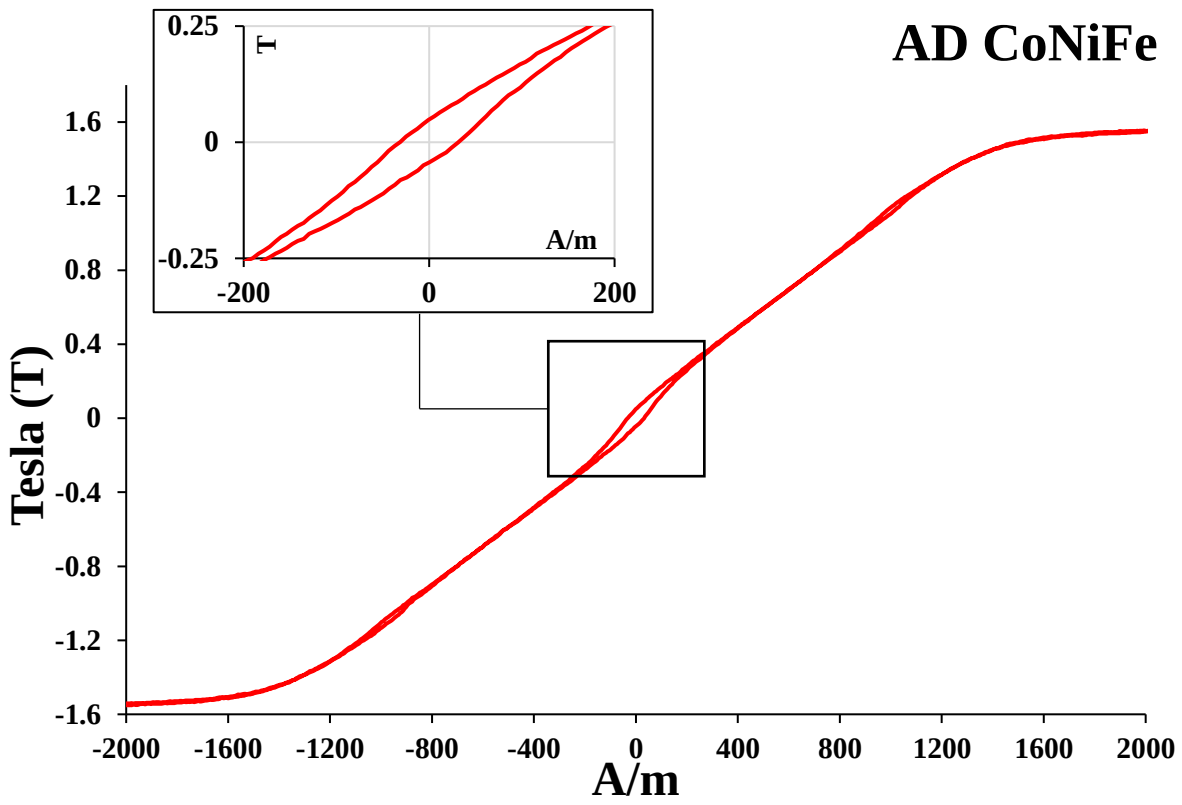


Figure 106 - Hysteresis Loop of 1.5cm x 1.5cm sample of AD CoNiFe

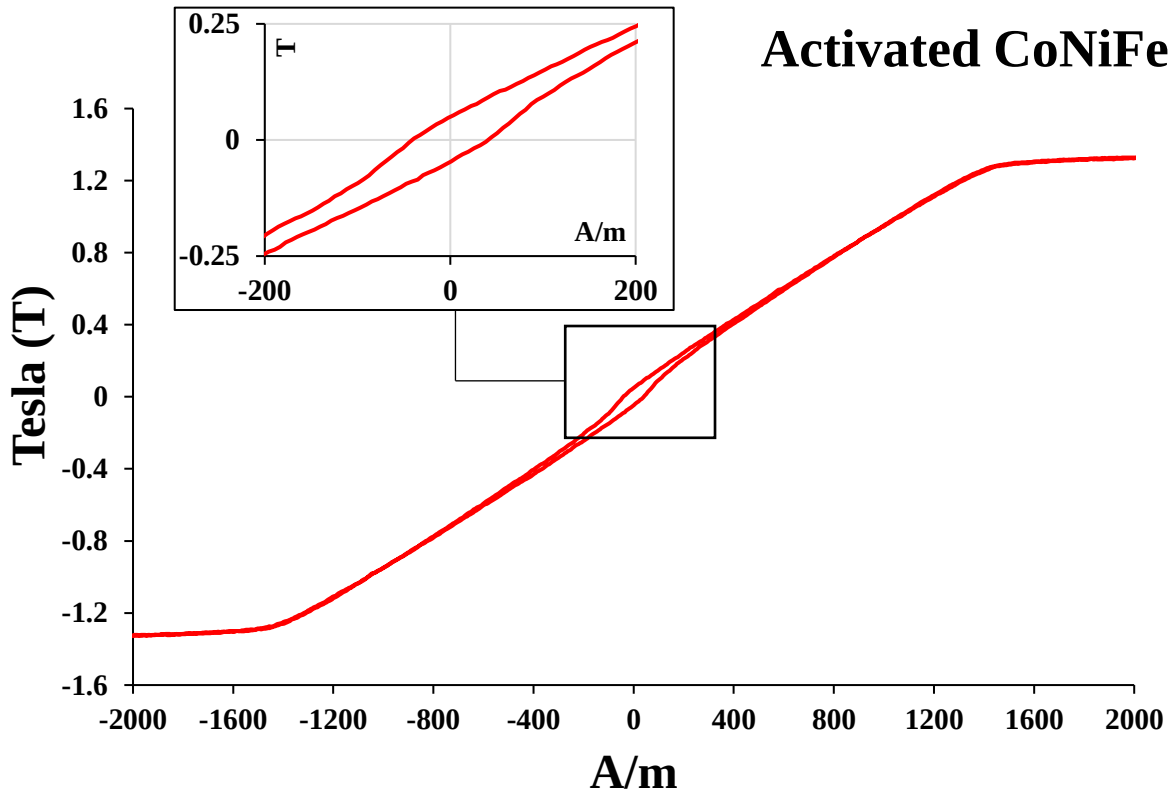


Figure 107 - Hysteresis Loop of 1.5cm x 1.5cm sample of Oxi-CoNiFe

As shown by the results, unlike the NiFe, the oxidation process seemed to diminish the magnetic properties of CoNiFe. Starting with magnetic saturation, Oxi-CoNiFe saw a near -20% decrease, much like NiFe (-18%).

However, both retentivity & coercivity saw an increase of >30%, which shows that the material was withholding its magnetic field after the external field was removed and requires more energy to remove the material's field. Overall, this shows that the CoNiFe has lost some of its soft magnetic capabilities after oxidation. The anisotropy field of CoNiFe also saw a -10% decrease once oxidised, reducing the external magnetic field strength required to saturate the material. These results can be used to estimate that the material's permeability & devices inductance / Q-factor will also see diminished results in comparison to the AD CoNiFe.

Permeability - Permeameter:

The permeability of seven, 3.3 µm thick, and 1.5x1.5 cm sized samples of AD & Oxi-CoNiFe were measured. The relative (**μ_r**), real (**μ_r'**) & imaginary (**μ_r''**) permeabilities are listed below in Table 21, along with the material's **Q-Factor** & loss tangent (**tan(δ)**). The median was calculated due to the outliers in the results. The percentage increase/decrease was also calculated between the As-Deposited & Oxidised samples. Standard deviation (STD%) was calculated based on the median results.

Much like NiFe after oxidation, the permeability's of CoNiFe also saw a decrease, which on its own, is considered to be negative. However, when calculating the Q-Factors of the AD & Oxi-CoNiFe, there was an improvement, with an average 15% increase. The loss tangent also saw an improvement, with a -13% average decrease. This shows that the material was more efficient with its overall permeability, despite the decline, and that the material loses less electromagnetic energy. Based on this, the AC Resistance of a device should see an improvement.

However, despite these improvements, the overall device takes into consideration all the magnetic and electrical properties of the device. With this in mind, it is possible that despite the improvements seen in the permeability results, they are unable to outweigh the substantial diminished results of the magnetic properties, leading to an overall diminished result for the overall device.

Sample Type	Sample Number	μr 10 MHz	μr' 10 MHz	μr'' 10 MHz	Q-Factor @ 10MHz	tan(δ) 10 MHz
As-Deposited CoNiFe	1	684.1	666.9	152.2	4.383	0.2281
	2	667.2	656.4	119.1	5.514	0.1814
	3	644.5	633.5	118.7	5.339	0.1873
	4	682.2	667.9	138.9	4.808	0.2080
	5	680.7	666.8	137.1	4.864	0.2056
	6	684.5	670.1	139.3	4.810	0.2079
	7	677.6	665.2	129.3	5.145	0.1944
	Median	**680.7**	**666.8**	**137.1**	**4.864**	**0.2056**
	Average	**674.4**	**661.0**	**133.5**	**4.980**	**0.2018**
	STD %	**2.1**	**1.9**	**8.8**	**7.8**	**7.6**
Oxidised CoNiFe	1	656.2	643.1	130.2	4.939	0.2025
	2	677.6	666.8	120.7	5.525	0.1810
	3	609.7	602.0	96.6	6.235	0.1604
	4	652.2	641.5	117.6	5.455	0.1833
	5	666.6	653.7	130.2	5.020	0.1992
	6	625.1	618.1	92.8	6.664	0.1501
	7	619.8	612.2	96.6	6.339	0.1578
	Median	**652.2**	**641.5**	**117.6**	**5.525**	**0.1810**
	Average	**643.9**	**633.9**	**112.1**	**5.740**	**0.1763**
	STD %	**3.9**	**3.7**	**14.0**	**12.2**	**11.4**
% Increase / Decrease Δ (Oxidised – Non-Oxidised)	**Median**	**-4.20%**	**-3.80%**	**-14.21%**	**+13.79%**	**-11.96%**
% Increase / Decrease Δ (Oxidised – Non-Oxidised)	**Average**	**-4.53%**	**-4.10%**	**-16.04%**	**+15.26%**	**-12.64%**
Improvement / Worsening		↓	↓	↓	↑	↓

Table 21 - Relative, Real & Imaginary Permeability & Loss Tangent of AD & Oxi-CoNiFe.

3.6.3 – CoNiFe Devices Properties

As with the NiFe materials, each of the four inductor designs (MS1, MS2, MC1, MC2) were produced on the AD CoNiFe & Oxi-CoNiFe device wafer. Each device was tested and a comparison made between the core materials in each device. Peak efficiency was found to be at 10 MHz; therefore, all electrical parameters were considered at such.

In general, it was believed that the oxidation process should: decrease AC resistance of the device, causing lower core loss, increase the inductance of the devices & combined increase the Q-Factor of the overall device. Below in Figures 108-119 show the inductance, AC resistance & Q-Factor of each of the four designs for both the AD NiFe (Non-Active W24) and Oxi Cores (Active W25). It should be noted that W24 and W25 simply refer to the test number that was assigned by the device probe and were never removed in error. Table 23 shows the overall results for each design for both CoNiFe materials.

CoNiFe MS1 Inductor:

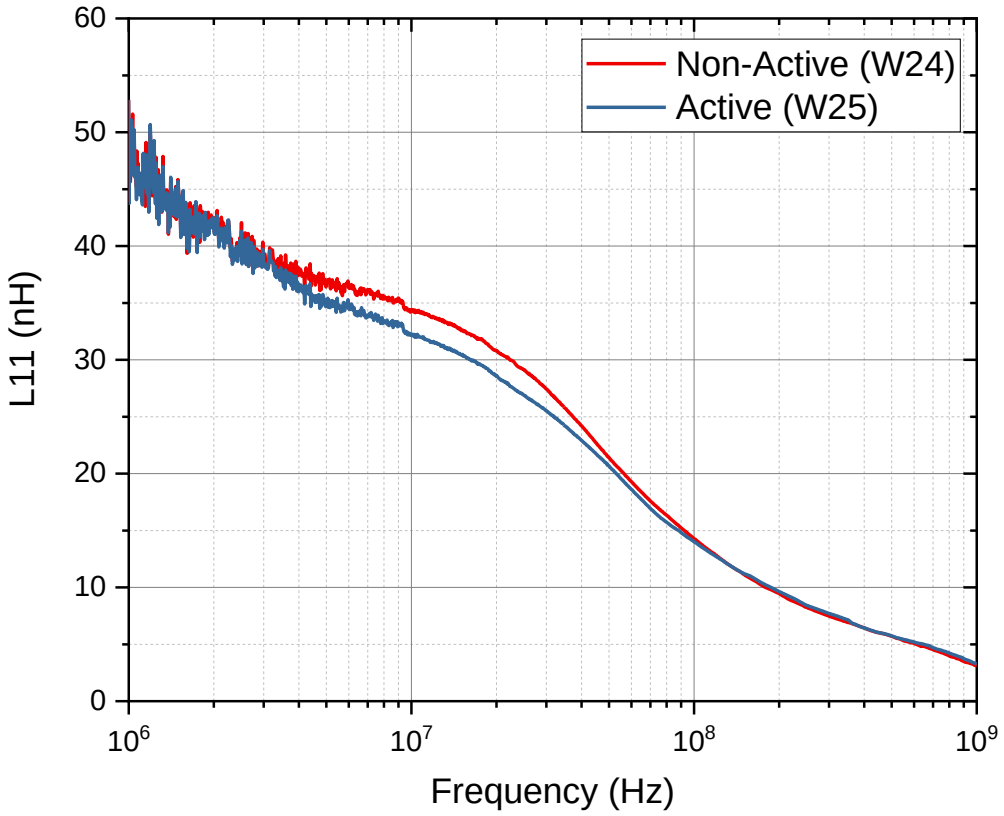


Figure 108 - Inductance of CoNiFe MS1 Inductor Devices

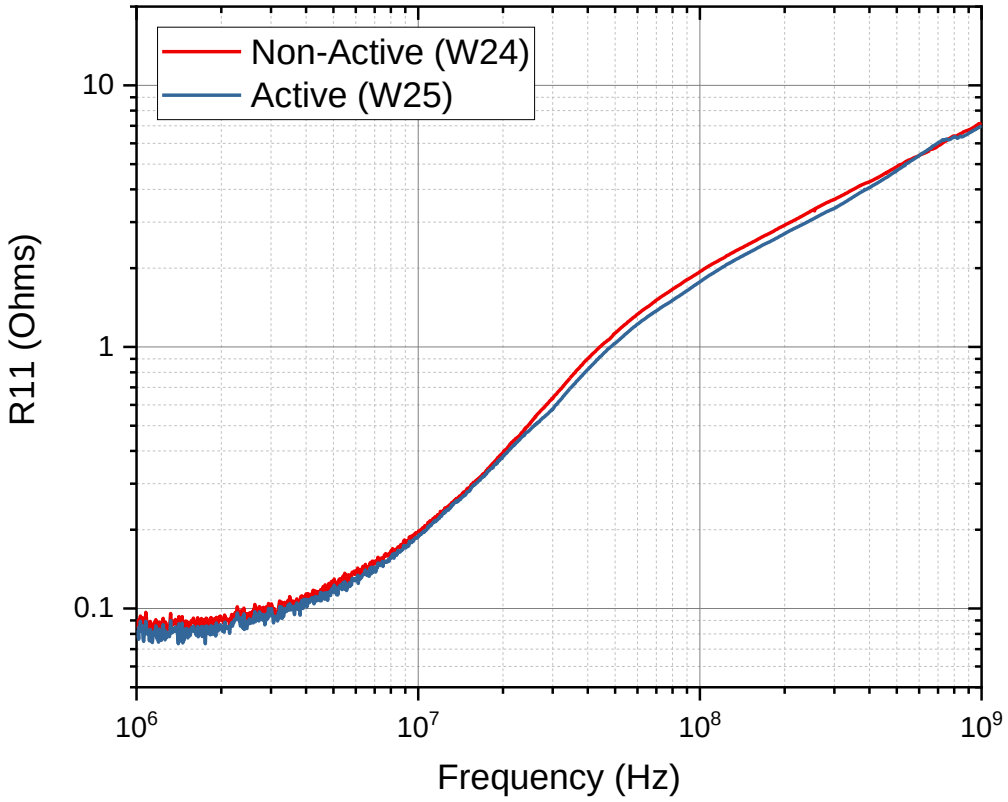


Figure 109 - AC Resistance of CoNiFe MS1 Inductor Devices

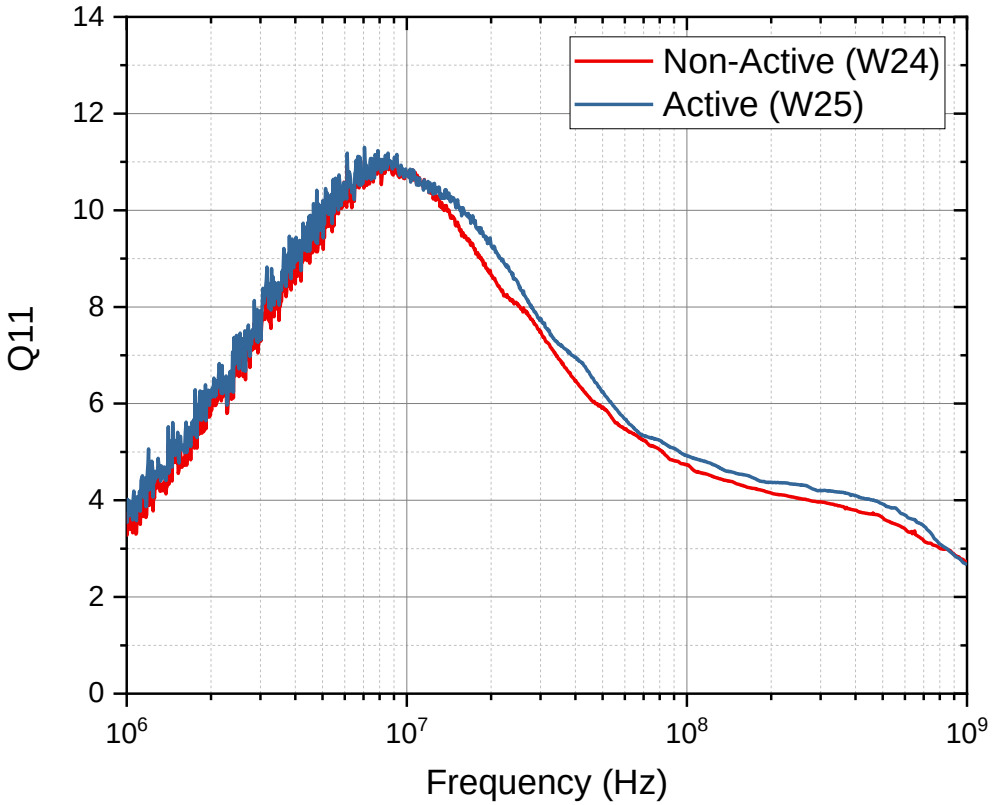


Figure 110 - Q-Factor of CoNiFe MS1 Inductor Devices

CoNiFe MS2 Inductor:

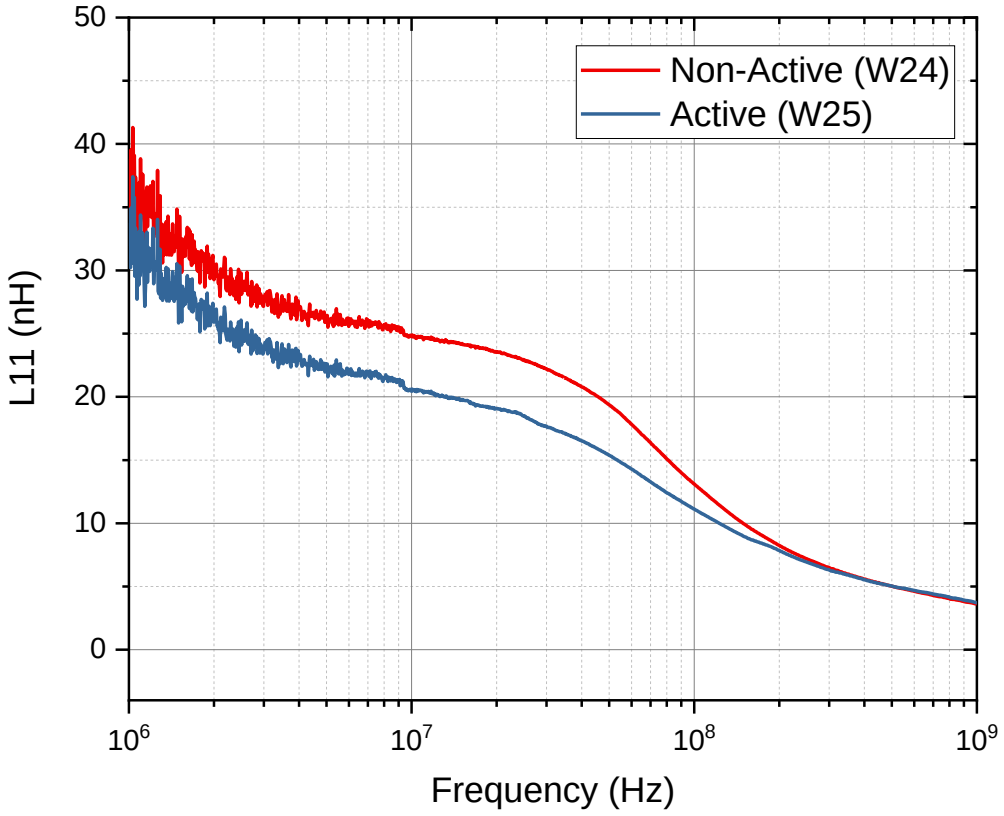


Figure 111 - Inductance of CoNiFe MS2 Inductor Devices

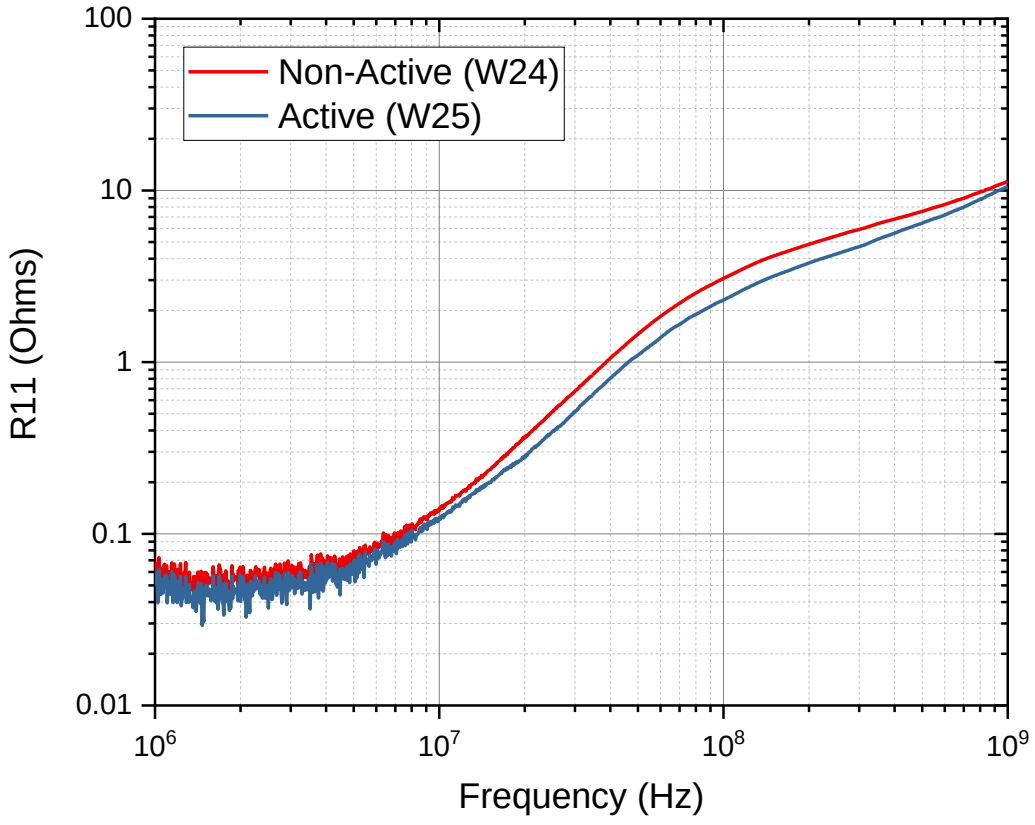


Figure 112 - AC Resistance of CoNiFe MS2 Inductor Devices

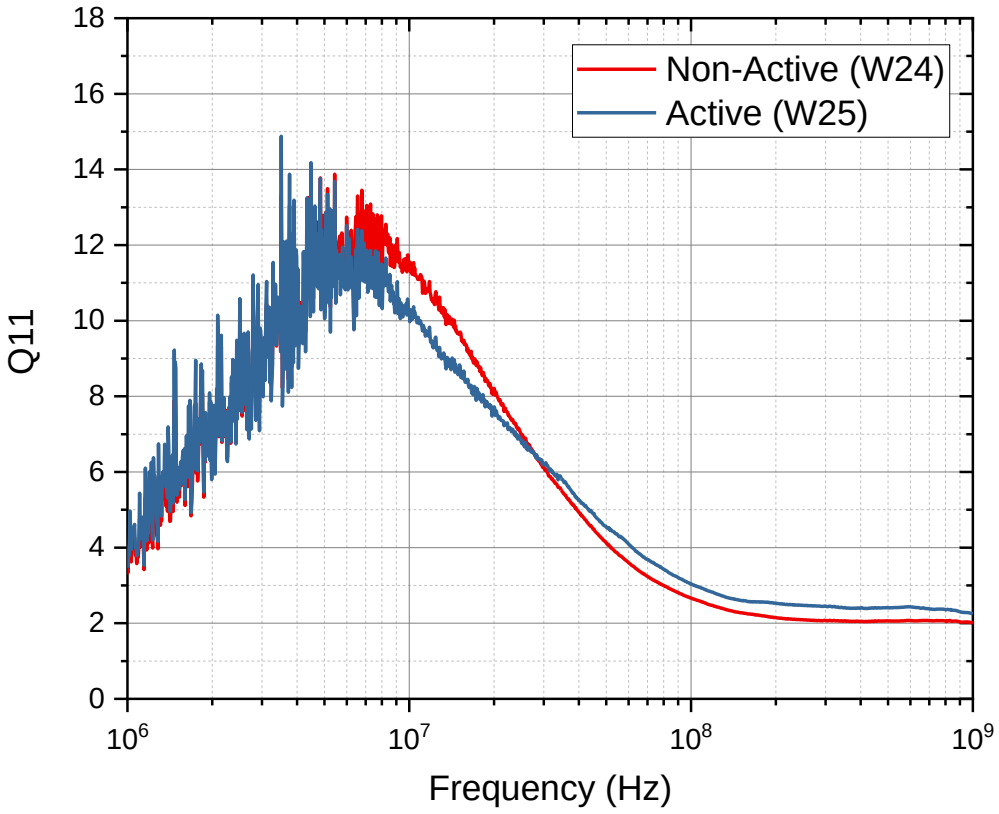


Figure 113 - Q-Factor of CoNiFe MS2 Inductor Devices

CoNiFe MC1 Inductor:

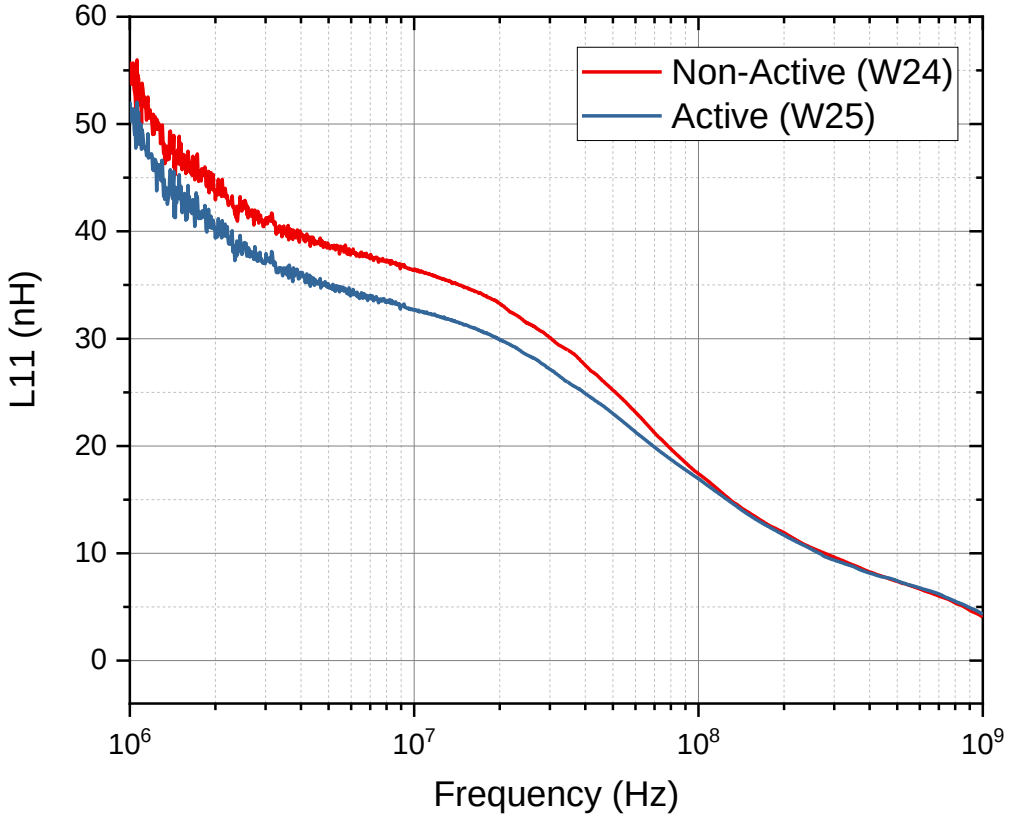


Figure 114 - Inductance of CoNiFe MC1 Inductor Devices

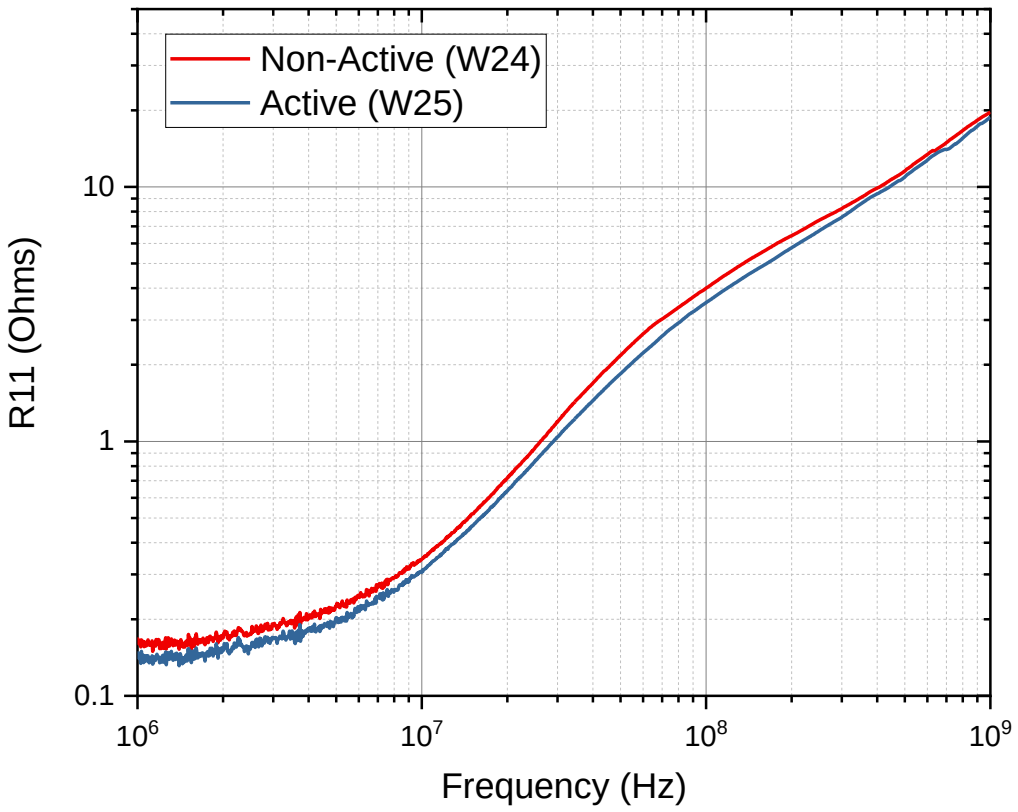


Figure 115 - AC Resistance of CoNiFe MC1 Inductor Devices

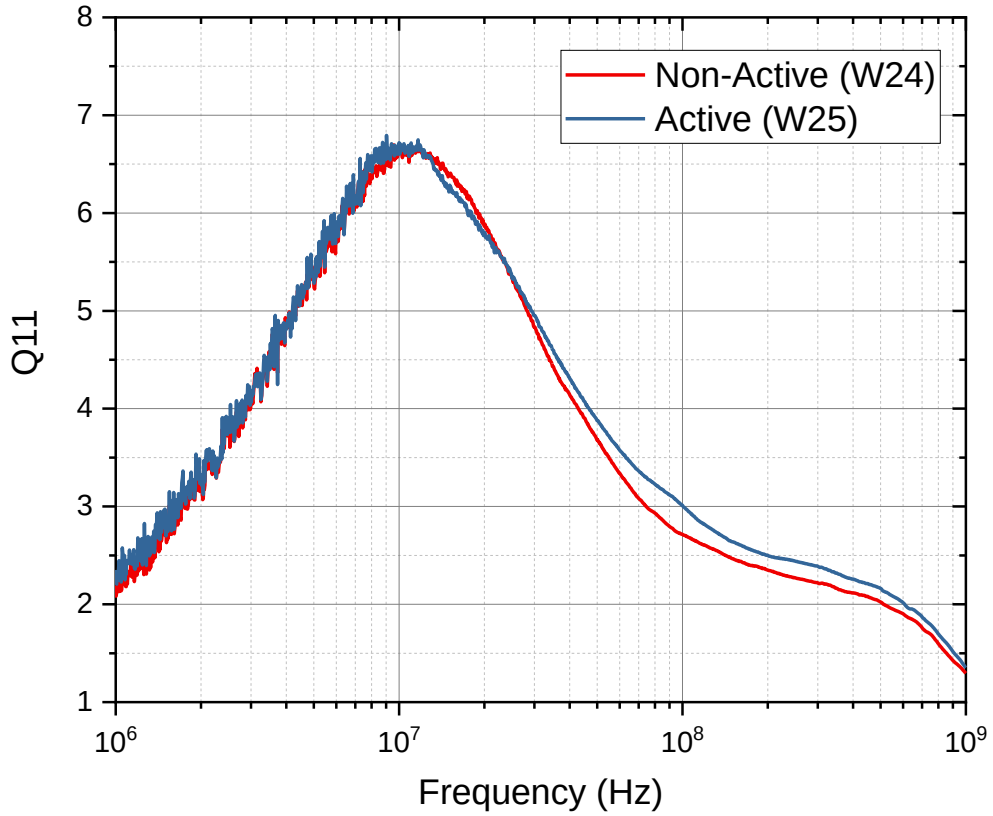


Figure 116 - Q-Factor of CoNiFe MC1 Inductor Devices

CoNiFe MC2 Inductor:

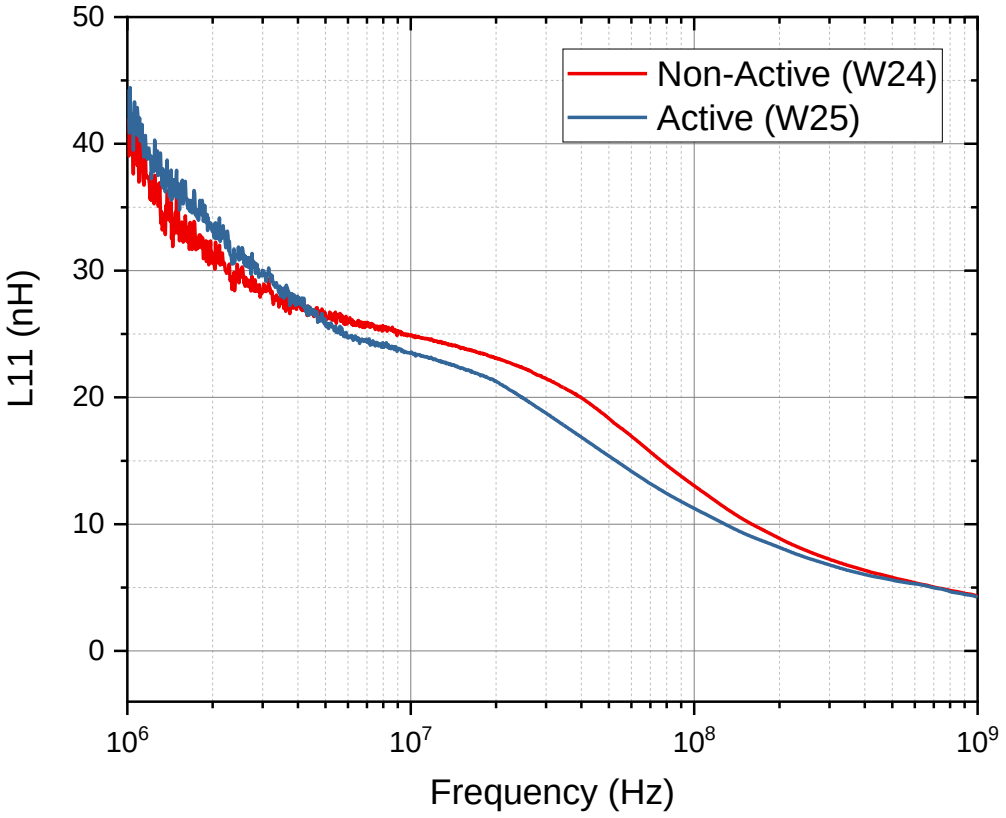


Figure 117 - Figure 116 - Inductance of CoNiFe MC2 Inductor Devices

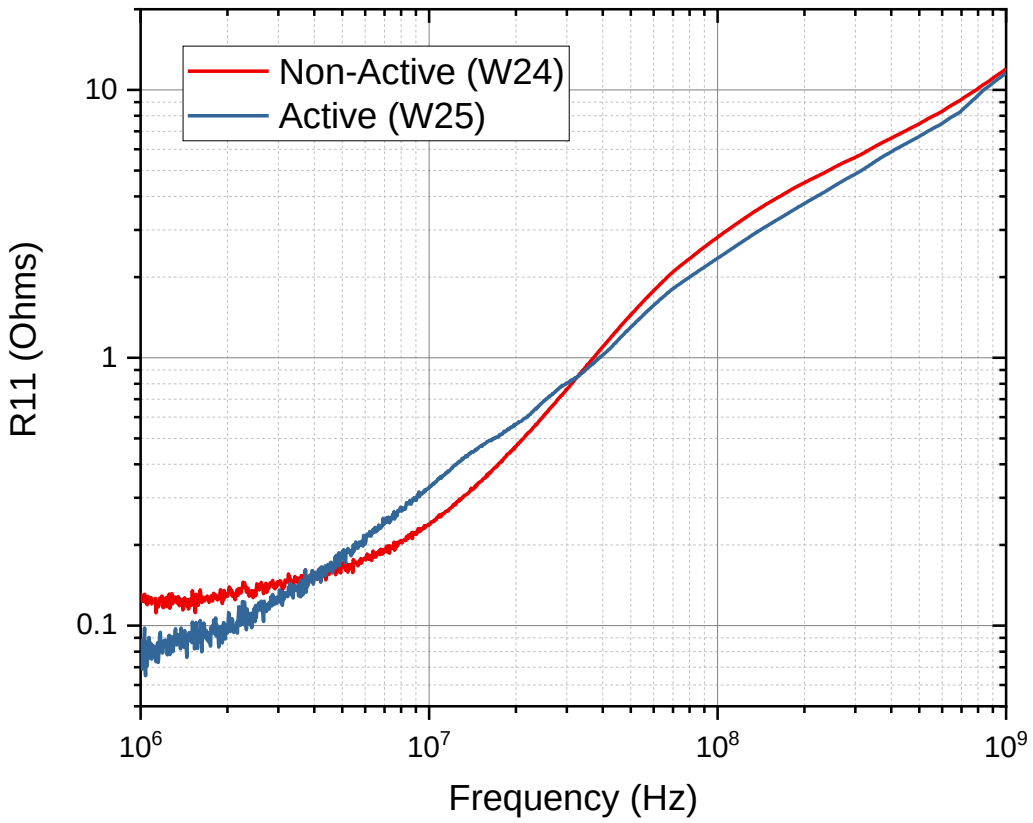


Figure 118 - AC Resistance of CoNiFe MC2 Inductor Devices

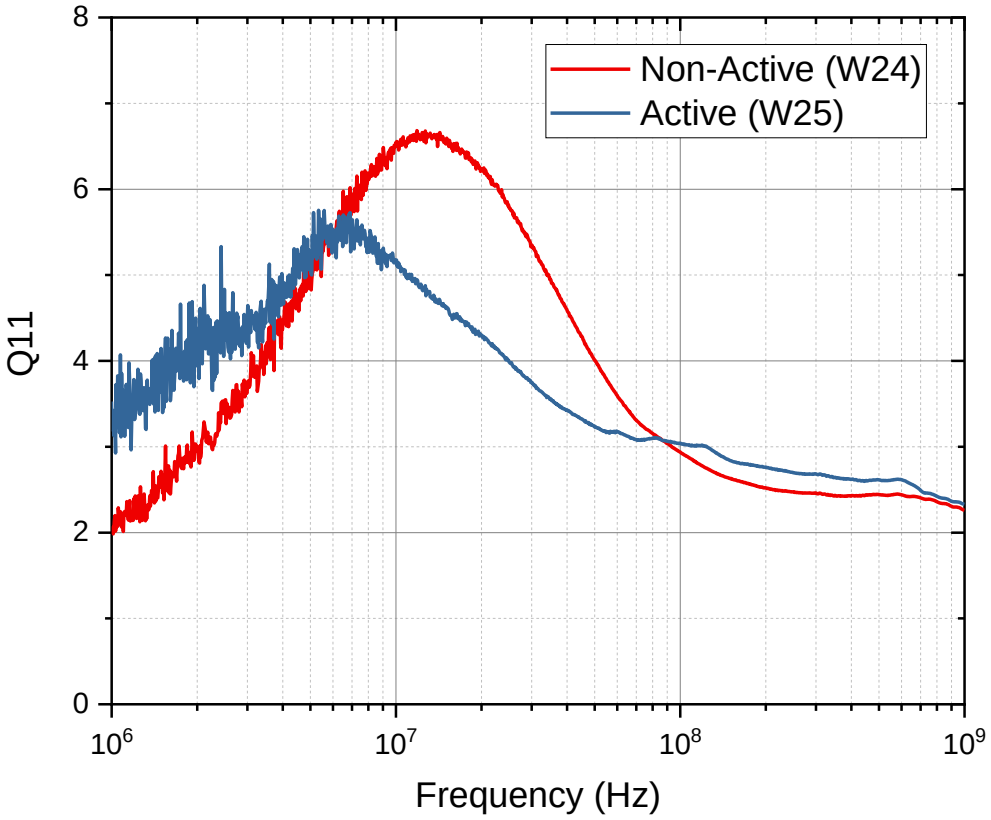


Figure 119 - Q-Factor of CoNiFe MC2 Inductor Devices

Total Results:

Type	Property	MS1	MS2	MC1	MC2	Average
Non-Oxidised CoNiFe	L11 (nH)	34.40	24.89	36.50	24.94	30.18
	R11 (Ω)	0.20	0.14	0.35	0.24	0.23
	Q11	10.75	11.32	6.63	6.50	8.8
Oxidised CoNiFe	L11 (nH)	32.23	20.62	32.71	23.58	27.29
	R11 (Ω)	0.19	0.13	0.31	0.33	0.24
	Q11	10.70	9.97	6.60	5.18	8.11
% Increase Δ (Oxidised – Non-Oxi)	L11 (nH)	-6.31	-17.14	-10.37	-5.46	-9.82
	R11 (Ω)	-3.62	-11.48	-10.69	37.93	3.04
	Q11	-0.40	-11.90	-0.42	-20.40	-8.28
Improvement or Worsening	L11 (nH)	↓	↓	↓	↓	↓
	R11 (Ω)	↓	↓	↓	↑	↓
	Q11	↓	↓	↓	↓	↓

Table 22 - Inductance, AC Resistance & Q-Factor of the MS1, MS2, MC1 & MC2 devices with AD CoNiFe & Oxi-CoNiFe

Discussion:

Despite the improvements in the permeability results (material's Q-Factor & loss tangent), as expected the overall device result, the device's Q-Factor was diminished by an average decrease of -8% once the CoNiFe was oxidised. It should be noted that these results saw a large amount of variability depending on the device.

The devices inductance saw an average decrease of -10%, which was expected based on the magnetic results of the CoNiFe materials. The range of inductance decrease was from -5% to -20%. The average AC resistance, as expected, saw an increase, though minor, of 3%. However, the AC resistance range was quite substantial. For instance, MC2's AC resistance was diminished, with huge +38% increase, a significant outlier in comparison to the other devices which saw an improvement, with a decrease between -3% to -12%. MC2 saw the most considerable AC resistance improvement, with a -12% decrease.

For Q-factor, its range was also broad. MS1 & MC1 saw an average -0.40% decrease, showing near no improvement once oxidised. MC2 saw the most significant reduction at -20%, as expected based on its AC resistance, while MS2 saw a -12% decrease, despite the largest AC resistance improvement.

Comparing the oxidation of NiFe to CoNiFe, it is estimated that the change in the composition of Ni and Fe in both materials to metal oxides/hydroxides is based on percentage ratio. These composition changes assume that all the metal in each material fully oxidised, and the EDX did not detect unreacted CoNiFe or NiFe. Despite not all of the NiFe / CoNiFe reacting to form oxidised forms, the EDX for Oxi-NiFe & Oxi-CoNiFe is assumed to only have detected the top layer of the core material, i.e. the oxidised versions of the metal.

In NiFe, nickel saw a ~64% composition conversion, from 45.34% Ni in AD NiFe to 28.95% in Oxi-NiFe. Iron saw a ~57% conversion, from 54.66% Fe in AD NiFe to 31.37% in Oxi-NiFe. For CoNiFe, despite the decreased iron and nickel content, this percentage conversion remains the same, with nickel seeing a ~64% conversion, from 15.92% in AD CoNiFe to 10.23% in Oxi-CoNiFe. Iron saw a ~56% conversion, from 20.69% in AD CoNiFe to11.66% in Oxi-NiFe. Cobalt saw a ~65% conversion, from 63.39% in AD to 41.06% Oxi-CoNiFe.

Assuming full conversion of cobalt, iron and nickel to oxidised material, this would still lead to the conclusion that Oxi-CoNiFe would have less nickel & iron oxides than Oxi-NiFe. The diminished results for Oxi-CoNiFe is therefore believed to have been caused by the decreased content of nickel and iron hydro/oxides and the formation of cobalt oxides, many of which are antiferromagnetic.

Co_3O_4 shows extremely unfavourable antiferromagnetic properties, with a high coercivity and a low squareness ratio (M_r/M_s). CoO also shows antiferromagnetic properties [133, 134]. Co_2O_3 is the only cobalt oxide produced once the CoNiFe was oxidised that can be considered to be ferromagnetic. This oxide has been shown to improve the magnetic properties of multiple ceramics. [135, 136]

It is therefore believed that an alternative CoNiFe alloy; one with a high iron and nickel content in comparison to cobalt, i.e. $Co_{\leq 20}Fe_{\geq 40}Ni_{\geq 40}$ could show the improved magnetic and electrical properties as seen in Oxi-NiFe, while still maintaining enough cobalt to increase the alloys corrosion resistance and working frequency.

The large variations in device results could have been caused by the core. The large standard deviations in the permeability results indicate variations in the thickness of the core material; either in terms of the electroplated material thickness or the oxidation layer thickness. Based on the complexity of the Oxi-CoNiFe, in terms of it having multiple layers as seen by the TEM, it stands to reason that certain areas may have had differing thicknesses or crystal structure. It can be deduced that areas with less Oxidised CoNiFe would perform better based on the lack of antiferromagnetic cobalt oxides.

3.7 – Summary of Results

	As-Deposited NiFe	Oxidised NiFe	As-Deposited CoNiFe	Oxidised CoNiFe
Core Composition Properties				
Cobalt	-	-	63.39	41.06
Nickel	45.34	28.95	15.92	10.23
Iron	54.66	31.37	20.69	11.66
Oxygen	-	39.68	-	37.05
Predominant Crystalline Structure	Poly-Nanocrystalline	Amophorous	Poly-Nanocrystalline	Poly-Nanocrystalline
Colouration	Silver	Red-Brown	Silver	Red-Green
Magnetic Core Properties				
B_{sat} (T)	1.57	1.29	1.56	1.23
B_r (mT)	104.50	65.88	29.59	41.08
H_c (A/m)	48.74	38.20	19.92	26.95
H_k (A/m)	738.95	776.36	1337.10	1203.09
Relative Permeability	840.94	739.34	674.40	643.87
Real Permeability	830.21	734.97	660.97	633.90
Imaginary Permeability	133.78	79.99	133.49	112.08
Materials Q-Factor	6.21	9.31	4.98	5.74
Loss Tangent	0.1611	0.1080	0.2018	0.1763
Device Properties				
Frequency (MHz)	4	4	10	10
L (nH)	54.67	59.39	30.18	27.29
R (Ω)	0.28	0.22	0.23	0.24
Devices Q-Factor	4.75	6.4	8.8	8.11

Table 23 - Total Composition, Magnetic Core & Device Results for AD & Oxi-NiFe & CoNiFe

Chapter 4 - Conclusion

This research led to the fabrication of micro-inductor at the wafer level, with each wafer containing four different inductor designs (MC1, MC2, MS1, MS2). These devices contained an electrodeposited (and possibly oxidised) magnetic material as a core, wrapped in an electrically conductive material (copper) to create the electrical windings. Depending on the design, the device saw seven to nine 140-380 µm thick copper windings wrap a 3.4-6.7 mm^2 3.3 µm thick magnetic core, all within an ~9-15 mm^2 area. These devices were imaged via SEM, 3-D X-Ray, light microscope and via a standard camera throughout the build process to show the detailed fabrication and intricacy of the devices. Each wafer contained over 400 fully operational devices which were then separated and individually tested. The four wafers differed in the magnetic material that was deposited and used as the core for the devices. These materials were NiFe, Oxidised NiFe, CoNiFe and Oxidised CoNiFe.

$Ni_{45}Fe_{55}$ was electroplated onto two wafers using a freshly prepared Tyndall in-house bath. With the use of dummy wafers to calculate plating rates, the required 3.3 µm of the material was electrodeposited. When tested, this NiFe material showed a B_{sat} of ~1.57 T, a B_r of ~105 mT a H_c of ~49 A/m, a H_k of ~739 A/m, a relative permeability of ~841, a loss tangent of 0.1611 and an overall material Q-Factor of 6.21. Once entirely fabricated, these NiFe devices were also tested and showed an inductance of ~55 nH, an AC resistance of 0.28 Ω and overall device Q-Factor of 4.75.

This oxidation process saw the NiFe's magnetic and electrical properties improve, leading to devices using the Oxi-NiFe performing significantly better when compared to the original as-deposited version. The Oxi-NiFe material had an 18% drop in B_{sat}; however, the retentivity, coercivity and anisotropic field of the material had an ~37%, ~22% and ~5% improvement, respectively. This lead to an overall improvement of the NiFe device, with the Oxi-NiFe device's inductance, AC resistance and Q-Factor showing a ~10%, ~22% and ~36% improvement, respectively, in comparison to the AD NiFe devices.

These improvements were due to the changes in the structural and chemical composition, with the oxidation seeing the integration of oxygen into the material, as the nickel and iron metal was oxidised to form $Ni(OH)_2$ and Fe_2O_3, as confirmed by TEM and SAED. This oxygen integration allowed for the crystal lattice to change from the typical fcc cubic lattice to a trigonal crystal symmetry with rhombohedral lattices, as well allowing for the increased

porosity of the material, as shown by the presence of void holes in the structure, as shown by TEM.

300 cycles or even 450 CV cycles did not see the complete oxidation of the AD NiFe material, as proven by TEM results. Therefore hypothetically, if an entire AD NiFe deposit (3.3μ m for device cores) could be oxidised by CV oxidation, ultrasoft coercivity results (< 10A/m) could be seen, assuming a continuous improvement of coercivity as more of the core was oxidised, as well as an increase in other magnetic, electrical and device results. However based on the CV process of NiFe oxidation, for a 3.3 μm thick sample, this process could take up to 70-80 hours, assuming a linear conversion rate.

For CoNiFe, an entirely new bath was created to produce a 3.3 μm CoNiFe film with the approximate composition of $Co_{63}Ni_{16}Fe_{22}$. This as-deposited material was chosen as the integration of Co into a material increases its corrosion resistance, a necessary improvement for cores that are intended to work in high-frequency applications. This material also saw specific improvements in comparison to NiFe, such as coercivity & anisotropy and more importantly; the working frequency. It was therefore anticipated that when oxidised, the Oxi-CoNiFe would see even further improvements, creating a new candidate material for high-frequency devices.

The as-deposited CoNiFe material showed a B_{sat} of 1.56 T, a B_r of ~30 mT, a H_c of ~20 A/m, a H_k of ~1337 A/m, a relative permeability of ~674, a loss tangent of 0.2018 and overall material Q-Factor of 4.98. Once entirely fabricated, the AD CoNiFe devices showed an improved working frequency in comparison to AD & Oxi-NiFe, from 4 MHz to 10 MHz.

The oxidation of CoNiFe saw diminished results, with ~19.5%, ~39%, ~35%, ~10%, ~4.5% deterioration in B_{sat}, B_r, H_c, H_k & relative permeability respectively. The loss tangent and material Q-Factor saw an increase ~13% & ~15% respectively. Once entirely fabricated the Oxi-CoNiFe devices were compared to the AD CoNiFe devices, with results showing a deterioration of device inductance and more importantly the Q-factor by ~10% & ~8% respectively, despite the improvement in AC resistance of ~3%.

TEM results estimated the crystalline structure of CoNiFe to be the face-centred/body-centred cubic lattice mix, of the Fm-3m space group, O_h point group. Once oxidised, the Oxi-CoNiFe remained an fcc/bcc cubic lattice mix, although the space group changed to an Fd-3m space group, O_h point group, with a (111) & (220) crystal plane.

The oxidation process of CoNiFe also only saw the oxidation of 250 nm of material, despite the 400 cycles. Based on the increased chemical resistance of CoNiFe in comparison to NiFe due to addition of cobalt, it was expected that the material would take longer to oxidise. Based on the TEM results, for full oxidation of 3.3 μm of CoNiFe, the oxidation process could take twice as long as NiFe, at 140-160 hours. However, based on the formation of antiferromagnetic cobalt oxides, converting more of the AD CoNiFe to Oxi-NiFe would most likely be further detrimental to the material's properties based on the current AD CoNiFe composition.

Based on the composition of NiFe/CoNiFe and their oxidised counterparts, a composition conversion percentage was calculated, showing the percentage composition change of nickel and iron in both NiFe and CoNiFe once oxidised. For both materials, the change in the composition of nickel and iron was ~64% and 56%, respectively, once oxidised. For cobalt in CoNiFe the composition change percentage was ~65% once oxidised, with the Co percentage in AD CoNiFe falling from 63.39% to 41.06% in Oxi-CoNiFe.

These changes in the composition were caused by the addition of oxygen to the material as it is oxidised; however, it is clear that Oxi-CoNiFe contains far less nickel and iron oxides than Oxi-NiFe. The oxides formed in Oxi-NiFe, such as NiO and Fe_2O_3 are known to be ferromagnetic, while $Ni(OH)_2$ is known to be paramagnetic However, the cobalt oxides formed, mainly Co_3O_4 and CoO are known to antiferromagnetic, and only Co_2O_3 is paramagnetic. Based on these findings, the formation of these Co_3O_4 and CoO most likely caused the diminished results of Oxi-CoNiFe. Based on the oxides formed and the composition of the Oxi-CoNiFe, it was estimated that fabricating an alternative CoNiFe material, with a composition of $Co_{\leq 60}Fe_{\geq 20}Ni_{\geq 20}$ could show the improved magnetic and electrical properties as seen in Oxi-NiFe due to decrease antiferromagnetic cobalt oxide formation and increase in iron and nickel oxides, while still maintaining enough cobalt to increase the alloys corrosion resistance and working frequency. The oxidation timeframe should, therefore, also decrease.

The oxidation process for magnetic alloys has been shown to be capable of working with alloys other than just NiFe. Based on the results, it can be concluded that Co, Fe and Ni-based alloys, such as CoNiFe (or others such as CoFe) can be oxidised. It may be possible to make changes to this process that will increase the speed of oxidation or limit the growth of certain unwanted oxides, especially for cobalt oxide growth.

Bibliography

Permission from all relative parties for the use of copyright figures in this dissertation was confirmed and received electronically via email or by the Copyright Clearance Center at http://www.copyright.com/. Each figure is clearly labelled with its relevant citation, which are listed below.

1. Hurley, W.G. and W.H. Wölfle, *Transformers and inductors for power electronics: Theory, design and applications*. 2013: John Wiley & Sons.
2. Purcell, E.M. and D.J. Morin, *Electricity and magnetism*. 2013: Cambridge University Press.
3. Singh, Y., *Electro Magnetic Field Theory*. 2011: Pearson Education India.
4. Jjbeard, *Inductor*, Inductor.svg, Editor. 2006, Wikipedia: https://commons.wikimedia.org/wiki/File:Inductor.svg.
5. Zureks, *Solenoid*, Solenoid-1.png, Editor. 2008, Wikipedia: https://commons.wikimedia.org/wiki/File:Solenoid-1.png.
6. Peripitus, *Toroidal inductor*, T. inductor.jpg, Editor. 2007, Wikipedia: https://commons.wikimedia.org/wiki/File:Toroidal_inductor.jpg.
7. Nave, R., *Solenoids as Magnetic Field Sources*. Hyper Physics: http://hyperphysics.phy-astr.gsu.edu/hbase/hframe.html.
8. Nave, R., *Approximate Inductance of a Toroid*. Hyper Physics: http://hyperphysics.phy-astr.gsu.edu/hbase/magnetic/indtor.html.
9. Elert, G. *Inductance*. 2019 [cited 2019; Available from: https://physics.info/inductance/.
10. Jiles, D., *Introduction to magnetism and magnetic materials*. 2015, CRC press. p. 44-45, 332-352.
11. Podder, P., et al. *Ultra-low loss integrated magnetics platform for high frequency power delivery networks*. in *CIPS 2020; 11th International Conference on Integrated Power Electronics Systems*. 2020. VDE.
12. Podder, P., et al. *Electrical Characterisation of Thin Film CZTB Solenoid Inductors for PwrSiP*. in *PwrSoc 18*. 2018. Hsinchu, Taiwan: PwrSoc.
13. Sturcken, N. *DC-DC Power Conversion with CMOS Integrated Thin-Film Inductors*. in *IEEE Workshop on Power Systems on Chip (PowerSOC)*. 2016.
14. Sturcken, N., et al. *Magnetic thin-film inductors for monolithic integration with CMOS*. in *2015 IEEE International Electron Devices Meeting (IEDM)*. 2015. IEEE.
15. Rohan, J.F., et al., *Electroless thin film CoNiFe–B alloys for integrated magnetics on Si*. Electrochimica Acta, 2009. **54**(6): p. 1851-1856.
16. NDT Resource Center, *Hysteresis Loop*. 2019, NDT Resource Center: https://www.nde-ed.org/EducationResources/CommunityCollege/MagParticle/Physics/HysteresisLoop.htm.
17. Chetvorno, *Laminated core eddy currents 2*, L.c.e.c. 2.svg, Editor. 2016, Wikipedia: https://commons.wikimedia.org/wiki/File:Laminated_core_eddy_currents_2.svg.
18. Zhang, G., M. Graef, and F. van Roosmalen. *The rationale and paradigm of" more than Moore"*. in *56th Electronic Components and Technology Conference 2006*. 2006. IEEE.
19. Arden, W., et al., *More-than-Moore white paper*. Version, 2010. **2**: p. 14.

20. Foley, R., et al. *Technology roadmapping for power supply in package (PSiP) and power supply on chip (PwrSoC)*. in *2010 Twenty-Fifth Annual IEEE Applied Power Electronics Conference and Exposition (APEC)*. 2010. IEEE.
21. Zou, J., et al., *Development of three-dimensional inductors using plastic deformation magnetic assembly (PDMA).* IEEE Transactions on Microwave Theory and Techniques, 2003. **51**(4): p. 1067-1075.
22. Zolfaghari, A., A. Chan, and B. Razavi, *Stacked inductors and transformers in CMOS technology.* IEEE Journal of Solid-State Circuits, 2001. **36**(4): p. 620-628.
23. Zhang, H.J., *Basic concepts of linear regulator and switching mode power supplies.* Linear Technology, 2013. **140**.
24. Hayes, J.G. and G.A. Goodarzi, *Electric Powertrain*. 2017: Wiley Online Library. 51.
25. BUTTAY, C., *Buck Operating*, B. operating.svg, Editor. 2006, Wikipedia: https://commons.wikimedia.org/wiki/File:Buck_operating.svg.
26. O'Mathuna, C., et al., *Review of integrated magnetics for power supply on chip (PwrSoC).* IEEE Transactions on Power Electronics, 2012. **27**(11): p. 4799-4816.
27. Roy, S., et al., *Pulse reverse plating for integrated magnetics on Si.* Journal of magnetism and magnetic materials, 2005. **290**: p. 1524-1527.
28. Hitachi Metals Ltd. *FINEMET®*. 2005. **Apr.05**.
29. Lee, D.W., K.-P. Hwang, and S.X. Wang, *Fabrication and analysis of high-performance integrated solenoid inductor with magnetic core.* IEEE Transactions on Magnetics, 2008. **44**(11): p. 4089-4095.
30. Park, J.-W., F. Cros, and M.G. Allen, *Planar spiral inductors with multilayer micrometer-scale laminated cores for compact-packaging power converter applications.* IEEE Transactions on Magnetics, 2004. **40**(4): p. 2020-2022.
31. Brunet, M., et al., *Electrical performance of microtransformers for DC-DC converter applications.* IEEE Transactions on Magnetics, 2002. **38**(5): p. 3174-3176.
32. Wang, N., et al., *High-frequency micro-machined power inductors.* Journal of Magnetism and Magnetic Materials, 2005. **290**: p. 1347-1350.
33. McLyman, C.W.T., *Transformer and inductor design handbook*. 2016: CRC press.
34. Wu, H., et al., *High-frequency magnetic thin-film inductor integrated on flexible organic substrates.* IEEE Transactions on Magnetics, 2017. **53**(11): p. 1-7.
35. Mack, C., *Fundamental principles of optical lithography: the science of microfabrication*. 2008: John Wiley & Sons.
36. Xiao, H., *Introduction to semiconductor manufacturing technology*. 2000: Prentice Hall.
37. VLSI Expert, *Effects of Etching Processes*, Etching, Editor. 2014, VLSI Expert: http://www.vlsi-expert.com/2014/07/effect-of-etching-process_28.html.
38. Mack, C.A., *The Lithography Tutor - Depth of Focus*, in *Microlithography World*. 1995, PennWell Corp. p. 20-21.
39. Yang, H.R., et al. *Lithography process controllers and photoresist monitoring by signal response metrology (SRM)*. in *Metrology, Inspection, and Process Control for Microlithography XXIX*. 2015. International Society for Optics and Photonics.
40. Mack, C.A. *Resolution and depth of focus in optical lithography*. in *Microlithographic Techniques in IC Fabrication*. 1997. International Society for Optics and Photonics.
41. ALLRESIST GmbH. *What are photoresists composed of, and how do they work?* 2019; Available from: http://www.allresist.com/faq-photoresists-composition/.
42. MicroChemicals GmbH. *Photoresist Processing* 2019; Available from: https://www.microchemicals.com/products/photoresists.html.

43. Iam, M., *Photoresist of Photolithography*, P.o. Photolithography.png, Editor. 2017, Wikipedia: https://commons.wikimedia.org/wiki/File:Photoresist_of_Photolithography.png.
44. Smokefoot, *Structure of novolak segment*, NovolakCresol.png, Editor. 2019, Wikipedia: https://commons.wikimedia.org/wiki/File:NovolakCresol.png.
45. Murata, M., M. Koshiba, and Y. Harita, *Positive Photoresist Chemistry*, in *Progress in Pacific Polymer Science*. 1991, Springer. p. 283-294.
46. Levinson, H.J., *Photochemistry of Novolak/DNQ g- and i-line Resists*, in *Principles of lithography*. 2005, SPIE press. p. 68-70.
47. Ohba, K., *Overview of photo-definable benzocyclobutene polymer.* Journal of Photopolymer Science and Technology, 2002. **15**(2): p. 177-182.
48. *Processing Procedures for CYCLOTENE 4000 Series Photo BCB Resins*. 2005 Feb 2005 [cited 2019; Available from: http://msdssearch.dow.com/PublishedLiteratureDOWCOM/dh_096d/0901b8038096dae3.pdf.
49. Shieu, F. and M. Shiao, *Effect of a Ti interlayer on the bond strength and thermal stability of the Cu/benzocyclobutene-divinyl tetramethyldisiloxane interface.* Journal of adhesion science and technology, 1998. **12**(1): p. 19-28.
50. Yang, D.-Q. and E. Sacher, *Argon ion treatment of the Dow Cyclotene 3022 surface and its effect on the adhesion of evaporated copper.* Applied surface science, 2001. **173**(1-2): p. 30-39.
51. Born, M. and E. Wolf, *Principles of optics: electromagnetic theory of propagation, interference and diffraction of light*. 2013: Elsevier.
52. Neutronix-Quintel. *PHOTOGRAPHY SPECIALIST - Specializing in the remanufacturing custom engineering of the PLA 501/600 series mask aligners*. n.d [cited 2019 27.08.2019]; Available from: http://www.acrosemi.com/neutronix/pdf/pla_data_sheet.pdf.
53. Rothschild, M., *Projection optical lithography.* Materials Today, 2005. **8**(2): p. 18-24.
54. ASTM, S., *Standard test methods for measuring adhesion by tape test.* Annu. B. ASTM Stand., 2009. **6**: p. 1-8.
55. Microchemicals GmbH *Resist Adhesion*. 2005.
56. Rossnagel, S. and J. Hopwood, *Metal ion deposition from ionized mangetron sputtering discharge.* Journal of Vacuum Science & Technology B: Microelectronics and Nanometer Structures Processing, Measurement, and Phenomena, 1994. **12**(1): p. 449-453.
57. Denton Vacuum, *Magnetron Sputtering Solutions*, MagnetronSputtering.jpg, Editor. 2019, Denton Vacuum: www.dentonvacuum.com.
58. Angstrom Sciences. *Magnetron Sputtering*. n.d [cited 2019 23.07.2019]; Available from: https://www.angstromsciences.com/magnetron-sputtering-deposition.
59. Quorum Technologies Ltd *Q300T D Plus Brochue*. 2018.
60. Wasa, K. and S. Hayakawa, *Handbook of Sputter Deposition Technology: Principles, Technology and Applications (Materials Science and Process Technology Series)*. 1993: New York: William Andrew.
61. Spindler, M., et al., *Chemical etching of Tungsten thin films for high-temperature surface acoustic wave-based sensor devices.* Thin Solid Films, 2016. **612**: p. 322-326.
62. Kanani, N., *Electroplating: basic principles, processes and practice*. 2004: Elsevier.
63. Schlesinger, M. and M. Paunovic, *Modern electroplating*. Vol. 55. 2011: John Wiley & Sons.
64. Haynes, W.M., D.R. Lide, and T.J. Bruno, *CRC handbook of chemistry and physics : a ready-reference book of chemical and physical data*. 2016.

65. Paul Flowers, K.T., Richard Langley. *Electrolysis*. 2019 [cited 2019 25.07.2019]; Available from: https://chem.libretexts.org/Bookshelves/General_Chemistry/Map%3A_Chemistry_-_Atoms_First_(OpenSTAX)/16%3A_Electrochemistry/16.7%3A_Electrolysis.
66. Jayakrishnan, D.S., *Electrodeposition: the versatile technique for nanomaterials*, in *Corrosion Protection and Control Using Nanomaterials*. 2012, Elsevier. p. 86-125.
67. Romankiw, P.C.A.L.T., *Magnetically Soft Materials in Data Storage: Their Properties and Electrochemistry*, in *Advances in Electrochemical Science and Engineering*. 2008. p. 227-321.
68. Nickel Institute, *Nickel Plating Handbook*. 2014, https://www.nickelinstitute.org/media/2323/nph_141015.pdf: Nickel Institute.
69. Nakanishi, T., et al., *Pulsed electrodeposition of nanocrystalline CoNiFe soft magnetic thin films.* Journal of the Electrochemical Society, 2001. **148**(9): p. C627-C631.
70. Chandrasekar, M. and M. Pushpavanam, *Pulse and pulse reverse plating—Conceptual, advantages and applications.* Electrochimica Acta, 2008. **53**(8): p. 3313-3322.
71. Fink, Y. and G. Beach, *Lecture 25 - Hysteresis in Ferromagnetic Materials*. 2013, MIT OpenCourseWare: https://ocw.mit.edu/courses/materials-science-and-engineering/3-024-electronic-optical-and-magnetic-properties-of-materials-spring-2013/lecture-notes/MIT3_024S13_2012lec25.pdf.
72. Gardner, D.S., et al., *Review of on-chip inductor structures with magnetic films.* IEEE Transactions on Magnetics, 2009. **45**(10): p. 4760-4766.
73. Flynn, D., R. Dhariwal, and M. Desmulliez, *A design study of microscale magnetic components for operation in the MHz frequency range.* Journal of Micromechanics and Microengineering, 2006. **16**(9): p. 1811.
74. Godsell, J.F., et al., *Precessional dynamics of Ni 45 Fe 55 thin films for ultrahigh frequency integrated magnetics.* Journal of Applied Physics, 2010. **107**(3): p. 033907.
75. Wang, N., et al., *Micro-inductors integrated on silicon for power supply on chip.* Journal of Magnetism and Magnetic Materials, 2007. **316**(2): p. e233-e237.
76. Rhen, F.M., et al., *High-frequency permeability of electroplated CoNiFe and CoNiFe–C alloys.* Journal of Magnetism and Magnetic Materials, 2008. **320**(20): p. e819-e822.
77. Osaka, T., et al., *A soft magnetic CoNiFe film with high saturation magnetic flux density and low coercivity.* Nature, 1998. **392**(6678): p. 796.
78. Heck, C., *Magnetic materials and their applications*. 2013: Elsevier. p. 392.
79. Chenna, A., et al., *Characterisation of electroplated Ni45Fe55 thin films on n-Si (111).* Surface Engineering, 2019. **35**(2): p. 189-198.
80. Dionigi, F., et al., *Design criteria, operating conditions, and nickel–iron hydroxide catalyst materials for selective seawater electrolysis.* ChemSusChem, 2016. **9**(9): p. 962-972.
81. Görlin, M., et al., *Oxygen evolution reaction dynamics, faradaic charge efficiency, and the active metal redox states of Ni–Fe oxide water splitting electrocatalysts.* Journal of the American Chemical Society, 2016. **138**(17): p. 5603-5614.
82. Dionigi, F. and P. Strasser, *NiFe-Based (Oxy) hydroxide Catalysts for Oxygen Evolution Reaction in Non-Acidic Electrolytes.* Advanced Energy Materials, 2016. **6**(23): p. 1600621.
83. Anthony, R., *Technology platform for the fabrication of micro-inductors on silicon for dc-dc conversion*, in *Electrical and Electronic Engineering*. 2018, Univeristy College Cork.
84. Lu, Z., et al., *Three-dimensional NiFe layered double hydroxide film for high-efficiency oxygen evolution reaction.* Chemical communications, 2014. **50**(49): p. 6479-6482.

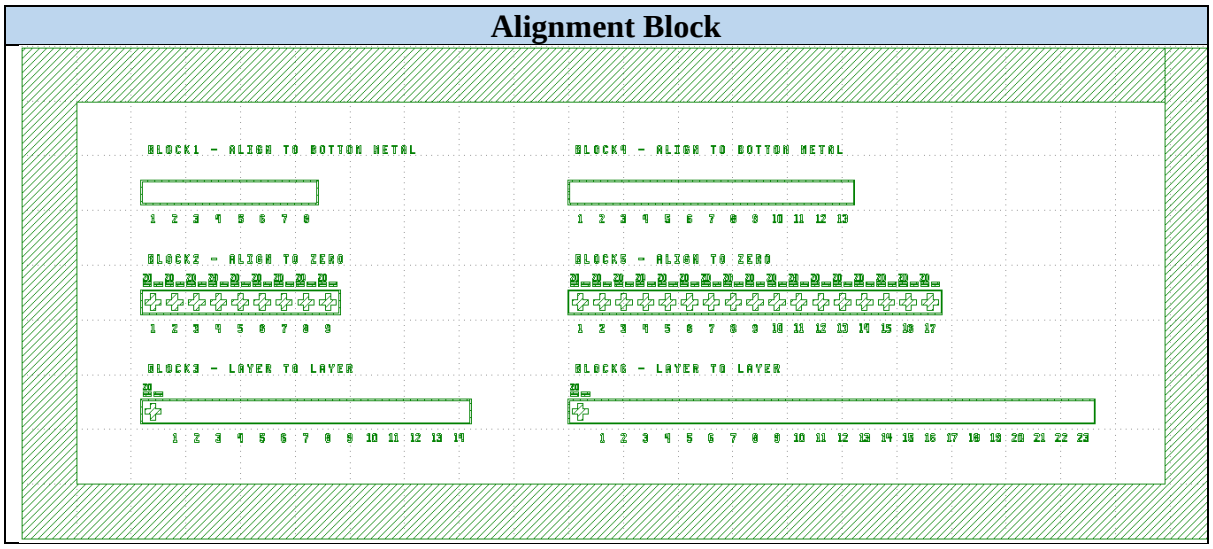
85. Niu, L., et al., *Production of Two-Dimensional Nanomaterials via Liquid-Based Direct Exfoliation.* Small, 2016. **12**(3): p. 272-293.
86. Harvey, A., et al., *Production of Ni(OH)2 nanosheets by liquid phase exfoliation: from optical properties to electrochemical applications.* Journal of Materials Chemistry A, 2016. **4**(28): p. 11046-11059.
87. McAteer, D., et al., *Liquid Exfoliated Co(OH)2 Nanosheets as Low-Cost, Yet High-Performance, Catalysts for the Oxygen Evolution Reaction.* Advanced Energy Materials, 2018. **8**(15).
88. Trotochaud, L., et al., *Nickel–iron oxyhydroxide oxygen-evolution electrocatalysts: the role of intentional and incidental iron incorporation.* Journal of the American Chemical Society, 2014. **136**(18): p. 6744-6753.
89. Browne, M.P., et al., *The goldilocks electrolyte: examining the performance of iron/nickel oxide thin films as catalysts for electrochemical water splitting in various aqueous NaOH solutions.* Journal of Materials Chemistry A, 2016. **4**(29): p. 11397-11407.
90. Elgrishi, N., et al., *A Practical Beginner's Guide to Cyclic Voltammetry.* Journal of Chemical Education, 2017. **95**(2): p. 197-206.
91. Mabbott, G.A., *An introduction to cyclic voltammetry.* Journal of Chemical education, 1983. **60**(9): p. 697.
92. Kissinger, P.T. and W.R. Heineman, *Cyclic voltammetry.* Journal of Chemical Education, 1983. **60**(9): p. 702.
93. Tompkins, H. and J. Augis, *The oxidation of cobalt in air from room temperature to 467 C.* Oxidation of Metals, 1981. **16**(5-6): p. 355-369.
94. Ismail, K.M. and W. Badawy, *Electrochemical and XPS investigations of cobalt in KOH solutions.* Journal of applied electrochemistry, 2000. **30**(11): p. 1303-1311.
95. Grdeń, M. and J. Jagiełło, *Oxidation of electrodeposited cobalt electrodes in an alkaline electrolyte.* Journal of Solid State Electrochemistry, 2013. **17**(1): p. 145-156.
96. Tian, L., et al., *Electrochemical study on cobalt film modified glassy carbon electrode and its application.* Electrochimica Acta, 2010. **55**(9): p. 3083-3088.
97. Abd El Haleem, S.M. and E.E. Abd El Aal, *Electrochemical behaviour of iron in alkaline sulphide solutions.* Corrosion Engineering, Science and Technology, 2013. **43**(2): p. 173-178.
98. Guzman, R.S., J. Vilche, and A. Arvia, *The potentiodynamic behaviour of iron in alkaline solutions.* Electrochimica Acta, 1979. **24**(4): p. 395-403.
99. Macdonald, D.D. and D. Owen, *The electrochemistry of Iron in lM lithium hydroxide solution at 22 and 200 C.* Journal of The Electrochemical Society, 1973. **120**(3): p. 317-324.
100. Lyons, M.E.G., R.L. Doyle, and M.P. Brandon, *Redox switching and oxygen evolution at oxidized metal and metal oxide electrodes: iron in base.* Physical Chemistry Chemical Physics, 2011. **13**(48): p. 21530-21551.
101. Song, I., D. Gervasio, and J. Payer, *Electrochemical behaviour of iron and iron oxide thin films in alkaline (1 M KOH) aqueous solution: a voltammetry study for cathodic instability of coating/metal interface.* Journal of applied electrochemistry, 1996. **26**(10): p. 1045-1052.
102. Bewick, A., M. Kalaji, and G. Larramona, *In-situ infrared spectroscopic study of the anodic oxide film on iron in alkaline solutions.* Journal of electroanalytical chemistry and interfacial electrochemistry, 1991. **318**(1-2): p. 207-221.
103. Tschinkel, W., H. Neugebauer, and A. Neckel, *In situ FTIR spectroscopy of iron electrodes in alkaline solutions II. External reflection absorption spectroscopy.* Journal of The Electrochemical Society, 1990. **137**(5): p. 1475-1480.

104. Andersson, B. and L. Öjefors, *Slow potentiodynamic studies of porous alkaline iron electrodes.* Journal of The Electrochemical Society, 1976. **123**(6): p. 824-828.
105. Seghiouer, A., et al., *Electrochemical oxidation of nickel in alkaline solutions: a voltammetric study and modelling.* Journal of Electroanalytical Chemistry, 1998. **442**(1-2): p. 113-123.
106. Okuyama, M. and S. Haruyama, *Passive film formed on nickel in a neutral solution.* Corrosion Science, 1974. **14**(1): p. 1-14.
107. Hummel, R., R. Smith, and E. Verink Jr, *The passivation of nickel in aqueous solutions—I. The identification of insoluble corrosion products on nickel electrodes using optical and ESCA techniques.* Corrosion science, 1987. **27**(8): p. 803-813.
108. Smith, R., R. Hummel, and J. Ambrose, *The passivation of nickel in aqueous solutions—II. An in situ investigation of the passivation of nickel using optical and electrochemical techniques.* Corrosion science, 1987. **27**(8): p. 815-826.
109. Lyons, M., et al., *Hydrous Nickel Oxide: Redox Switching and the Oxygen Evolution Reaction in Aqueous Alkaline Solution.* Journal of The Electrochemical Society, 2012. **159**: p. H932-H944.
110. Visscher, W. and E. Barendrecht, *Anodic oxide films of nickel in alkaline electrolyte.* Surface Science, 1983. **135**(1-3): p. 436-452.
111. Vuković, M., *Voltammetry and anodic stability of a hydrous oxide film on a nickel electrode in alkaline solution.* Journal of applied electrochemistry, 1994. **24**(9): p. 878-882.
112. Burke, L. and D. Whelan, *Growth of electrochromic film on nickel in base under potential cycling conditions.* Journal of Electroanalytical Chemistry and Interfacial Electrochemistry, 1980. **109**(1-3): p. 385-388.
113. MicroChemicals GmbH. *AZ® 9200-Series - Thick Resists for High Resolution*. [cited 2019 01.04.2019]; AZ 9260 Photoresist Specs]. Available from: https://www.microchemicals.com/products/photoresists/az_9260.html.
114. KG, D.I.M.S.G.C., *Bright Copper ACG 8*. 2004, Schlötter Galvanotechnik: www.schloetter.com. p. 8.
115. *Product Datasheet - SA-1m Single Cell Electroplating System* 2018, Digital Matrix: https://www.platingpower.com/.
116. Uhm, Y.R., K.Y. Park, and S.J. Choi, *The effects of current density and saccharin addition on the grain size of electroplated nickel.* Research on Chemical Intermediates, 2015. **41**(7): p. 4141-4149.
117. Riastuti, R., et al. *Effect of saccharin as additive in nickel electroplating on SPCC steel*. in *AIP Conference Proceedings*. 2018. AIP Publishing.
118. Martyak, N., *Electroplating of low-stress nickel.* CA Patent, 1998. **2236933**: p. A1.
119. Rasmussen, A.A., P. Møller, and M.A. Somers, *Influence of 1, 3, 6 naphthalene trisulfonic acid on microstructure & hardness in electrodeposited Ni-layers.* Plating and surface finishing, 2002. **89**(10): p. 46-49.
120. Srimathi, S. and S.M. Mayanna, *Electroplating of Fe-Ni alloys: Effects of sulphamic acid and sulphosalicylic acid.* Journal of applied electrochemistry, 1986. **16**(1): p. 69-74.
121. Smistrup, K., P.T. Tang, and P. Møller, *Pulse reversal permalloy plating process for MEMS applications.* ECS Transactions, 2007. **3**(25): p. 179-189.
122. Ghaemi, M., E. Ghafouri, and J. Neshati, *Influence of the nonionic surfactant Triton X-100 on electrocrystallization and electrochemical performance of lead dioxide electrode.* Journal of power sources, 2006. **157**(1): p. 550-562.

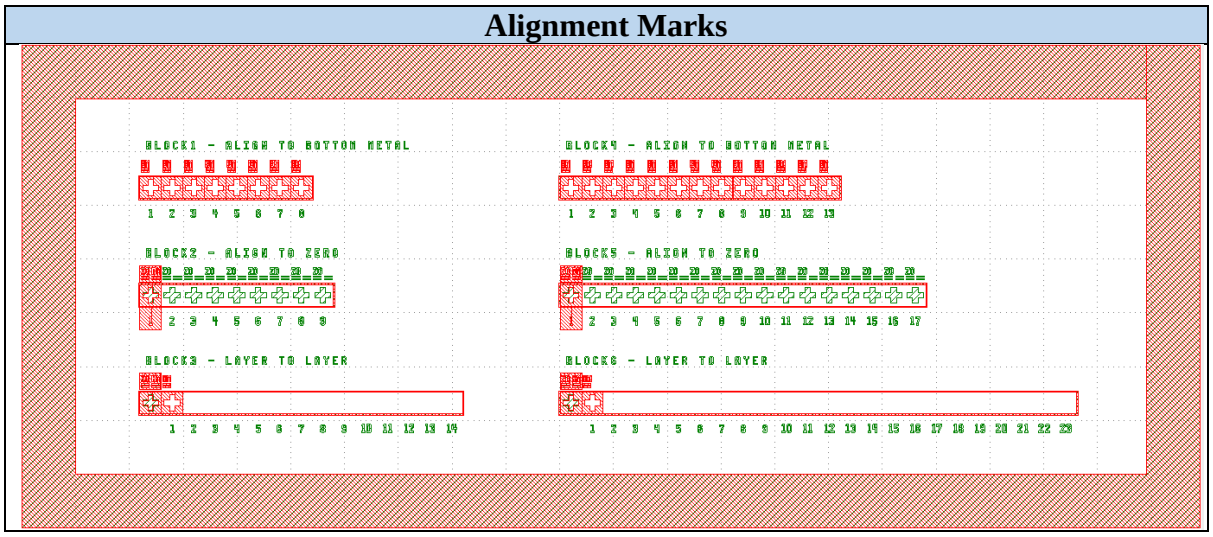
123. Tabakovic, I., V. Inturi, and S. Riemer, *Composition, structure, stress, and coercivity of electrodeposited soft magnetic CoNiFe films: thickness and substrate dependence.* Journal of the Electrochemical Society, 2002. **149**(1): p. C18-C22.
124. Tabakovic, I. and S. Riemer, *Roughness development in electrodeposited soft magnetic CoNiFe films in the presence of organic additives.* Journal of the Serbian Chemical Society, 2003. **68**(4): p. 349-361.
125. Kim, J., et al., *Highly laminated soft magnetic electroplated CoNiFe thick films.* IEEE Magnetics Letters, 2013. **4**: p. 5000204-5000204.
126. Osaka, T., et al., *Effects of saccharin and thiourea on sulfur inclusion and coercivity of electroplated soft magnetic CoNiFe film.* Journal of the Electrochemical Society, 1999. **146**(9): p. 3295-3299.
127. Metakam GmbH. *Platinised Titanium*. [cited 2019 12.08.2019]; Available from: http://www.metakem.de/en/products/anodes/platinised-titanium.html.
128. Ohashi, K., et al., *Newly developed inductive write head with electroplated CoNiFe film.* IEEE transactions on magnetics, 1998. **34**(4): p. 1462-1464.
129. Ohshima, N., et al., *Digests of the 24th Annual Conference on Magnetics in Japan.* The Magnetics Society of Japan, 2000: p. 359.
130. M. Saito, N.I., K. Ohashi, *Abstract 621*, in *The Electrochemical Society Meeting Abstracts*. Oct 22-27 2000,: Pheonix, AZ.
131. and Mm5713, *Face-centred Cubic Lattice*, F.-c.C. Lattice.png, Editor. 2015, https://commons.wikimedia.org/: https://commons.wikimedia.org/wiki/File:Face-centred_Cubic_Lattice.png.
132. S.D. Marcum, J.M.Y.-R. *Bragg Diffraction Of X-Rays And Of Electrons*. 2000 [cited 2019 29.11.19].
133. Apátiga, L. and V. Castano, *Magnetic behavior of cobalt oxide films prepared by pulsed liquid injection chemical vapor deposition from a metal-organic precursor.* Thin Solid Films, 2006. **496**(2): p. 576-579.
134. Wang, X., et al., *Weak Ferromagnetism and Exchange Bias in Antiferromagnetic Cobalt Oxide Nanoparticles.* Journal of Magnetics, 2018. **23**(4): p. 487-490.
135. Wang, Y., et al., *Hydrogenation induced transformation of paramagnetism to room-temperature ferromagnetism in co-doped TiO2 ceramics.* Journal of Electroceramics, 2006. **16**(4): p. 389-391.
136. Wu, X., et al., *Enhanced multiferroic property in Co2O3-added BiFeO3–BaTiO3 ceramics.* Journal of the Ceramic Society of Japan, 2015. **123**(1442): p. 972-977.

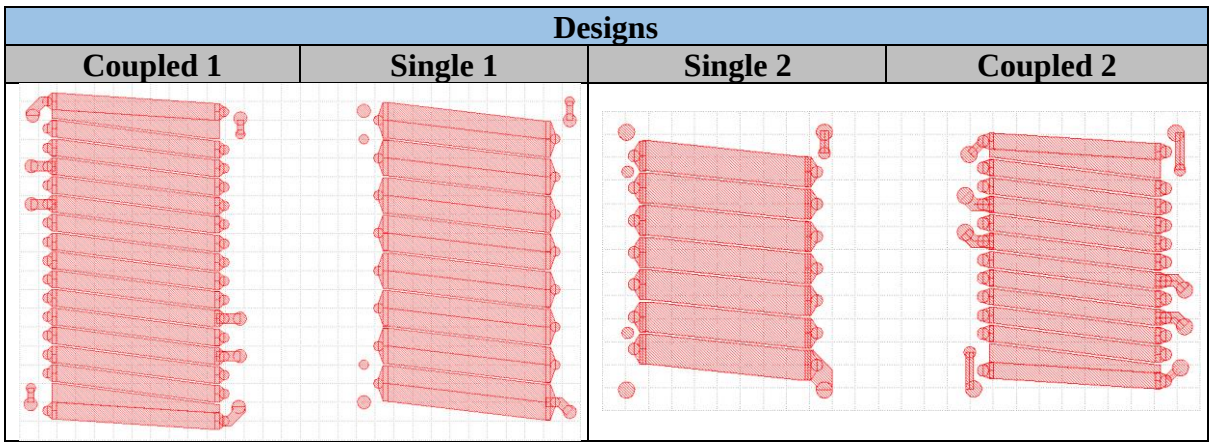
Appendix A – Device Photomask Set

Zero Level

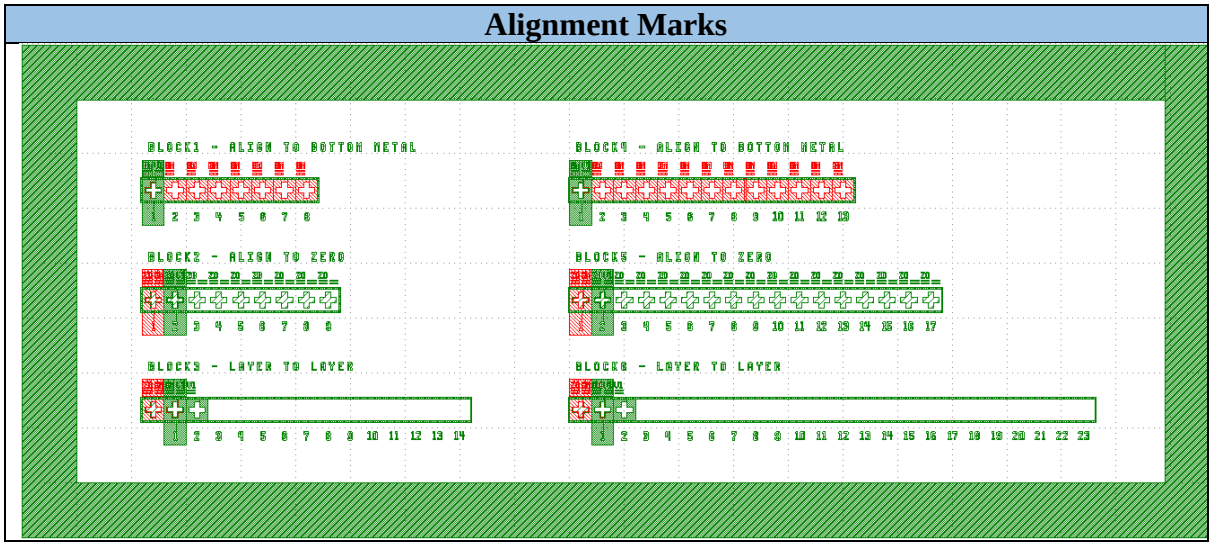


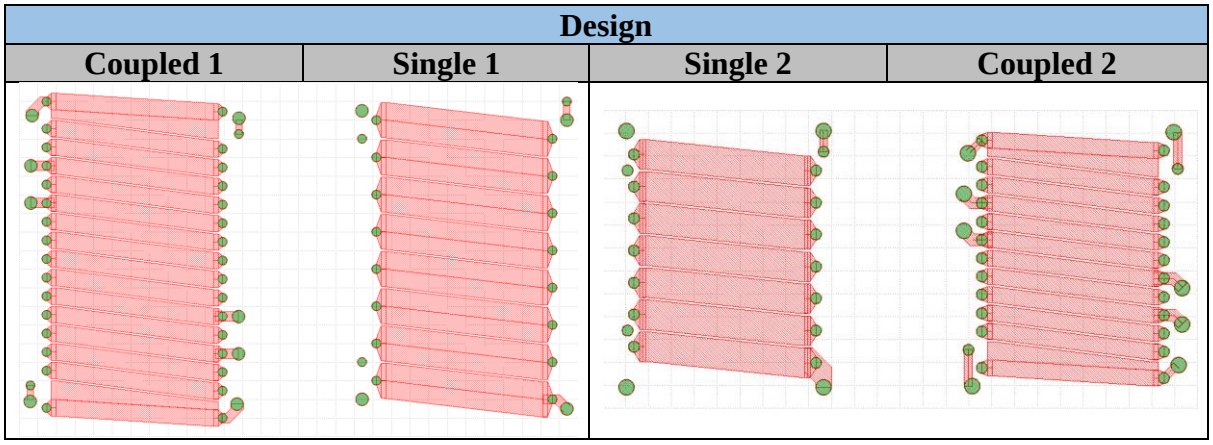
Bottom Metal Windings



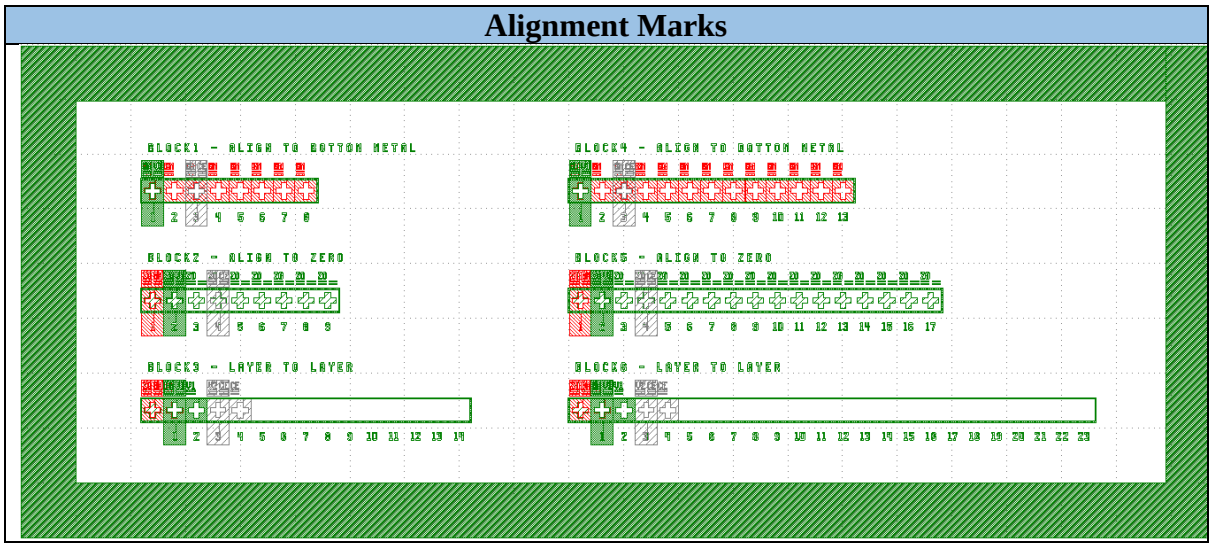


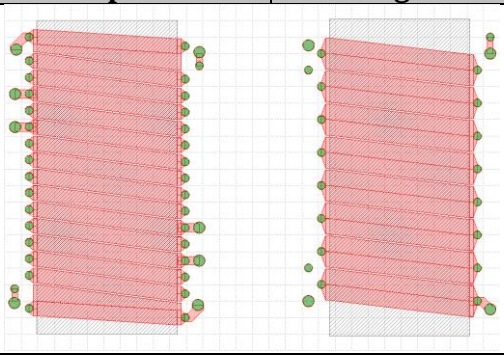
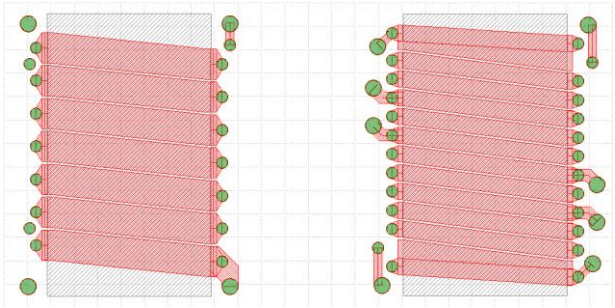
Via 1 – Bottom Via



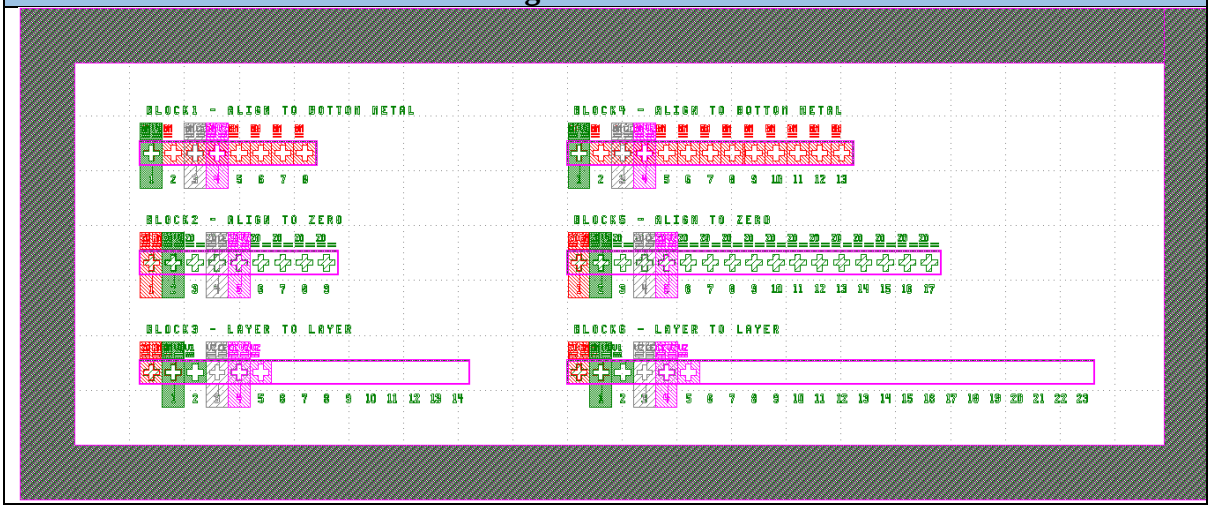


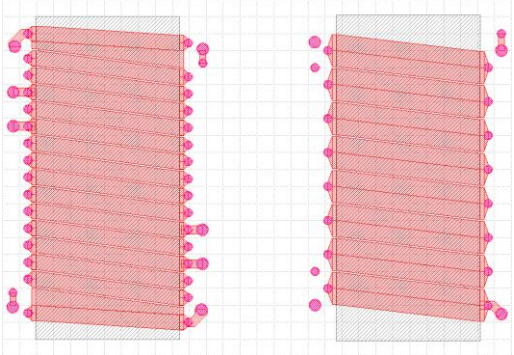
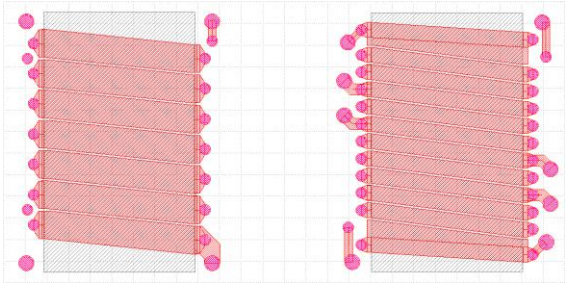
Inductor Core



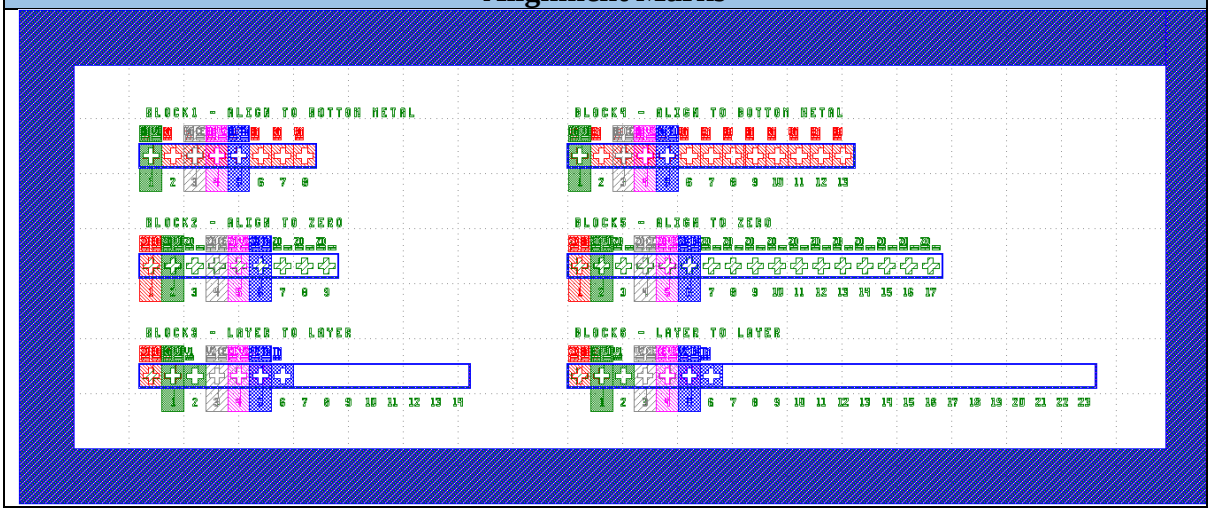
Design			
Coupled 1	Single 1	Single 2	Coupled 2
			

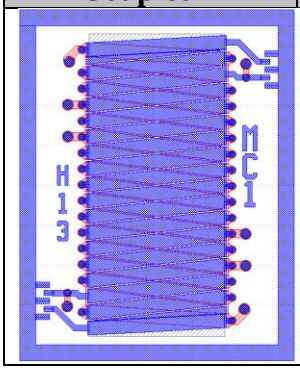
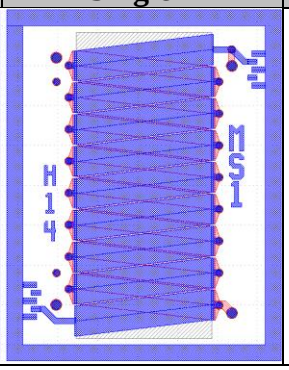
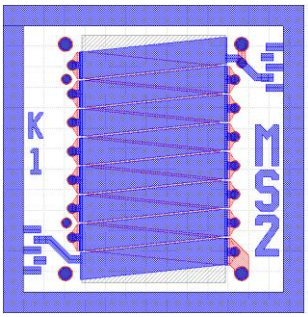
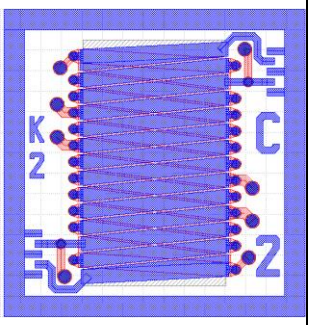
Via 2 – Top Via

Alignment Marks


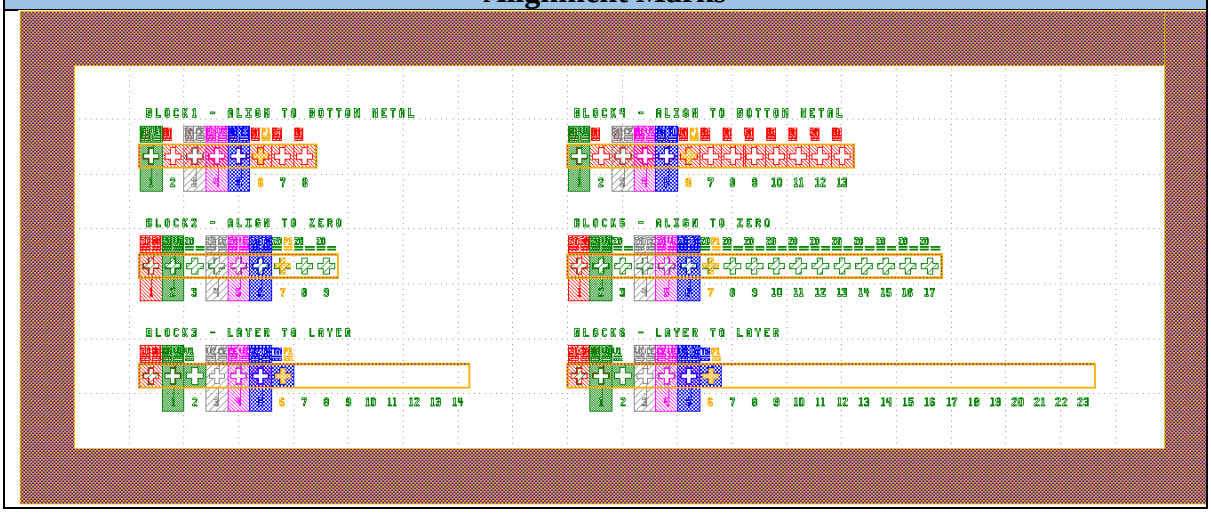
Design			
Coupled 1	Single 1	Single 2	Coupled 2
			

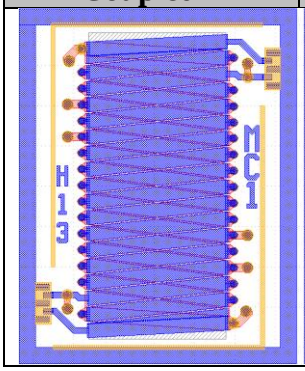
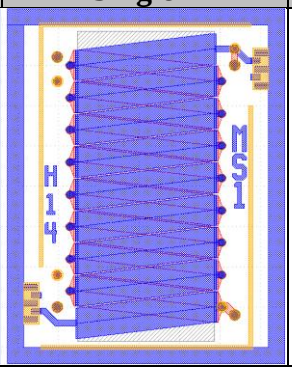
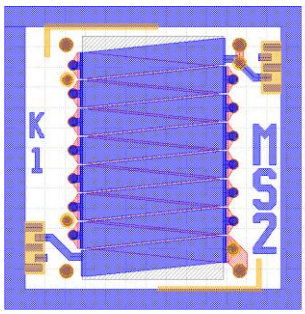
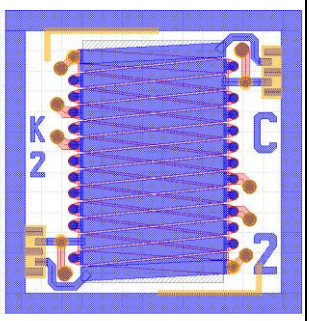
Top Metal Windings

Alignment Marks


Design			
Coupled 1	Single 1	Single 2	Coupled 2
			

Passivation

Alignment Marks


Design			
Coupled 1	Single 1	Single 2	Coupled 2
			

Full Mask Layout

